Chlorinated contaminants mitigation during pyro-gasification of wastes using CaO reactant : experimental and life cycle assessment

Yuanjun Tang

Université Fédérale
Toulouse Midi-Pyrénées

THÈSE

En vue de l'obtention du

DOCTORAT DE L'UNIVERSITÉ DE TOULOUSE

Délivré par :

IMT - École Nationale Supérieure des Mines d'Albi-Carmaux

Cotutelle internationale avec
Institute for thermal power engineering of Zhejiang University

---

Présentée et soutenue par :
Yuanjun TANG

le 27 novembre 2018

Titre :
Chlorinated contaminants mitigation during pyro-gasification of wastes using CaO reactant: Experimental and life cycle assessment

---

École doctorale et discipline ou spécialité
ED MEGEP : Génie des procédés et de l'Environnement

Unité de recherche :
Centre RAPSODEE, UMR CNRS 5302, IMT Mines Albi

Directeur/trice(s) de Thèse :
Ange NZIHOU, Professeur, IMT Mines Albi
Yong CHI, Professeur, Institute for thermal power engineering, Zhejiang University
Elsa WEISS-HORTALA, Maître-assistant, IMT Mines Albi

Jury :

Catherine AZZARO-PANTEL, Professeur, INP INSIACET Toulouse, Présidente
Roger GADIOU, Professeur, Inst. de Science des Matériaux Mulhouse, Rapporteur
Yann ROGAUME, Professeur, ENSTIB Epinal, Rapporteur
Marco BARATIERI, Professeur, Faculty of Sc. and Technology Bolzano, Examinateur

Content

Abbreviation list

Al	Aluminum
AP	Acidification potential
APC	Air pollution control
ad	air-dried basis
ar	as-received basis
BET	Brunauer-Emmett-Teller
BTX	Benzene, Toluene, and Xylene
BTXN	Benzene, Toluene, Xylene, and Naphthalene
$CaCl_2$	Calcium Chloride
CaClOH	Calcium Hydroxychloride
$CaCO_3$	Calcium carbonate, or limestone
CaO	Calcium oxide
$Ca(OH)_2$	Calcium hydroxide
Ca/Cl	Ca, Cl molar ratio
CH_4	Methane
CHP	Combined heat and electricity
Cl	Chlorine
CO_2	Carbon dioxide
CO	Carbon monoxide
EDS	Energy-dispersive X-ray spectroscopy
EP	Eutrophication Potential
EPA	Environmental Protection Agency
ESEM	Environmental Scanning Electron Microscope
FAETP	Freshwater aquatic ecotoxicity
FC	Fixed Carbon
FSF	Fraser–Suzuki Function

GC	Gas Chromatography
GC/MS	Gas Chromatography -Mass Spectrometry
GWP	Global warming
GHG	Greenhouse gas
HCl	Hydrogen Chloride
H_2	Hydrogen
HME	HCl Mitigation Efficiency
HTP	Human toxicity potential
IC	Ion Chromatography
IGCC	Gas turbine combined cycle
IPCC	Intergovernmental Panel on Climate Change
ISO	International Organization for Standardization
KAS	Kissinger-Akahira-Sunose
KCl	Potassium Chloride
LCA	Life cycle assessment
LCI	Life cycle inventory
LCIA	Life cycle impact assessment
LHV	Lower heating value
MFA	Material Flow Analysis
MSW	Municipal solid waste
NaCl	Sodium Chloride
OFW	Ozawa–Flynn–Wall
NP	Nutrient enrichment
PE	Polyethylene
PLD	Product-Layer Diffusion
PVC	Polyvinyl Chloride
PP	Polypropylene
Py-GC/MS	Pyrolysis-Gas Chromatography/Mass Spectrometry
RDF	Refuse derived fuels
SEM	Scanning Electron Microscopy
SETAC	Society of Environmental Toxicology and Chemistry
S-MSW	Simulated Municipal Solid Waste
SRF	Solid recovered fuel
TETP	Terrestrial Ecotoxicity

TG/DTG	Thermogravimetric and derivative thermogravimetric
TGA	Thermogravimetric analyzer
WtE	Waste-to-Energy
XRD	X-ray diffraction
XRF	X-Ray Fluorescence

Chapter 1

Background and literature review

The objective of this chapter is to provide insights and background on current research progress: HCl release from MSW thermal conversion and its control methods; role of CaO reactant on in-furnace tar cracking and upgrading; and LCA methodology and its application on MSW thermal conversion systems. With the overall aim, the structure of this chapter is set as follows:

- **Section 1.1** presents the background and explains the motivation of the present study;

- **Section 1.2** introduces the presence of chlorine in MSW and HCl release from MSW thermal conversion process; besides, the state-of-the-art regarding dehydrochlorination methods are summarized;

- **Section 1.3** focuses on the introduction of reactivity of CaO on pyro-gasification syngas quality enhancement and tar cracking and upgrading;

- **Section 1.4** presents the principle and framework of LCA as evaluation tool for waste system, and its current status application in WtE technologies;

- **Section 1.5** details the structure and contents of the thesis.

1.1 Background and motivation of the thesis

It has to be acknowledged that with the booming of social economy and urbanization all around the world, municipal solid waste (MSW) generation increased dramatically in the past several decades, especially in developing countries. According to the world bank [1], approximately 1.3 billion tons of MSW is generated annually in 2016; and this value is expected to reach 2.2 billion tons by 2025 according to their estimations. **Figure 1. 1**

presents the MSW generation amount in China and France during 2007-2016 [1]. As illustrated, MSW generations in France is quite stable in this period, ranging from 34.1 million tons to 34.8 million tons; however, MSW generation in China increased rapidly from 152.2 million tons in 2007 to 203.6 million tons in 2016, with a quite high annual increasing of ca. 3.3%. Although the total MSW generation amount in China is approximately 5 times higher than that in France, MSW generation per capita in China is nearly 1/5 of that in France. This reflects the fact that developed countries tend to generate more MSW per person as compared to developing Countries. However, due to the huge population in China, the total generation amount of MSW is very high and keeps increasing.

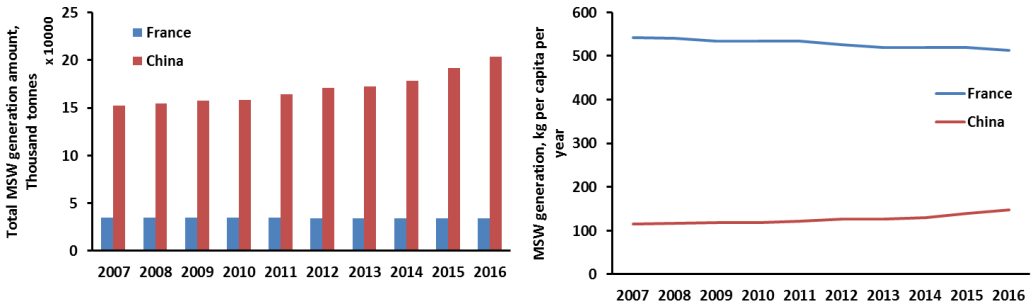

Figure 1. 1 MSW generation in France and China during 2007-2010，data derived from [1]

Under such circumstance, the treatment of MSW has become one of the biggest challenges facing with by the modern societies, owning to its huge amount and serious consequences if not properly treated (for example, air emissions, soil contaminations, groundwater pollution, and even serious public health risks). In recent years, the sanitary landfill is the most popular technology used for MSW treatment in many Countries, because it is the least expensive alternative [2, 3]. However, concerns with respect to MSW have increasingly been shifted from disposal to integrate waste management. The waste hierarchy, as defined by European Directive 2006/12/EC [4] and updated by Directive 2008/98/EC [5] in 2008, ranks the waste management strategies from the top priority of waste prevention, followed by waste reuse, recycling, recovery, and the final option waste disposal. The hierarchy is mainly based on the principle that which waste treatment option is best for the environment. **Figure 1. 2** illustrates the preference and contents of the waste hierarchy according to the Department for Environment Food & Rural Affairs of the U.K. [6].

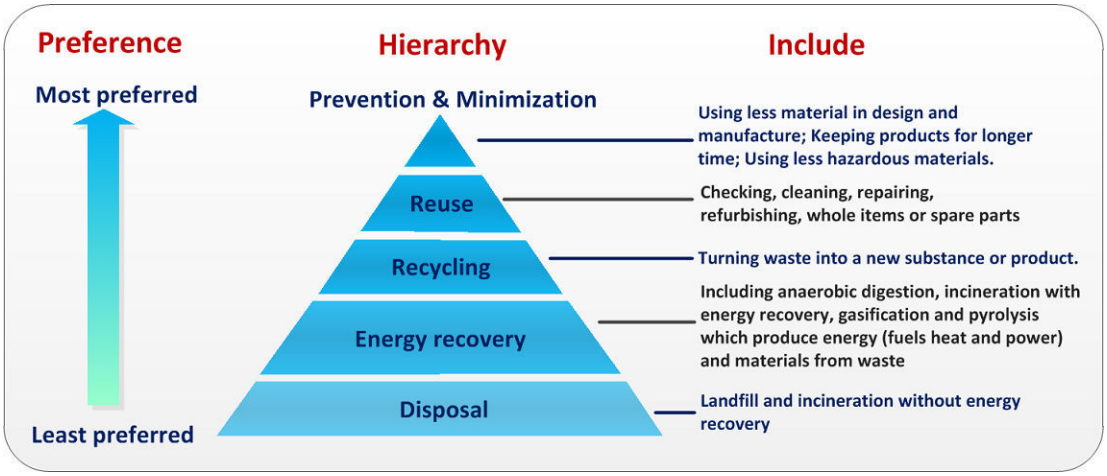

Figure 1. 2 Preference and contents of the waste hierarchy as regulated by European Directive, data derived from [6]

In regard to the waste treatment strategies adopted by different regions, **Figure 1.3** summarizes the share of treatment methods in the E.U. Countries during 2004 to 2015 [7]. As the figure indicates, the most popular MSW treatment methods include landfill, incineration and recycling. And in European countries, recycling has performed an important role in waste management systems. Besides, incineration has also played an increasingly important role in waste management over the past decades, mainly due to the advantages of significant waste reduction, complete disinfection, as well as energy recovery [8]. By incineration, approximately 70% of weight and 90% of volume of MSW are reduced and around 20% of the energy content is able to be recovered in the form of electricity and/or heat [9-11]. Data from the literature revealed that in 2012, approximately 14.5 million tons of MSW (more than 28% of total generated MSW in France) were incinerated in 126 MSW incineration plants [11].Therefore, it is well recognized as an efficient energy recovery method as depicted also in the E.U. waste hierarchy.

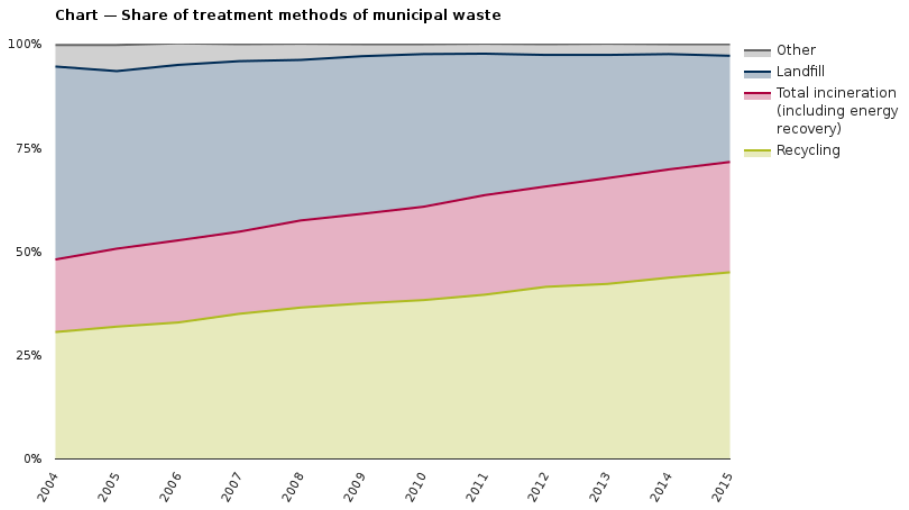

Figure 1. 3 Share of MSW treatment methods in the EU during 2004-2015, data source from Eurostat database [7]

Although MSW incineration becomes more and more popular in recent years, problems are still existing for its popularizing in some Countries and regions, mainly concerning the harmful emissions, especially heavy metals, dioxins and furans, and greenhouse gas emissions [12]. Moreover, due to the relatively high content of chlorine (Cl) in MSW, hydrogen chloride (HCl) is usually generated as a consequence of high temperature thermal conversion. The presence of HCl in incineration flue gas may cause serious problems like high temperature corrosion, toxic organic contaminants (mainly dioxins, furans, and VOCs) formation, acidification, etc. Besides, due to the corrosion potential aroused by HCl gas, the temperature and pressure of the steam for electricity generation are strictly limited at 400 ^{o}C and 40 bar, resulting in the relatively low electricity generation efficiency of MSW incineration plants. According to the statistical results by Beylot et al. [11], the net electricity generation efficiency is as low as 14.96% when only electricity is recovered from French MSW incineration plants. Therefore, chlorine-content contaminants in incineration flue gas must be removed in order to lower the environmental burdens as well as to improve the electricity generation efficiency. Currently, HCl is usually removed together with acid gases by air pollution control (APC) systems, which basically works in temperature range of lower than 300 ^{o}C. Although the removal efficiency of HCl by APC systems is high enough, HCl has already served as corrosive agent and chlorine source for polychlorinated dibenzo-p-dioxins and polychlorinated dibenzofurans (PCDD/Fs) formation during flue gas cooling down under

such conditions. Therefore, HCl removal at higher temperature (i.e. before it causes problems such as corrosion, Cl-source for PCDD/Fs formation, etc.) is of great importance.

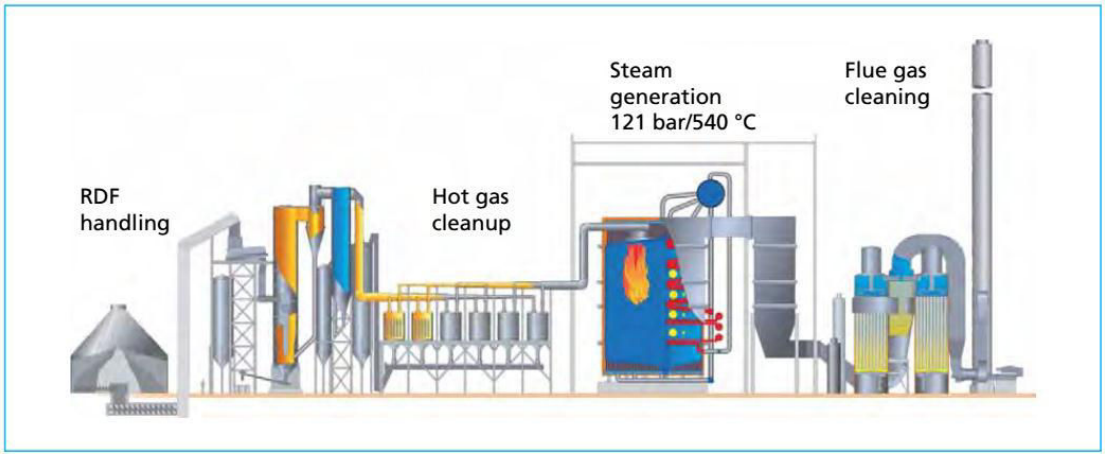

Figure 1. 4 Conceptual diagram of Kymijärvi II RDF gasification power plant, located in Lahti region, Finland, data acquired from [13]

MSW pyro-gasification technology offers the possibilities to achieve the aforementioned target. MSW pyro-gasification technology is defined as thermochemical conversion treatment of MSW to intermediate products (such as produced gas, tar, and char) in the absence of oxygen (pyrolysis) or in partial combustion conditions (gasification). Compared to "single-step" incineration, pyro-gasification-based WtE technique, i.e. "two-step oxidation", makes it possible to decrease dioxins and NO_x emission as a result of the reducing atmosphere [14, 15]; and the intermediate products could be cleaned to remove contaminants prior to the subsequent combustion thanks to the two separated conversion steps. The idea has been put into practice by Kymijärvi II power plant, located in Lahti region, Finland [16]. In this novel gasification plant, the solid recovered fuel (SRF) is firstly gasified in a circulating fluidized bed (CFB) gasifier at temperature of 850-900 ^{o}C; then the produced combustible gas is cooled down to around 400 ^{o}C and then undergoes hot gas cleanup devices to remove corrosive chlorine-content contaminants and particulate matters (PM) by ceramic candle filters; and finally, the purified syngas is combusted to generate a steam with high parameters (temperature of 540 ^{o}C and pressure of 120 bar) in the boiler and thus gives a higher overall power production efficiency [13, 17]. **Figure 14** exhibits the conceptual diagram of Kymijärvi II power plant [13].

As discussed, the improvement of both energy efficiency enhancement and environmental impacts reduction is quite obvious by the advanced Kymijärvi II MSW gasification power plant thanks to the hot syngas purification stage. However, energy degradations still exist when cooling down the produced syngas before being purified; besides, the ex-situ removal of chlorine-content contaminants makes the whole gasification-based WtE system more complex and increases the operation difficulties. Realizing these facts, the in-furnace dechlorination by using CaO reactant is proposed and investigated in the present work.

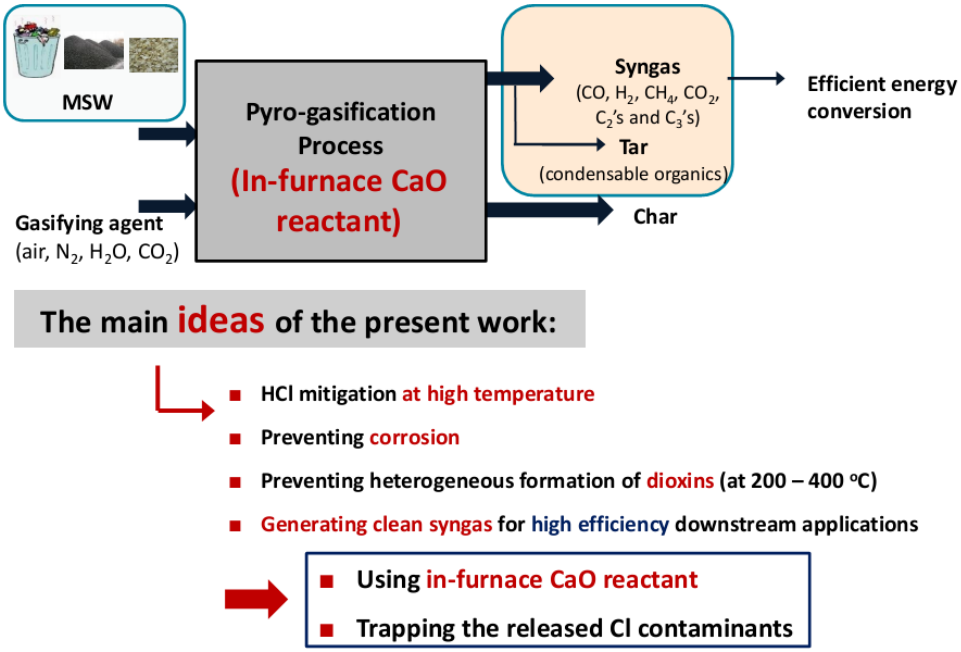

Figure 1. 5 The main ideas of this study: investigate in-furnace capture of chlorine to avoid the release of HCl by using in-situ CaO reactant

Accordingly, the motivation of the present thesis is to investigate the in-situ removal of chlorine-content contaminants by adding reactants during MSW pyro-gasification process. The primary idea of the present work, as illustrated in **Figure 1.5**, is to prevent the chlorine-content contaminants from discharging into the produced gas by using in-situ CaO reactant. Therefore, effect of CaO for the removal of the released HCl is investigated and discussed in this dissertation. Moreover, effect of CaO reactant on pyrolytic tar upgrading is also studied.

1.2 HCl release and control methods during waste thermal conversion

It is well recognized that chlorine (Cl) content in MSW is relatively high and ranges from 800 to 2500 mg/kg according to Jhong-Lin Wu et al. [18]. The presence of chlorine in MSW is mainly in the form of inorganic chlorine such as NaCl or KCl and organic chlorine such as PVC or rubber [19]. However, no matter inorganic chlorine or organic chlorine, the main Cl-content contaminants produced from MSW thermal treatment is HCl. According to the literature, HCl concentration in the incinerator out flow can be as high as 800-2000 mg/Nm^3. Besides, enrichment of Cl in incineration fly ash due to condensation is serious and its concentration is typically from 1.8 to 9.1 wt. % [20]. As aforementioned in previous section, the presence of HCl in incineration flue gas causes significant adverse effects on both electricity generation efficiency and environment burdens. Therefore, thorough investigation of HCl release characteristics as well as its control methods is of great importance.

1.2.1 Presence and release of chlorine from MSW

1.2.1.1 Chlorine contained in inorganic source

As one of the major presence form of chlorine in MSW, inorganic chlorine plays an important role in MSW management. The presence of inorganic chlorine in MSW is mainly related to alkali chlorides (for example NaCl in food waste and KCl in agricultural residues) [21-25]. Among MSW fractions, food waste is the most important inorganic chlorine sources, according to Ma et al. [23], approximately more than 45% of the total chlorine contained in MSW comes from food waste. Although inorganic chlorine takes a high proportion of the total chlorine in MSW, it is believed that only a small amount of chlorine is converted directly from alkali chlorides to HCl or other Cl-content contaminants [26]. The reason may be attributed to the relative high binding energy of alkali chlorides (for example, NaCl 787 kJ/mol, and KCl 717 kJ/mol) [22, 27]. Takasuga et al. reported that NaCl does not produce HCl itself in the case of direct heating [28]. However, the presence of water, sulfur, O_2, and even some inorganic materials like SiO_2 and Al_2O_3 facilitates the formation of HCl from alkali chlorides [29, 30]. The formation routes can be described as follows (taking NaCl as example):

$$NaCl + H_2O \rightarrow NaOH + HCl \quad (1.1)$$

$$2NaCl + H_2O \rightarrow Na_2O + 2HCl \quad (1.2)$$

$$2NaCl + mSiO_2 + H_2O \rightarrow 2HCl + Na_2O\left(SiO_2\right)_m \quad (1.3)$$

$$2NaCl + mSiO_2 + Al_2O_3 + H_2O \rightarrow 2HCl + Na_2O\left(SiO_2\right)_m\ Al_2O_3 \quad (1.4)$$

$$2NaCl + SO_2 + O_2 \rightarrow Cl_2 + Na_2SO_4 \quad (1.5)$$

$$4NaCl + 2SO_2 + O_2 + 2H_2O \rightarrow 4HCl + 2Na_2SO_4 \quad (1.6)$$

$$2NaCl + SO_2 + H_2O \rightarrow 2HCl + Na_2SO_3 \quad (1.7)$$

1.2.1.2 Chlorine contained in organic source

Apart from inorganic chlorine content, organic chlorine is also important or even more important in regard to chlorine-content contaminants formation during waste thermal conversion. Generally, organic chlorine contained in MSW are mainly in the forms of chlorinated plastics, for example, polyvinyl chloride (PVC), chlorinated polyethylene (CPE), polyvinyl dichloride (PVDC), electronic waste, textiles, leathers, rubbers [31-33], among which, PVC is the most representative organic chlorine source in MSW and have attracted worldwide concerns in the last decades [34, 35]. Theoretically, chlorine content in PVC is as high as 56 wt. % of the total mass. Unlike inorganic chlorine, organic chlorine in PVC releases easily and thoroughly during thermal conversion. Pyrolytic degradation of PVC experiments revealed a two-stage reaction mechanism associated with: (1) thorough dehydrochlorination (de-HCl) occurring in low temperature range of 200 ^{o}C – 400 ^{o}C; and (2) further degradation of the de-HCl PVC polyene chains taking place at temperature range of 400 ^{o}C – 550 ^{o}C [36-39]. Therefore, organic chlorine contained in MSW is easy to be released and causes serious problems.

1.2.2 Possible hazards from HCl emission during MSW thermal conversion

1.2.2.1 Cause of acid rain in local area

Acid rain is defined as the accumulation of atmospheric acidic substances in wet or dry conditions in the ecosystem with pH lower than 5.6 [40, 41]. Acid rain is one of the most serious environmental issues facing by the world. Especially in China, approximately 40% of the main land is affected by acid rain, and China is the third largest acid rain area, ranking only after Europe and North America [41].

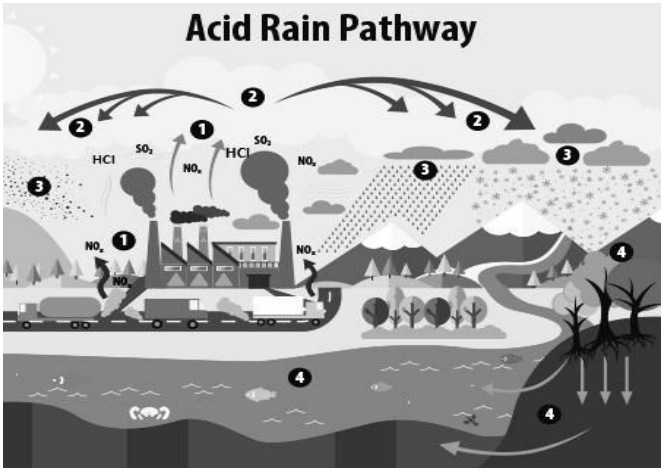

Figure 1. 6 Graphic principle of acid rain formation pathway: (1) Emissions of SO_2, NO_x and HCl are released into the air, where (2) the pollutants are transformed into acid particles that may be transported in a long distance, (3) the acid particles then fell to the earth as wet and dry deposition (dust, rain, snow, or etc.) and (4) may cause harmful effects on soil, forests and water, data obtained from [42]

HCl is considered the third largest source of acid rain formation (the first and second sources are SO_2 and NO_x, respectively). The formation path of acid gas from HCl is depicted in **Figure 1.6** [42] Different from SO_2 and NO_x, which may be transported to a quite long distance before falling to the ground, HCl is highly soluble in rainwater; therefore, it is a local pollution source and will affect directly the local surroundings of the emission source [43].

Typically, the potential harm of acid rain is summarized as follows [44]:

- Firstly, acid rain significantly affects the aquatic ecosystems. The low pH value of acid rain causes acidification of the water, leading to structural and functional imbalances of the aquatic ecosystem. On the one hand, the growth and reproduction of fish will be affected; on the other hand, it leads to the change of composition and acid resistance of water, for example, algae and fungi content may increase, and other animals and plants may decrease simultaneously.
- Secondly, acid rain affects the terrestrial ecosystems. The impacts are mainly on two aspects: soil and vegetation. In the case of soil, acid rain may change the physical and chemical properties of soil. And also it may activate some harmful and/or toxic elements contained in soil. In terms of vegetation, the fell of acid rain directly

destroy the vegetation. Besides, the impact on soil will also indirectly affect the growth of plants.

- Thirdly, acid rain causes damages on buildings and artifacts. Acid rain will react with metals, concrete and other materials under certain conditions, thus affect buildings and artifacts exposed to rainwater.

- Last but not least, the formation of acid rain will have an adverse impact on human health. On the one hand, it directly irritates our skin and may cause various respiratory diseases such as asthma; on the other hand, it will result in the inrush of harmful elements into the water, causing water pollution, thereby pollutes food and fish that indirectly affect human health.

1.2.2.2 High temperature corrosion of the boiler

As aforementioned, the presence of chlorine in MSW and the formation of HCl significantly restrict the steam quality for electricity generation. Typically in waste incinerator, the temperature and pressure of the produced steam are 400 ^{o}C and 4.0 MPa, which is much lower than that of coal-fired power plants at around 550 ^{o}C, 22 MPa for traditional subcritical power plants, or 565 ^{o}C, 24.3 MPa for supercritical power plants, resulting in a quite low electricity generation efficiency of around 20% [11, 45]. However, this value for coal-fired power plant is in the range of 33-37% and 37-40% for subcritical and supercritical power plants, respectively [45]. High temperature corrosion of the equipment by HCl is responsible for this problem. The formed HCl gas may cause serious damages in incineration chamber, water wall tube and super heater through chemical reactions with metal/metal oxide [46-48]. The principle of high temperature corrosion occurred on the surface of the equipment are illustrated in **Figure 1.7** [49].

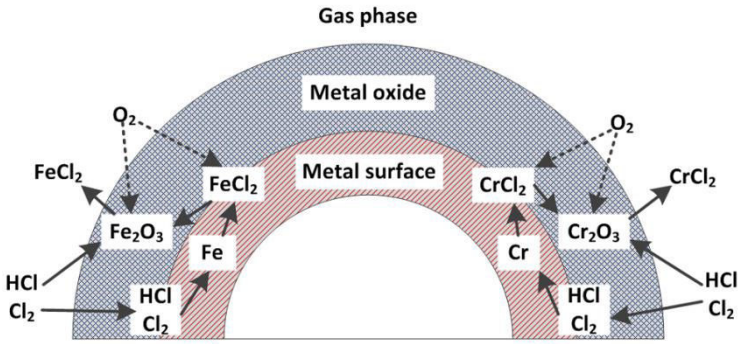

Figure 1. 7 Schematic diagram of high temperature corrosion occurred on the surface of the equipment, data obtained from Wang [49]

Table 1. 1 Chemical reactions related to high temperature corrosion

Chemical reaction	Equation
$Fe + 2HCl \rightarrow FeCl_2 + H_2$	1.8
$FeO + 2HCl \rightarrow FeCl_2 + H_2O$	1.9
$Fe_2O_3 + 2HCl + CO \rightarrow FeO + FeCl_2 + H_2O + CO_2$	1.10
$Fe_3O_4 + 2HCl + CO \rightarrow 2FeO + FeCl_2 + H_2O + CO_2$	1.11
$Cr_2O_3 + 4HCl + H_2 \rightarrow 2CrCl_2 + 3H_2O$	1.12
$2Fe + 3Cl_2 \rightarrow 2FeCl_3$	1.13
$Cr + Cl_2 \rightarrow CrCl_2$	1.14
$2Cr_2O_3 + 4Cl_2 + O_2 \rightarrow 4CrO_2Cl_2$	1.15

Accordingly, the high temperature corrosion process related to HCl or Cl_2 are described as: 1) direct chemical reactions between HCl/Cl_2 with metal/metal oxides to form metal chlorides which melts at low temperature, resulting in the loss of materials; 2) the formation of low-melting eutectic mixtures by metal/metal oxides and low-melting chlorides such as NaCl and sulfate, thereby accelerating the high-temperature corrosion process; 3) diffusion of chlorine into the defects, such as grain boundaries, voids, and etc., of the metal, causing internal chlorination of the metal matrix and accelerating the corrosion rate. Therefore, once HCl or Cl_2 exists in the flue gas, the high temperature corrosion reactions will keep going. Possible chemical reactions are summarized in **Table 1.1** [48, 49].

1.2.2.3 Chlorine source for formation of polychlorinated dibenzo-p-dioxins and polychlorinated dibenzofurans (PCDD/Fs)

Previous studies revealed that the formation of PCDD/Fs (i.e. dioxins) during MSW thermal conversion is mainly through homogeneous and heterogeneous pathways [20, 50-53]. The homogeneous pathway occurs at temperature between 400 and 800 °C, involving the conversion from structurally related precursors (such as chlorinated phenols and chlorobenzenes) to dioxins [50, 52]. In regard to the heterogeneous pathway, there are two formation mechanisms [20, 54]: one is called de novo process, which occurs at temperature range of 200 - 400 °C and proceeds through catalytic chlorination and oxidation

reactions of carbonaceous materials from elemental C, H, O, and Cl directly to dioxins; and the other one is named precursor routes, which also takes place at the temperature range of 200 - 400 °C and refers to the formation of dioxins from structurally related species, mainly chlorinated organic compounds like chlorobenzene, chlorophenol, polychlorinated biphenyls, and so on.

As indicated, no matter homogeneous and heterogeneous dioxins formation pathways, chlorine and chlorinated-contaminants play important roles. With special concerns to the heterogeneous pathways, as aforementioned in general introduction section, the temperature window for heterogeneous synthesis overlaps with the working temperature of APC systems, which means before being removed from incineration flue gas, the heterogeneous synthesis of dioxins is occurred. Realizing this fact, high temperature removal of chlorine-content contaminants is very meaningful for the inhibition of dioxins formation during MSW thermal treatment.

1.2.3 Current HCl emission regulations

Table 1. 2 HCl emission standards for MSW incineration plants in China, the European Union and the United States [55-58]

Countries or regions	Emission standards	Regulations
China	60 mg/m^3 (hourly average values) 50 mg/m^3 (daily average values)	Standard for pollution control on the municipal solid waste incineration
The European Union	60 mg/m^3 (half-hourly average values) 10 mg/m^3 (daily average values)	DIRECTIVE 2000/76/EC OF THE EUROPEAN PARLIAMENT AND OF THE COUNCIL of 4 December 2000 on the incineration of waste
The United States	25 mg/m^3, or 29 ppmV or 95% reduction of HCl emissions for existing large MSW combustion units; 20 mg/m^3, or 25 ppmV or 95% reduction of HCl emissions for new large MSW combustion units	Standards of Performance for New Stationary Sources and Emission Guidelines for Existing Sources: Large Municipal Waste Combustors
	250 ppmV or 50% reduction of potential HCl emissions for existing small MSW combustion units	Emission Guidelines for Existing Small Municipal Waste Combustion Units

Due to the potential harmfulness of HCl on both human health and the environment, HCl emission is strictly regulated worldwide. HCl emission standard in China [55], the European Union [56], and the United States [57, 58] are presented in **Table 1.2**.

1.2.4 HCl control methods

In order to meet the strict requirements of the emission regulations as well as to reduce air emission caused by waste thermal treatment, several control methods are proposed and applied to reduce HCl emission. The control method can be summarized as: 1) HCl emission control before waste thermal treatment by MSW pre-treatment; 2) HCl emission control during waste thermal treatment by in-furnace reactant; and 3) HCl emission control after waste thermal treatments by air pollution control facilities. The general principles of HCl elimination method for waste thermal conversion are presented as follows.

1.2.4.1 HCl control before waste thermal treatment

The most effective method to prevent the formation of chlorine content contaminants from MSW thermal treatments is to remove the chlorine contained in raw MSW. Therefore, pre-treatment of waste before thermal conversion is an effective HCl emission control strategies. Pre-treatment methods such as water washing [59-61], source-separated collection [62-65], and low-temperature thermal treatment is commonly used ways to lower the chlorine content:

- **Water washing**

Pre-treatment by water washing is effective to remove most of the water-soluble choline contained in MSW. As previously mentioned in **Section 1.1.1**, inorganic chlorine content in MSW is mainly in the form of NaCl and KCl; and it is water-soluble. Deng et al. found that by washing with deionized water, more than 90% of chlorine content in rice husk can be removed [59].

- **Sorting**

Water washing treats mainly inorganic chlorine content in MSW. For organic chlorine, the most effective pre-treatment method is source-separated collection and waste recycling, especially for chlorine-content plastics. Unfortunately, PVC, the most important organic chlorine source in MSW, is not currently recycled in many Countries and regions and mixed in

the non-recyclable plastics according to Kikuchi et al. [66] and Themelis at al. [67], resulting in the high organic Cl content in MSW.

- **Low-temperature thermal treatment**

It is reported that chlorine content in organic source, such as PVC, releases at low temperature range of 200-360 ^{o}C [68, 69]. Therefore, the idea of low-temperature thermal pre-treatment is to pre-pyrolyze the Cl content MSW before being thermally treated. And it is usually divided into two steps: (1) low temperature pyrolysis of raw MSW at 200-360 °C to release most Cl by dehydrochlorination reaction, and (2) thermal treatment of de-HCl MSW at higher temperatures.

1.2.4.2 HCl control after waste thermal treatment

Currently, the most important HCl control method is the use of APC systems after thermal treatment process to meet the emission standards [70]. Therefore, HCl removal is usually accomplished together with water-soluble acid gases such as hydrofluoric acid (HF), sulphur dioxide (SO_2), and etc. The acid gas removal efficiency depends highly on the selected method and equipment, the flue gas composition, and the sorbents. Typically, the most commonly used technologies for acid gases removal are: (1) dry treatment method with calcium bicarbonate ($NaHCO_3$) or calcium hydroxide ($Ca(OH)_2$) injection; (2) wet scrubbing method; and (3) semi-dry treatment method with the use of $Ca(OH)_2$ slurry [71-73].

- **Dry treatment method**

Regarding to dry treatment method of acid gases in the flue gas, fine sorbents powder, mostly hydrated lime or $NaHCO_3$, is directly injected into the furnace or the flue gas pipeline to remove the acid gases content. Among the sorbents, $NaHCO_3$ is a promising alternative sorbent, which has higher reaction rates, lower consumption, and produces fewer residues; however it has a relatively higher unit cost. Dry treatment method for acid gases with $NaHCO_3$ is based on the following reaction that take place at least 130 ^{o}C.

$$2NaHCO_3 \rightarrow Na_2CO_3 + H_2O + CO_2 \quad (1.16)$$

The decomposition of $NaHCO_3$ produces Na_2CO_3, which has a very high specific surface area and can effectively react with HCl to form NaCl, thus immobilizing the generated HCl in the flue gas.

The sorbent is usually introduced through a nozzle into the transfer line or into a de-acidification reactor to realize adequate contact time of gas and sorbents. De-acidification reactions occur on the surface of the sprayed dry $Ca(OH)_2$ or Na_2CO_3 particle to form solid chlorides. The produced solids, as well as unreacted sorbent, are then separated in the dust collector.

To meet the strict requirements of acid gases emission regulations, sufficient contact time of de-acidification sorbent and flues gas is essential. The reaction rates depend on the reaction temperature, the moisture content, the concentration of acid gases in the flue gas, and the physical properties (for example: particle size, pore distribution, specific surface area and etc.) of the sorbents.

- **Wet treatment method**

Generally, the wet scrubbing method has the best performance regarding to the term of acid gases removal efficiency. Meanwhile, the amount of the required reactants can be less when compared with dry treatment methods. Typically, wet scrubbing method can be divided into two stages: the first stage is to quench the flue gas to the temperature of 60-70 ^{o}C by spraying water, since most of the flue gas entering the wet scrubber is unsaturated; the second stage is the injection of the solution and/or slurry for the absorption of acid gases. Wet scrubbers are usually placed after the particle matter removal equipment, to prevent their clogging by sludge.

Several low-soluble calcium salts are generated during the absorption reaction of acid gases (for example chlorides, sulphates, and phosphates...). Thus, the circulating water has to be purified, concentrated and filtered, in order to avoid salt depositing. Meanwhile, the produced wastewater needs to be treated before being discharged.

- **Semi-dry treatment methods**

Semi-dry scrubber system is the most preferable treatment methods applied in MSW incineration plants in China. Generally, by using the semi-dry acid gases treatment methods, the sorbent slurry is sprayed into the reaction tower by nozzles or rotary atomiser to produce fine droplets. The evaporation of the moisture content slightly increases the humidity and decreases the temperature of the flue gas, resulting in an improvement of acid gases removal efficiency.

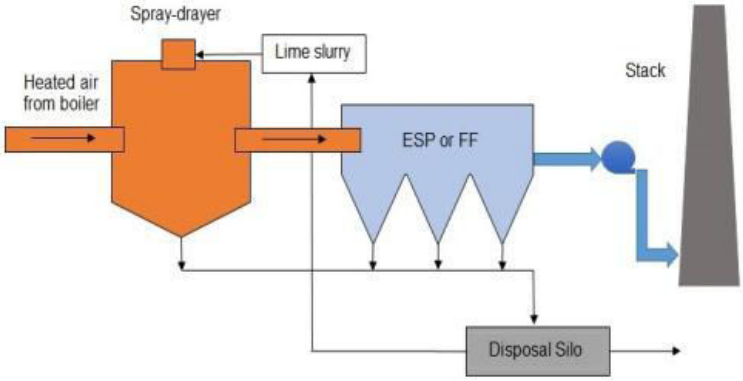

Figure 1. 8 Spray Drying Gas Cleaning System, data obtained from Razvan Lisnic et al. [74]

Figure 1. 8 presents the typical schematic diagram of semi-dry scrubber system named Spray Drying Absorption (SDA) system. As presented in the **Figure 1.5**, the slurry and flue gas move in co-current flows. The SDA system includes the following steps: first is the preparation of the sorbent slurry; then, atomisation and spraying the slurry into the scrubber and reacts with flue gas for acid gases absorption; and the final step is the drying and discharging of the generated solids. Typically, SDA uses 9 to 13 wt. % lime slurry, sprayed by a fast rotating atomiser situated at the top of the absorption tower. The reaction products between the sorbent slurry and acid gases are mostly in the form of dry salts, since most of the water is evaporated.

To sum up, the advantages and disadvantages of the aforementioned three HCl removal methods are summarized in **Table 1. 4**.

Table 1. 3 advantages and disadvantages of the aforementioned three HCl removal methods

HCl removal method	Advantages	Disadvantages
Dry treatment method	Operation temperature is relatively high (thus spray de-superheating system is not essential); Equipment is simple and inexpensive; No wastewater or corrosion.	1, excessive use of sorbent due to the low reaction rates (typically three times higher the stoichiometric amounts); 2, removal efficiency (typically at 50 to 80 %) is not high enough to meet the emission standard; 3, the efficiency of downstream particle removal equipment is affected due to the excessive use of fine sorbents; 4, the requirement for the design and distribution of nozzles is improved, since the sorbents needs to be uniformly distributed throughout the entire reaction zone; and 5, costs are high due to the preparation of the sorbent (acquisition, purification, transportation, grind, storage and etc.).
Wet treatment method	Relatively high removal efficiency, more than 95 % for HCl removal; Organic pollutants and heavy metals can be removed at the same time by cooling and using of scrubbing solution.	Wastewater generation, containing chlorides and heavy metals; Off-gas must be reheated to above 140 °C to prevent the formation of a white plume at the stack outlet, which is quite energy consuming. Investments and operating costs are quite high.
Semi-dry treatment methods	No wastewater produced; Operating temperature is usually 140 °C or higher(thus spray de-superheating system is not essential); Water consumption is lower than wet scrubbers and the exhaust gas can be discharged directly after removal of PM.	Higher operation costs because of reagents used; Higher maintenance costs for dust removal equipment

1.2.4.2 HCl control during waste thermal treatment

The use of in-furnace reactant is the main strategy for the removal of released HCl during waste thermal treatment. By using the sorbents, Cl is captured by either physical adsorption or chemical absorption and is immobilized into solid residues. Different kinds of sorbent have been examined for the in-furnace removal of released HCl, for example alkaline and alkaline earth metal content sorbents, CaO [69, 75-78], Magnesium Oxide [76, 79], $CaCO_3$ [69, 76, 80, 81], $Ca(OH)_2$ [69, 80], $NaHCO_3$ [80, 82]; and natural minerals, dolomite [78, 83, 84], olivine [78, 83].

Among the sorbents, calcium-based reactants are the most popular choices due to abundant sources, relatively cheap and high HCl removal efficiency by reactions presented in **Equation 1.17 - 1.22** [85, 86].

$$CaO + HCl \leftrightarrow CaClOH \quad (1.17)$$

$$CaO + 2HCl \leftrightarrow CaCl_2 + H_2O \quad (1.18)$$

$$CaCO_3 + HCl \leftrightarrow CaClOH + CO_2 \quad (1.19)$$

$$CaCO_3 + 2HCl \leftrightarrow CaCl_2 + H_2O + CO_2 \quad (1.20)$$

$$Ca(OH)_2 + HCl \leftrightarrow CaClOH + H_2O \quad (1.21)$$

$$Ca(OH)_2 + 2HCl \leftrightarrow CaCl_2 + 2H_2O \quad (1.22)$$

Min-Hwan Cho et al. investigated the addition of CaO during PVC-content plastics gasification and found that the chlorine contents in the produced gas and condensate are greatly reduced by more than 85% [78]. Tan et al. studied the high temperature dry injection of $Ca(OH)_2$ into furnace for HCl removal and optimized the working condition at temperature of around 600 ^oC and n(Ca)/n(Cl) molar ratio of 2.5:1, with HCl adsorption efficiency of 74.4% [87]. Matsukat et al. [88] pointed out the removal efficiency of HCl is greatly affected by moisture content in gas streams and the presence of HCl improves the removal efficiency of SO_2 when performing simultaneous dechlorination and desulfuration by calcined limestone. Matsuda et al. discussed the effect of CaO incorporated with Fe_2O_3 on in situ dry sorption of Cl-compounds and found that the loading of Fe_2O_3 promotes the absorption of Cl by CaO [89].

Moreover, reaction kinetics analysis of HCl removal by Ca-based sorbents (CaO, $CaCO_3$, $Ca(OH)_2$, etc.) also attracts worldwide concerns [90-94]. Mura et al. investigated the reaction kinetics between CaO and HCl and concluded that the apparent activation energy of

chemical reaction and product-layer diffusion is 28.1 and 37 kJmol^{-1}, respectively [95]. Weinell et al. [96] studied the reaction between HCl and limestone at the temperature range of 60-1000 ^{o}C and concluded that the reaction is mainly controlled by product-layer diffusion according to unreacted shrinking core model; they also point out that at temperature higher than 500 ^{o}C, the absorption of HCl is limited by chemical reaction equilibrium. Gullett et al. modeled the reaction kinetics between Ca-based sorbents and HCl, and stated that at temperature range of 150-350 ^{o}C, the apparent activation energy is 28.1 kJmol^{-1} and it can be described as first order reaction with respect to HCl [97].

Accordingly, CaO is selected as the dehydrochlorination sorbent in this study. The gas-solid reaction mechanism is investigated by performing HCl breakthrough experiments and effect of in-reactor CaO on released HCl mitigation during MSW pyrolysis is also identified.

1.3 Effect of CaO on pyro-gasification syngas quality enhancement and tar cracking and upgrading

Besides serving as dehydrochlorination sorbents, the addition of CaO into MSW pyro-gasification reactor can also acts as a reactant for syngas quality enhancement and tar cracking [98-101]. This section is dedicated to briefly introduce the recent research process on the reactivity of CaO on these aspects.

1.3.1 CaO as pyro-gasification syngas quality enhancement reactant

The addition of in-furnace CaO reactant takes effect via several pathways on syngas quality enhancement [102]. On the one hand, CaO can be served as a good CO_2 acceptor and reacts with CO_2 to form $CaCO_3$ (CaO carbonization reaction as presented in **Eq. 1.23**). The reduction of CO_2 in the reaction system will lead to the enhancement of water gas shift reaction (as shown in **Eq. 1.24**) towards the direction to hydrogen production [103-105]. Dong et al. investigated the effect of in-furnace addition of CaO reactant during bio-char steam gasification, and concluded that CaO addition as in-situ reactant at 700 ^{o}C produces as high H_2 yield as that gasified at 800 ^{o}C without reactant [106].

$$CaO + CO_2 \leftrightarrow CaCO_3 \quad (1.23)$$

$$CO + H_2O \leftrightarrow CO_2 + H_2 \quad (1.24)$$

On the other hand, CaO can significantly reduce the organic impurities content (especially tar compounds) in the produced gas and converts them to combustible gases.

Both the removal of impurities and the enhancement of combustible gases generation are favorable for the downstream use of the produced gas. **Eq. 1.25** conceptually introduces the impact of CaO on tar cracking.

$$Tar \xrightarrow{CaO} \alpha H_2 + \beta CO + \gamma CO_2 + hydrocarbons + \cdots \quad (1.25)$$

1.3.2 CaO as pyrolysis tar upgrading reactant

Apart from being treated as impurities, tar generated from MSW pyro-gasification contains a large amount of high value added compounds, like benzene, toluene, xylene, and naphthalene (BTXN); therefore, the recovery of these chemicals from pyro-gasification tar is also one of the research hotspots [107-109].

CaO is considered as one of the base reactants used for pyro-gasification tar upgrading during MSW thermal conversions [110-112]. According to Kabir et al. [113], the performance of CaO is quite encouraging; the addition of CaO together with the feedstock significantly changes the compositions of tar by eliminating acids and reducing phenol as compared with non-catalytic tar species; also it is effective to reduce the relative content of linear aldehydes, but promotes the formation of cycloalkanes and aromatics. Wang et al. compared the non-catalytic and catalytic pyrolysis of corncob using thermogravimetry analyzer coupled with Fourier transform infrared spectroscopy (TGA–FTIR) apparatus, and observed that the pyrolytic tar is completely deacidified by adding CaO reactant and the conversion of acid compounds promotes the generation of hydrocarbons and CH_4; besides, the oxygenated compounds are also decreased due to the addition of CaO reactant [114]. According to Wiggers et al., the alkali and alkaline metal oxides as base reactants can be used to reduce the oxygenated functions in bio-oil to hydrocarbons by catalytic decarboxylation and decarbonylation reactions [115].

Accordingly, the role of CaO reactant on MSW pyrolytic tar reduction and tar composition upgrading are investigated in **Chapter 5** and **Chapter 6** in the present thesis.

1.4 Life cycle assessment and its application on MSW management

Life cycle assessment (LCA) modeling is also conducted in the present work of MSW thermal conversion system, especially pyro-gasification-based WtE systems. LCA is an evaluation methodology concerning the entire life cycle stages of a system from cradle to grave, i.e., from raw material acquisition throughout products processing, manufacture,

transportation, utilization, and final disposal or recycling [116]. It is well recognized as a holistic and systematic methodology and it is effective to quantify the relevant energy and material input and output streams and the overall environmental burdens of a specified system [117, 118].

1.4.1 Principles and framework of LCA

LCA is firstly defined and developed by SETAC (Society of Environmental Toxicology and Chemistry) in 1990 [119]. And then it is regulated by ISO standards concerning the principles and frameworks of LCA and the definition and implementation of LCA is thus standardized [120-122]. A general consensus on the methodological framework between the two bodies has started to emerge, forming today's four-phase LCA framework as shown schematically in **Figure 1.9**.

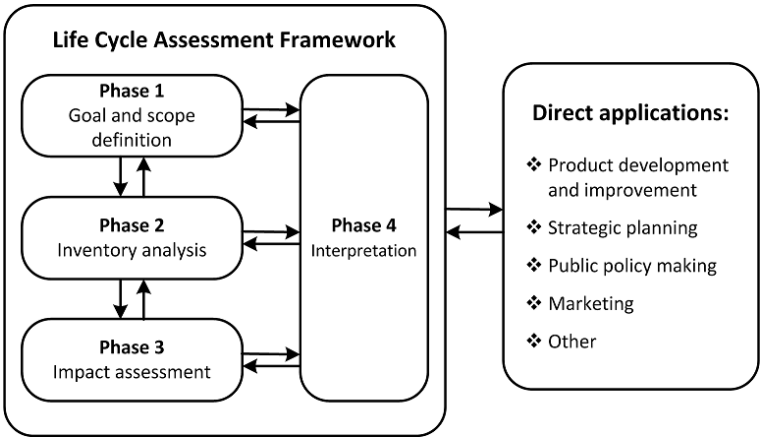

Figure 1. 9 Phases and applications of an LCA standardized by ISO, data obtained from the work of Jun Dong [102]

As illustrated, a LCA study consists of four phases: (1) goal and scope definition; (2) life cycle inventory (LCI) analysis; (3) life cycle impact assessment (LCIA); and (4) interpretation [120-122]. Accordingly, the implementation of LCA in waste thermal conversion systems is summarized in details as follows:

1.4.2 Goal and scope definition

Goal and scope definition is the most fundamental step of a LCA study, which explains the purpose of the study and determines the functional unit (FU), system boundary and allocation decisions [123, 124]. Typically for LCA studies associated to waste management, the aims at evaluate the environmental impacts caused by the implementation of waste

management activities. **Figure 1.10 s**ummarizes the concerns of recent LCA studies in waste management fields [125], mainly including: 1) waste generation and collection; 2) waste treatment, biological treatment (composting, anaerobic digestion, bio-drying, and etc.), mechanical and chemical pretreatment, and thermal treatment (incineration, gasification, co-combustion, pyrolysis, and etc.); and 3) final use or disposal of the products. When conducting a specified case study, the techniques, life cycle stages as well as the boundary of the scenario must be defined and explained according to the aim of the study.

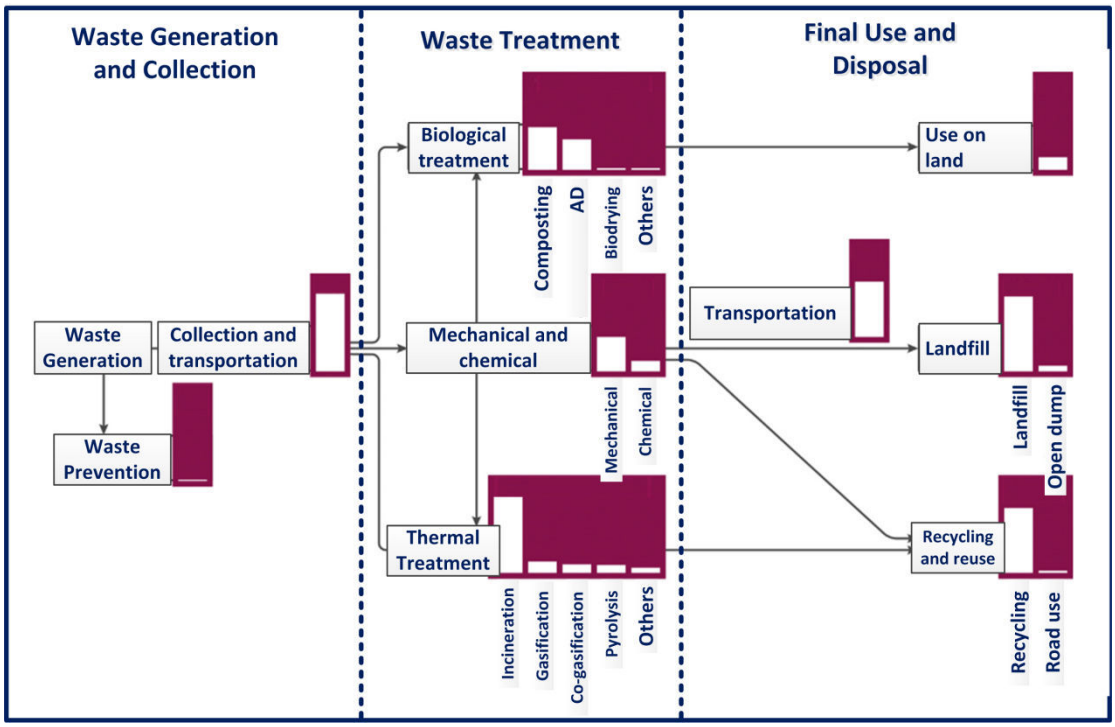

Figure 1. 10 LCA concerns in waste management field, data source from Laurent et al. [125]

1.4.3 Life cycle inventory

Life Cycle Inventory (LCI) analysis is to create a data inventory to quantify input and output energy and material flows. The input of water, energy, raw material and the output of air emissions, waste water, solid residues and the products (energy/material) should all be included in a thorough LCA analysis. To develop the inventory, a flow model of the technical system is usually and illustrated with a flow chart that includes the activities, inputs and outputs. Data used in LCI must be related to the functional unit.

As it is well recognized, the availability and quality of inventory data are the most important part of LCA studies [126]. However, detailed operational data for waste management systems, especially pyro-gasification-based WtE systems, are usually hard to acquire, either due to its scarce commercial applications or because those data are usually kept confidential. Fortunately, thanks to the contributions by some companies and research groups, several databases and software are developed for commercial applications to help with the establishment of LCA studies, for example Ecoinvent database, GaBi Database, SimaPro software, GaBi software, and etc. [127, 128]. In this work, LCA case studies of pyro-gasification-based WtE systems are performed using GaBi software and GaBi Database.

1.4.4 Life cycle impact assessment

Inventory analysis is followed by life cycle impact assessment (LCIA). The aim of LCIA is to evaluate the significance of potential environmental impacts based on the inventory data. Generally, a LCIA usually consist of the following steps:

- Selection of the impact assessment methods. Numerous impact assessment methods have been recently developed including: CML, Eco-indicator 99, ReCiPe, EDIP2003, and etc.
- Selection of the considered impact categories. Based on the impact assessment method selected, the impact categories should be identified, including: acidification, climate change, depletion of abiotic resources, ecotoxicity, eutrophication, human toxicity, ozone layer depletion, and so on.
- Classification of the inventory data. Based on the data inventory, emissions are classified and assigned to specific impact categories.
- Quantification of the contributions to the chosen impact categories using characterization factors. The categorized inventory data are unified to the same equivalence units by characterization factors (**characterization**).
- Further optional steps including normalization, grouping, and weighting may be conducted depending on the goal and scope of the LCA study.

1.4.5 Life cycle interpretation

The final stage of a LCA study is to interpret the results from LCI and/or LCIA to identify, quantify, check, and evaluate information of the considered systems. According to ISO 14040 [120], the LCA interpretation should include the following steps:

- identify and compare the environmental impacts of the contributors on basis of LCI and LCIA results;
- evaluate the systems by considering the aim defined in goal and scope definition stage;
- validate the parameters adopted by sensitivity analysis and consistency checks;
- and, draw conclusions, discussions and recommendations.

1.5 Structure and research content of the study

The structure and research content of this thesis is shown in **Figure 1. 11**, with a brief introduction of each chapter summarized as follows.

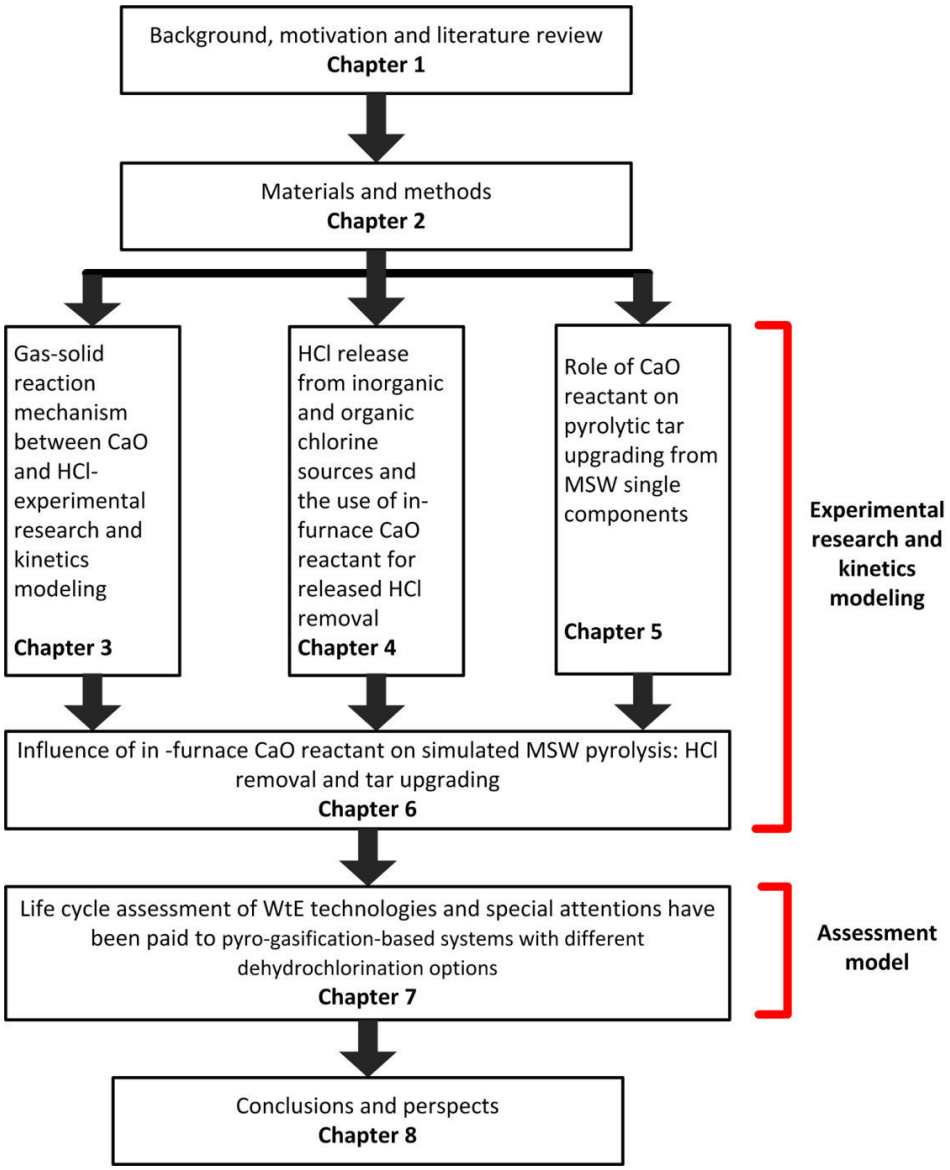

Figure 1. 11 Structure and main contents of the thesis

- **Chapter 1** is dedicated to the background and literature review which firstly presents chlorine content and emission from MSW and the state-to-art control methods. Then the effect of CaO on both HCl mitigation and tar cracking and upgrading are summarized. LCA is applied as the evaluation model; its definition, implementation procedures and current development are thus extensively reviewed.

- **Chapter 2** presents the materials and methods. Characterization of the feedstock and reactant is firstly conducted. Then, the experimental apparatus, procedures, and working conditions are explained. Products sampling and measurement are detailed. Last but not least, FactSage simulation and LCA modeling are further introduced.

- **Chapter 3** is focused on the investigation of the reaction mechanism between CaO reactant and HCl. Both thermodynamic calculation and kinetics modeling are theoretically analyzed. HCl breakthrough experiments are conducted on CaO reactant bed to determine the effect of key parameters. Morphology analysis of the spent CaO reactants is carried out to support the experimental results.

- **Chapter 4** is dedicated to determine the emission characteristics of chlorine-content contaminants from inorganic and organic chlorine source. Both thermodynamic simulation and experimental research are conducted in this chapter. Besides, effect of CaO on in-furnace HCl mitigation is investigated.

- **Chapter 5** analyzes the role of CaO reactant on pyrolytic tar upgrading from MSW single components. Analytical Py-GC/MS apparatus is used to conduct the experiments; the effects of temperature and CaO reactant on tar compositions are identified.

- **Chapter 6** uses simulated MSW as feedstock to determine the effect of in-furnace CaO on both HCl mitigation and tar cracking and upgrading.

- **Chapter 7** conducts LCA modeling work related to pyro-gasification technology. Firstly, LCA evaluation of four typical pyro-gasification and incineration plants is conducted to reveal their overall environmental burdens. Moreover, pyro-gasification-based WtE systems with different dehydrochlorination strategies are further modeled: 1) conventional gasification systems; 2) novel gasification and ex-situ dehydrochlorination system as performed by Lahti Energia; and 3) hypothetical gasification and in-situ dehydrochlorination system.

Finally, the general conclusions related to the present work are summarized, and prospects are proposed for future research works to complete the current investigations.

1.6 Bibliography

[1] Hoornweg D, Bhada-Tata P. What a waste: a global review of solid waste management. Washington DC: The World Bank; 2012.

[2] Rukapan W, Khananthai B, Chiemchaisri C, Chiemchaisri W, Srisukphun T. Short-and long-term fouling characteristics of reverse osmosis membrane at full scale leachate treatment plant. Water Science and Technology. 2012;65:127-34.

[3] Pinjing H, Fan L, Hua Z, Liming S. Reference to the Circular Economy as a Guiding Principle. Waste as a Resource. 2013;37:144.

[4] Directive Waste Framework. Directive 2006/12/EC of the European Parliament and of the Council of 5 April 2006 on waste. Official Journal of the European Union. 2006;144.

[5] Council of European Communities. Directive 2008/98/EC of the European Parliament and of the Council of 19 November 2008 on waste and repealing certain Directives. Official Journal of the European Union L. 2008;312.

[6] Department for Environment Food & Rural Affairs U. Guidance on applying the Waste Hierarchy. 2011.

[7] Eurostat SE. Waste statistics (2018). 2017.

[8] Arena U. Process and technological aspects of municipal solid waste gasification. A review. Waste management. 2012;32:625-39.

[9] Lopes EJ, Queiroz N, Yamamoto CI, da Costa Neto PR. Evaluating the emissions from the gasification processing of municipal solid waste followed by combustion. Waste Management. 2018;73:504-10.

[10] Thanopoulos S, Karellas S, Kavrakos M, Konstantellos G, Tzempelikos D, Kourkoumpas D. Analysis of Alternative MSW Treatment Technologies with the Aim of Energy Recovery in the Municipality of Vari-Voula-Vouliagmeni. Waste and Biomass Valorization. 2018:1-17.

[11] Beylot A, Hochar A, Michel P, Descat M, Ménard Y, Villeneuve J. Municipal Solid Waste Incineration in France: An Overview of Air Pollution Control Techniques, Emissions, and Energy Efficiency. Journal of Industrial Ecology. 2017.

[12] Kwak T-H, Maken S, Lee S, Park J-W, Min B-r, Yoo YD. Environmental aspects of gasification of Korean municipal solid waste in a pilot plant. Fuel. 2006;85:2012-7.

[13] Bolhàr-Nordenkampf M, Isaksson J. Refuse derived fuel gasification technologies for high efficient energy production. Waste Management: Waste to Energy. 2014;4:379-88.

[14] Bridgwater AV. Review of fast pyrolysis of biomass and product upgrading. Biomass and Bioenergy. 2012;38:68-94.

[15] Noma T, Ide K, Yoshikawa J, Kojo K, Matsui H, Nakajima R, et al. Development of waste gasification and gas reforming system for municipal solid waste (MSW). J Mater Cycles Waste. 2012;14:153-61.

[16] Lahti Energia. http://www.lahtigasification.com/.

[17] Bolhar-Nordenkampf M, Isaksson J. Operating experiences of large scale CFB-gasification plants for the substitution of fossil fuels. 24th European Biomass Conference, Amsterdam–The Netherlands2016.

[18] Wu J-L, Lin T-C, Wang Y-F, Wang J-W, Wang C-T, Kuo Y-M. Polychlorinated dibenzo-p-dioxin and dibenzofuran (PCDD/F) emission behavior during incineration of laboratory waste. Part 1: Emission profiles obtained using chemical assay and bioassay. Aerosol Air Qual Res. 2014;14:1199-205.

[19] Fang S, Yu Z, Ma X, Lin Y, Chen L, Liao Y. Analysis of catalytic pyrolysis of municipal solid waste and paper sludge using TG-FTIR, Py-GC/MS and DAEM (distributed activation energy model). Energy. 2018;143:517-32.

[20] Zhou H, Meng A, Long Y, Li Q, Zhang Y. A review of dioxin-related substances during municipal solid waste incineration. Waste management. 2015;36:106-18.

[21] Ma W, Rotter S, Hoffmann G, Lehmann A. Origins of chlorine in MSW and RDF: species and analytical methods. WIT Transactions on Ecology and the Environment. 2008;109:551-8.

[22] Materazzi M. Fate and Behaviour of Inorganic Constituents. Clean Energy from Waste: Springer; 2017. p. 191-214.

[23] Ma W, Hoffmann G, Schirmer M, Chen G, Rotter VS. Chlorine characterization and thermal behavior in MSW and RDF. Journal of hazardous materials. 2010;178:489-98.

[24] Materazzi M, Lettieri P, Mazzei L, Taylor R, Chapman C. Fate and behavior of inorganic constituents of RDF in a two stage fluid bed-plasma gasification plant. Fuel. 2015;150:473-85.

[25] Xu C, Zhao T, He Y. Effect of cathode gas diffusion layer on water transport and cell performance in direct methanol fuel cells. Journal of Power Sources. 2007;171:268-74.

[26] Wey M, Liu K, Yu W, Lin C, Chang F. Influences of chlorine content on emission of HCl and organic compounds in waste incineration using fluidized beds. Waste management. 2008;28:406-15.

[27] Cheng S-C, Chen S-H, Shiea J. Desorption flame-induced atmospheric pressure chemical ionization mass spectrometry for rapid real-world sample analysis. Mass Spectrometry. 2017;6:S0065-S.

[28] Takasuga T, Makino T, Tsubota K, Takeda N. Formation of dioxins (PCDDs/PCDFs) by dioxin-free fly ash as a catalyst and relation with several chlorine-sources. Chemosphere. 2000;40:1003-7.

[29] Frandsen FJ, Lith Sv. Detailed investigation of Cl-corrosion initiated by deposits formed in biomass-fired boilers. Final report. 2009.

[30] Camperos Guevara SH. Statistical lifetime modeling of FeNiCr alloys for high temperature corrosion in waste to energy plants and metal dusting in syngas production plants 2016.

[31] Coda B, Aho M, Berger R, Hein KR. Behavior of chlorine and enrichment of risky elements in bubbling fluidized bed combustion of biomass and waste assisted by additives. Energy & Fuels. 2001;15:680-90.

[32] Liu Z, Wang H-q, Zhang X-d, Liu J-w, Zhou Y-y. Dechlorination of organochloride waste mixture by microwave irradiation before forming solid recovered fuel. Waste Management. 2017;62:118-24.

[33] Rotter VS, Kost T, Winkler J, Bilitewski B. Material flow analysis of RDF-production processes. Waste Management. 2004;24:1005-21.

[34] Blazevska-Gilev J, Spaseska D. Formal kinetic analysis of PVC thermal degradation. Journal of the University of Chemical Technology and Metallurgy. 2010;45:251-4.

[35] Sun Q-L, Shi X-G, Lin Y-L, He Z, Xiao W, Cheng C-G, et al. Thermogravimetric-mass spectrometric study of the pyrolysis behavior of PVC. Journal of China University of Mining and Technology. 2007;17:242-5.

[36] Castro A, Soares D, Vilarinho C, Castro F. Kinetics of thermal de-chlorination of PVC under pyrolytic conditions. Waste management. 2012;32:847-51.

[37] Slapak M, Van Kasteren J, Drinkenburg A. Determination of the pyrolytic degradation kinetics of virgin-PVC and PVC-waste by analytical and computational methods. Computational and Theoretical Polymer Science. 2000;10:481-9.

[38] Zhu H, Jiang X, Yan J, Chi Y, Cen K. TG-FTIR analysis of PVC thermal degradation and HCl removal. Journal of analytical and applied pyrolysis. 2008;82:1-9.

[39] Miranda R, Yang J, Roy C, Vasile C. Vacuum pyrolysis of commingled plastics containing PVC I. Kinetic study. Polymer Degradation and stability. 2001;72:469-91.

[40] Ramlall C, Varghese B, Ramdhani S, Pammenter NW, Bhatt A, Berjak P. Effects of simulated acid rain on germination, seedling growth and oxidative metabolism of recalcitrant-seeded Trichilia dregeana grown in its natural seed bank. Physiologia plantarum. 2015;153:149-60.

[41] Liang G, Hui D, Wu X, Wu J, Liu J, Zhou G, et al. Effects of simulated acid rain on soil respiration and its components in a subtropical mixed conifer and broadleaf forest in southern China. Environmental Science: Processes & Impacts. 2016;18:246-55.

[42] Agency USEP. What is Acid Rain? 2018.

[43] Williams-Jones G, Rymer H. Hazards of volcanic gases. The Encyclopedia of Volcanoes (Second Edition): Elsevier; 2015. p. 985-92.

[44] Agency USEP. Effects of Acid Rain. 2018.

[45] Li F, Fan L-S. Clean coal conversion processes–progress and challenges. Energy & Environmental Science. 2008;1:248-67.

[46] El Haleem SA, El Wanees SA, El Aal EA, Farouk A. Factors affecting the corrosion behaviour of aluminium in acid solutions. I. Nitrogen and/or sulphur-containing organic compounds as corrosion inhibitors for Al in HCl solutions. Corrosion Science. 2013;68:1-13.

[47] Wang ZF. Affection of High Sulfur and Naphthenic Acid Crude Oil Acted on Refinery Equipment. Applied Mechanics and Materials: Trans Tech Publ; 2013. p. 21-4.

[48] James P, Pinder L. Effect of coal chlorine on the fireside corrosion of boiler furnace wall and superheater/reheater tubing. Materials at High Temperatures. 1997;14:187-96.

[49] Ting W. Study of calcium oxide dechlorination in biomass fluidized bed gasifier. Nanjing, China: Southest University; 2016.

[50] Altarawneh M, Dlugogorski BZ, Kennedy EM, Mackie JC. Mechanisms for formation, chlorination, dechlorination and destruction of polychlorinated dibenzo-p-dioxins and dibenzofurans (PCDD/Fs). Progress in Energy and Combustion Science. 2009;35:245-74.

[51] Vermeulen I, Van Caneghem J, Vandecasteele C. Indication of PCDD/F formation through precursor condensation in a full-scale hazardous waste incinerator. Journal of Material Cycles and Waste Management. 2014;16:167-71.

[52] Rathna R, Varjani S, Nakkeeran E. Recent developments and prospects of dioxins and furans remediation. Journal of environmental management. 2018;223:797-806.

[53] Collina E, Lasagni M, Piccinelli E, Anzano MN, Pitea D. The rate-determining step in a low temperature PCDD/F formation from oxidative breakdown of native carbon in MSWI fly ash. Chemosphere. 2016;165:110-7.

[54] Zhang M, Buekens A. De novo synthesis of dioxins: a review. International Journal of Environment and Pollution. 2016;60:63-110.

[55] China State Environmental Protection Administration. Pollution Control Standard for Municipal Solid Waste Incineration (GB 18485-2014). Beijing: China Environmental Science Press; 2014.

[56] Directive E. Directive on the incineration of waste. Directive 2000/76/EC; 2000.

[57] Agency UEP. Commercial and Industrial Solid Waste Incineration Units: Reconsideration and Final Amendments; NonHazardous Secondary Materials That Are Solid Waste. 2013.

[58] Agency UEP. Emission Guidelines for Existing Small Municipal Waste Combustion Units. 2000.

[59] Deng L, Zhang T, Che D. Effect of water washing on fuel properties, pyrolysis and combustion characteristics, and ash fusibility of biomass. Fuel Processing Technology. 2013;106:712-20.

[60] Jensen PA, Sander B, Dam-Johansen K. Removal of K and Cl by leaching of straw char. Biomass and Bioenergy. 2001;20:447-57.

[61] Bakker RR, Jenkins BM. Feasibility of collecting naturally leached rice straw for thermal conversion. Biomass and Bioenergy. 2003;25:597-614.

[62] Nasrullah M, Vainikka P, Hannula J, Hurme M. Elemental balance of SRF production process: solid recovered fuel produced from commercial and industrial waste. Fuel. 2015;145:1-11.

[63] Sarc R, Lorber KE. Production, quality and quality assurance of Refuse Derived Fuels (RDFs). Waste management. 2013;33:1825-34.

[64] Velis CA, Wagland S, Longhurst P, Robson B, Sinfield K, Wise S, et al. Solid recovered fuel: materials flow analysis and fuel property development during the mechanical processing of biodried waste. Environmental science & technology. 2013;47:2957-65.

[65] Garcés D, Díaz E, Sastre H, Ordóñez S, González-LaFuente JM. Evaluation of the potential of different high calorific waste fractions for the preparation of solid recovered fuels. Waste Management. 2016;47:164-73.

[66] Kikuchi R, Kukacka J, Raschman R. Grouping of mixed waste plastics according to chlorine content. Separation and Purification technology. 2008;61:75-81.

[67] Themelis NJ. Chlorine Sources, Sinks, and Impacts in WTE Power Plants. 18th Annual North American Waste-to-Energy Conference: American Society of Mechanical Engineers; 2010. p. 77-84.

[68] Kim S. Pyrolysis kinetics of waste PVC pipe. Waste management. 2001;21:609-16.

[69] Zhu HM, Jiang XG, Yan JH, Chi Y, Cen KF. TG-FTIR analysis of PVC thermal degradation and HCl removal. Journal of Analytical and Applied Pyrolysis. 2008;82:1-9.

[70] Hammoud A, Kassem M, Mourtada A. Solid waste to energy strategy in Lebanon: Potential, technology and design. Renewable Energies for Developing Countries (REDEC), 2014 International Conference on: IEEE; 2014. p. 75-81.

[71] Ji L, Lu S, Yang J, Du C, Chen Z, Buekens A, et al. Municipal solid waste incineration in China and the issue of acidification: A review. Waste Management & Research. 2016;34:280-97.

[72] Tian H, Gao J, Hao J, Lu L, Zhu C, Qiu P. Atmospheric pollution problems and control proposals associated with solid waste management in China: a review. Journal of hazardous materials. 2013;252:142-54.

[73] Zhou Q, Huang GH, Chan CW. Development of an intelligent decision support system for air pollution control at coal-fired power plants. Expert Systems with Applications. 2004;26:335-56.

[74] LISNIC R, JINGA SI. STUDIU PRIVIND STADIUL ACTUAL ȘI TENDINȚELE VIITOARE ALE TEHNOLOGIILOR DE DESULFURARE A GAZELOR DE ARDERE: REVIEW STUDY ON CURRENT STATE AND FUTURE TRENDS OF FLUE GAS DESULPHURIZATION TEHNOLOGIES: A REVIEW. Revista Română de Materiale/Romanian Journal of Materials. 2018;48:83-90.

[75] Sun Z, Yu F-C, Li F, Li S, Fan L-S. Experimental study of HCl capture using CaO reactants: activation, deactivation, reactivation, and ionic transfer mechanism. Industrial & Engineering Chemistry Research. 2011;50:6034-43.

[76] Dou B, Gao J, Baek SW, Sha X. High-temperature HCl removal with sorbents in a fixed-bed reactor. Energy & fuels. 2003;17:874-8.

[77] Bie R, Li S, Yang L. Reaction mechanism of CaO with HCl in incineration of wastewater in fluidized bed. Chemical engineering science. 2005;60:609-16.

[78] Cho M-H, Choi Y-K, Kim J-S. Air gasification of PVC (polyvinyl chloride)-containing plastic waste in a two-stage gasifier using Ca-based additives and Ni-loaded activated carbon for the production of clean and hydrogen-rich producer gas. Energy. 2015;87:586-93.

[79] Dou B-l, Gao J-s, Sha X-z. A study on the reaction kinetics of HCl removal from high-temperature coal gas. Fuel processing technology. 2001;72:23-33.

[80] Fontana A, Laurent P, Jung C, Gehrmann J, Beckmann M. Municipal waste pyrolysis (2) chlorine capture by addition of calcium and sodium-based sorbents. Erdoel, Erdgas, Kohle. 2001;117:362-6.

[81] López A, de Marco I, Caballero BM, Laresgoiti MF, Adrados A. Dechlorination of fuels in pyrolysis of PVC containing plastic wastes. Fuel Processing Technology. 2011;92:253-60.

[82] Kong Y, Davidson H. Dry sorbent injection of sodium sorbents for SO2, HCl and mercury mitigation. 18th Annual North American Waste-to-Energy Conference: American Society of Mechanical Engineers; 2010. p. 317-20.

[83] Cho M-H, Mun T-Y, Choi Y-K, Kim J-S. Two-stage air gasification of mixed plastic waste: Olivine as the bed material and effects of various additives and a nickel-plated distributor on the tar removal. Energy. 2014;70:128-34.

[84] Poskrobko S, Łach J, Król D. Experimental investigation of hydrogen chlorine bonding with limestone and dolomite in the furnace of a stoker-fired boiler. Energy & Fuels. 2010;24:5851-8.

[85] Bausach M, Krammer G, Cunill F. Reaction of Ca (OH) 2 with HCl in the presence of water vapour at low temperatures. Thermochimica acta. 2004;421:217-23.

[86] Xie X, Li Y, Wang W, Shi L. HCl removal using cycled carbide slag from calcium looping cycles. Applied Energy. 2014;135:391-401.

[87] Tan J, Yang G, Mao J, Dai H. Laboratory study on high-temperature adsorption of HCl by dry-injection of Ca (OH) 2 in a dual-layer granular bed filter. Frontiers of Environmental Science & Engineering. 2014;8:863-70.

[88] Matsukata M, Takeda K, Miyatani T, Ueyama K. Simultaneous chlorination and sulphation of calcined limestone. Chemical Engineering Science. 1996;51:2529-34.

[89] Matsuda H, Ito T, Kuchar D, Tanahashi N, Watanabe C. Enhanced dechlorination of chlorobenzene and in situ dry sorption of resultant Cl-compounds by CaO and Na2CO3 sorbent beds incorporated with Fe2O3. Chemosphere. 2009;74:1348-53.

[90] Liu ZS. Advanced experimental analysis of the reaction of Ca (OH) 2 with HCl and SO2 during the spray dry scrubbing process. Fuel. 2005;84:5-11.

[91] Partanen J, Backman P, Backman R, Hupa M. Absorption of HCl by limestone in hot flue gases. Part I: the effects of temperature, gas atmosphere and absorbent quality. Fuel. 2005;84:1664-73.

[92] Partanen J, Backman P, Backman R, Hupa M. Absorption of HCl by limestone in hot flue gases. Part II: importance of calcium hydroxychloride. Fuel. 2005;84:1674-84.

[93] Partanen J, Backman P, Backman R, Hupa M. Absorption of HCl by limestone in hot flue gases. Part III: simultaneous absorption with SO2. Fuel. 2005;84:1685-94.

[94] Chyang C-S, Han Y-L, Zhong Z-C. Study of HCl mitigation by CaO at high temperature. Energy & Fuels. 2009;23:3948-53.

[95] Mura G, Lallai A. On the kinetics of dry reaction between calcium oxide and gas hydrochloric acid. Chemical Engineering Science. 1992;47:2407-11.

[96] Weinell CE, Jensen PI, Dam-Johansen K, Livbjerg H. Hydrogen chloride reaction with lime and limestone: kinetics and sorption capacity. Industrial & Engineering Chemistry Research. 1992;31:164-71.

[97] Gullett BK, Jozewicz W, Stefanski LA. Reaction kinetics of calcium-based sorbents with hydrogen chloride. Industrial & engineering chemistry research. 1992;31:2437-46.

[98] Han L, Wang Q, Ma Q, Yu C, Luo Z, Cen K. Influence of CaO additives on wheat-straw pyrolysis as determined by TG-FTIR analysis. Journal of Analytical and Applied Pyrolysis. 2010;88:199-206.

[99] Han L, Wang Q, Yang Y, Yu C, Fang M, Luo Z. Hydrogen production via CaO sorption enhanced anaerobic gasification of sawdust in a bubbling fluidized bed. International journal of hydrogen energy. 2011;36:4820-9.

[100] Zhou C, Stuermer T, Gunarathne R, Yang W, Blasiak W. Effect of calcium oxide on high-temperature steam gasification of municipal solid waste. Fuel. 2014;122:36-46.

[101] Jordan CA, Akay G. Effect of CaO on tar production and dew point depression during gasification of fuel cane bagasse in a novel downdraft gasifier. Fuel processing technology. 2013;106:654-60.

[102] Dong J. MSWs gasification with emphasis on energy, environment and life cycle assessment: Ecole des Mines d'Albi-Carmaux; 2016.

[103] Florin NH, Harris AT. Enhanced hydrogen production from biomass with in situ carbon dioxide capture using calcium oxide sorbents. Chemical Engineering Science. 2008;63:287-316.

[104] Florin NH, Harris AT. Hydrogen production from biomass coupled with carbon dioxide capture: the implications of thermodynamic equilibrium. International Journal Of Hydrogen Energy. 2007;32:4119-34.

[105] Xu G, Murakami T, Suda T, Kusama S, Fujimori T. Distinctive effects of CaO additive on atmospheric gasification of biomass at different temperatures. Industrial & engineering chemistry research. 2005;44:5864-8.

[106] Dong J, Nzihou A, Chi Y, Weiss-Hortala E, Ni M, Lyczko N, et al. Hydrogen-Rich Gas Production from Steam Gasification of Bio-char in the Presence of CaO. Waste and Biomass Valorization. 2017;8:2735-46.

[107] Zhang L, Liu R, Yin R, Mei Y. Upgrading of bio-oil from biomass fast pyrolysis in China: A review. Renewable and Sustainable Energy Reviews. 2013;24:66-72.

[108] Yan L, Bai Y, Liu Y, He Y, Li F. Effects of low molecular compounds in coal on the catalytic upgrading of gaseous tar. Fuel. 2018;226:316-21.

[109] Chang W, Qinglan H, Dingqiang L, Qingzhu J, Guiju L, Bo X. Production of light aromatic hydrocarbons from biomass by catalytic pyrolysis. Chinese Journal of Catalysis. 2008;29:907-12.

[110] Kobayashi J, Kawamoto K, Fukushima R, Tanaka S. Woody biomass and RPF gasification using reforming catalyst and calcium oxide. Chemosphere. 2011;83:1273-8.

[111] Tang S, Tian S, Zheng C, Zhang Z. Effect of Calcium Hydroxide on the Pyrolysis Behavior of Sewage Sludge: Reaction Characteristics and Kinetics. Energy & Fuels. 2017;31:5079-87.

[112] Wang J, Zhong Z, Ding K, Zhang B, Deng A, Min M, et al. Co-pyrolysis of bamboo residual with waste tire over dual catalytic stage of CaO and co-modified HZSM-5. Energy. 2017;133:90-8.

[113] Kabir G, Hameed B. Recent progress on catalytic pyrolysis of lignocellulosic biomass to high-grade bio-oil and bio-chemicals. Renewable and Sustainable Energy Reviews. 2017;70:945-67.

[114] Wang D, Xiao R, Zhang H, He G. Comparison of catalytic pyrolysis of biomass with MCM-41 and CaO catalysts by using TGA–FTIR analysis. Journal of Analytical and Applied Pyrolysis. 2010;89:171-7.

[115] Wiggers VR, Beims RF, Ender L, Simionatto EL, Meier HF. Renewable Hydrocarbons from Triglyceride's Thermal Cracking. Frontiers in Bioenergy and Biofuels: InTech; 2017.

[116] Meneses M, Concepción H, Vrecko D, Vilanova R. Life cycle assessment as an environmental evaluation tool for control strategies in wastewater treatment plants. Journal of Cleaner Production. 2015;107:653-61.

[117] Kamo T. Overview of the waste plastic recycling system in Japan and future tasks. 6th international symposium on feedstock recycling of polymeric materials, Toledo2011. p. 15-8.

[118] Lee C-K, Kim Y-K, Pruitichaiwiboon P, Kim J-S, Lee K-M, Ju C-S. Assessing environmentally friendly recycling methods for composite bodies of railway rolling stock using life-cycle analysis. Transportation Research Part D: Transport and Environment. 2010;15:197-203.

[119] Society of Environmental Toxicology and Chemistry (SATAC). Guidelines for life-cycle assessment: a code of practice: Pensacola; 1993.

[120] Standardization IOf. Environmental Management: Life Cycle Assessment; Principles and Framework: ISO; 2006.

[121] Organization IS. Environmental Management: Life Cycle Assessments: Requirements and Guidelines: ISO; 2006.

[122] Klöpffer W. The critical review of life cycle assessment studies according to ISO 14040 and 14044. The International Journal of Life Cycle Assessment. 2012;17:1087-93.

[123] Clift R, Doig A, Finnveden G. The application of life cycle assessment to integrated solid waste management: Part 1—Methodology. Process Safety And Environmental Protection. 2000;78:279-87.

[124] Zhou Z, Tang Y, Chi Y, Ni M, Buekens A. Waste-to-energy: A review of life cycle assessment and its extension methods. Waste Management & Research. 2018;36:3-16.

[125] Laurent A, Bakas I, Clavreul J, Bernstad A, Niero M, Gentil E, et al. Review of LCA studies of solid waste management systems–Part I: Lessons learned and perspectives. Waste management. 2014;34:573-88.

[126] Thanh NP, Matsui Y. Assessment of potential impacts of municipal solid waste treatment alternatives by using life cycle approach: a case study in Vietnam. Environmental monitoring and assessment. 2013;185:7993-8004.

[127] Martínez-Rocamora A, Solís-Guzmán J, Marrero M. LCA databases focused on construction materials: A review. Renewable and Sustainable Energy Reviews. 2016;58:565-73.

[128] Speck R, Selke S, Auras R, Fitzsimmons J. Life cycle assessment software: Selection can impact results. Journal of Industrial Ecology. 2016;20:18-28.

Chapter 2

Materials and methods

In this chapter, feedstock and reactants used in this study are characterized; the experimental setup, working conditions, products sampling and analysis method, and life cycle assessment methodology are explained. This chapter can be divided into four parts and the contents are:

- **Section 2.1** introduces the characterization results of the feedstock and reactants used in the present study;

- **Section 2.2** presents the experimental facilities used and the experimental procedures: including vertical fixed bed reactor for absorption of HCl by CaO reactant at moderate high temperature, fixed bed tubular furnace reactor for pyrolysis of PVC and/or simulated MSW without/with CaO addition, Py-GC/MS equipment for pyrolytic tar cracking and upgrading experiments. Besides, the experimental working conditions with specific purpose are detailed in this section;

- **Section 2.3** gives product sampling and analysis methods including: produced gas collection and characterization by Gas Chromatography (GC), HCl sampling and analysis by ion chromatography; tar collection and characterization by gas chromatography/mass spectrometry (GC/MS), and solids collection and analysis including thermogravimetric analysis (TGA), Scanning Electron Microscopy (SEM), Energy Disperse Spectroscopy micro-analysis (EDS), X-ray diffraction (XRD), X-ray fluorescence (XRF) and gas adsorption (Brunauer-Emmett-Teller, BET);

- **Section 2.4** introduces thermodynamic equilibrium simulation principles and FactSage 6.3 software;

- **Section 2.5** introduces the life cycle impact assessment (LCIA) methodology adopted in this work.

2.1 Materials characterization

2.2.1 Feedstock

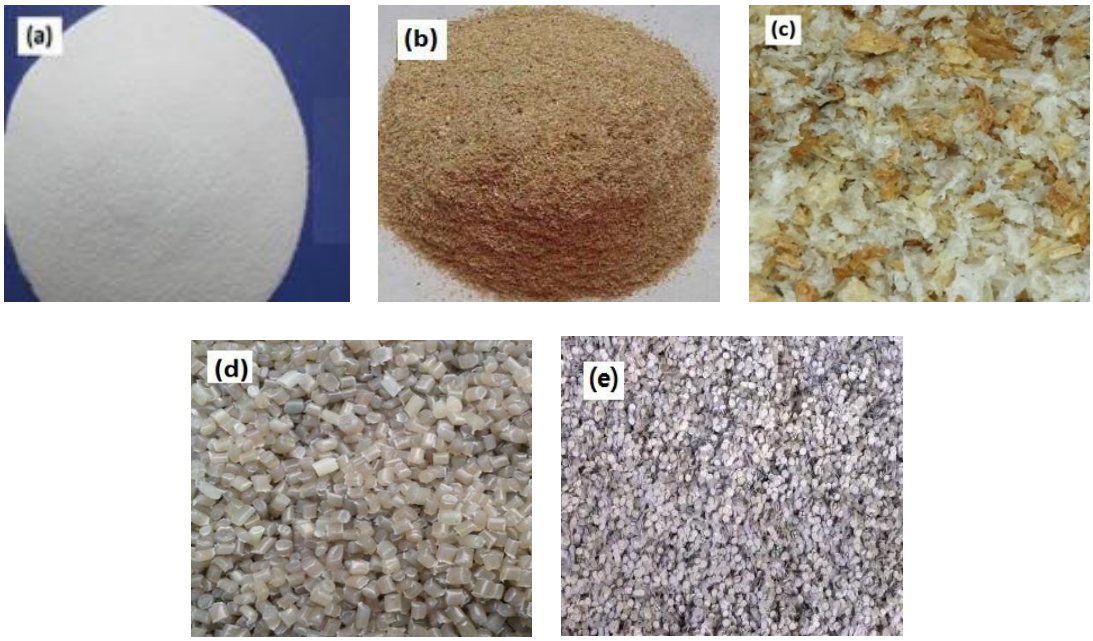

Figure 2. 1 Pictures of MSW components: (a), PVC pellet; (b), wood; (c), food waste; (d), PE pellet; and (e), paper

Feedstock used in this work mainly includes: inorganic chlorine source (NaCl), organic chlorine source (PVC plastic), and MSW (consists of five typical components, food waste, paper, wood, PVC plastic and PE plastic). To maintain the consistence of the feedstock in the experiments, simulated MSW single components (for example, bread, paper, wood saw dust, PVC and PE) are adopted in the experiments instead of using raw MSW fractions; for simulated MSW (S-MSW), the different components are artificially mixed, and the mass fractions are determined according to the typical waste composition in Hangzhou, China [1]. **Figure 2.1** presents the pictures of MSW components.

Before the experiment, feedstocks are ground into sizes of less than 1 mm and then dried at 105 ^{o}C for 24 hours. Physical composition and the ultimate and proximate analysis results of S-MSW components as well as the prepared S-MSW are presented in **Table 2.1** and **Table 2.2**.

Table 2. 1 Proximate and ultimate analysis of MSW components

	Proximate analysis [a] (ad, wt. %)				Ultimate analysis [a] (ad, wt. %)						LHV [a] (MJ/kg)
	M	V	FC	A	C	H	O[b]	N	S	Cl	
PVC	0.00	95.80	4.20	0.00	38.90	4.90	0.00	0.00	0.00	56.20	19.30
Wood	9.65	55.25	33.89	1.20	42.90	5.43	39.96	0.27	0.58	0.00	17.04
Paper	7.64	71.61	7.66	13.09	34.05	3.24	41.82	0.12	0.04	0.00	12.81
Bread	6.43	71.33	20.77	1.46	43.40	5.53	39.04	1.99	0.36	1.79	17.11
PE	0.14	98.47	0.09	1.30	83.08	11.20	4.07	0.01	0.20	0.00	45.48

[a] M: moisture; V: volatiles; FC: fixed carbon; A: ash; C: carbon; H: hydrogen; O: oxygen; N: nitrogen; S: sulfur; LHV: lower heating value;

[b] by difference.

Table 2. 2 Overall composition and proximate and ultimate analysis of S-MSW

Overall composition (ar, wt.%) [a]									
Food waste	Paper	Polyethylene (PE)	Polyvinyl chloride (PVC)					Wood	
55.0	15.0	15.0	10.0					5.0	
Proximate analysis (ad, wt.%) [a]				Ultimate analysis (ad, wt.%) [a]					
Moisture	Ash	Volatile	Fixed Carbon	C	H	N	S	Cl	O [b]
5.19	3.02	77.09	14.70	47.47	5.97	1.13	0.26	6.60	30.35

[a] according to the as-received basis;

[b] by difference.

2.2.2 CaO reactant

Table 2. 3 Physicochemical properties of the prepared CaO reactant

Particle size, mm	Specific surface area, m^2/g	Total pore volume, cm^3/g	Average pore diameter, nm
0.25 - 0.43 mm (40-60 mesh)	2.37	0.039	25.0
0.13-0.18 mm (80-120 mesh)	6.28	0.097	23.1

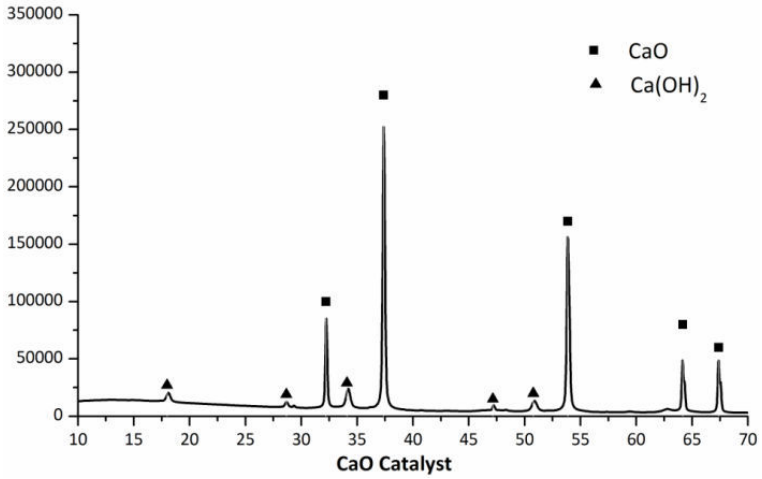

Figure 2. 2 XRD analysis of CaO reactant

CaO is used as in-furnace reactant in the present work to achieve: 1) produced gas quality enhancement; 2) tar reduction and reforming; and 3) HCl gas capture during waste pyro-gasification. CaO reactant is produced according to the Chinese national standards of chemical industry "HG/T 4205-2011" with 98% purity, by Beijing Kang Pu Hui Wei Technology Co. Ltd, China [2]. Prior to the experiments, CaO reactant is ground and sieved to different particle sizes. In order to avoid absorbing water from air, the sieved CaO reactant is dried at 105 ^{o}C for 12 hours and then calcined in N_2 atmosphere at 800^{o}C for 2h. The physicochemical properties of prepared CaO reactant are listed in **Table 2. 3** and the XRD patterns are shown in **Figure 2. 2**. The apparatus used in this section is detailed in **Section 2.3**.

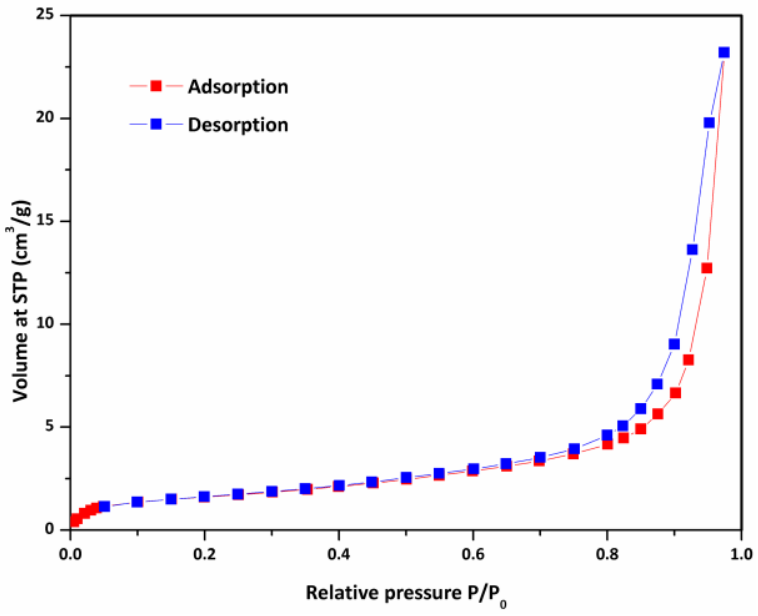

(a)

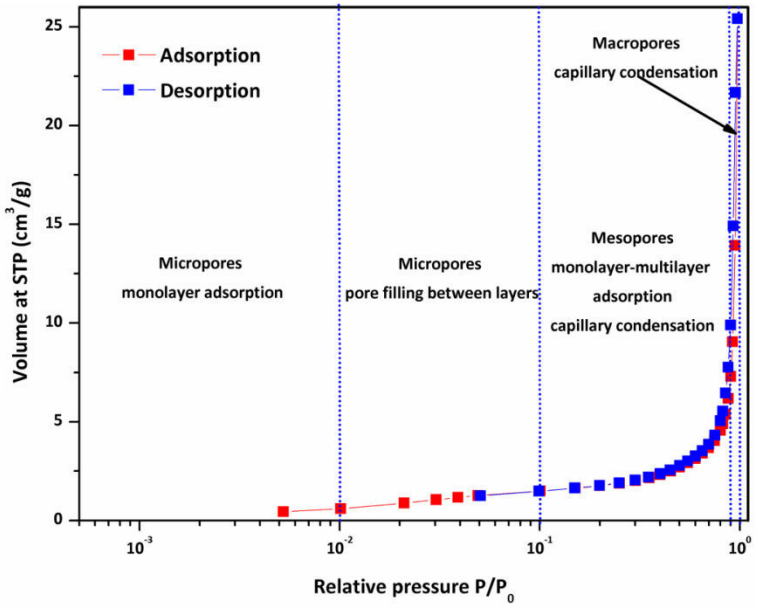

(b)

Figure 2. 3 N_2 adsorption-desorption (a) isotherms and (b) Log isotherms of CaO reactant with particle size of 0.25 - 0.43 mm (40-60 mesh)

In order to determine the pore characteristics of CaO, N_2 adsorption-desorption isotherms and logarithmic isotherms curves are plotted in **Figure 2. 3**. According to classification by the International Union of Pure and Applied Chemistry (IUPAC) [3], the isotherms belongs to Type IV isotherm with an obvious hysteresis loop. Typically for type IV isotherm, the characteristic features of the absorption isotherm can be described as follows:

1) the initial stage is attributed to monolayer adsorption and the inflection point indicates the saturated monolayer adsorption capacity; 2) the next stage is the flat region and reflects the beginning of the multilayer adsorption; and 3) the final stage is associated with the capillary condensation taking place in mesopores. According to the International Union of Pure and Applied Chemistry (IUPAC) [3], hysteresis loop in multilayer range of isotherms is usually associated with capillary condensation in mesopore structures. The hysteresis loop of the CaO reactant is matched by the Type H3, which does not exhibit any limiting adsorption amount even at high P/P_0 conditions. Therefore, the pores are characterized as the aggregates of slit-shaped pores.

The N_2 adsorption-desorption logarithmic isotherms curves are also plotted in **Figure 2. 3**. According to Ohba [4, 5], pore size distribution of the sorbent can be divided into several categories based on relative pressure of the logarithmic isotherms: adsorption in relative pressure range of 10^{-6}-10^{-4} is mainly associated with ultramicropore filling; adsorption in P/P_0 range of 10^{-4}-10^{-2} is related to monolayer adsorption of micropores; adsorption in the range of 10^{-2}-10^{-1} is considered to be pore filling between adsorption layers in micropores; in P/P_0 range of 0.1-0.9, the adsorption is mainly classed into monolayer-multilayer adsorption and capillary condensation in mesopores; and in the range of 0.9-1, the adsorption is mainly regarded as capillary condensation in macropores. As illustrated in **Figure 2. 3**, N_2 adsorption increases significantly in relative pressure range of 0.1-1, indicating that there is a great deal of mesopores and macropores existing in the selected reactant.

For each chapter of the present work, different feedstock and reactant are used. **Table 2.4** summarizes the details.

Table 2. 4 Use of feedstock and reactant in different experiments

Chapter	Experiments	Feedstock	Reactant	Apparatus
3	HCl gas mitigation by CaO reactant	Gas mixtures	CaO	Vertical tubular furnace reactor
4	HCl release and mitigation characteristics from inorganic source (NaCl) and organic source (PVC)	NaCl; PVC	CaO	TGA Fixed bed tubular furnace
5	Tar formation and composition during MSW pyrolysis with/without CaO reactant	MSW single component: Food, PVC, and Wood	CaO	Py-GC/MS
6	Characteristics of S-MSW pyrolysis with/without CaO reactant	Simulated-MSW	CaO	Fixed bed tubular furnace

2.2 Experimental apparatus and procedures

2.2.1 Reaction between CaO and HCl gas at moderate high temperature

2.2.1.1 Vertical tubular furnace reactor

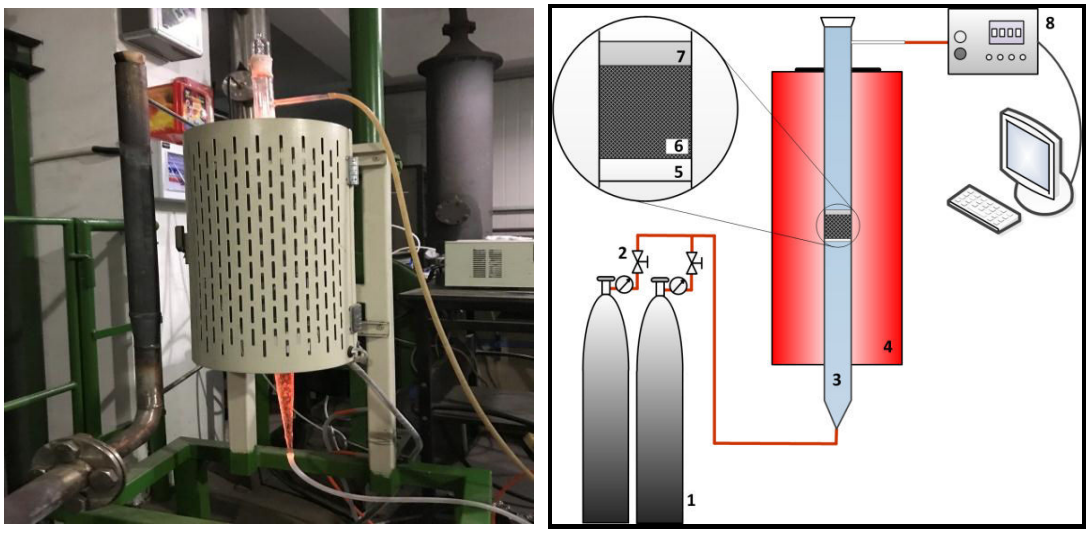

Figure 2. 4 General photograph and schematic diagram of the vertical tubular furnace reactor: 1, gas source; 2, gas flow meter; 3, vertical quartz tubular reactor; 4, electric heater and temperature controller; 5, quartz filter; 6, CaO reactant for HCl mitigation; 7, quartz wool; 8, HCl gas detector

HCl mitigation experiments are conducted using a vertical tubular reactor, as depicted in **Figure 2. 4**. The experimental system consists mainly of: 1) gas source unit; 2) electric heater and temperature controller unit; 3) main reaction chamber; and 4) HCl gas analysis unit.

- gas source unit: in this experiment, high pressure steel cylinders are used as the gas source, the used gas includes: 2000 part per million volume (ppmv) HCl gas (nitrogen balance), CO_2 gas, simulated syngas (containing 1.6 vol.% H_2, 1.2 vol.% CH_4, 2.5 vol.% CO, 6 vol.% CO_2, and N_2 balance);
- electric heater and temperature controller unit: a programmed temperature control heating system is used in this experiment, with the precision of the temperature controller of ±1 ^{o}C;
- main reaction chamber: due to the high corrosion properties of HCl gas, a vertical quartz tubular reactor is adopted, with 600.0 mm in height and 22.0 mm in inner diameter;
- HCl gas analysis unit: the off-gas is detected by Gasmet equipment (GASMET 4030; Gasmet Technologies Oy, Pulttitie 8A, FI-00880 Helsinki, Finland); and the exhaust gas is cleaned by a bottle of 0.1 mol/L sodium hydroxide (NaOH) solution before being discharged.

2.2.1.2 Operating conditions and experimental procedure

The effects of absorption temperature, inlet HCl gas concentration, and inlet gas composition on HCl mitigation by CaO reactant are investigated in this part. **Table 2.5** presents the experimental conditions. Temperature series at moderate high level of 550, 650, 750, and 850 °C is selected; and the effect of raw HCl concentration (2000 ppmv, 1000 ppmv, and 500ppmv) is also considered. Besides, the effect of CO_2 content (12 vol. %) as well as the influence of simulated syngas (the simulated syngas contains 1.6 vol. % H_2, 1.2 vol. % CH_4, 2.5 vol. % CO, 6 vol. % CO_2, and N_2 balance; for these experiments, 50 vol. % 2000 ppmv HCl gas and 50 vol. % simulated syngas are used). Repeated runs are conducted under identical conditions to ensure the repeatability of the results.

Table 2. 5 Experimental conditions of HCl mitigation by CaO reactant at moderate high temperature

No.	Temperature, ^{o}C	HCl concentration, ppmV	Gas flowrate, L/min	Atmosphere
1#	550	2000	2.0	N_2
2#	650			
3#	750			
4#	850			
5#	750	1000	2.0	N_2
6#		500	2.0	
7#	750	1000	2.0	12 vol.% CO_2
8#		1000	2.0	50 vol.% simulated syngas

Note: the effect of temperature: 1#, 2#, 3# and 4#; the effect of raw HCl concentration: 3#, 5# and 6#; the effect of atmosphere: 3#, 7# and 8#.

Before the experiments, air leakage of the reactor and connection pipes have to be carefully tested, since the leakage of HCl and CO gases are quite dangerous. At the beginning of the experiments, 2.0 g of CaO reactant is accurately weighed and placed on the top of the quartz filter. Quartz wool is used to protect CaO reactant bed. Then the reactor is heated to a desired temperature with 2.0 L/min N_2 as purge gas. At the same time, the detector is turned on and connected for preheating and purging. When the temperature of the reactor as well as the HCl gas detector reaches the desired temperature and becomes stable, the inlet gas is switched to the experimental conditions. During the experiments, HCl concentration is monitored and recorded every 2 seconds by the detector. The outlet gas from the detector is cleaned by 0.1 mol/L NaOH solutions before being discharged.

2.2.2 Influence of CaO reactant on HCl release and mitigation from inorganic and organic sources of chlorine

2.2.2.1 Fixed bed tubular furnace experimental set-up

Fixed bed tubular furnace experimental set-up is used to investigate the influences of temperature and CaO absorbent on HCl release and control. As depicted in **Figure 2. 5**, the experimental system consists of three units: 1) gas source unit, 2) electrical tubular furnace unit, and 3) sampling unit.

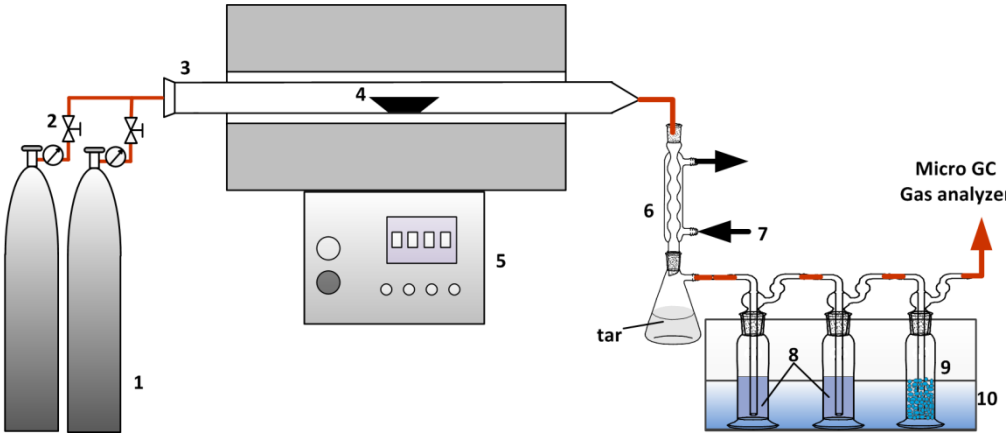

Figure 2. 5 Schematic diagram of the experimental fixed bed tubular furnace apparatus. 1, gas source; 2, gas flowmeter; 3, quartz tubular furnace; 4, quartz boat; 5, electric heater and temperature controller; 6, condenser for tar collection; 7, cooling water; 8, HCl mitigation solution (0.1 mol/L NaOH); 9, silica gel; 10, ice-water bath

- gas source unit: in this experiment, high pressure steel cylinders are used as gas source; gas used includes: N_2 and O_2;
- electric heater and temperature controller unit: a programmed temperature control heating system is used in this experiment, with the precision of the temperature controller of ±1 ^{o}C; the main reactor is a quartz tube, with 40.0 mm in inner diameter and 700.0 mm in length; feedstock is placed in a quartz boat during the experiments;
- sampling unit: tar sampling is conducted by a water-cooling condenser; the produced HCl gas is trapped by 0.1 mol/L NaOH solution; incondensable gas products are collected by gas bag.

2.2.2.2 Operating conditions and experimental procedure

The effect of temperature and addition of CaO reactant on Cl-content contaminants released from inorganic chlorine (NaCl) and organic chlorine (PVC) thermal conversion are experimentally investigated. **Table 2.6** illustrates the experimental conditions conducted in **Chapter 4**. The release characteristics of HCl from NaCl and PVC under redox atmosphere are identified. Besides, the effect of CaO reactant on HCl removal efficiency during PVC pyrolysis is studied. Temperature series of 550, 650, 750, and 850 ^{o}C, Ca/Cl molar ratio of 1:2, 1:1, 2:1, and 4:1, and CaO particle sizes of 0.25-0.43 mm and 0.13-0.18 mm are compared.

Table 2. 6 Experimental conditions of the influence of CaO reactant on HCl release and control from inorganic and organic sources

Feedstock	Temperature, ^{o}C	Reactant	Ca/Cl molar ratio	Atmosphere
NaCl	550, 650, 750, 850, 950	no	-	N_2; O_2; Air; Air + water vapor
PVC	100, 150, 200, 225, 250, 275, 300, 325, 350, 400, 500, 600, 700, 800	no	-	N_2; Air
PVC	550, 650, 750, 850	40-60 mesh CaO 80-120 mesh CaO	1:2; 1:1; 2:1; 4:1	N_2

For the experimental runs, pure N_2 is used as the carrier gas and supplied by the gas source. The tubular furnace is electrically-heated, with a thermocouple inserted in its middle to monitor the temperature profile. The quartz tube is 40.0 mm in inner diameter and 700.0 mm in length. During the experiments, the produced gas passes firstly a condenser for tar collection; and then, three impingers are used to trap the produced HCl gas. The impingers are immersed in an ice-water bath; among the impingers, the first two are filled with 0.1 mol/L NaOH solution, and the third one contains silica gel for moisture removal.

2.2.2.3 Thermogravimetric Analyzer (TGA)

A set of experiments are also conducted in **Chapter 4** by thermogravimetric analyzer (TGA, 951 Dupont Instrument) to record the mass change of non-catalytic and catalytic pyrolysis of PVC. The analyzer from Dupont Instrument is a horizontal module composed of two separate chambers disposed on the two sides of the balance housing. The experimental procedures of the TGA are the following. For non-catalytic PVC pyrolysis, pure PVC is accurately weighted and placed into the platinum pan of the analyzer; the apparatus is then heated from room temperature to 900 ^{o}C at different heating rate of 5, 10, and 20 ^{o}C/min under N_2 atmosphere. For catalytic pyrolysis cases, pure PVC is firstly mixed with CaO reactant at specific Ca/Cl molar ratio. Then the mixture is accurately weighted and placed into the analyzer; the same heating rate and temperature program are adopted as non-catalytic cases. The obtained results are then used for kinetics modeling of PVC dehydrochlorination process.

2.2.3 Influence of CaO reactant on Tar upgrading from Waste Single Component Pyrolysis

2.2.3.1 Pyrolysis-Gas Chromatography/Mass Spectrometry (Py-GC/MS) experimental apparatus

The role of CaO reactant on pyrolytic tar composition upgrading from waste single components is investigated using a Py-GC/MS experimental set-up. As illustrated in **Figure 2.6**, the experimental system consists of two parts: 1) pyrolysis reaction part; and 2) gas chromatography (GC) -mass spectrometry (MS) detection part.

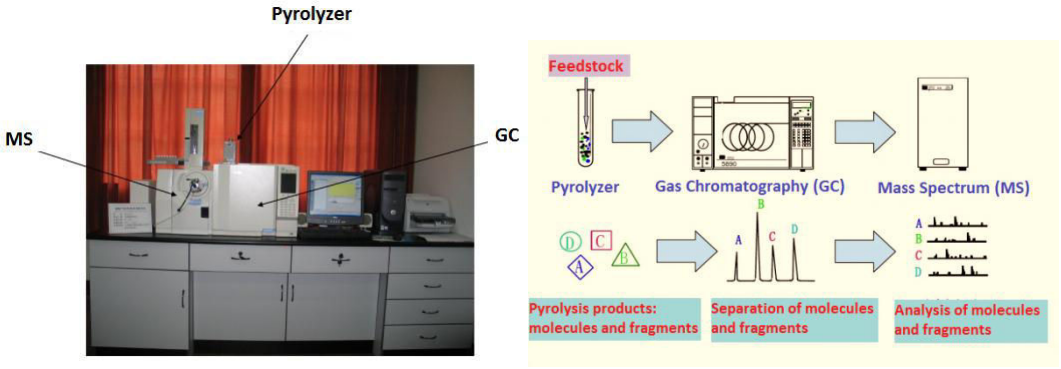

Figure 2. 6 General photograph and schematic diagram of the Py-GC/MS experimental apparatus

- pyrolysis reaction part: pyrolysis reactions takes place in a CDS5200 Pyroprobe with a platinum filament to heat the quartz-tube micro-reactor; the maximum temperature of the pyrolyzer reaches 1400 ^{o}C;
- gas chromatography-mass spectrometry (GC-MS) detection part: pyrolysis products (mainly volatiles) are detected by GC-MS (Thermo scientific, Trace DSQII) immediately. The injector temperature was kept at 250 ^{o}C. A DB-WAX capillary column with the size of 30m*0.25m*0.25μm is used as the chromatographic separation; the purge gas is Helium (the purity is 99.999%) with flow rate of 1.0 L/min; the temperature is programmed to increase from 40 ^{o}C to 250 ^{o}C at 8 ^{o}C/min; M/Z values between 35 to 450 are detected by the mass spectrometer at a scan rate of 2337.1 amu/s.

2.2.3.2 Operating conditions and experimental procedure

Table 2.7 summarizes the experimental conditions conducted in **Chapter 5**. The effect of CaO reactant on tar formation and tar composition from MSW single components are

investigated by Py-GC/MS apparatus. Besides, the effect of temperature and CaO reactant on PVC pyrolysis tar formation is further compared.

Table 2. 7 Experimental conditions of the effect of temperature and CaO reactant on tar cracking and upgrading

No.	Feedstock	Temperature, ^{o}C	Reactant	Reactor type
1#	Food	750	Without CaO	Py-GC/MS apparatus
2#	Wood			
3#	PVC			
4#	Food	750	With CaO	Py-GC/MS apparatus
5#	Wood			
6#	PVC			
7#	PVC	550	Without CaO	Py-GC/MS apparatus
8#		650		
9#		850		
10#	PVC	550	With CaO	Py-GC/MS apparatus
11#		650		
12#		850		

Before the experiments, the pyrolyzer is successively filled with some quartz wool, feedstock, and further some quartz wool. For CaO reactant pyrolysis experiments, CaO is uniformly mixed with the feedstock prior to be added into the pyrolyzer. For each run, approximately 5 mg of feedstock is used. Fast pyrolysis analysis is performed under Helium atmosphere and the heating rate is set as 10 000 °C/s to the desired final temperature.

2.2.4 Influence of CaO reactant on simulated MSW pyrolysis

Simulated MSW, as aforementioned in **Section 2.2.1**, is used as feedstock to conduct pyrolysis experiments with/without CaO reactant in **Chapter 6**. The experimental apparatus used is fixed type tubular furnace as illustrated in **Section 2.2.2**. The experimental procedures are also similar; besides gas products from S-MSW pyrolysis are collected, identified and analyzed.

Table 2. 8 Experimental conditions of influence of CaO reactant on simulated MSW pyrolysis

Experimental runs	Temperature oC	CaO reactant	Ca/Cl molar ration	a	b	c
1#	550	Without	-			
2#	650					
3#	750					
4#	850					
5#	550	With	2:1			
6#	650					
7#	750					
8#	850					
9#	650	With	1:2			
10#			1:1			
11#			4:1			
12#	750	With	1:2			
13#			1:1			
14#			4:1			

[a] focusing on the effect of temperature on product yields and properties during S-MSW pyrolysis;

[b] focusing on the effect of temperature and CaO reactant on product yields and properties during S-MSW pyrolysis;

[c] focusing on the effect of temperature and Ca/Cl molar ratio on HCl mitigation.

Before the test, tubular furnace is firstly preheated to the desired temperature by electrical heater under N_2 atmosphere. When the temperature is stable, 5.0 g of S-MSW is accurately weighed and placed in a dried quartz boat. For experiments with CaO reactant, S-MSW is uniformly mixed with CaO reactant before being added into the boat. Then N_2 carrier gas flow is adjusted to 120 NmL/min and the quartz boat is pushed into the center of the quartz tubular furnace in a short time to avoid air leaking in. The reaction time is set identical for all the experimental runs as 30 min. The produced gas is collected by a gas bag during this period. At the end of each test, the electrical heater is turned off immediately, but the carrier gas is kept until the temperature is cooled down to room temperature. **Table 2.8** summarizes the experimental working conditions adopted in **chapter 6**.

The effect of temperature and CaO reactant on pyrolytic product properties (for example product mass distribution, produced gas composition, tar yield and composition, solids yield and etc.) and HCl mitigation efficiency is investigated. A temperature series of 550, 650, 750, and 850 ^{o}C is examined.

2.3 Sampling and analysis

2.3.1 HCl sampling and analysis

The sampling method of HCl produced from waste pyrolysis is in accordance with the USA EPA METHOD 0051. As depicted in **Figure 2.5**, 0.1 mol/L NaOH is used to absorb the produced HCl together with Cl_2 (trace amount). Ice water bath is used to minimize the loss of absorbing solution, and at the end of the sampling train, silica gel is used to dry the produced gas and to protect the dry gas meter and pump. After the experiments, the absorbed solution is then quantitatively transferred to a volumetric flask and dilute with water. Ion chromatography (IC, Thermo Fisher Scientific) is used to determine the Cl^- content of the diluted solution. The amount of HCl collected by the solution can be obtained by:

$$M_{HCl} = \frac{C_{Cl^-} \times V_s}{M_{Cl^-}} \tag{2.1}$$

where, M_{HCl} is the mole of HCl trapped by the absorption solution; C_{Cl^-} represents the concentration of Cl^- detected by IC; V_s is the volume of the diluted sample in the volumetric flask; M_{Cl^-} is the molecular weight of Cl^-, 35.5 g/mol.

In order to determine the effect of CaO reactant on HCl gas removal, HCl mitigation efficiency (HME) is defined as follows:

$$\text{HME}=\left(1-\frac{\text{HCl generation with CaO reactant}}{\text{HCl generation without CaO reactant}}\right)\text{x}100\% \tag{2.2}$$

where, HRE represents for HCl mitigation efficiency.

2.3.2 Tar sampling and analysis

Tar yield and tar composition are investigated in **Chapter 5** and **Chapter 6**. Tar is collected from the water cooling condenser as depicted in **Figure 2.5**. Liquid products in condenser as well as that adhered on wall surface and in connection pipe are washed and extracted by dichloromethane solution. Then it is separated into organic and inorganic fractions. After evaporating the dichloromethane content of the organic fraction, the remaining part is treated as tar yield. Beside the total yield, effect of temperature and CaO reactant on tar composition is investigated. Tar composition is identified by Gas Chromatography/Mass Spectrometry (GC/MS, Agilent 7890B/5977A). The percentage of the

identified tar compounds is represented by the ratio of the corresponding peak area to the total peak areas.

2.3.3 Produced gas sampling and analysis

Produced gas from S-MSW pyrolysis (**Chapter 6**) is determined and analyzed to evaluate the effect of CaO reactant on produced gas quality enhancement. All the produced gas is collected in a gas bag during the whole period of each experimental run. A micro gas chromatograph (micro GC-490 analyzer, Agilent) is used to measure the molar composition of the produced gas, and the gas contains mainly N_2, CO, CO_2, CH_4, H_2, and C_2H_m (the sum of C_2H_2, C_2H_4 and C_2H_6). More detailed information about the analyzer can be obtained from the work of Dong [6]. N_2 is regarded as the tracer gas to determine the effluent gas volume. The total gas yield can be obtained by the following equation:

$$Y_{gas} = \frac{\left(\frac{V_{N2}}{x_{N2}} - V_{N2} \right)}{m_{S\text{-}MSW}} \tag{2.3}$$

where, Y_{gas} is the total gas yield from S-MSW pyrolysis, mL/g-S-MSW; V_{N2} represents the total volume of the purge gas N_2 during the experimental period, mL; x_{N2} is the molecular fraction of N_2 in the produced gas, %; and $m_{S\text{-}MSW}$ is the mass of the feedstock, g.

2.3.4 Solid characterization

Solid samples, including selected MSW feedstock, solid products and CaO reactant are characterized by using TGA, FESEM, XRD/EDS, XRF and BET. Details are presented as follows.

- **X-ray fluorescence (XRF)**

  XRF analysis is performed with an Energy Dispersive X-ray fluorescence spectrometer (EPSILON 3XL) from PANanalytical company. The electrical power of the X-ray is 15 W. Filters are positioned on the beam route to the sample to avoid detector saturation. The resolution range of the high resolution Silicium Drifft SDD detector is 135 eV to 5.9 keV.

- **Scanning Electron Microscope (SEM) and Energy-dispersive X-ray spectroscopy (EDS) measurement**

  A scanning electron microscope (SEM, Carl Zeiss, Utral 55) is used to observe the

surface morphology of both the reactants and the solid products by scanning the sample surface with a focused beam of electrons. The electrons are accelerated through a high voltage (20 kV). And the electrons interact with atoms in the sample and produce signals containing information about the s surface morphology of the sample.

EDS is used to detect the elemental composition and chemical characterization of a sample surface by determining the interaction of X-ray excitation and sample surfaces.

- **X-ray diffraction (XRD)**

XRD is used to identify molecular structure of a crystal by diffracting the incident X-rays into specific directions. It is performed in a Philips diffractometer (from PANalytical, X'pert Pro MPDmodel) with a θ–θ Bragg-Brentano configuration, a current of 45 kV and an intensity of 40 mA. The radiation wavelength is of 1.543 Å. Diffraction peaks have been recorded in the 10- 70 degrees in 2θ and a speed of 0.042°/sec.

- **BET measurement**

BET measurement is used to determine the specific surface area, pore volume and structure of solid samples. Determination of the specific surface area is based on the adsorption isotherm. More detailed knowledge for the operating mechanism of BET could be found in the work from Ducousso [7]. The used BET analyzer is an ASAP 2010 type from Micromeritics. Argon is used as the adsorption gas, and the Brunauer-Emmett-Teller model is used for the determination of specific surface area; pore size and pore volume is evaluated using the Horvath-Kawazoe model. Based on the results, porosity, which represents the fraction of void space in a specified material, could be obtained by equation (2.4):

$$P(\%) = \frac{V_p}{V_T} \times 100\% \tag{2.4}$$

where, V_p stands for the total pore volume detected by BET analysis; V_T is the total or bulk volume of material; P denotes porosity.

2.3.5 Mass balance and chlorine balance calculation

To make sure the correctness of the interpretation of the experimental results, experiments are repeated at least three times and the reported data are the average value of the trials. Besides, mass balance of each experiment is calculated by comparing the input flows such as feedstock, reactant, and the gas agent and the output flows like produced gas, condensate and solid residues. Mass balances of all the experimental runs are in the range of 85-103%, which is quite acceptable to ensure the quality of experimental data. Incomplete recovery of condensates, estimation of the produced gas yield and the uncertainties of the measurement may be responsible for the deviation of the mass balance closure from 100%.

Special attention has been paid to the chlorine content in feedstock as well as in products. Chlorine balance is also calculated during MSW pyrolysis experiments. In contrast to mass balance, chlorine balance closure is not achieved; chlorine balances for all the experimental runs varies from 75% to 92%, mainly due to the small amount of total chlorine content and loss of HCl in the sampling line.

2.4 Thermodynamic simulation using FactSage software

2.4.1 General principle of thermodynamic equilibrium simulation

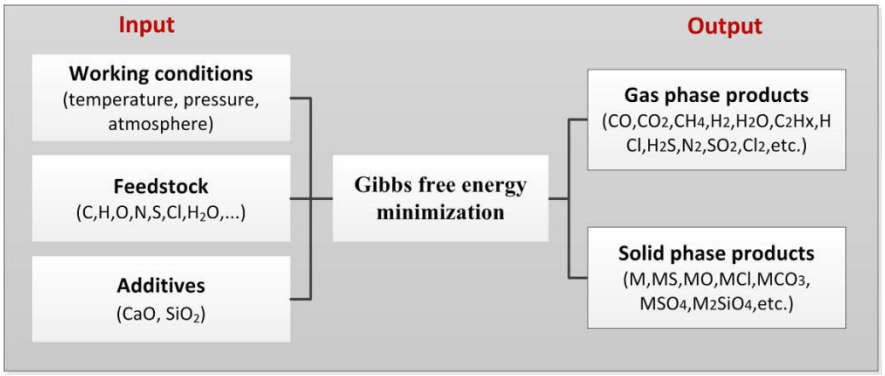

Figure 2. 7 General principle of the thermodynamic equilibrium calculation system

As illustrated in **Figure 2.7**, thermodynamic equilibrium simulation in this work uses the principle of minimizing the total Gibbs free energy to realize the thermodynamic equilibrium of the considered system. Generally, Gibbs free energy is considered as a thermodynamic potential to quantify the useful potential work, which can be acquired from the target system [1, 8, 9]. For a given system with constant temperature and pressure, when it reaches thermodynamic equilibrium state, the total amount of the Gibbs free energy is minimized.

Therefore, the principle of minimizing the total Gibbs free energy can be used to estimate the possible product species for a given system according to its elemental composition.

During the simulation, the system input includes the working conditions, feedstock and the reactant, and the final equilibrium state is determined by calculating all the possible species derived from the input elements with the minimum Gibbs free energy.

For a given condition of specified temperature and pressure, the total Gibbs free energy of the considered system can be obtained by:

$$G = \sum \mu_i \cdot n_i \left(n_i \geq 0,\ i = 1, 2, 3, ..., N \right) \tag{2.5}$$

Where n_i represents the moles of the i^{th} possible component in the system, u_i is the free energy of the i^{th} possible component, N is the total amount of the possible species in the considered system.

When the considered system reaches equilibrium state, the proper n_i values for the components should minimize the function G. Besides, n_i should also satisfy the following conditions:

1) $n_i \geq 0$;

2) And for a given element j, $\sum_i a_{ij} \cdot n_i = B_j$, where B_j is the total molar amount of element j, a_{ij} is the molecular amount of element j in the i^{th} component (satisfied with the fundamental principle of mass conservation).

2.4.2 Thermodynamic simulation software FactSage 6.3

In this thesis, thermodynamic simulation software, FactSage 6.3, is used to perform the theoretical calculations as presented in **Figure 2.8**. FactSage is believed one of the most commonly used chemical thermodynamics databases and also computing systems in the world [10, 11]. It is a fusion of two thermochemical packages named FACT-Win/F*A*C*T and ChemSage/SOLGASMIX by Thermfact/CRCT (Montreal, Canada) and GTT-Technologies (Aachen, Germany), respectively.

Figure 2. 8 Main menu of FactSage 6.3 software

The FactSage software consists of a series of modules, including general information, database, calculation (reaction, predom, Eph, Equilib, Phase Diagram, and OptiSage) and manipulation modules [12]. Among which, the Equilib calculation module is one of the most widely used program. As aforementioned, the software uses the Gibbs energy minimization algorithm to calculate the concentrations of all possible chemical species when specified elements or compounds react or partially react to reach a chemical equilibrium state at given conditions.

In this work, the release of HCl from chlorine sources is theoretically simulated by FactSage 6.3; the effect of temperature, atmosphere, moisture content as well as reactants on product distribution is identified. The obtained simulation results provide a better understanding of the experimental results and it can be used from reaction mechanism perspective to explain the experimental results when both experimental and simulative data are assimilated.

2.5 Life cycle assessment

The definition and general introduction of LCA is explained in **Chapter 1**. This section details the LCIA methodology adopted in the present work. In this study, the CML (baseline) methodology (created by the University of Leiden in the Netherlands) is used [13]. The CML impact category method is one of the most popular and well-acceptable LCIA methodology [14] and the impact categories are illustrated in **Table 2. 9**.

Table 2. 9 Impact categories included in the method CML (baseline)

Method: CML (baseline)		
Impact category group	Name of the impact category in the method	Characterization unit
Acidification Potential	Acidification potential - average Europe	kg SO_2 equivalent
Climate change Potential	Climate change - GWP100	kg CO_2 equivalent
Depletion of abiotic resources Potential	Depletion of abiotic resources - elements, ultimate reserves	kg antimony equivalent
	Depletion of abiotic resources - fossil fuels	MJ
Ecotoxicity Potential	Freshwater aquatic ecotoxicity - FAETP inf	kg 1,4-dichlorobenzene equivalent
	Marine aquatic ecotoxicity - MAETP inf	kg 1,4-dichlorobenzene equivalent
	Terrestrial ecotoxicity - TETP inf	kg 1,4-dichlorobenzene equivalent
Eutrophication Potential	Eutrophication - generic	kg PO_4^- equivalent
Human toxicity Potential	Human toxicity - HTP inf	kg 1,4-dichlorobenzene equivalent
Ozone layer depletion Potential	Ozone layer depletion - ODP steady state	kg CFC-11 equivalent
Photochemical oxidation Potential	Photochemical oxidation - high NOx	kg ethylene equivalent

Among the categories, six of them are considered and compared in this work, including three non-toxic and three toxic impacts: non-toxic, Climate change - GWP100, Acidification Potential - AP, and Eutrophication Potential - EP; and toxic, Terrestrial ecotoxicity - TETP, Freshwater aquatic ecotoxicity - FAETP and Human toxicity - HTP. Detailed characterization unit and normalization references have been indicated in **Table 2.10**.

Table 2. 10 Selected life cycle impact categories, characterization and normalization references based on CML (baseline) method from GaBi software

Impact categories	Unit	Characterization	Factor	Normalization(in per year, world, 2000)
Global warming potential (GWP100)	kg CO_2-equivalent	CO_2	1	4.22E+13
		CH_4	28	
		N_2O	265	
Acidification potential (AP)	kg SO_2-equivalent	SO_2	1.2	2.39E+11
		NO_x	0.5	
		HCl	0.88	
		NH_3	1.60	
Eutrophication Potential (EP)	kg PO^{4-} -equivalent	NO_x	0.13	1.58E+11
		N_2O	0.27	
		NH_3	0.35	
Terrestrial ecotoxicity (TETP)	kg 1,4-dichlorobenzene eq.	HF	2.9E-03	1.09E+12
		PCDD/Fs	1.2E+04	
Freshwater aquatic ecotoxicity (FAETP)	kg 1,4-dichlorobenzene eq.	HF	4.6	2.36E+12
		PCDD/Fs	2.1E+06	
Human toxicity (HTP)	kg 1,4-dichlorobenzene eq.	HCl	0.5	2.58E+12
		PM	0.82	
		NH_3	0.1	
		HF	2.9E+03	
		NOx	1.2	
		SO2	9.6E-02	

2.6 Bibliography

[1] Dong J, Chi Y, Tang Y, Ni M, Nzihou A, Weiss-Hortala E, et al. Partitioning of Heavy Metals in Municipal Solid Waste Pyrolysis, Gasification, and Incineration. Energy & Fuels. 2015;29:7516-25.

[2] Technology CMoIaI. Chinese national standards of chemical industry-Calcium oxide for industrial use (HG/T 4205-2011). Beijing: Chinese Environmental Science Press; 2011.

[3] Sing KS. Reporting physisorption data for gas/solid systems with special reference to the determination of surface area and porosity (Recommendations 1984). Pure and applied chemistry. 1985;57:603-19.

[4] Ohba T, Suzuki T, Kaneko K. Relationship between DR-plot and micropore width distribution from GCMC simulation. Carbon. 2000;13:1892-6.

[5] Maes N, Zhu H-Y, Vansant E. The use of the logarithmic adsorption isotherm for the determination of the micropore-size distribution. Journal of Porous Materials. 1995;2:97-105.

[6] Dong J, Nzihou A, Chi Y, Weiss-Hortala E, Ni M, Lyczko N, et al. Hydrogen-Rich Gas Production from Steam Gasification of Bio-char in the Presence of CaO. Waste and Biomass Valorization. 2017;8:2735-46.

[7] Ducousso M. Gasification biochar reactivity toward methane cracking. Albi, France: École Nationale Supérieure des Mines d'Albi-Carmaux conjointement avec l'INP Toulouse; 2015.

[8] Néron A, Lantagne G, Marcos B. Computation of complex and constrained equilibria by minimization of the Gibbs free energy. Chemical engineering science. 2012;82:260-71.

[9] Bartel CJ, Millican SL, Deml AM, Rumptz JR, Tumas W, Weimer AW, et al. Physical descriptor for the Gibbs energy of inorganic crystalline solids and prediction of temperature-dependent materials chemistry. arXiv preprint arXiv:180508155. 2018.

[10] Bale C, Bélisle E, Chartrand P, Decterov S, Eriksson G, Hack K, et al. FactSage thermochemical software and databases—recent developments. Calphad. 2009;33:295-311.

[11] Bale C, Bélisle E, Chartrand P, Decterov S, Eriksson G, Gheribi A, et al. FactSage thermochemical software and databases, 2010–2016. Calphad. 2016;54:35-53.

[12] GTT-Technologies TC. The Integrated Thermodynamic Databank System FactSage©. 2018.

[13] Aitor P. Acero CR, Andreas Ciroth. LCIA methods Impact assessment methods in Life Cycle Assessment and their impact categories. 2016.

[14] Raugei M, Bargigli S, Ulgiati S. Life cycle assessment and energy pay-back time of advanced photovoltaic modules: CdTe and CIS compared to poly-Si. Energy. 2007;32:1310-8.

Chapter 3

Experimental and kinetics study on HCl mitigation by CaO reactant

3.1 Introduction

As it has been indicated in **Chapter 1**, HCl is usually generated as a consequence of high chlorine (Cl) content in MSW. The presence of HCl in flue gas causes serious problems associated with corrosion, toxic organic contaminants formation, acidification, etc. Currently, HCl is usually removed together with acid gases by air pollution control (APC) systems in WtE plants, which basically works in the temperature range lower than 300 ^{o}C [1-3]. Although the removal efficiency of HCl by APC systems is high enough for the emission control of HCl gas, the presence of HCl in flue gas has already acted the role of corrosive agent and chorine source for polychlorinated dibenzo-p-dioxins and polychlorinated dibenzofurans formation during flue gas cooling down under such conditions [3]. Therefore, the primary aim of this work is to investigate the role of CaO reactant on in-furnace HCl immobilization to avoid the release of HCl into produced gases. Under such circumstance, the obtained high quality pyro-gasification products can be further utilized in an energy efficient and environmental friendly approach.

As aforementioned in **Chapter 1**, calcium-based absorbents are the most commonly used reactants due to their abundant sources, relatively cheap and high removal efficiency. Therefore, CaO reactant is selected in the presented work. In order to investigate the effect of in-situ CaO reactant on HCl capture, gas-solid reaction mechanism between CaO and HCl is investigated in this chapter by performing breakthrough experiments as well as thermodynamic and kinetic modeling. Accordingly, the structure of this chapter is presented as follows:

- **Section 3.2** theoretically investigates the gas-solid reaction mechanisms between CaO and HCl. The Gibbs free energy of the reaction and standard equilibrium constant is estimated by thermodynamic analysis. Kinetic modeling using shrinking unreacted core model is also performed;

- **Section 3.3** is dedicated to investigate the effect of key parameters on HCl mitigation by CaO reactant. The varied conditions include the reaction temperature, raw HCl gas concentration and the presence of other gas species. Morphology analysis of the spent CaO reactants is also performed to determine the formation of product-layer;

- **Section 3.4** summarizes the findings obtained in this chapter.

3.2 Gas-solid reaction mechanism between CaO and HCl

3.2.1 Thermodynamic analysis of the reaction between CaO and HCl

The well recognized absorption reaction of HCl gas by CaO is described as follows [4, 5]:

$$CaO_{(s)} + 2HCl_{(g)} \rightarrow CaCl_{2(s)} + H_2O_{(g)} \quad (3.1)$$

The absorption reaction is actually reversible at high temperature, which means temperature will affect the thermodynamic equilibrium of the reaction. Therefore, thermodynamic analysis of dehydrochlorination reaction is of great interest. According to the reaction presented in **Eq. (3.1)**, the reaction enthalpy, Gibbs free energy and standard chemical reaction equilibrium constant of the dehydrochlorination reaction at standard temperature and pressure (STP) can be estimated by:

$$\Delta_r H_m^\theta = \left(\sum_i r_i \Delta_r H_{m,j}^\theta \right)_{\text{products}} - \left(\sum_i r_i \Delta_r H_{m,j}^\theta \right)_{\text{reactants}} \quad (3.2)$$

$$\Delta_r G_m^\theta = \left(\sum_i r_i \Delta_r G_{m,j}^\theta \right)_{\text{products}} - \left(\sum_i r_i \Delta_r G_{m,j}^\theta \right)_{\text{reactants}} \quad (3.3)$$

$$InK^\theta = -\Delta_r G_m^\theta / RT \quad (3.4)$$

where, $\Delta_r H_m^\theta$ and $\Delta_r G_m^\theta$ are enthalpy of formation and Gibbs free energies of formation at STP, respectively; j refers to a specific product or reactant and r_i refers to its stoichiometric coefficient; K^θ is standard chemical reaction equilibrium constant at STP and R is ideal gas constant and the value is 8.314 J/(K*mol). However, considering the high reaction

temperature in this work, the effect of temperature on $\Delta_rH_m^\theta$, $\Delta_rG_m^\theta$, and K^θ must be taken into account. The Gibbs-Helmholtz equation reveals that the change of Gibbs free energy of a system is a function of temperature as [6]:

$$\left(\frac{\partial(\Delta G/\mathrm{T})}{\partial T}\right)_P = -\frac{\Delta H}{T^2} \tag{3.5}$$

Therefore, for reactions at constant pressure, **Eq.(3.5)** becomes:

$$\frac{\partial(\Delta_r G_m^\theta/\mathrm{T})}{\partial T} = -\frac{\Delta_r H_m}{T^2} \tag{3.6}$$

Combining **Eq.(3.6)** and the integral form of **Eq.(3.4)**, the reaction constant as a function of temperature can be obtained as:

$$InK^\theta(T) - InK^\theta(T_0) = \int_{T_0}^{T} \frac{\Delta_r H_m}{RT^2} dT \tag{3.7}$$

According to the Kirchhoff's law of thermochemistry, Δ_rH_m can be obtained as [7]:

$$\Delta_r H_m(T) = \Delta_r H_m^\theta(T_0) + \int_{T_0}^{T} \Delta_r C_p \mathrm{d}T \tag{3.8}$$

where, C_p represents the specific heat capacity at constant pressure, and it can be estimated by the Shomate Equation according to [8, 9]:

$$C_p = a + b\times T + c\times T^2 + d\times T^3 + \frac{e}{T^2} \tag{3.9}$$

And Δ_rH_m can thus be obtained by [8]:

$$\Delta_r H_m(T) = \Delta_r H_m^\theta(T_0) + \Delta a\times T + \Delta b\times T^2/2 + \Delta c\times T^3/3 + \Delta d\times T^4/4 - \Delta e/T + \Delta f - \Delta h \tag{3.10}$$

Where *a*, b, c, d, e, f, and h are the coefficients for the calculation of the specific heat capacity at temperature of T. Accordingly, when Δ_rH_m is determined, K^θ can be calculated based on **Eq. (3.7)**; and similarly, Δ_rH_m under different temperature can be obtained based on **Eq. (3.4)**. **Table 3.1** summarizes the specific heat capacity coefficients and thermodynamic data for the reactants and products from **Eq.(3.1)** [10].

Table 3. 1 The specific heat capacity calculation coefficients and thermodynamic data

		CaO	$CaCl_2$		HCl	H_2O
Cp, J/(mol*K)	Temperature range	298-3200	298-1045	1045-3000	298-1200	500-1700
	a	49.95	87.30	102.53	32.12	30.09
	b	4.89	-35.08	2.01E-08	-13.46	6.83
	c	-0.35	44.13	-9.23E-09	19.87	6.79
	d	0.05	-9.85	1.41E-09	-6.85	-2.53
	e	-0.83	-0.67	2.61E-09	-0.05	0.08
	f	-652.97	-822.90	-815.00	-101.62	-250.88
	h	-635.09	-795.80	-774.09	-92.31	-241.83
$\Delta_f H_m^\theta$ (298), kJ/mol		-634.9	-795.4		-92.3	-285.8
$\Delta_f G_m^\theta$(298), kJ/mol		-603.3	-748.8		-95.3	-237.1
C_p(298), J/(mol*K)		42.0	72.9		29.1	75.3

The calculation results are reported in **Table 3.2**, results reveal that within the temperature range of 500-1200 K, the Gibbs free energy of the reaction is always negative, indicating that the gas-solid reaction between CaO and HCl could spontaneously occur. However, with the increasing of temperature, the Gibbs free energy of reaction rises continuously and the standard equilibrium constant declines significantly by approximately twelve orders of magnitude from $6.97X10^{16}$ at temperature of 500K to $2.28\ X10^{4}$ at temperature of 1200K. This means that although the reaction is still spontaneous, the degree of the reaction toward the formation of $CaCl_2$ and H_2O will significantly be inhibited due to the shift of chemical equilibrium. It is notable that although the reaction is spontaneous from thermodynamic perspective, the reaction rate is significantly affected by the kinetics; therefore, kinetic investigation of the considered reaction system is of great importance.

Table 3. 2 Thermodynamic calculation results of Gibbs free energy and standard equilibrium constant

T/K	ΔrHm(K) , kJ/mol	ln K^{θ}	K^{θ}	ΔrGm(K) , kJ/mol
500	-216.41	38.78	$6.97X10^{16}$	-161.22
550	-216.24	34.08	$6.33\ X10^{14}$	-155.84
600	-216.06	30.18	$1.28\ X10^{13}$	-150.54
650	-215.85	26.89	$4.77\ X10^{11}$	-145.32
700	-215.62	24.09	$2.90\ X10^{10}$	-140.21
750	-215.36	21.69	$2.62\ X10^{9}$	-135.22
800	-215.06	19.60	$3.26\ X10^{8}$	-130.37
850	-214.73	17.79	$5.30\ X10^{7}$	-125.69
900	-214.36	16.20	$1.08\ X10^{7}$	-121.21
950	-213.94	14.81	$2.69\ X10^{6}$	-116.94
1000	-213.48	13.58	$7.93\ X10^{5}$	-112.93
1050	-212.96	12.51	$2.71\ X10^{5}$	-109.20
1100	-212.39	11.57	$1.06\ X10^{5}$	-105.80
1150	-211.76	10.75	$4.65\ X10^{4}$	-102.75
1200	-211.07	10.03	2.28 X104	-100.11

3.2.2 Kinetics analysis of the reaction between CaO and HCl

As aforementioned in last section, thermodynamic analysis determines whether the reaction system is spontaneous; but the reaction rate is affected by the reaction kinetics. Therefore, kinetics modeling of the considered reaction system (as illustrated in **Eq. (3.1)**) is investigated in this section.

The grain model and shrinking unreacted core model are often used to describe a non-catalytic gas-solid reaction for porous and nonporous solid reactant, respectively, with the purpose to determine the rate-limiting step of the process by either chemical reaction or product-layer diffusion (PLD) and to estimate the key kinetic parameters, for example chemical reaction rate constant and diffusivity for PLD process [4, 11]. The shrinking unreacted core model is used in this study, because the used CaO reactant is nonporous [12].

3.2.2.1 Ideal shrinking unreacted core model

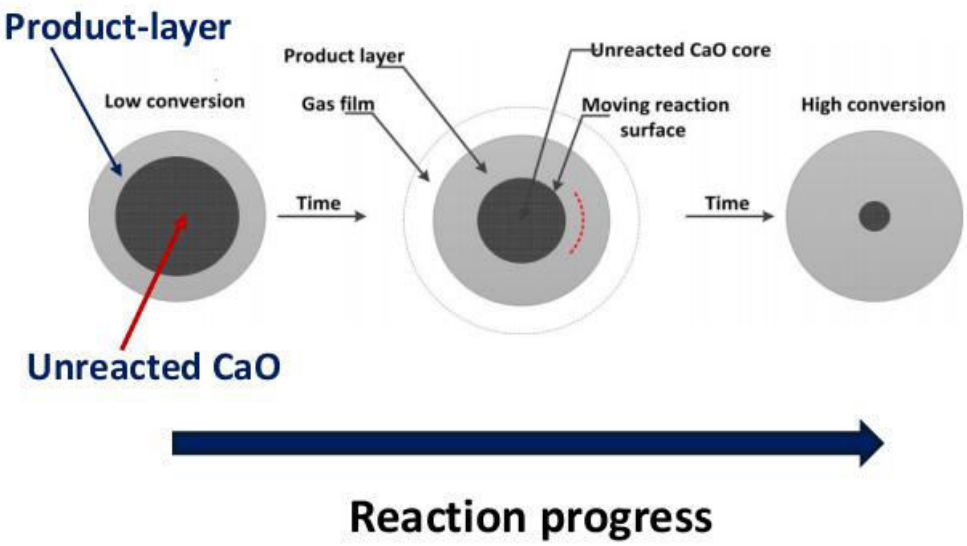

Figure 3. 1 Schematic diagram of the reaction between CaO and HCl, showing the growth of the $CaCl_2$ product-layer and the consumption of unreacted CaO core

As mentioned in **Eq. (3.1)**, the gas-solid reaction in this study is considered between the isothermal spherical CaO particle and a constant concentration of HCl gas flow to form a solid phase ($CaCl_2$ product-layer) and H_2O. As the reaction goes on, the unreacted CaO core is gradually consumed and the thickness of the product-layer is increased [4]. **Figure 3.1** shows the reaction process of the growth of the $CaCl_2$ product-layer and the consumption of unreacted CaO core. Assumption has been made that no HCl gas is diffused into the unreacted CaO core, since the reactant is non-porous. The diffusion of HCl through the $CaCl_2$ product-layer is possible, since it is considered porous. Also, it is assumed that the surface reaction is considered so fast that as soon as HCl reaches the surface of the unreacted CaO core, the reaction occurs and HCl is consumed. Therefore, the reaction surface (i.e. the core surface) moves towards the center of spherical CaO particle. However, as presented in **Figure 3.1**, although the formed product-layer is mainly consisted of $CaCl_2$, it is assumed in the simplified theoretical model that the overall particle size (R, represents the overall particle size of both the product-layer and the unreacted CaO core) remains unchanged.

The reaction between the isothermal spherical CaO particle and a constant concentration of HCl gas flow (from the ambient environment) can be described as [13, 14]:

- external diffusion step: diffusion of the HCl gas through the surrounding gas film of the solid particle to reach its surface;

- internal diffusion step: diffusion of the HCl gas through the porous product-layer (the produced $CaCl_2$ layer considered in this work) to the unreacted CaO surface;
- chemical reaction step: chemical reaction occurs between HCl gas and unreacted solid CaO on the core surface;
- internal diffusion step: diffusion of the product gas H_2O vapor through the porous product-layer to the solid surface;
- And external diffusion: diffusion of the product gas H_2O through the gas film to the bulk.

As depicted in **Figure 3.1**, parameters related to the reaction processes are described as: R refers to total radius of the overall particles including unreacted CaO core and product-layer; r_c is the radius of the unreacted spherical CaO core; C_{Ag}, C_{As}, C_{Ac} and C_A are the concentrations of the HCl (g) gas in the bulk gas, on the surface of the overall particle, on the surface of the unreacted CaO core, and at any intermediate location ($r_c \leq r \leq R$) in the $CaCl_2$ product-layer.

In order to determine the kinetics parameters of the process, calculations focusing on one rate-limiting step at a time are conducted. It means for example that when external diffusion is considered as rate-limiting steps; the effect of internal diffusion and chemical reaction rate is negligible. Since the kinetic mechanism of external and internal diffusion steps are similar, only external diffusion of HCl, internal diffusion of HCl and chemical reaction are investigated as the rate-limiting steps

External diffusion of HCl as the rate-limiting step

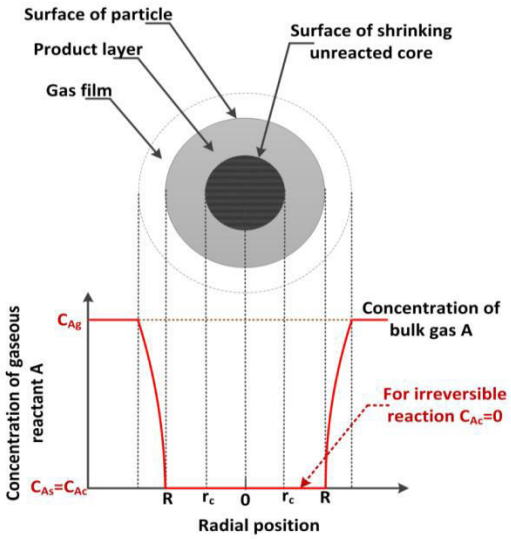

Figure 3. 2 Concentration of HCl under the condition that the reaction is only limited by gas film diffusion (A refers to HCl gas)

Figure 3.2 exhibits the change of HCl gas concentration under the assumption that external diffusion is the only rate-limiting step. It means that the effective diffusivity of HCl through the porous $CaCl_2$ product-layer and the reaction rate constant k_s are very large. In that case, the concentrations of HCl on the product-layer surface C_{As} and on the core surface C_{Ac} are more or less the same and close to zero, as presented in **Figure 3.2**.

Under such circumstance, the conversion rate of CaO can be described by [4]:

$$X_{CaO} = 1 - \left(\frac{r_c}{R}\right)^3 = \frac{t}{\tau_g} = G(x) \tag{3.13}$$

where, X_{CaO} is the conversion rate of solid reactant CaO; k_g represents the mass transfer constant of HCl gas surrounding the reactant; and τ_g is the time needed for the total conversion of CaO and $\tau_g = \frac{\rho_{CaO} R}{6 k_g C_{Ag}}$. It is obvious that under such conditions, the conversion rate of CaO is a linear function of time.

Internal diffusion of HCl through the product-layer as the rate-limiting step

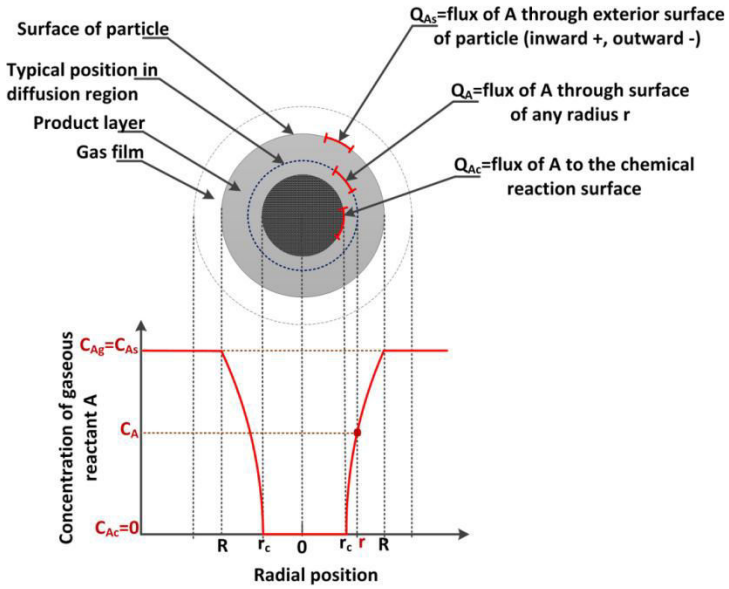

Figure 3. 3 Concentration of HCl gas under the condition that the reaction is only limited by internal diffusion of HCl through the product-layer (A refers to HCl gas)

Figure 3.3 presents the concentration of reactant HCl under the condition of the reaction is only limited by internal diffusion through the product-layer. In that case, the external diffusion of HCl through the gas film and the chemical reaction on the core surface are considered very fast. Therefore, HCl flow concentration in the environmental C_{Ag} is equal to that on the product-layer surface C_{As} ($C_{Ag} = C_{As}$) and the concentration on the core surface C_{Ac} is approximately zero ($C_{Ac} = 0$), as presented in **Figure 3.3**.

Under such condition, the conversion rate of CaO can be described by [15]:

$$\frac{t}{\tau_p} = \left(1 - 3\left(\frac{r_c}{R}\right)^2 + 2\left(\frac{r_c}{R}\right)^3\right) = 1 - 3\left(1 - X_{CaO}\right)^{\frac{2}{3}} + 2\left(1 - X_{CaO}\right) = P(x) \qquad (3.14)$$

where, τ_p is the time taken for the complete conversion of CaO and $\tau_p = \frac{\rho_{CaO} R^2}{12 D_e C_{Ag}}$; D_e refers to the effective diffusivity of HCl through the porous $CaCl_2$ product-layer.

Chemical reaction at core surface as the rate-limiting step

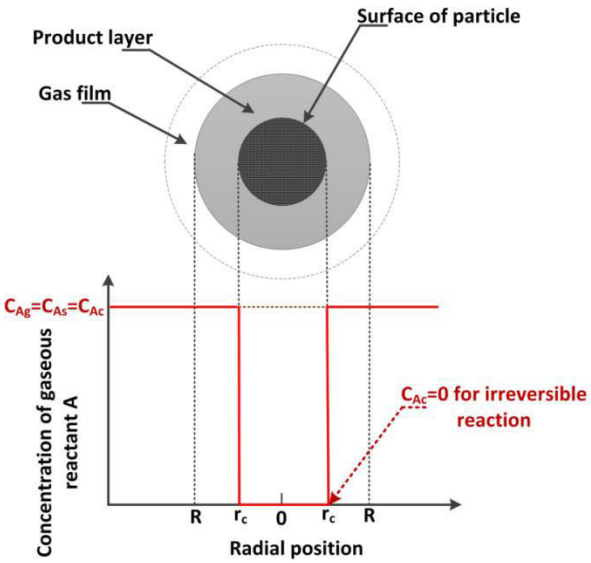

Figure 3. 4 Concentration of HCl gas under the condition that the reaction is only limited by gas-solid chemical reaction (A refers to HCl gas)

Figure 3.4 shows the change of HCl gas concentration under the condition that the reaction is only limited by gas-solid chemical reaction. In this case, the internal and external diffusion of HCl gas is very fast and only the surface reaction is slow. Therefore, $C_{Ag} = C_{As}$ and $C_{Ac} = 0$.

Under such condition, the conversion rate of CaO can be described by [15]:

$$\frac{t}{\tau_c} = \left(1 - \frac{r_c}{R}\right) = \left(1 - \left(1 - X_{CaO}\right)^{\frac{1}{3}}\right) = C(x) \tag{3.15}$$

where, τ_c is the time taken to achieve complete conversion of CaO, and $\tau_c = \frac{\rho_{CaO} R}{2 k_s C_{Ag}}$.

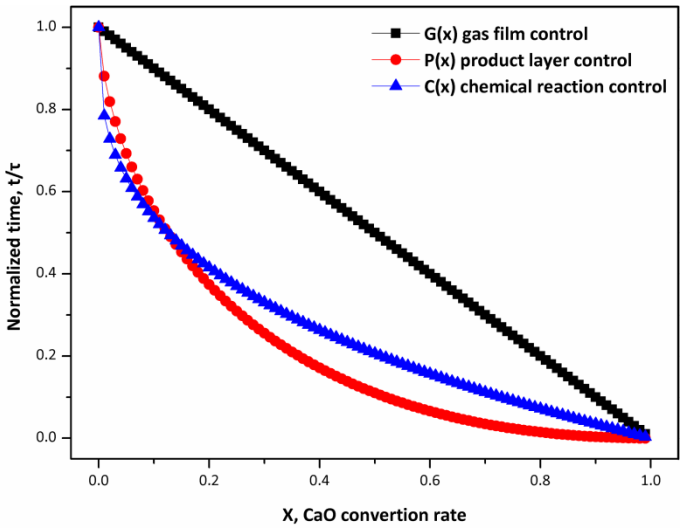

Figure 3. 5 Normalized reaction time as a function of CaO reactant conversion rate

Figure 3.5 summarizes the results of the normalized reaction time as a function of CaO conversion rate under the calculation of ideal shrinking unreacted core model. As presented, **Eq. (3.14)**, **Eq. (3.15)**, and **Eq. (3.16)** are defined as G(x), P(x), and C(x), respectively. If G(x) is linearly dependent on the reaction time t, the overall reaction is considered to be controlled by external diffusion; if P(x) is linearly dependent on the reaction time t, the overall reaction is considered to be controlled by internal diffusion; and if C(x) is linearly dependent on the reaction time t, the overall reaction is considered to be controlled by chemical reaction rate.

3.2.2.2 Estimation of kinetic parameters

Previous studies revealed that compared with internal diffusion and chemical reaction rate, external diffusion of gas-solid reactions, i.e. the resistance of reactant gas from the bulk to the solid particle, is not significant and is negligible [16-18]. Therefore, it is not taken into account in this work.

When considering the change of the particle size, the conversion rate of CaO under the condition that the internal diffusion is rate-limiting can be modified to the following equation [4, 15]:

$$P(x)=3\left(\frac{Z-\left(Z+(1-Z)(1-X_{CaO})^{2/3}\right)}{Z-1}-(1-X_{CaO})^{2/3}\right) \quad (3.16)$$

where, Z represents the ratio of molar volume of product $CaCl_2$ to that of reactant CaO, and the value is selected as 3.04 in the present work.

Therefore, the reaction time t and the conversion rate of CaO reactant can be described when both internal diffusion of HCl in the product-layer and chemical reaction on CaO core surface are the rate-limiting steps:

$$\frac{t}{\tau_c}=C(x)+\theta^2 P(x) \quad (3.17)$$

where, $\theta^2=\frac{\tau_p}{\tau_c}=\frac{k_s R}{6D_e}$ represents the ratio of the product-layer diffusion resistance to the chemical reaction resistance, which can be used to determine whether the process is limited by diffusion or chemical reaction rate. When θ^2 <<1, it means the diffusion resistance is much lower than the reaction resistance and the process is controlled by chemical reaction; when θ^2 >10, the process is mainly governed by product-layer diffusion; and when 1< θ^2 <10, it means both product-layer diffusion and chemical reaction are determining factors for the process.

By least-squares fitting of **Eq. (3.17)** to the experimental data, values of τ_p, τ_c, and θ^2 can be determined. And then the effective diffusivity of HCl through the porous $CaCl_2$ product-layer D_e and the chemical reaction rate k_s can be calculated. According to the Arrhenius equation, the chemical reaction rate k_s can be determined by:

$$k_s=A\exp\left(\frac{-E}{RT}\right) \quad (3.18)$$

where A is the pre-exponential factor in min^{-1}; E is the activation energy in kJ/mol; R is the ideal gas constant and its value is 8.314 J/(mol*K). And therefore:

$$\ln k_s=-(E_C/R)(1/T) \quad (3.19)$$

$$\ln D_e=-(E_P/R)(1/T) \quad (3.20)$$

Where, E_c and E_p represent the apparent activation energy of chemical reaction and product-layer diffusion, respectively.

3.3 Experimental results

Mitigation of HCl gas by CaO reactant under moderate high temperature are investigated in a vertical tubular reactor and the experimental set-up, working conditions and experimental procedures are described in **Chapter 2**. The effect of reaction temperature, raw HCl gas concentration, purge gas velocity, and purge gas composition are determined and the kinetic parameters are estimated according to experimental data. In this section, several parameters to explain the experimental results are defined as:

Breakthrough time: the time when the outlet concentration of HCl is detected to be higher than 20 ppm, (due to the fluctuation of the detector, 20 ppm (i.e. c/c_0 = 20 ppm /2000 ppm = 0.01) instead of 1 ppm is selected as the limit for breakthrough; in cases of varying the raw HCl concentration, 10 ppm for c_0 = 1000 ppm and 5 ppm for c_0 = 500 ppm is used to measure the breakthrough time);

Saturation time: the time when the outlet concentration of HCl is detected to be higher than 1980 ppm (similarly, 990 ppm for c_0 = 1000 ppm and 495 ppm for c_0 = 500 ppm is used to measure the saturation time);

The total amount of HCl gas absorbed by one gram of CaO reactant is calculated according to:

$$m_{HCl/g\text{-}CaO} = 10^{-3}\int_0^t \frac{(c_0 - c_t)\times V \times 36.5}{V_{HCl}\times m_{CaO}}dt \tag{3.21}$$

where, $m_{HCl/g\text{-}CaO}$ represents the HCl mitigation amount by one gram of CaO reactant during the experiment; c_0 refers to the inlet concentration of HCl; c_t is the instant outlet concentration of HCl at time t; V represents the gas flowrate; 36.5 is the molecular weight of HCl; V_{HCl} is the molar volume of HCl; and m_{CaO} is the mass weight of CaO reactant used. The HCl mitigation rate, which indicates the reaction rate between HCl and CaO during the mitigation process, can be estimated by taking into account the absorption amount of HCl over a period of time, and it is obtained by:

$$k_{HCl} = \frac{\Delta m_{HCl}}{\Delta t} = \frac{10^{-3}\int_t^{t+\Delta t} \frac{(c_0 - c_t)\times V \times 36.5}{V_{HCl}\times m_{CaO}}dt}{\Delta t} \tag{3.22}$$

where, k_{HCl} represents the HCl mitigation rate; Δm_{HCl} is the absorption amount of HCl over a period of time Δt. The results are reported as follows:

3.3.1 Effect of temperature on HCl mitigation by CaO reactant

3.3.1.1 Breakthrough experimental and kinetics modeling results

In this section, the fixed parameters are: the raw HCl concentration is 2000 ppm, gas flowrate is 2.0 L/min and the amount of CaO used is 2.0 g. Under such conditions, the effect of reaction temperature on HCl mitigation is investigated. Experiments are carried out in moderate high temperature ranges from 550 to 850 ^{o}C. **Figure 3.6** presents HCl breakthrough curves of CaO reactants under different temperature. Outlet HCl concentration is normalized by $c/c_{0,}$ in which c represents the instant HCl concentration and c_0 refers to raw HCl concentration. Results reveal that increasing the temperature significantly decrease the breakthrough and saturation time during HCl mitigation using CaO reactant. When the temperature is increased from 550 to 850 ^{o}C, the breakthrough and saturation time decline from 197.8 to 21.8 min and 268.9 to 69.6 min, respectively.

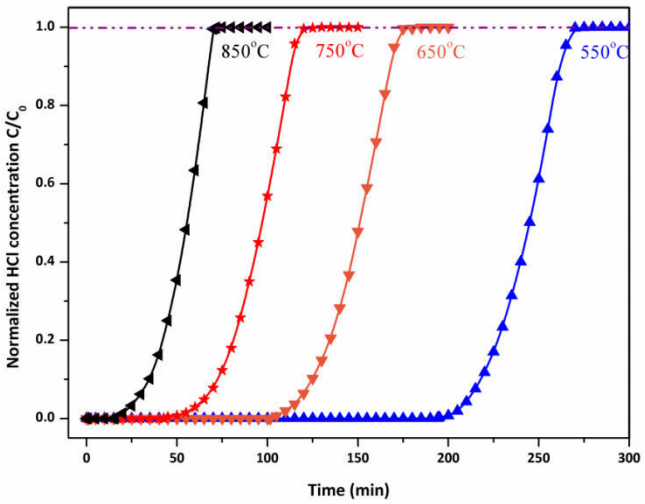

Figure 3. 6 The HCl breakthrough curves of CaO reactants under different temperature

It is well recognized that temperature is a dominant factor determining gas-solid absorption process by affecting both physical adsorption and chemical reaction. On the one hand, from thermodynamic point of view, physical adsorption is an exothermic process, therefore, increasing the temperature will cause adverse effects on physical adsorption of gases by solid sorbents; and also, chemical reaction highly relies on temperature by breaking chemical bonds as well as shifting the chemical equilibrium. On the other hand, kinetically speaking, higher temperature will enhances the diffusion rate of HCl in the product-layer, but

at higher temperature, the surface properties (for example specific surface area, pore structure and pore volume) of the sorbent will significantly be changed, thus the diffusion of gases and chemical reaction rate on particle surface will be influenced. Results from **Section 3.1** demonstrated that higher temperature will shift the dehydrochlorination reaction equilibrium towards the direction of $CaCl_2$ decomposition. Therefore, increasing the temperature will largely reduce HCl mitigation efficiency by CaO reactant from both physical adsorption and chemical reaction point of view.

With regard to HCl mitigation capacity, **Figure 3.7** exhibits the total HCl mitigation amount and the mitigation rate with time using CaO reactant within the considered reaction temperature ranges.

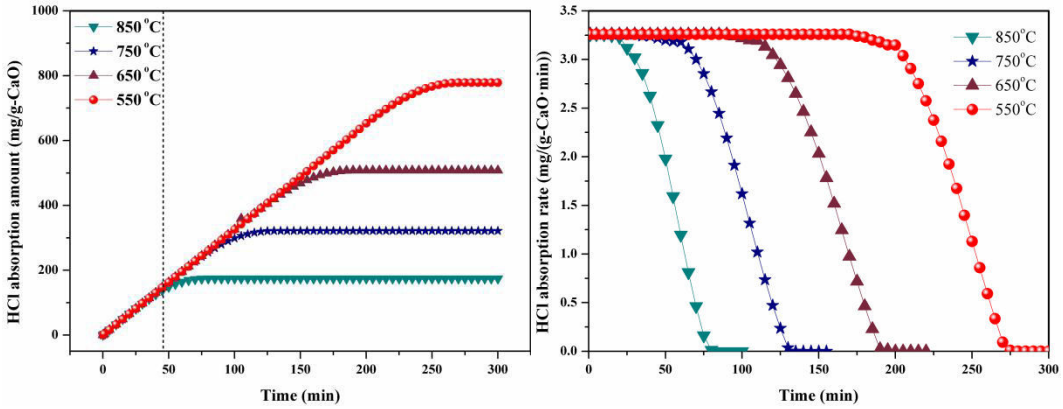

Figure 3. 7 The total HCl mitigation amount and mitigation rate with time under different reaction temperature

Results indicate that the total HCl mitigation amount decreased continuously from 778.9 to 173.9 mg/g-CaO when the temperature is increased from 550 to 850 °C. At the initial stage (~50 min), HCl mitigation amount is almost identical under different absorption temperature. It is mainly due to the fact that at the beginning, HCl mitigation rate remains the same under different temperature. As shown in **Figure 3.6**, before breakthrough time, HCl gas is completely absorbed by the CaO bed; therefore the mitigation rate as well as absorption amount in this stage is directly determined by raw HCl flowrate. With the further increase of reaction time, the mitigation rate is significantly inhibited due to the formation of the solid $CaCl_2$ product-layer and the reduction of surface properties by calcination and sintering of CaO reactant (for example the reduction of specific surface area, pore volume, porosity, and etc.). As illustrated in **Figure 3.7**, at higher temperature, HCl mitigation rate decrease earlier and faster, which is also confirmed by the fact that the gradient of the

breakthrough curves (concentration wave front) became steeper at higher temperature as presented in **Figure 3.6**.

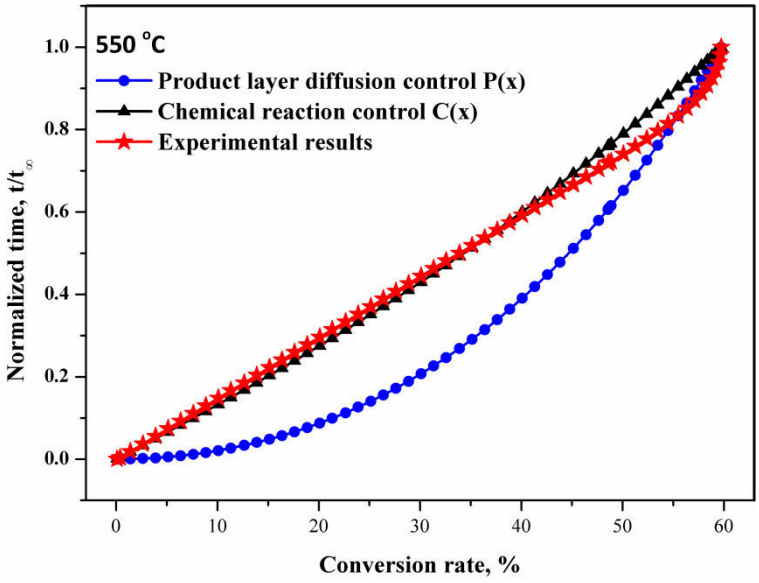

Figure 3. 8 Experimental and calculated P(x), C(x) vs CaO conversion rate curves at 550 °C

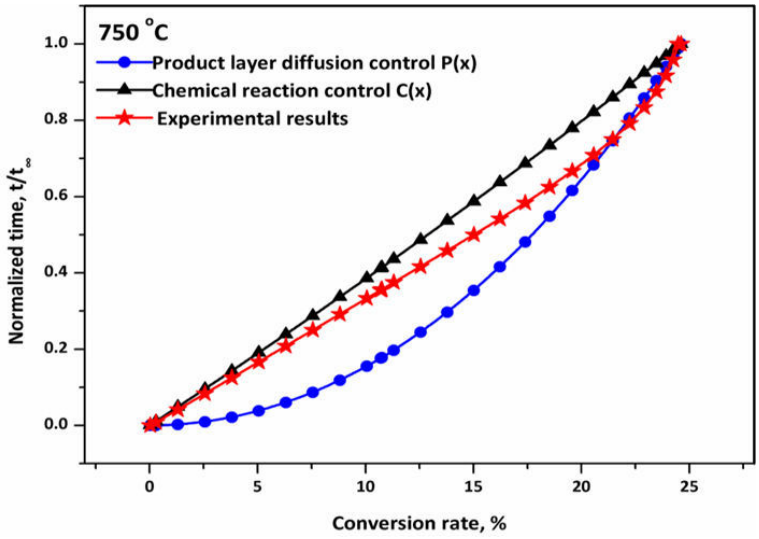

Figure 3. 9 Experimental and calculated P(x), C(x) vs CaO conversion rate curves at 750 °C

In order to identify the rate-limiting step during the absorption process, the normalized time vs CaO conversion rate at temperature of 550 and 750 °C are plotted in **Figure 3.8** and **3.9**, respectively. The normalized reaction time (calculation results by P(x), C(x) and experimental results) vs CaO reactant conversion rate is presented to investigate the rate-limiting steps during the whole mitigation reaction.

As shown in **Figure 3.8**, at reaction temperature of 550 ^{o}C, the experimental results fit well with C(x) at CaO conversion rate of 0 – 35%, indicating that at the initial stage, the reaction is mainly controlled by chemical reaction; however, at the conversion rate of around 55 – 60%, experimental results fit well with P(x), revealing that at the end stage of the reaction, product-layer diffusion is the rate limiting step; both chemical reaction on sorbent surface and HCl diffusion through the formed product-layer are the main rate-limiting steps in the intermediate stage of the reaction.

Similar tendency is also observed at reaction temperature of 750 ^{o}C (**Figure 3.9**), chemical reaction control and product-layer diffusion control are the crucial mechanisms at the initial and final stage of the process, since the experimental results fit well with C(x) and P(x) at each stages, respectively; while the combined effect is observed in middle process of the reaction (i.e. CaO conversion rate at around 5 – 22.5%).

According to **Section 3.2.2.2**, the corresponding kinetic parameters τ_p, τ_c, θ^2, k_s, D_p, E_c and E_p are listed in **Table 3.3**. According to the estimation results, the value of θ^2 is always in the range of $1 < \theta^2 < 10$, which indicates that the absorption of HCl by CaO reactants is limited by both chemical reaction and product-layer diffusion.

Table 3. 3 Estimation of kinetic parameters τ_p, τ_c, θ^2, k_s, D_p, E_c and E_p of HCl mitigation by CaO at different temperature

Temperature, ^{o}C	τ_c*10^5 s	τ_p*10^5 s	θ^2	k_s*10^{-3}, m/s	D_p*10^{-8}, m^2/s	E_c, kJ/mol	E_p, kJ/mol
550	4.84	6.85	1.42	10.20	3.58	44.17	17.39
650	2.53	5.34	2.11	5.91	4.60		
750	1.46	5.16	3.5	3.42	4.34		
850	0.85	3.08	3.62	1.79	7.98		

- τ_p and τ_c represents the total time taken when the conversion is only controlled by product-layer diffusion or chemical reaction, respectively; θ^2 refers to the ratio of τ_p/τ_c; k_s and D_p is reaction rate and effective diffusivity through the product-layer; E_c and E_p represent the apparent activation energy of chemical reaction and product-layer diffusion, respectively.

3.3.1.2 Morphology analysis of the spent CaO reactants

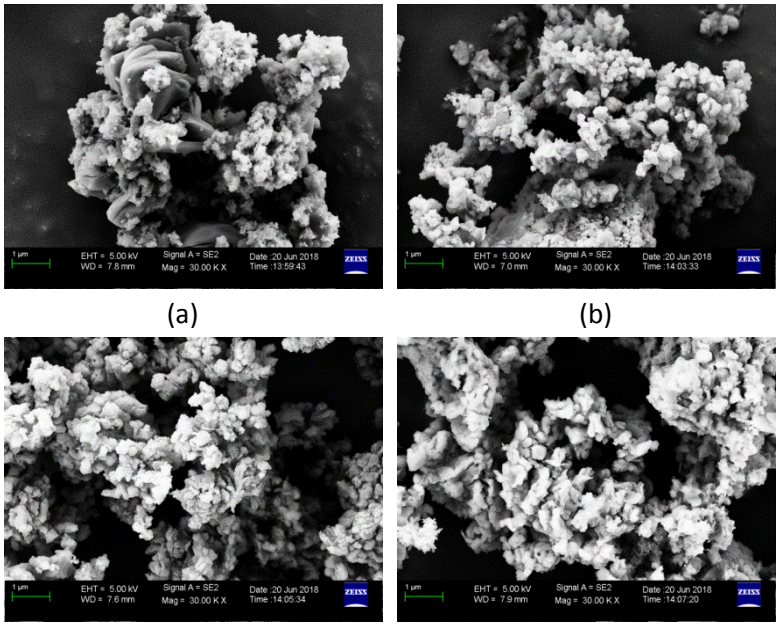

Figure 3. 10 Formation of the product-layer at temperature of 650 °C: a, t/t_f= 0.1; b, t/t_f= 0.3; c, t/t_f= 0.5; d, t/t_f= 1 (t_f refers to the saturation time of the process)

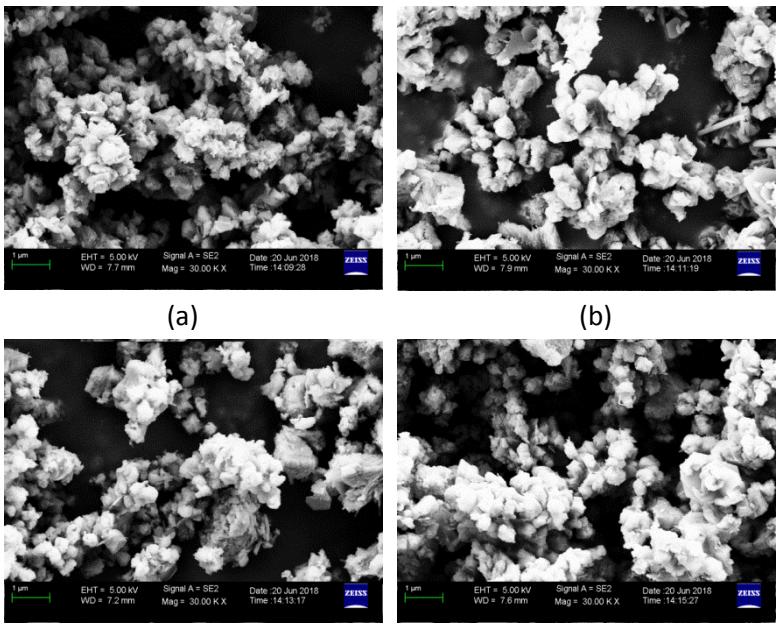

Figure 3. 11 Formation of the product-layer at temperature of 750 °C: a, t/t_f= 0.1; b, t/t_f= 0.3; c, t/t_f= 0.5; d, t/t_f= 1

Figure 3.10, **Figure 3.11**, and **Figure 3.12** presents the micrograph of the spent CaO reactant at normalized time of t/t_f= 0.1, 0.3, 0.5, and 1 under the reaction temperature of 650, 750, and 850 ^{o}C, respectively. Results clearly reveal the formation process of the solid product-layer. The nucleation of the solid products is firstly appeared on CaO reactant surface, then the solid product grows gradually to cover the entire unreacted CaO core, and finally the formed product-layer becomes denser and the contact of the gas and solid reactants are restrained. Taking the results obtained at temperature of 650 ^{o}C as an example, the formation of the solid products on CaO particle surface is in cluster forms in the initial stage of the absorption experiments (as seen in **Figure 3.10 (a)**, t/t_f = 0.1). The formed solid product is a loose and porous structure and adhered on the unreacted CaO core surface in this stage. During this period, the active sites on CaO reactant surface are consumed and physical adsorption and chemical reaction between CaO reactant and HCl will thus be slowed down because of the reduction of available reaction positions on CaO surface. As the reaction goes on, the formed solid product-layer grows and gradually covers most of the unreacted CaO reactant (as seen in **Figure 3.10 (b)**, t/t_f = 0.3); therefore, diffusion of HCl through the generated product-layer plays a more important role during this reaction period. Finally, at t/t_f = 1 (as seen in **Figure 3.10 (d)**), a much denser product-layer is produced and covers the entire surface of CaO reactant, meanwhile diffusion of HCl through the layer becomes much harder. Therefore, HCl mitigation reaction is blocked.

At temperature of 750 ^{o}C as presented in **Figure 3.11**, the nucleation of the solid products is also observed in the initial stage; however, as the reaction goes, the formed product-layer becomes much denser and smooth. It is mainly due to the fact that the melting temperature of the produced $CaCl_2$ is around 772 ^{o}C, therefore, at higher temperature, melting of the product-layer produces a compact and nonporous surface. However, further increase the reaction temperature to 850 ^{o}C as shown in **Figure 3.12**, the final product shows a fluffier and looser surface. The decomposition and evaporation of the formed solid products are responsible for the formation of the porous particle surfaces.

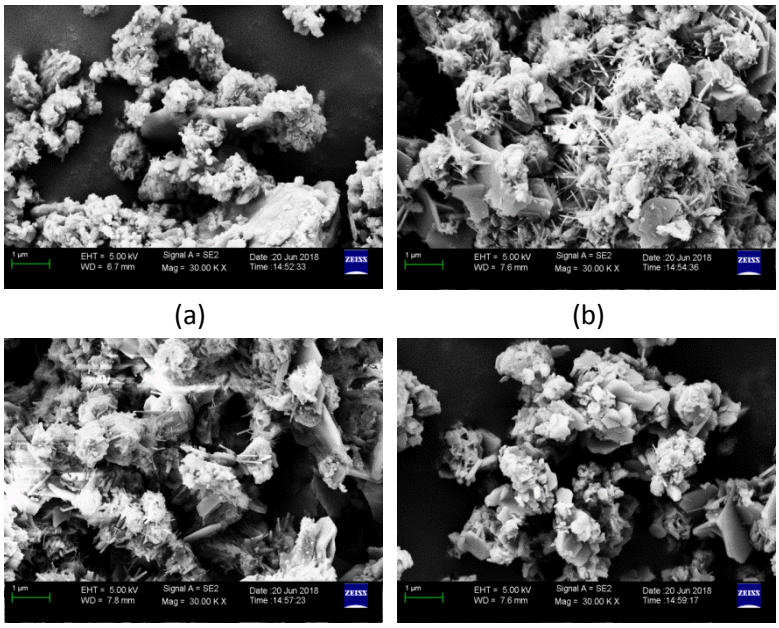

(a) (b)

(c) (d)

Figure 3. 12 Formation of the product-layer at temperature of 850 ^{o}C: a, t/t_f= 0.1; b, t/t_f= 0.3; c, t/t_f= 0.5; d, t/t_f= 1

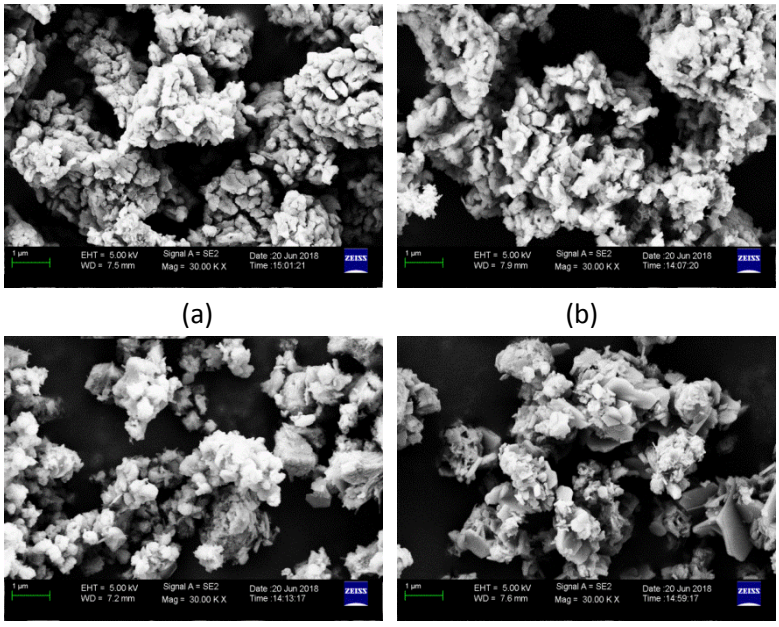

(a) (b)

(c) (d)

Figure 3. 13 The formed product-layer of the final spent CaO reactants: a, 550 ^{o}C; b, 650 ^{o}C; c, 750 ^{o}C; d, 850 ^{o}C

Table 3. 4 Specific surface area, pore volume and porosity of the spent CaO reactant

	Raw CaO	550 °C	650 °C	750 °C	850 °C
S_{BET}, m^2/g	2.4	4.2	2.6	1.5	2.1
Total pore volume*10^{-2}, cm^3/g	3.9	4.4	2.7	1.6	2.1
Porosity, %	4.5	5.0	3.1	1.8	2.4

Figure 3.13 exhibits the micrograph of the final spent CaO reactant at different reaction temperature and their corresponding physical properties are listed in **Table 3.4**. As illustrated, the spent CaO reactant at reaction temperature of 550 °C has a higher specific surface area and total pore volume when compared with raw CaO. The reason may be attributed to the preparation of CaO reactant; as aforementioned in **Section 2.2**, raw CaO reactant is calcined at 800 °C for 2h to decompose impurities, and the surface area and pore volume are thus significantly reduced due to calcination. Therefore, raw CaO in the present work is considered nonporous and the shrinking unreacted core model is used to determine the reaction kinetics. HCl mitigation at 550 °C by CaO reactant generates a relatively high porous product-layer, thus increases the porosity of the sorbents. However, when the reaction temperature is increased from 550 to 750 °C, specific surface area and pore volume of the spent CaO reduces continuously from 4.2 to 1.5 m^2/g and $4.4x10^{-2}$ to $1.6x10^{-2}$ cm^3/g, respectively. The phenomena further confirm that the reduction of surface area and closure of pore structures are responsible for the decline of HCl mitigation efficiency at higher temperature. On the contrary, the specific surface area and pore volume are slightly increased to 2.1 m^2/g and $2.1x10^{-2}$ to $1.6x10^{-2}$ cm^3/g at temperature of 850 °C. This is mainly due to the decomposition and evaporation of gas-solid reaction products (i.e. the product-layer). However, at temperature of 850 °C, HCl mitigation efficiency is also reduced as compared with that at 750 °C, which indicates that the shift of chemical reaction equilibrium plays a more important role under such circumstance.

3.3.2 Effect of raw HCl concentration on HCl mitigation by CaO reactant

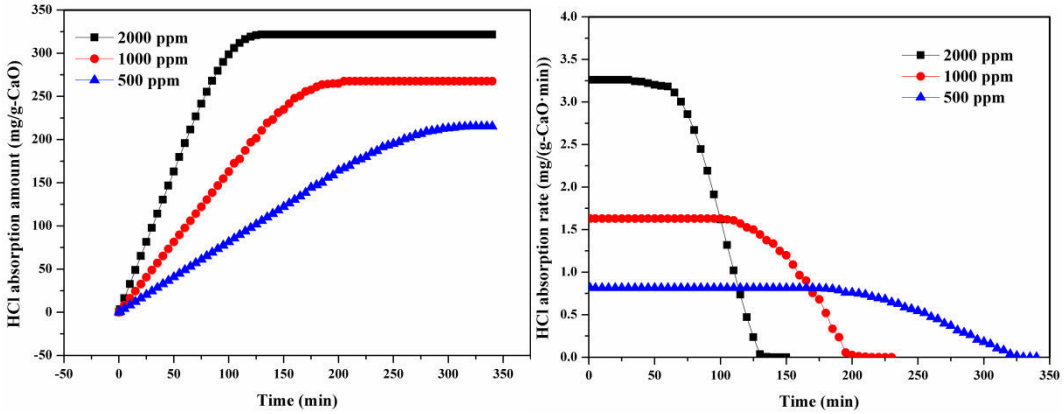

Figure 3. 14 Effect of raw HCl concentration on total HCl mitigation amount and HCl mitigation rate by CaO reactant

As previously discussed in **Section 3.2.2**, raw HCl concentration in the gas mixtures, i.e. C_{Ag} is one of the determining factors to estimate the total time taken for the complete conversion of CaO under both chemical reaction control and product-layer diffusion control mechanisms (i.e. τ_c and τ_p). Therefore, it is further investigated in this work. Experiments are conducted under the condition of: reaction temperature is 750 ^oC; mass of CaO used is 2.0 gram; flow rate of the gas mixtures is 2.0 L/min; and HCl raw concentrations are 2000, 1000, and 500 ppm.

The total HCl mitigation amount and the mitigation rate are presented in **Figure 3.14**. As illustrated, the total HCl mitigation amount decreased from 321.5 to 215.4 mg/g-CaO when decreasing the raw HCl concentration from 2000 ppm to 500 ppm, while the corresponding breakthrough time and saturation time increased from 51 to 177 min and 115 to 326 min, respectively. Experimental results agree well with kinetic modeling estimations, indicating that the total time taken for complete conversion of CaO increase with the decrease of C_{Ag}, since C_{Ag} is in the denominator of the equations to calculate τ_c and τ_p. The HCl mitigation rate is also exhibited in **Figure 3.14**. Results reveal that increasing raw HCl gas concentration significantly increases the mitigation rate. This is reasonable, since both physical adsorption and chemical reaction rates are affected by HCl concentration: on the one hand, higher concentration difference between gas and solid sorbent will increase the driving force of physical adsorption, thus to overcome the mass transfer resistance; on the other hand, increasing HCl concentration facilitates the chemical reaction rate between CaO and HCl by enhancing the collision probabilities. Therefore, the maximum mitigation rate is decreased

from 3.26 to 0.81 mg/(g-CaO*min) when lower the raw HCl concentration (as aforementioned, it is determined directly by raw HCl concentration before breakthrough time).

3.3.3 Effect of carrier gas composition on HCl mitigation by CaO reactant

Previous concerns are mainly focused on the absorption of HCl in N_2 atmosphere; however, for actual waste pyro-gasification systems, the presence of HCl in the produced gas is always accompanied with other gases compositions, which may also react with CaO reactant and thus influence the HCl mitigation efficiency. Therefore, the effect of gas composition on HCl mitigation is further investigated. Experiments are conducted at temperature of 750 ^{o}C, gas flow rate of 2.0 L/min. The presence of 12% CO_2 and 50% simulated syngas are evaluated in the present study. Due to the introduction of CO_2 and simulated syngas, raw HCl concentration decreases to 1000 ppm, and the detailed gas compositions are summarized in **Table 3.5**.

Table 3. 5 Experimental conditions adopted to investigate the effect of gas composition on HCl mitigation by CaO reactant

No.	Temperature, ^{o}C	HCl concentration, ppm	Gas flowrate, L/min	Gas composition, vol.%
1#	750	1000	2.0	CO_2 12, and N_2 balance
2#	750	1000	2.0	H_2 1.6, CH_4 1.2, CO 2.5, CO_2 6.0, and N_2 balance

The effect of gas compositions on total HCl mitigation amount and the mitigation rate are presented in **Figure 3.15**. Results reveal that the presence of CO_2 (gas containing 12% CO_2) slightly reduces the breakthrough time of HCl mitigation by CaO reactant from ca. 106 to 88 min. The competition of dechlorination reaction (as presented in **Eq. (3.1)**) and CaO carbonation reaction (**Eq. (3.23)**) is responsible for this phenomenon, since CO_2 may also occupy the active sites on CaO core surface and inhibit the reaction between HCl and CaO. However, the saturation time and total HCl mitigation amount is slightly promoted by approximately 10 min and 10 mg/g-CaO. One possible explanation may be attributed to the inverse calcination reaction of $CaCO_3$ (**Eq. (3.24)**), according to the literature [19], the decomposition of $CaCO_3$ can continuously produce active sites and increase pore volume and structures on the produced $CaCO_3$ layer, and thus enhance HCl mitigation.

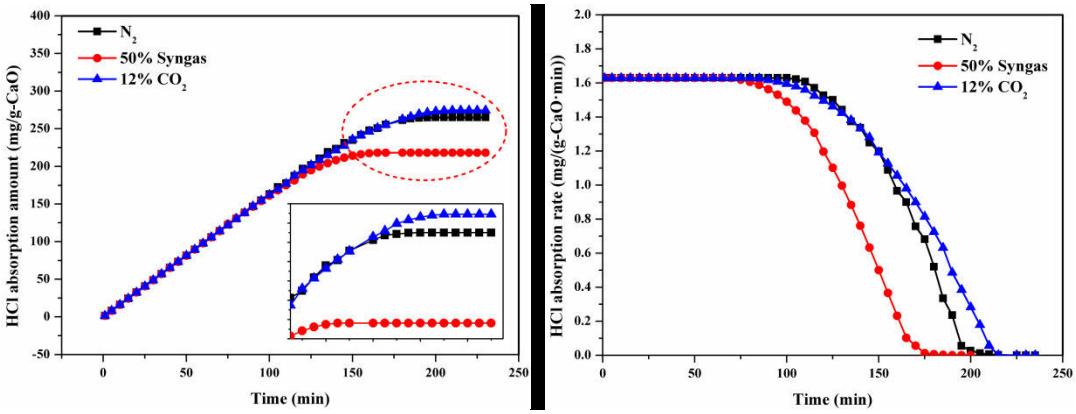

Figure 3. 15 Effect of gas composition on total HCl mitigation amount and HCl mitigation rate by CaO reactant

$$CaO + CO_2 \rightarrow CaCO_3 \quad (3.23)$$

$$CaCO_3 \rightarrow CaO + CO_2 \quad (3.24)$$

With regard to the presence of simulated syngas, adverse effects are also observed, revealing that the reduction of breakthrough time is about 30 min and the total HCl mitigation amount is about 45 mg/g-CaO. The content of CO_2 in simulated syngas (6.0 vol. %) is one of the reasons causing the problem. Moreover, according to Nzihou et al. and Abdoulmoumine et al. [20, 21], the presence of CO and H_2, accounting to 2.5 vol. % and 1.6 vol. % in the present study, will occupy the number of free active sites (mainly O^{2-} ion) on CaO surface, and thus lead to the degradation of the quality of CaO surface and decrease HCl mitigation efficiency. This is quite important for pyro-gasification systems, since CO and H_2 are the mainly target gases for waste pyro-gasification processes.

The experimental results are summarized in **Table 3.6**. Results reveal that increasing the temperature, reducing raw concentration of HCl gas, and the presence of CO_2, CO, and H_2 in carrier gas will cause the reduction of total HCl mitigation amount and lower CaO bed conversion efficiency.

Table 3. 6 Summary of HCl breakthrough experimental results

Fixed parameter	Varied parameter	Breakthrough time, min	Saturation time, min	HCl mitigation amount, mg/g-CaO	CaO bed conversion rate, %	Maximum HCl mitigation rate, mg/(g-CaO *min)
2000 ppm; 2.0 L/min	550 °C	197.8	268.9	778.9	59.8	3.26
	650 °C	106.0	179.3	507.2	38.9	3.26
	750 °C	51.4	115.8	321.5	24.7	3.26
	850 °C	21.8	69.6	173.9	13.4	3.26
2.0 L/min; 750 °C	1000 ppm	105.9	200.0	264.9	20.3	1.63
	500 ppm	177.1	326.1	215.4	16.5	0.81
1000 ppm; 2.0 L/min; 750 °C	12% CO_2	87.9	209.98	274.5	21.05	1.63
	50% syngas	74.2	164.3	218.5	16.8	1.63

3.4 Summary of the chapter

In this chapter, the gas-solid reaction mechanism between CaO reactant and HCl gas is studied by both theoretical calculation and experimental investigation. Thermodynamic analysis is firstly conducted to determine the Gibbs free energy and standard equilibrium constant of the reaction. Then breakthrough experiments and kinetic modeling of the reaction are performed to identify the effect of key parameters on HCl mitigation efficiency. Last but not least, the micrograph of the spent CaO reactant is examined to reveal the formation mechanism of the product-layer.

The following conclusions can be obtained:

- Thermodynamic analysis reveals that the reaction between CaO and HCl is inhibited when increasing the temperature due to the shift of chemical reaction equilibrium.

- Experimental results reveal that increasing the temperature, reducing raw concentration of HCl gas, and the presence of CO, and H_2 in carrier gas cause the reduction of total HCl mitigation amount and CaO bed conversion efficiency. Higher temperature shifts the chemical equilibrium of the absorption reaction and reduces surface area and pore volumes of CaO reactant; lower raw HCl concentration increases the breakthrough and saturation time, but decreases HCl mitigation amount and CaO bed conversion efficiency due to the reduction of both physical adsorption and chemical reaction rates; and the presence of CO, and H_2 will occupy the number of free active sites on CaO surface and cause adverse effects on HCl mitigation. The proposed reaction mechanisms are described as follows:

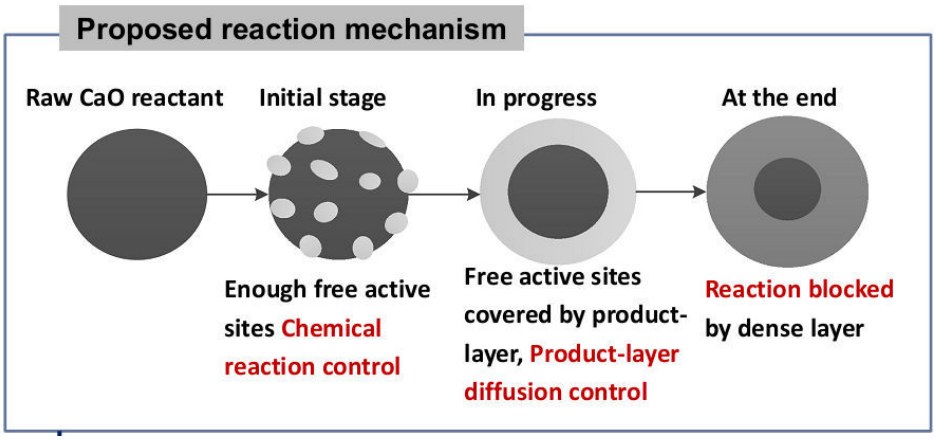

- Estimation results of kinetic modeling indicate that the ratio of product-layer diffusion resistance to chemical reaction resistance (i.e. θ^2) is always in the range of $1 < \theta^2 < 10$, which means that HCl mitigation by CaO reactant, is limited by both chemical reaction and product-layer diffusion.

- Morphology analysis reveals the formation process of the product-layer and the examination of the spent CaO physical properties further indicates that both the shifts of chemical equilibrium and the reduction of surface area and closure of pore structures at higher temperature are responsible for the decline of HCl mitigation efficiency by CaO.

3.5 Bibliography

[1] Jurczyk M, Mikus M, Dziedzic K. Flue gas cleaning in municipal Waste-to-Energy plants-Part 2. Infrastruktura i Ekologia Terenów Wiejskich. 2016.

[2] Jurczyk M, Mikus M, Dziedzic K. Flue gas cleaning in municipal waste-to-energy plants-Part 1. Infrastruktura i Ekologia Terenów Wiejskich. 2016.

[3] Lu J-W, Zhang S, Hai J, Lei M. Status and perspectives of municipal solid waste incineration in China: A comparison with developed regions. Waste Management. 2017;69:170-86.

[4] Zhan R. Kinetic study of low temperature sulfur dioxide and hydrogen chloride removal using calcium-based sorbents: Ohio University; 1999.

[5] Chyang C-S, Han Y-L, Zhong Z-C. Study of HCl mitigation by CaO at high temperature. Energy & Fuels. 2009;23:3948-53.

[6] contributors W. Gibbs–Helmholtz equation. Wikipedia, The Free Encyclopedia; 2018.

[7] Ma DW, Zhang YN, Xu ZS, Cheng C. Influence of intermediate ZnO on the crystallization of PbSe quantum dots in silicate glasses. Journal of the American Ceramic Society. 2014;97:2455-61.

[8] Wu J, Chen Z, Ma W, Dai Y. Thermodynamic Estimation of Silicon Tetrachloride to Trichlorosilane by a Low Temperature Hydrogenation Technique. Silicon. 2017;9:69-75.

[9] P.J. Linstrom and W.G. Mallard E. NIST Chemistry WebBook, NIST Standard Reference Database Number 69. National Institute of Standards and Technology; retrieved August 22, 2018.

[10] Haynes WM. CRC handbook of chemistry and physics: CRC press; 2014.

[11] Sedghkerdar MH, Mahinpey N. A modified grain model in studying the CO2 capture process with a calcium-based sorbent: a semianalytical approach. Industrial & Engineering Chemistry Research. 2015;54:869-77.

[12] Lee KT, Koon OW. Modified shrinking unreacted-core model for the reaction between sulfur dioxide and coal fly ash/CaO/CaSO4 sorbent. Chemical Engineering Journal. 2009;146:57-62.

[13] Deshpande A, Krishnaswamy S, Ponnani K. Pulsed Micro-reactor: An alternative to estimating kinetic parameters of non-catalytic gas–solid reactions. Chemical Engineering Research and Design. 2017;117:382-93.

[14] Abbasi E, Hassanzadeh A, Abbasian J. Regenerable MgO-based sorbent for high temperature CO2 removal from syngas: 2. Two-zone variable diffusivity shrinking core model with expanding product layer. Fuel. 2013;105:128-34.

[15] Shih S-M, Lai J-C, Yang C-H. Kinetics of the reaction of dense CaO particles with SO2. Industrial & Engineering Chemistry Research. 2011;50:12409-20.

[16] Ahmed HM, El-Geassy A-HA, Viswanathan NN, Seetharaman S. Kinetics and mathematical modeling of hydrogen reduction of NiO–WO3 precursors in fluidized bed reactor. ISIJ international. 2011;51:1383-91.

[17] Tang H, Guo Z, Kitagawa K. Simulation study on performance of z-path moving-fluidized bed for gaseous reduction of iron ore fines. ISIJ international. 2012;52:1241-9.

[18] Shirchi S, Khoshandam B, Hormozi F. Reduction kinetics of cobalt oxide powder by methane in a fluidized bed reactor. Journal of the Taiwan Institute of Chemical Engineers. 2015;51:171-6.

[19] Wong Y, Tan Y, Taufiq-Yap Y, Ramli I. Effect of calcination temperatures of CaO/Nb2O5 mixed oxides catalysts on biodiesel production. Sains Malaysiana. 2014;43:783-90.

[20] Nzihou A, Stanmore B, Sharrock P. A review of catalysts for the gasification of biomass char, with some reference to coal. Energy. 2013;58:305-17.

[21] Abdoulmoumine N, Adhikari S, Kulkarni A, Chattanathan S. A review on biomass gasification syngas cleanup. Applied Energy. 2015;155:294-307.

Chapter 4

Influence of CaO reactant on HCl release and control from inorganic and organic sources of chlorine

4.1 Introduction

In **chapter 3**, absorption of HCl gas by CaO reactant and the gas-solid reaction mechanism are investigated. Results reveal that the use of CaO reactant is effective to capture HCl contained in the flue gas. In this chapter, the conversion of Cl-contained contaminants from inorganic and organic chlorine source in MSW is firstly identified and then the use of in-furnace CaO reactant on the produced HCl mitigation is examined.

It is well recognized that, chlorine is one of the most important raw materials in chemical industry; according to Euro Chlor's year book, more than 9.1 million tons of chlorine is consumed in European Countries in 2017, among which 32.5% is consumed in the field of PVC production, 31.8% is used to produce isocyanates and oxygenated compounds, 8.6% and 4.5% is applied for the solvents & epichlorohydrin and chloromethane industries, 12.4% is employed to produce inorganics, and the rest is used for the generation of other organics [1]. Considering the important role of chlorine in modern chemical industry as well as the abundant amount of inorganic chlorides existing in the natural world, chlorine content in MSW is as high as 800-2500 mg/kg according to Jhong-Lin Wu et al [2].

As aforementioned in **Section 1.2**, the presence of chlorine in MSW is mainly in two forms: in inorganic form, such as NaCl or KCl; and in organic chlorine source form like PVC or rubbers [3-5]. During waste thermal treatment, chlorine is liable to be released as a

consequence of high temperature. And the produced Cl-compounds may participate in various reactions in the furnace, leading to several serious consequences, for example, high temperature corrosion, heavy metal evaporation and dioxins and furans formation. Besides, the emitted Cl-content species, especially toxic organic compounds, are considered to be persistent and have the potential to migrate widely throughout the ecosystem [6, 7]. Therefore, the formation of chlorine-contained contaminants from different kinds of chlorine sources is of great importance. The primary aim of this chapter is to investigate the fate of chlorine from both inorganic and organic sources. **Figure 4.1** summarized the possible transformation routes of inorganic and organic chlorine sources during MSW thermal treatments of pyro-gasification and incineration.

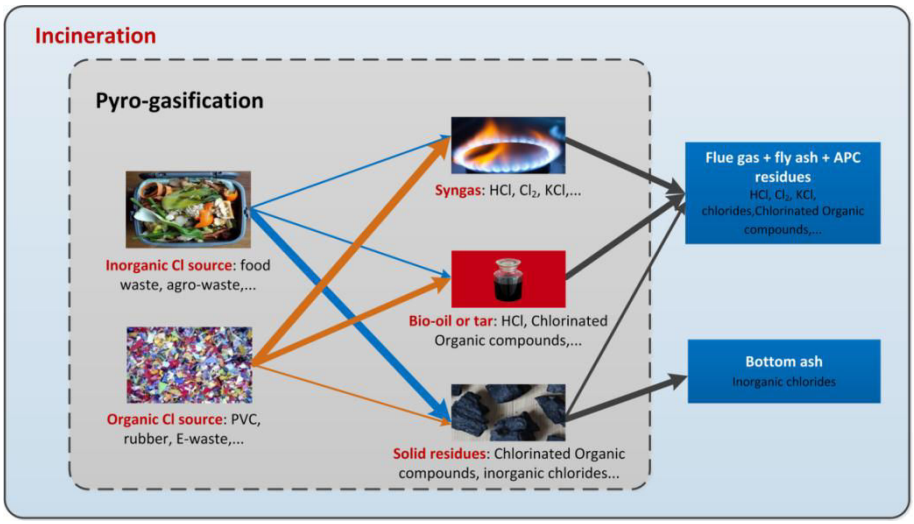

Figure 4. 1 Schematic diagram of the possible conversion routes of chlorine during MSW thermal treatments

In order to avoid high temperature corrosion caused by HCl in the flue gas and to reduce the formation of toxic pollutants such as dioxins and furans, the formed Cl-content contaminants should be removed. Therefore, the second goal of this chapter is to immobilize the chlorine in solid residues by using in-furnace CaO reactant. The effect of temperature, Ca/Cl molar ratio and the properties of CaO are investigated.

Accordingly, both experimental studies and thermodynamic simulations are conducted in this chapter to thorough understand the fate of chlorine and its control strategies during waste thermal conversion, the main content of the sections are summarized as follows:

I. **Section 4.2** is dedicated to evaluate the Cl-content contaminants formation from inorganic chlorine source NaCl; both thermodynamic equilibrium

simulation and experimental studies are conducted. The effect of temperature, atmosphere (N_2, air, and O_2), the presence of water and inorganic materials like SiO_2 are examined;

II. **Section 4.3** investigates HCl formation from organic chlorine source PVC. Both thermogravimetric and fixed bed tubular furnace experiments are carried out; effects of temperature and atmosphere on the conversion of chlorine from PVC to HCl are determined. Besides, reaction kinetics are modeled and the activation energy for dechlorination reaction is estimated;

III. **Section 4.4** focuses on the effect of in-furnace CaO on HCl mitigation from PVC; the effect of Ca/Cl molar ratio, temperature and CaO particle size on HCl mitigation efficiency are experimentally assessed. The morphology of the obtained residues is also identified to further understand the reaction mechanism of in-furnace dechlorination reactions.

4.2 Chlorinated pollutants release from inorganic and organic sources

4.2.1 Chlorinated pollutants from inorganic source-NaCl

The most typically inorganic chlorine source existing in food waste, NaCl, is used as the feedstock for experimental purposes. FactSage software is used to carry out the thermodynamic equilibrium simulation. Experiments are conducted on both thermogravimetric and fixed bed tubular furnace apparatus.

4.2.2.1 Thermodynamic equilibrium simulation of Cl-contained contaminants from NaCl

Thermodynamic simulations of the thermal behavior of NaCl under the considered working conditions are firstly theoretically investigated using FactSage software. The results could be served as the fundamental information to explain the phenomenon observed during the experiments. Simulation is performed using the same input condition of the experimental studies.

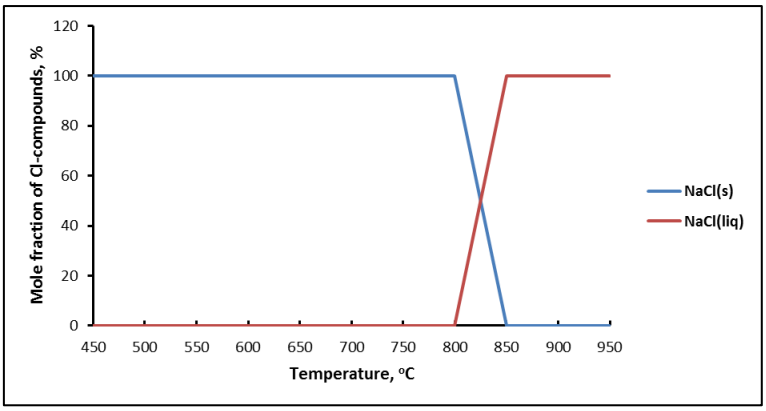

Figure 4. 2 Thermodynamic simulation results of pure NaCl under N_2 atmosphere

Figure 4.2 presents the thermodynamic behavior of NaCl under N_2 atmosphere as the molar fraction of Cl-compounds vs temperature. As illustrated in the diagram, NaCl is quite stable during pyrolysis; no decomposition or evaporation occurs in the temperature range of 450 - 950 ^{o}C. Within the temperature range of 450 - 800 ^{o}C, only the solid-phase NaCl (as presented in **Figure 4.2**, NaCl (s)) exists in the equilibrium system. Above 801 ^{o}C and up to 850 ^{o}C, the NaCl melting point, the solid-phase turned to liquid-phase (NaCl (liq) in the diagram). After this phase change stage, the liquid-phase NaCl is the only specie contained in the equilibrium system within the temperature considered in the present work (the boiling point of NaCl is 1465 ^{o}C).

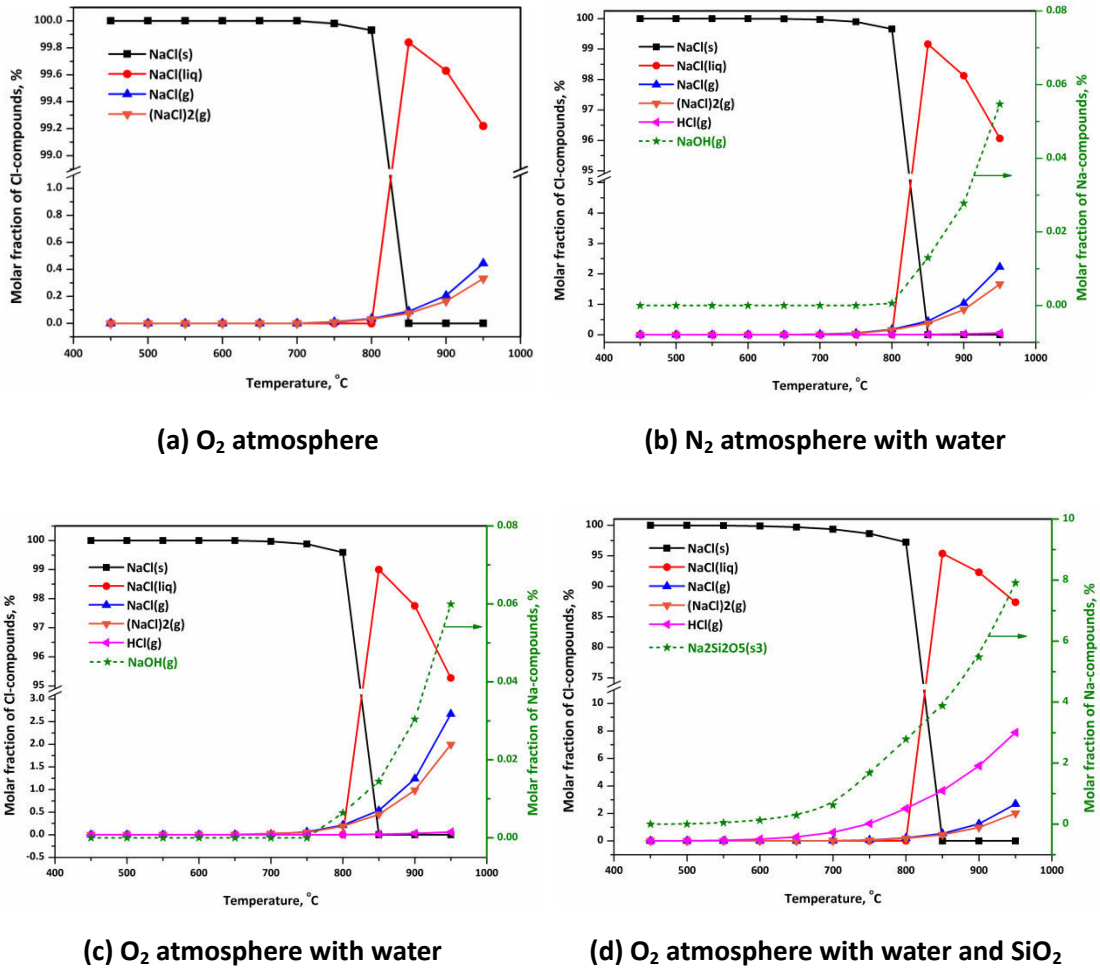

(a) O_2 atmosphere **(b) N_2 atmosphere with water**

(c) O_2 atmosphere with water **(d) O_2 atmosphere with water and SiO_2**

Figure 4. 3 Thermodynamic simulation results of NaCl under considered working conditions: (a) under O_2 atmosphere; (b) under N_2 atmosphere with water; (c) under O_2 atmosphere with water; and (d) with the presence of SiO_2 and water under O_2 atmosphere

In order to better reflect the behavior of NaCl during MSW thermal conversion, thermodynamic equilibrium calculations are carried out with respect to the effect of O_2 atmosphere, the presence of water, and the influence of inorganic material like SiO_2. Some of the most typical results are presented in **Figure 4. 3**.

In **Figure 4.3** (a), the effect of O_2 atmosphere on the thermodynamic behavior of NaCl is considered. In contrast to the results from N_2 atmosphere, O_2 atmosphere enhances the evaporation of NaCl in the forms of gas-phase NaCl and $(NaCl)_2$ (i.e., NaCl(g), $(NaCl)_2$(g)) at temperature higher than 750 °C. At temperature of 950 °C, the molar fraction of NaCl(g) and $(NaCl)_2$(g) in the total Cl-content species reach 0.45% and 0.33%, respectively. The molar fraction of NaCl(liq) decreases to around 99.22%.

The effect of water content on the thermodynamic behavior of NaCl is presented in **Figure 4.3** (b). Results reveal that the presence of water promotes the evaporation of NaCl in

the forms of NaCl(g) and $(NaCl)_2$(g) at temperature higher than 700 °C. Besides, H_2O also acts as a reactant to convert the chlorine from NaCl to HCl at temperature higher than 800 °C. Meanwhile, NaOH(g) is also formed according to the calculation, indicating that the chemical reaction **Eq.(4.1)** occurred in the equilibrium system. At temperature of 950 °C, NaCl(g), $(NaCl)_2$(g) and HCl(g) in the total Cl-components are equal to 2.23%, 1.66%, and 0.05% respectively; while the molar fraction of NaCl(liq) in the total Cl-content species decreases to 96.06%. Besides, the molar fraction of sodium contained in NaOH (g) to the total Na-content species is also determined, and the amount is about 0.05%.

$$NaCl + H_2O \rightarrow HCl + NaOH \tag{4.1}$$

Figure 4.3 (c) exhibits the effect of water on the thermodynamic behavior of chlorine from NaCl under O_2 atmosphere. Similar results are obtained as for water/N_2 atmosphere. However, both the evaporation in the forms of NaCl(g) and $(NaCl)_2$(g) and the formation of HCl(g) and NaOH(g) are slightly promoted under O_2 atmosphere with the presence of water. At temperature of 950 °C, the molar fraction of NaCl(g), $(NaCl)_2$(g) and HCl(g) in the total Cl-components is 2.67%, 1.99%, and 0.06% respectively; with regard to NaCl(liq), the proportion reduces to 95.27%. The molar fraction of NaOH (g) in the total Na-components is around 0.06%.

With respect to the effect of inorganic material, the presence of SiO_2 is theoretically calculated to represent the effect of ash content on the thermodynamic behavior of chlorine from inorganic chlorine. The results are shown in **Figure 4.3** (d). Results clearly demonstrate that the presence of SiO_2 significantly enhances the conversion of chlorine from NaCl to HCl. By adding SiO_2 into the system, the evaporation of NaCl in the forms of NaCl(g) and $(NaCl)_2$(g) remains at a same level at around 2.69% and 2.01%, respectively, if comparing those with the case of SiO_2 addition. However, the molar fraction of HCl increases largely as compared to the conditions without SiO_2, occupying approximately 7.9% of the total Cl-components at temperature of 950 °C. Besides, thermodynamic simulation confirms the formation of the metal-matrix compounds, i.e. $Na_2Si_2O_5$(s) as shown in **Figure 4.3** (d), and its molar fraction in the total Na-compounds reaches 7.91%. Therefore, the corresponding chemical reaction, as previously mentioned in **Section 1.2.1.1**, is responsible for the high conversion of chlorine from NaCl to HCl, and can be described as:

$$2NaCl + 2SiO_2 + H_2O \rightarrow 2HCl + Na_2Si_2O_5 \tag{4.2}$$

To summarize, theoretically equilibrium simulation by using FactSage demonstrates that the thermodynamic behavior of NaCl under N_2 atmosphere is quite stable; no evaporation or thermochemical conversion of NaCl in the temperature range of 450 - 950 ^{o}C is predicted. However, the interactions caused by O_2 atmosphere, water content, and the presence of SiO_2 would increase both the evaporation (in the forms of (NaCl(g) and $(NaCl)_2$(g)) and the thermochemical conversion from NaCl to HCl. Given the fact that the physical composition of MSW is quite complex, the presence of water and inorganic material (SiO_2, Al_2O_3, and etc.) is unavoidable; therefore, HCl release from inorganic chlorine source, for example NaCl, is worthy of further investigation.

4.2.2.2 Experimental study of Cl-contained contaminants from NaCl

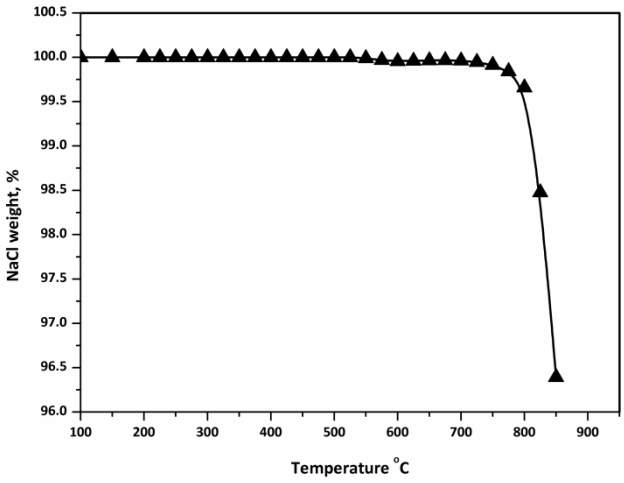

Figure 4. 4 TG analysis results of NaCl under N_2 atmosphere

Thermogravimetric experiments of NaCl under N_2 atmosphere are firstly conducted to identify the thermal behavior of pure NaCl with increasing temperature. As illustrated in **Figure 4.4,** NaCl is quite stable at lower temperature; no mass loss is observed before 700 ^{o}C. These results agree well with the observations from the thermodynamic equilibrium simulation. However, a slight mass loss of around 0.1% is observed when the temperature is higher than 750 ^{o}C, mainly due to the entrainment by the purge gas during TG experiments. Even at a temperature of 850 ^{o}C, the mass loss of NaCl is around 5.2%. This fact indicates that the total decomposition or evaporation of pure NaCl is quite low in the considered temperature ranges during pyrolysis.

Release of Cl-content contaminants form NaCl is also investigated using a fixed bed tubular furnace. The experimental set-up as well as the experimental procedure and the sampling method are described in **Section 2.2 & 2.3**.

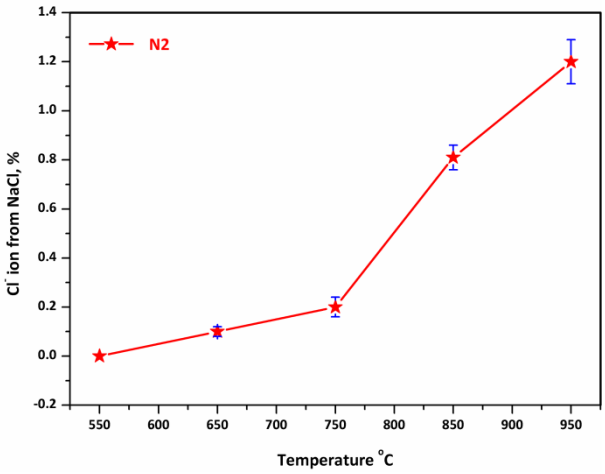

Figure 4. 5 Conversion of Cl^- ion from NaCl under N_2 atmosphere

Figure 4.5 presents the experimental results of NaCl thermal behavior under N_2 atmosphere. The percentage value of the y-axis represents the molar fraction of the detected Cl^- ion in the absorption solution to the total molecular amount of chlorine contained in raw NaCl, and it can be described by the following equation:

$$M_{Cl^-} = \frac{C_{Cl^-} * V / 35.5}{m_{NaCl} / 58.5} * 100\% \qquad (4.3)$$

where, M_{Cl^-} is the molar ratio of chlorine detected to that of the raw NaCl; C_{Cl^-} represents the concentration of Cl^- ion in the solution detected by Ion Chromatography (IC); V_s is the volume of the diluted sample in the volumetric flask; 35.5 is the molecular weight of Cl^- ion, g/mole; m_{NaCl} is the mass of NaCl sample used in the experiment; and 58.5 is the molecular weight of NaCl, g/mole; the Cl^- ion instead of HCl is considered in the formula mainly due to the fact that besides the produced HCl, the evaporated NaCl in the forms of NaCl(g) and $(NaCl)_2$(g) (as indicated by the thermodynamic equilibrium simulation) will also contribute to the concentration of Cl^- ion in the solution.

As aforementioned, the binding energy of NaCl is as high as 787 kJ/mol; therefore, thermal decomposition or evaporation of NaCl under pyrolysis conditions is low, which has been proven in both thermodynamic simulations and TGA experiments. As illustrated in

Figure 4.5 from the tubular furnace results, increasing the temperature facilitates the evaporation of NaCl from the furnace. At temperature of 550 °C, no Cl^- ion is detected from the absorption solution, indicating that the evaporation or conversion of NaCl is negligible. However, although a rising trend is obtained with temperature, the conversion rate is less than 1.4% even at higher temperature of 950 °C. Despite the relatively low conversion rate, it is worth mentioning that there is a remarkable increase of the rate between 750 °C and 850 °C. It is mainly due to the melting point of NaCl which is around 801°C. The conversion rate is increased by 0.6% from 750 °C to 850 °C, while the value is only 0.2% from 550 °C to 750 °C.

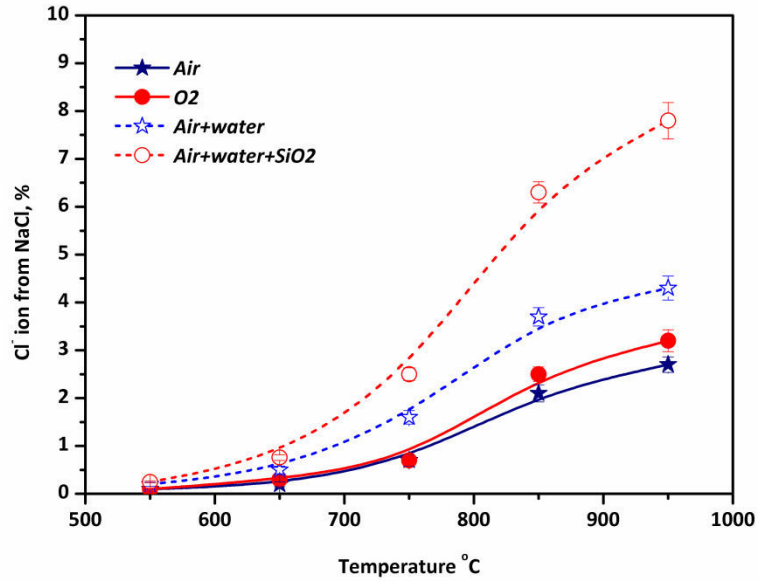

Figure 4. 6 Conversion of Cl^- ion from NaCl under air atmosphere and O_2 atmosphere and the effect of water and SiO_2

To further investigate the conversion behavior of chlorine from inorganic source during MSW thermal treatment, the effect of air/O_2 atmosphere and the presence of water and SiO_2 are experimentally determined and the results are exhibited in **Figure 4.6**. It can be concluded that the overall conversion rate of chlorine from NaCl to Cl^- ion is less than 8% even at higher temperature of 950 °C and with the presence of water and SiO_2. The amount of O_2 content slightly increases the conversion from NaCl to Cl^- ion; therefore, the effect of atmosphere on chlorine conversion rate from NaCl in descending order is: O_2 > air > N_2 (conversion rates at 950 °C are 3.2% > 2.7% > 1.2% respectively). The presence of water and SiO_2 significantly increases the chlorine conversion from NaCl to Cl^- ion. At temperature of 950 °C, the conversion rate is increased by 1.6% and 5.1% for the cases with the presence of water alone and with both water and SiO_2.

To sum up, results obtained from tubular furnace experiments are in good accordance with that from thermodynamic equilibrium simulation, indicating that the presence of O_2 and water will promote the release of Cl-compounds from the furnace by either evaporation or chemical conversion. Although the release level of Cl-contained contaminants from inorganic chlorine is as low as 2-8%, the remarkable amount of inorganic chlorine contained in MSW (as previously mentioned in **Section 1.2.1**, around 45% of the total chlorine content in MSW comes from food waste in inorganic forms) should be taken into consideration. Besides, the high proportion of water and inorganic materials contained in MSW in some Countries or regions will definitely facilitates the release of chlorine from inorganic source during waste thermal treatments. Therefore, inorganic chlorine may contribute to a considerable amount over the total HCl release contained in flue gas.

4.2.2 Chlorinated pollutants from organic source-PVC

4.2.2.1 TG and TG-FTIR analysis of Cl contaminants release from PVC pyrolysis

In order to investigate the thermal behavior of PVC during pyrolysis, thermogravimetric experiments of PVC are performed under N_2 atmosphere at heating rate of 10°C/min. The experimental results are exhibited in **Figure 4.7**.

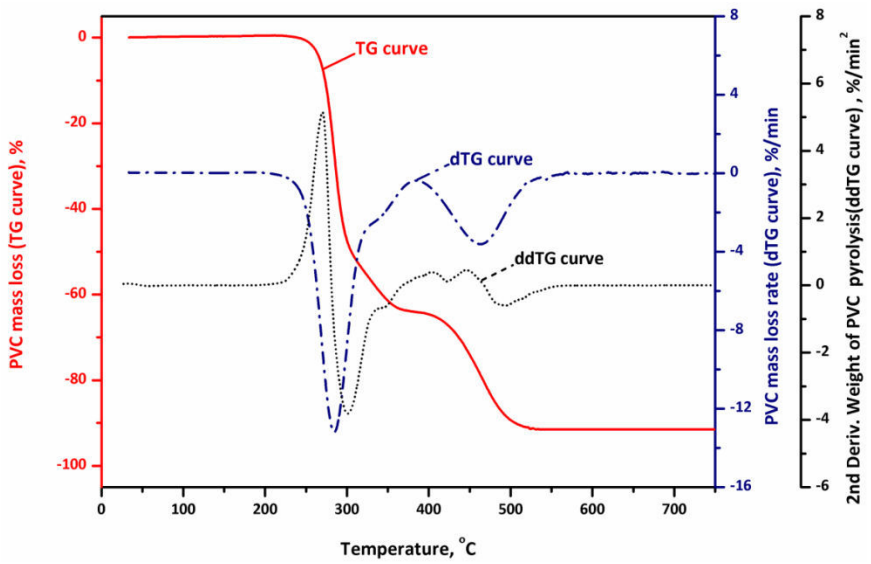

Figure 4. 7 TG, DTG and 2nd order DTG curves of PVC pyrolysis under N_2 atmosphere at heating rate of 10 °C/min

Results indicate that during pyrolysis, the mass weight loss of PVC starts from very low temperature at around 200 ^{o}C and ends up at around 550 ^{o}C, with an overall mass loss of approximately 92%. Therefore, decomposition reactions of PVC during thermal treatment are easy to occur and are quite completely achieved. From DTG curve in **Figure 4.7**, it is observed that there are two major weight loss peaks in the temperature ranges of 200-400 ^{o}C and 400-550 ^{o}C. The first significant degradation peak onsets at around 220 ^{o}C, which is associated with a mass loss over 60%. The second degradation peak begins at 400 ^{o}C, and the corresponding mass loss is higher than 30%. By considering the mass fraction of HCl in PVC, it is suggested from the previous findings that the first mass loss peak of PVC pyrolysis is mainly associated with dehydrochlorination reactions to generate HCl gases from PVC [8-10]. As previously mentioned in **Chapter 2**, the degradation of PVC polymer starts with the rupture of C-Cl bonds. The stoichiometric mass fraction of HCl in pure PVC is around 56%; therefore, it is believed that the decomposition of organic compounds also happens in the first degradation stage with the mass loss of around 60%, which is, on the other hand, also proven by the small shoulders from both DTG and DDTG curves at temperature of around 350 ^{o}C. Similar results are concluded by Soudais et al and Zhu et al, stating that the degradation of HCl from PVC in the first reaction stage is accompanied with the formation of a small amount of hydrocarbons, mainly aromatic compounds such as benzene [11, 12]. Characteristic parameters of TG and DTG curves are summarized in **Table 4. 1**.

Table 4. 1 Characteristic parameters of PVC pyrolysis

Material	PVC
Heating rate (^{o}C/min)	10
$T_{0.1}$ (^{o}C) [a]	272.6
T_{max} (^{o}C) [a]	284.5
$T_{0.9}$ (^{o}C) [a]	475.3
$t_{0.1-0.9}$(min) [b]	19.6
$(d_a/d_t)_{max}$ (%/min) [c]	13.2
$(d_a/d_t)_{mean}$ (%/min) [c]	3.0

[a] $T_{0.1}$, $T_{0.9}$, and T_{max} represents for the corresponding temperature when the mass conversion rate of PVC reaches 0.1, 0.9 and the maximum value;

[b] $t_{0.1-0.9}$ is the time duration of PVC mass conversion rate from 0.1 to 0.9;

[c] $(d_a/d_t)_{max}$ and $(d_a/d_t)_{mean}$ denote the maximum and average mass loss rate during thermal conversion.

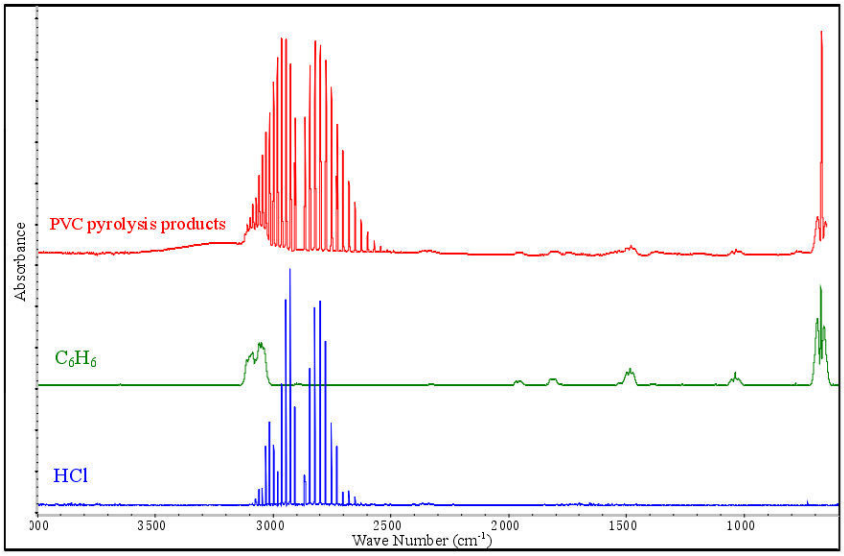

Figure 4. 8 Products identification of the first mass loss peak during PVC pyrolysis using TG-FTIR analysis

To better identify the products from dehydrochlorination process during PVC pyrolysis, TG analysis is coupled with a Fourier Transform Infrared Spectroscopy (FTIR) detector to determine the pyrolytic products. Products from the TG analyzer are directly analyzed by online Nicolet Netxus 670 Fourier transform spectrometer. **Figure 4.8** illustrates the identification results of the pyrolytic products of the maximum peak intensity in the first degradation stage. Results confirm that HCl generated from dehydrochlorination reaction of PVC is the most important product in the first degradation stage; meanwhile, a small amount of benzene is also formed [12]. According to Bockhorn et al. and Sørum et al., benzene is discharged immediately after HCl release from PVC since conjugated double bonds are formed after the dehydrochlorination process and the formation of benzene is thus enhanced [13, 14].

To sum up, thermal degradation of PVC is characterized as a two-step process, in which:

- the first degradation step is in the temperature range of around 200 to 400 ^{o}C with a high mass loss percentage of 60%; dehydrochlorination reactions are mainly taking place in this stage, accompanied with the formation of a small amount of benzene;
- the second degradation step occurs in the temperature range of 400-550 ^{o}C; in this stage, further decomposition and cracking of the polymer occurs to produce light hydrocarbons due to the increase of temperature; besides, aromatic compounds, such as benzene and its derivatives are also formed due to the abundant conjugated double bonds.

4.2.2.2 Cl-content contaminants release from PVC in fixed bed experiments

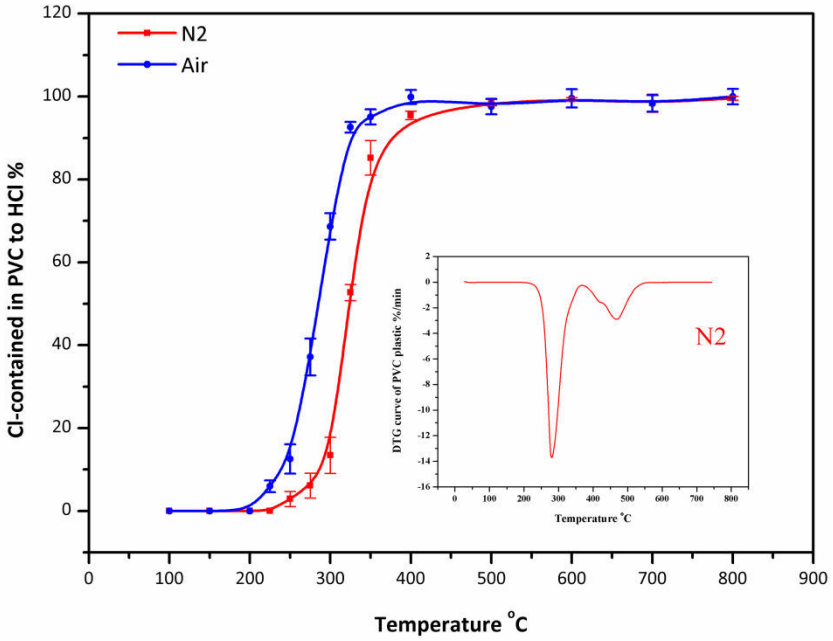

Figure 4. 9 HCl release from PVC pyrolysis and incineration in fixed bed tubular furnace reactor

Beside TG analysis focusing on the degradation kinetics of HCl release, fixed bed tubular furnace experiments are conducted to examine the effect of temperature and atmosphere on HCl released from PVC pyrolysis and incineration. The experimental facilities and the experimental procedures are described in **Chapter 2**. A series of temperature are considered: 100 °C, 150 °C, 200 °C, 225 °C, 250 °C, 275 °C, 300 °C, 325 °C, 350 °C, 400 °C, 500 °C, 600 °C, 700 °C, and 800 °C. The experimental results of HCl release from PVC pyrolysis and incineration are depicted in **Figure 4. 9**.

Results reveal that under both N_2 and air atmosphere, the release of HCl from PVC occurs in the temperature range of 200-450 °C; at temperature higher than 500 °C, almost all the chlorine contained in PVC is transferred to PVC by dehydrochlorination reactions (the conversion rate is higher than 98.3%). The results are in good accordance with the results obtained from TG analysis, indicating that HCl release from dehydrochlorination is mainly occurring in the temperature range of 200-400 °C. Loay Saeed et al. also found that when PVC is pyrolysed, HCl is the main gas released and the chlorine content for PVC pyrolytic char is less than 0.01 wt.%, indicating a nearly complete conversion of chlorine from PVC to HCl [15]. It is also notable that air atmosphere slightly shifts HCl release temperature to a lower level.

4.3 Influence of in-furnace CaO reactant on HCl mitigation efficiency

Because of the fact that HCl release from PVC is easy to occur in low temperature ranges and nearly all the chlorine contained in PVC is converted into HCl during thermal treatment, PVC is considered as feedstock to conduct the following experiments. The experiments are mainly focused on the effect of dechlorination temperature, Ca/Cl molar ratio, and CaO reactant particle size on in-furnace HCl mitigation by CaO reactant. Fixed bed tubular furnace is used to conduct the experiments. As aforementioned, HCl mitigation efficiency (HME) is defined as:

$$HME = \left(1 - \frac{HCl\ generation\ with\ CaO\ reactant}{HCl\ generation\ without\ CaO\ reactant}\right) \times 100\% \tag{4.4}$$

Accordingly, CaO conversion rate is also defined as the ratio of the stoichiometric mass of CaO converted to $CaCl_2$ via dechlorination reaction according to HCl mitigation efficiency to the total mass of CaO added, and it can be obtained as:

$$\eta_{CaO} = \frac{mass\ of\ CaO\ converted\ to\ CaCl_2\ via\ dechlorination\ reaction}{total\ mass\ of\ CaO\ added} \times 100\% \tag{4.5}$$

where η_{CaO} represents CaO conversion rate. The Ca/Cl molar ratio is defined as the ratio of the molecular amount of Ca contained in CaO reactant to the molecular amount of HCl produced from PVC pyrolysis as:

$$M_{Ca/Cl} = \frac{mass\ of\ CaO \times mass\ percentage\ of\ Ca / 40.1}{mass\ of\ PVC \times mass\ percentage\ of\ Cl / 35.5 \times conversion\ rate\ from\ Cl\ to\ HCl} \tag{4.6}$$

where $M_{Ca/Cl}$ is the Ca/Cl molar ratio; 40.1 is the molecular weight of Ca in g/mol; 35.5 is the molecular weight of Cl in g/mol.

4.3.1 Effect of Ca/Cl molar ratio on HCl mitigation by in-furnace CaO reactant

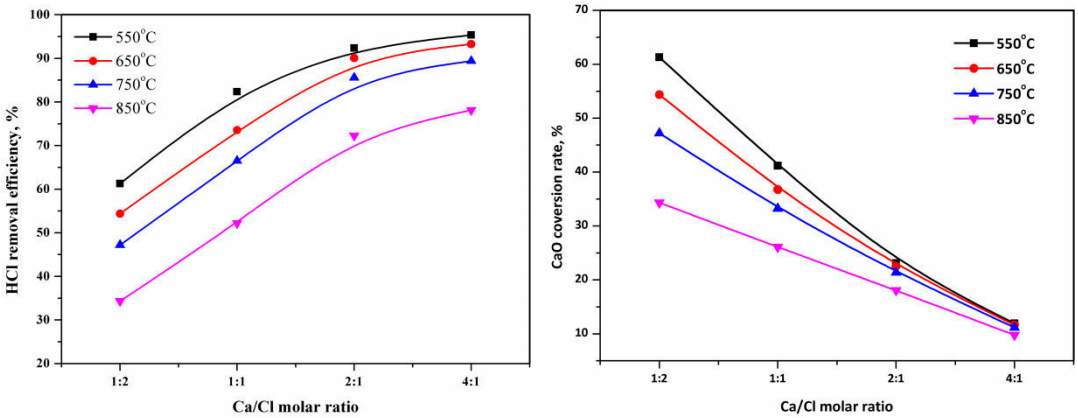

Figure 4. 10 Effect of Ca/Cl molar ratio on HCl mitigation efficiency and CaO conversion rate during PVC pyrolysis with the presence of in-furnace CaO

The influences of Ca/Cl molar ratio on HCl mitigation efficiency are depicted in **Figure 4.10**. It is obvious from the results that increasing the Ca/Cl molar ratio from 1:2 to 4:1 significantly facilitates the removal efficiency of HCl by CaO reactant, resulting in an improvement from 34.3%-61.3% to 78.1%-95.4% within the considered temperature range. Results from **Chapter 3** demonstrate that the dechlorination reaction between CaO and HCl is firstly limited by chemical reaction rate; therefore, increasing the amount of CaO provides more active sites on CaO surface for bonding HCl.

Considering the stoichiometric Ca/Cl molar ratio of dechlorination reactions as presented in **Eq. (4.13)** and **Eq. (4.14)**, the theoretical amount of CaO needed is equal to the amount of CaO with the Ca/Cl molar ratio of 2:1 or 1:1. However, experimental results show that stoichiometric Ca/Cl molar ratios, HCl mitigation efficiency is quite low, ranging from 34.3% - 61.3% for Ca/Cl ratio of 1:2 and 51.2% - 82.4% for Ca/Cl ratio of 1:1 under experimental temperature. Therefore, excessive use of CaO reactant than stoichiometric amount is essential to achieve acceptable HCl mitigation efficiency levels.

$$CaO + HCl \leftrightarrow CaClOH \tag{4.7}$$

$$CaO + 2HCl \leftrightarrow CaCl_2 + H_2O \tag{4.8}$$

As exhibited in **Figure 4.10**, when the Ca/Cl molar ratio reaches 2:1, HCl mitigation efficiency ranges from 92.4% at temperature of 550 °C to 72.2% at temperature of 850 °C, resulting in a remarkable enhancement of HCl mitigation efficiency by around 31% to 38% as

compared to that of the Ca/Cl molar ratio of 1:2. However, when the ratio is further increased to 4:1, a limited enhancement of HCl mitigation efficiency by around 5% is observed. The reason may be attributed to the fact that at higher Ca/Cl molar ratio conditions, there are enough active sites on CaO reactant particle surface for dechlorination reactions. This means that under such circumstance, the amount of CaO (or in other words, the number of the active sites on CaO surface) is no longer the limiting factor of the reactions; therefore, further increasing Ca/Cl molar ratio will lead to a slight improvement on HCl mitigation efficiency. Accordingly, the Ca/Cl molar ratio of 2:1 is believed the most effective amount of CaO for HCl gas removal under the experimental conditions. Fontana et al. [16]and Tan et al. [17] also found that the increase of the Ca/Cl molar ratio will enhance HCl mitigation effect of Ca-based reactants and the most proper Ca/Cl molar ratio is in the range of 2:1 to 3:1.

With respect to CaO conversion rate, the influences of Ca/Cl molar ratio on CaO conversion rate during PVC pyrolysis are also reported in **Figure 4. 10**. As illustrated, although HCl mitigation efficiency is improved with increasing Ca/Cl molar ratio, the corresponding CaO conversion rate declines continuously at the same time. At the Ca/Cl molar ratio of 1:2, the highest CaO conversion rate of 34.3% - 61.3% is obtained; however, at the Ca/Cl molar ratio of 4:1, CaO conversion rate declines significantly to 9.8% - 11.9%. The reduction of CaO conversion rate is reasonable, since with the increase of Ca/Cl molar ratio, the amount of CaO is more abundant. Taking into consideration at the working condition of the most effective Ca/Cl molar ratio of 2:1, CaO conversion rate is as low as 18.1% - 23.1%, the reuse of the spent in-furnace CaO reactant together with the fresh CaO can be regarded as a promising alternative to reduce the sorbent consumption.

Figure 4. 11 presents the SEM and EDS analysis of the spent CaO reactants at 750 ^{o}C with Ca/Cl molar ratio of 1:1 and 2:1. Besides, the elemental composition of the reactant surface obtained from EDS micro analyses are listed in **Table 4.1**.

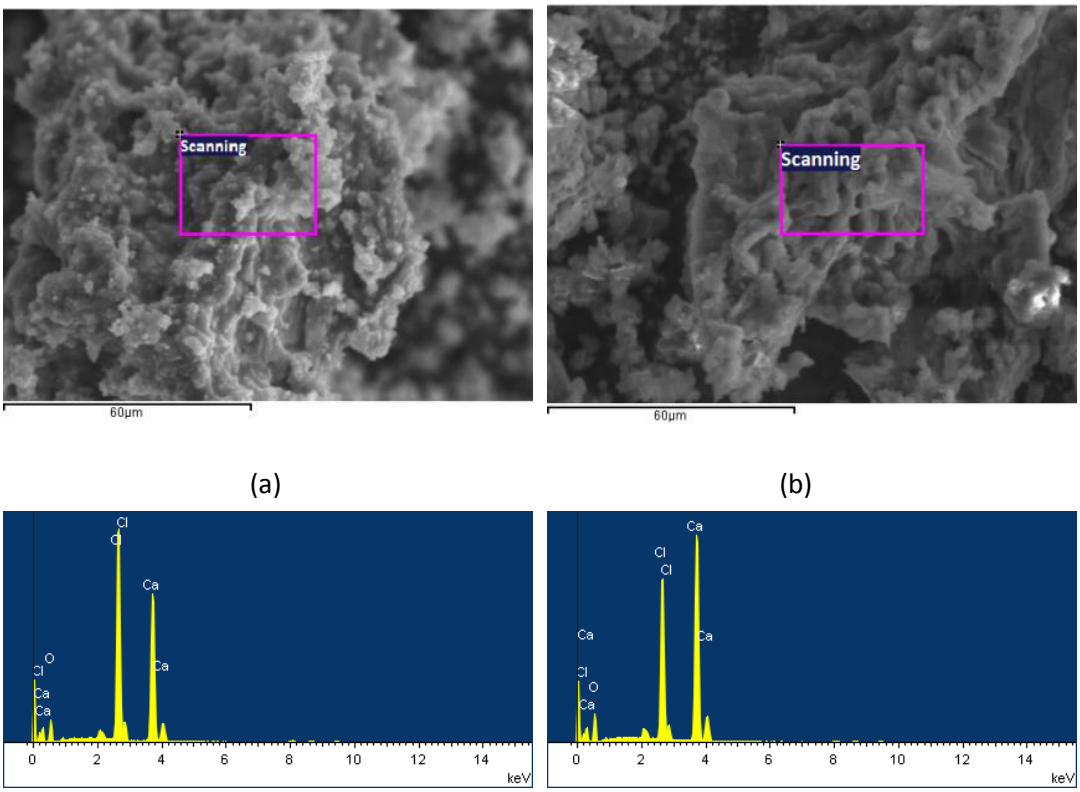

Figure 4. 11 SEM and EDS detection of the spent CaO reactants: (1) SEM, Ca/Cl molar ratio: 1:1, 750 °C; (2) SEM, Ca/Cl molar ratio: 2:1, 750 °C; (3) EDS, Ca/Cl molar ratio: 1:1, 750 °C; (4) EDS, Ca/Cl molar ratio: 2:1, 750 °C

Table 4. 2 Elemental composition of the spent CaO reactant by EDS analysis

Elements	Carbon (C) [a]	Oxygen (O) [a]	Chlorine (Cl) [a]	Calcium (Ca) [a]	Total
Ca/Cl=1:1 [b]	34.0	22. 2	17.6	26.2	100
Ca/Cl=2:1 [b]	23.7	32.3	8.6	35.4	100

[a] in atomic percentage;

[b] at temperature of 750 °C.

As presented in **Figure 4. 11** and **Table 4.2**, at a temperature of 750 °C, chlorine content in the residues obtained from the cases of Ca/Cl molar ratio at 1:1 and 2:1 is 17.6% and 8.6%, respectively, which further confirms that although HCl mitigation efficiency is improved at higher Ca/Cl molar ratio, the conversion of CaO to $CaCl_2$ (reflected by chlorine content in the residues) is decreased.

4.3.2 Effect of temperature on HCl mitigation by in-furnace CaO reactant

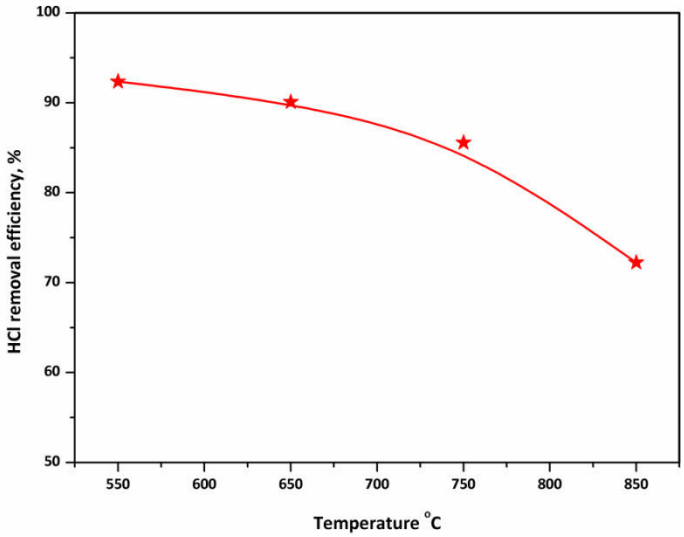

Figure 4. 12 Effect of temperature on HCl mitigation efficiency during PVC pyrolysis with the presence of in-furnace CaO reactant

Results from **Section 4.3.1** reveal that the most preferable Ca/Cl molar ratio under the experimental conditions is 2:1. Therefore, the effect of temperature on HCl mitigation efficiency experiments is conducted under such Ca/Cl molar ratio. Results are exhibited in **Figure 4. 12**.

As demonstrated, increasing the temperature causes adverse effects on HCl mitigation efficiency. HCl mitigation efficiency declined continuously from 92.4% to 72.2% when the experimental temperature is increased from 550 ^{o}C to 850 ^{o}C. The results agree well with the observations in **Chapter 3**, revealing that HCl mitigation capacity decreases with the increase of temperature. The reasons are mainly attributed to two aspects: on the one hand, both physical adsorption and chemical reaction between CaO and HCl are exothermic processes, which means increasing the temperature will shift the equilibrium to the direction of the formed dechlorination products (i.e. $CaCl_2$ or CaClOH), decomposition and thus reduce HCl mitigation efficiency; on the other hand, calcination and sintering of the reactant and the product-layer occur at higher temperature, which significantly reduces the specific surface area and pore volume and decreases the active sites on the reactant surface.

Moreover, it is noted that higher temperature accelerates the decrease of HCl mitigation efficiency; it is decreased by 6.8% from temperature of 550 ^{o}C to 750 ^{o}C, but reduced sharply by 13.3% when further increasing the temperature to 850 ^{o}C. According to

Brooke Shemwell et al [18], the binding capacity of CaO and HCl is limited at higher temperature due to the shift of the thermodynamic equilibrium of dechlorination reactions.

The evolution of the surface morphologies of the spent CaO reactant as well as their elemental composition analysis with the increase of temperature is depicted in **Figure 4. 13**. As exhibited, at temperature of 550 °C, the surface of the residues become loose and porous as compared to the surface of raw CaO reactant, indicating that solid products generated on the surface of the reactant through dechlorination reactions. At temperature of 650 °C, the sorbent surface is less porous and becomes dense, mainly due to the sintering of the reactant and the product-layer. At temperature of 750 °C, obvious melting of the product-layer (the melting temperature of $CaCl_2$ is 772 °C) is observed from the SEM photograph, resulting in the formation of a very smooth and compact surface. However, at temperature of 850 °C, the surface becomes again very loose and porous, mainly attributed to the evaporation and decomposition of the product-layer, i.e. $CaCl_2$. The SEM photographs confirm that at higher temperature, calcination and sintering of the reactant and the product-layer changes the surface properties and pore structure of the sorbent, thus reducing the capacity of CaO reactant for HCl mitigation.

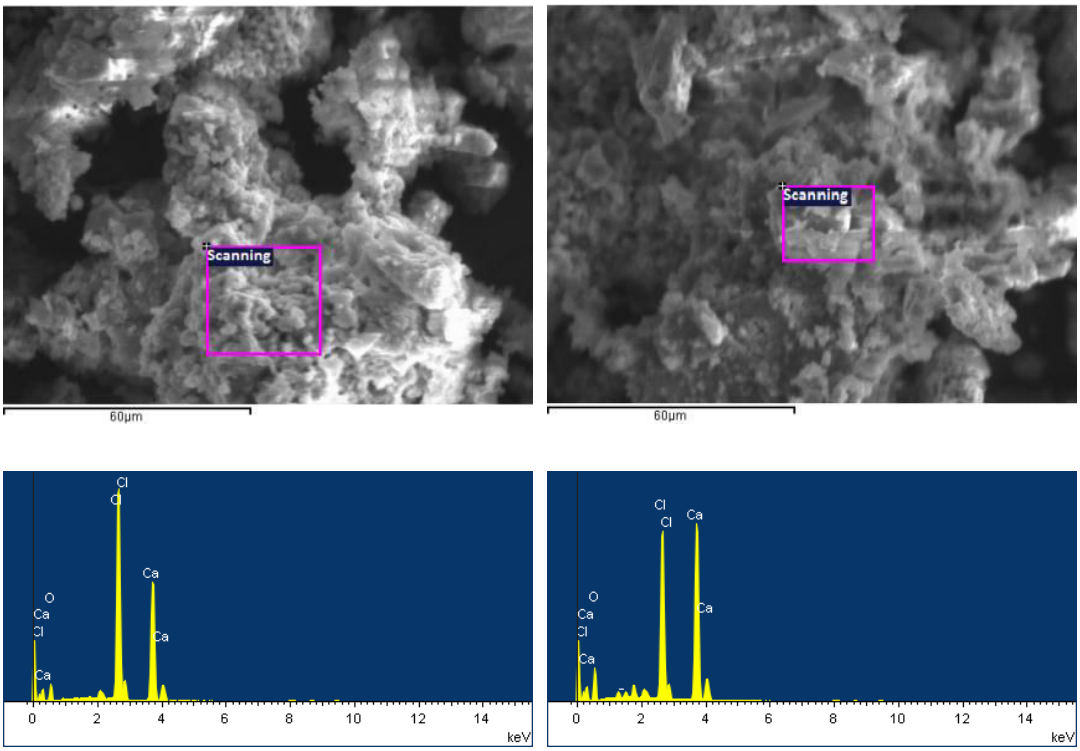

(a) 550 °C (b) 650 °C

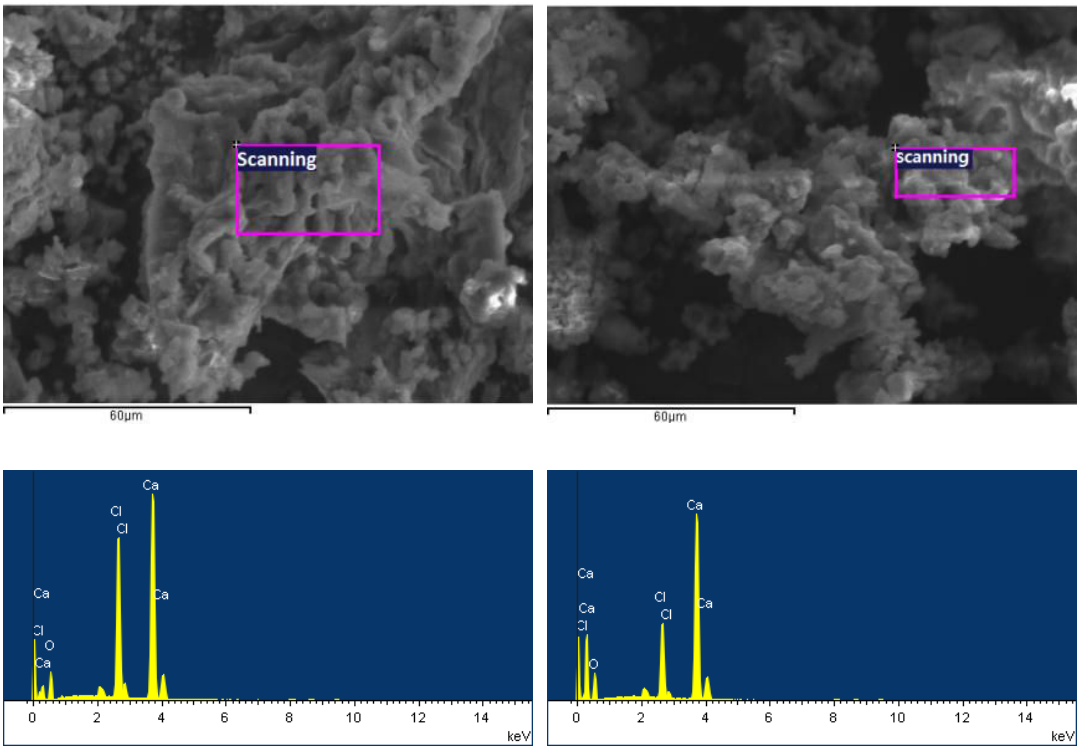

(c) 750 °C

(d) 850 °C

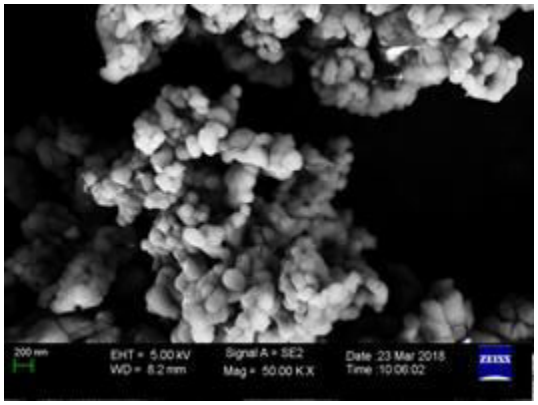

(e) fresh CaO

Figure 4. 13 SEM and EDS analysis of the spent CaO reactants at Ca/Cl molar ratio of 2:1: (1) 550 °C; (2) 650 °C; (3) 750 °C; (4) 850 °C; (e) SEM photograph of fresh CaO reactant

Table 4. 3 Elemental composition of the spent CaO reactant by EDS analysis

Elements	Carbon (C) [a]	Oxygen (O) [a]	Chlorine (Cl) [a]	Calcium (Ca) [a]
550 °C [b]	40.5	21.2	20.4	17.9
650 °C [b]	30.1	25.3	12.6	26.0
750 °C [b]	23.7	32.3	8.6	35.4
850 °C [b]	22.2	35.3	4.0	38.5

[a] in atomic percentage;

[b] at Ca/Cl molar ratio of 2:1.

The elemental compositions of the selected surface of the sorbent are also depicted in **Figure 4. 13**. Results reveal that with the increase of temperature, the relative intensity of elemental chlorine is significantly decreased. The molar fraction of chlorine of the selected surface is decreased from 20.4% at 550 °C to 4.0% at 850 °C. **Table 4.3** summarizes the elemental composition of the selected area on the reactant surface by EDS analysis, which further confirms the decline of HCl mitigation efficiency with respect to the reduction of the chlorine contained in the selected surface.

4.3.3 Effect of CaO particle size on HCl mitigation by in-furnace CaO reactant

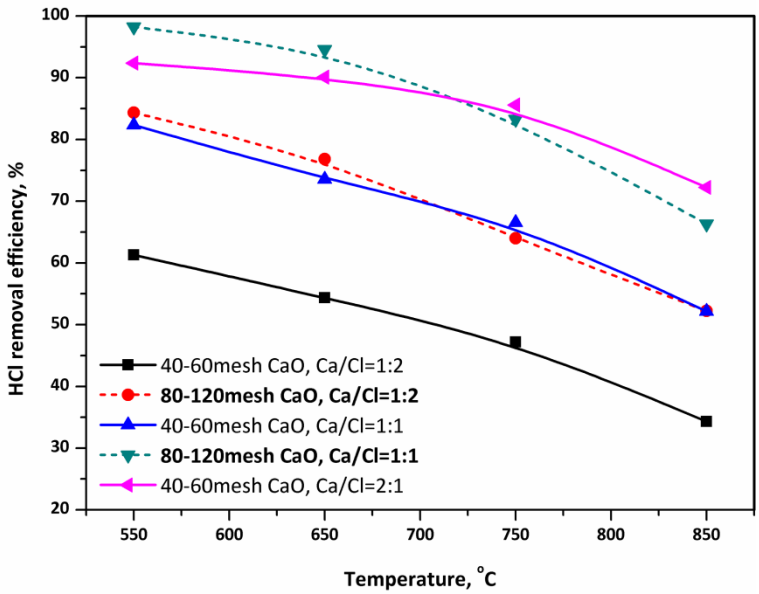

Figure 4. 14 Effect of CaO particle size on HCl mitigation efficiency during PVC pyrolysis with the presence of in-furnace CaO reactant

Besides the amount of CaO reactant used, physical properties of CaO such as specific surface area, pore volume and pore structure also play important roles in HCl mitigation behavior. Therefore, the effect of CaO reactant particle size on HCl mitigation efficiency is

experimentally investigated. Two kinds of CaO reactants are used: one is normally used in this work with particle size of 40-60 mesh (0.25-0.43 mm) and the other one is a finer CaO reactant with particle size of 80-120 mesh (0.125-0.18 mm). The results are shown in **Figure 4. 14**.

Results reveal that the particle size of the reactant also plays a quite important role in HCl mitigation efficiency. Higher HCl mitigation efficiency is obtained when finer CaO reactant is used in the furnace under the experimental situations. As presented in **Figure 4. 14**, when 80-120 mesh CaO reactant with the Ca/Cl molar ratio of 1:2 is used, HCl mitigation efficiency ranges from 52.3% to 84.3%, nearly reaching the same HCl mitigation efficiency level as that when 60-80 mesh CaO reactant with the Ca/Cl molar ratio of 1:1 is used (51.2% - 82.4%). Similarly, when 80-120 mesh CaO reactant with the Ca/Cl molar ratio of 1:1 is used, HCl mitigation efficiency is as high as 66.35% - 98.2% under the experimental temperature. These efficiencies are much closed to the aforementioned most preferable HCl mitigation conditions using the CaO reactant with the particle size of 60-80 mesh and the Ca/Cl molar ratio of 2:1 in **Section 4.3.2** (72.2%-92.4%).

The specific surface area of the CaO with the particle size of 80-120 mesh is 6.28 m^2/g, nearly 2.5 times higher than that of the CaO of 60-80 mesh (2.37 m^2/g). Therefore, finer reactants provide more surface area (or in other words, more active sites) for the both adsorption and chemical reactions of HCl by CaO, thus can significantly enhances the HCl mitigation efficiency. From this point of view, investigation in **Section 4.3.1**, when the Ca/Cl molar ratio is increased, increases not only the quantity of CaO reactant, but also the number of the active sites on its surface for both HCl physical adsorption and chemical dechloirination reaction. However, it is worth mentioning that the finer the particle size, the severer the attrition of the reactants may occur, resulting in the formation of more particulates and blocking the facilities [19]. Therefore, the particle size of the reactant should be carefully optimized with regards to both the effects on HCl mitigation and the adverse effect on particulates formation especially in commercial applications.

4.4 kinetic modeling of HCl release and control from PVC pyrolysis

Kinetic modeling of HCl release from PVC pyrolysis and the effect of CaO addition are investigated in this section. The model-free method is one of the most commonly used computation methods to estimate the reaction kinetic parameters (i.e. apparent activation energy and pre-exponential factor) without considering the pyrolytic mechanism. However,

the model-free method is only suitable for a single reaction [20, 21]. As aforementioned in **Figure 4.7** in **Section 4.2**, there are two distinct mass loss peaks of PVC pyrolysis TG curves, among which the first mass loss peak corresponds almost exclusively to dehydrochlorination process accompanied with a small amount of hydrocarbons, mainly aromatic compounds such as benzene [22]. Moreover, the reaction rate curve (DTG) has multiple peaks and shoulders, indicating that the pyrolytic reaction mechanisms are associated with a multi-step conversion. Regarding this fact, the model-free method is not suitable to identify the mechanisms, since it only considers the overlap of the multi-step decomposition processes [20, 23].

One possible solution to the aforementioned problem is to separate the DTG curves (the reaction rate) into the combination of several individual reaction process, and then uses the model-free methods to estimate the corresponding parameters of the separated pseudo-component reactions [20]. Recently, the Fraser–Suzuki function (FSF) has successfully been applied to curve-fit complex solid-state reactions into individual reactions [20, 24-28]. Therefore, this method is introduced in this work.

4.4.1 Kinetic modeling approach

4.4.1.1 Individual reactions of PVC pyrolysis with/without CaO reactant

As aforementioned, PVC pyrolysis can be divided into three single step reactions including: FSF_1: dehydrochlorination (de-HCl); FSF_2: formation of aromatic compounds like benzene (de-benzene); and FSF_3: further polyene decomposition and cyclization (de-polyene and cyclization). Therefore, it is assumed that the decomposition of the pseudo-components is independent and can be described by equations 4.9 - 4.11:

$$\mathrm{FSF_1}\text{: } \mathrm{R_1\text{-}HCl} \xrightarrow{k_1} HCl_{(g)} \tag{4.9}$$

$$\mathrm{FSF_2}\text{: } \mathrm{R_2} \xrightarrow{k_2} P_1(g) \tag{4.10}$$

$$\mathrm{FSF_3}\text{: } \mathrm{R_3} \xrightarrow{k_3} P_2(g) \tag{4.11}$$

where k refers to the reaction rate constant. When CaO reactant is used, it is considered that only the reaction rate and reaction degree of the independent single reaction is influenced, but the reaction process is not changed. Therefore, the pseudo-components decomposition can be described by equation 4.12-4.14:

$$\mathrm{FSF_1'}\text{: } \mathrm{R_1\text{-}HCl'} \xrightarrow{k_1'} HCl'_{(g)} \tag{4.12}$$

$$FSF_2': R_2' \xrightarrow{k_2'} P_1'(g) \tag{4.13}$$

$$FSF_3': R_3' \xrightarrow{k_3'} P_2'(g) \tag{4.14}$$

where k' refers to the reaction rate constant with CaO reactant.

4.4.1.2 Reaction kinetics

The kinetic expression for the rate of heterogeneous reactions can be described as:

$$\frac{da}{dt} = k(T) f(a) \tag{4.15}$$

where the conversion rate *a* is defined as the instant mass loss to the overall mass loss, and it is given by the following equations:

$$a = \frac{m_0 - m_t}{m_0 - m_f} \tag{4.16}$$

where a is the conversion rate; m_0, m_t and m_f represents for the initial weight, instant weight of the sample at t time and the final weight of the sample. According to the Arrhenius equation, the chemical reaction rate *k*(T) can be determined by:

$$k(T) = A\exp\left(\frac{-E}{RT}\right) \tag{4.17}$$

where A is the pre-exponential factor in min^{-1}; E is the activation energy in kJ/mol; R is the ideal gas constant and its value is 8.314 J/(mol*K). By combining the **Eq. (4.15)** and **Eq. (4.17)**, and taking into consideration the constant heating rate, β= dT/dt, the kinetics expressions can be described as:

$$\frac{da}{dT} = \left(\frac{A}{\beta}\right)\exp\left(\frac{-E}{RT}\right) f(a) \tag{4.18}$$

The integral form of Eq. (4.18) is:

$$g(a) = \int_0^a \frac{1}{f(a)} da = \frac{A}{\beta}\int_{T_0}^{T} \exp\left(\frac{-E}{RT}\right) dT \tag{4.19}$$

4.4.1.3 Fraser-Suzuki deconvolution

Deconvolution of the DTG curves using the FSF function can be described as:

$$\frac{\mathrm{d}a}{dT} = \sum_{i=1}^{Nc} c_i H_{p,i} \exp\left\{-\frac{\ln 2}{A_{s,i}^2}\ln\left[1 + 2A_{s,i}\frac{\left(T - T_{p,i}\right)}{W_{hf,i}}\right]^2\right\} \tag{4.20}$$

where the parameters H_p, T_p, W_{hf}, and A_s represents the height (K^{-1}), peak temperature (K), half-width of the separated DTG curves of the pseudo-components, and asymmetry (dimensionless), respectively; ci and Nc refer to the proportion of i-th pseudo-component

and the total number of the pseudo-components. The effects of the variation of the parameters H_p, T_p, W_{hf}, and A_s are depicted in **Figure 4.15**.

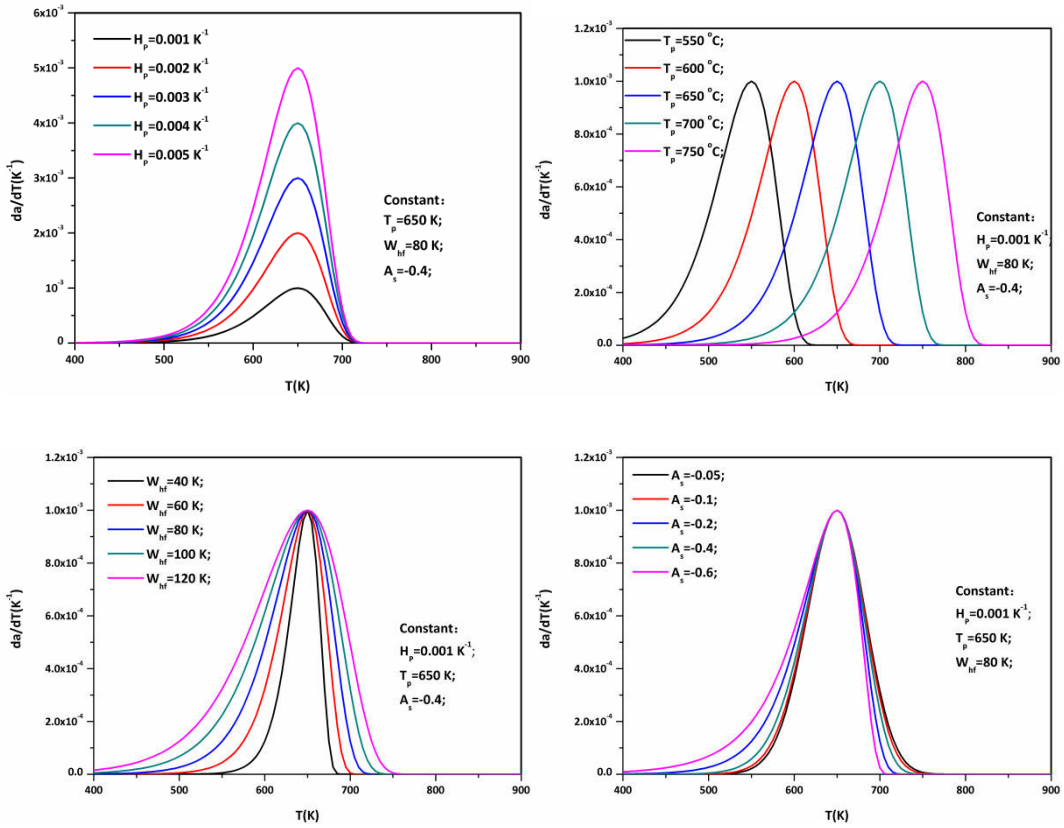

Figure 4. 15 Effect of the parameters in the Fraser-Suzuki function: 1, the height, H_p; 2, the Peak temperature, T_p; 3, the half width, w_{hf}; and 4, the symmetry, A_s

4.4.1.4 Activation energy determination

Several mathematic method are introduced to solve the kinetic equations and to estimate the activation energy. Among them, Ozawa–Flynn–Wall (OFW) method and Kissinger-Akahira-Sunose (KAS) method are most commonly applied [29, 30].

By OFW method, **Eq. (4.19)** can be linearized as [13]:

$$\ln(\beta) = \ln\left(\frac{AE}{Rg^*(a)}\right) - 5.331 - 1.052\frac{E}{RT} \tag{4.21}$$

And by KAS method, **Eq. (4.19)** can be linearized as [31, 32]:

$$\ln\left(\frac{\beta}{T^2}\right) = \ln\left(\frac{AR}{E^* g(a)}\right) - \frac{E}{RT} \tag{4.22}$$

Therefore, the kinetic parameters can be obtained by plotting ln (β) vs 1/T for OFW method and ln (β/T^2) vs 1/T for KAS method at the same conversion rate *a*. For the OFW

method, the apparent activation energy can be obtained from the slope of the straight line and is equal to -1.052*E/R, and for the KAS method, the apparent activation energy can be obtained from the slope of the straight line and is equal to -E/R.

4.4.2 Kinetic modeling results

4.4.2.1 Fraser-Suzuki deconvolution results

The Fraser-Suzuki deconvolution curves for pure PVC and PVC with CaO reactant during pyrolysis at 5, 10 and 20 °C/min are presented in **Figure 4. 16** and the corresponding Fraser-Suzuki deconvolution parameters are listed in **Table 4.4**. The calculation result fits well with the experimental data with a quite low deviation of less than 3.0%.

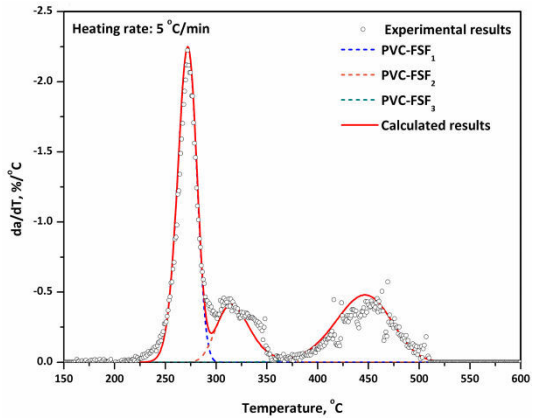

(a) PVC at 5 °C/min

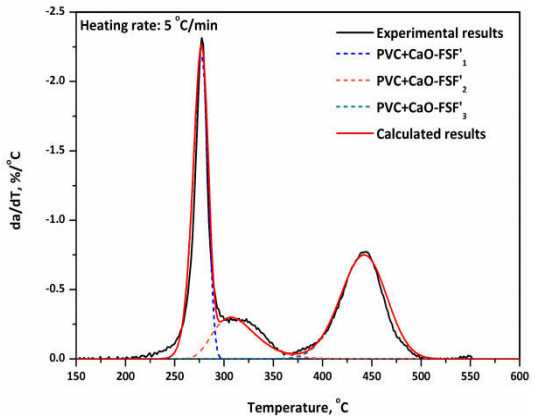

(b) PVC with CaO at 5 °C/min

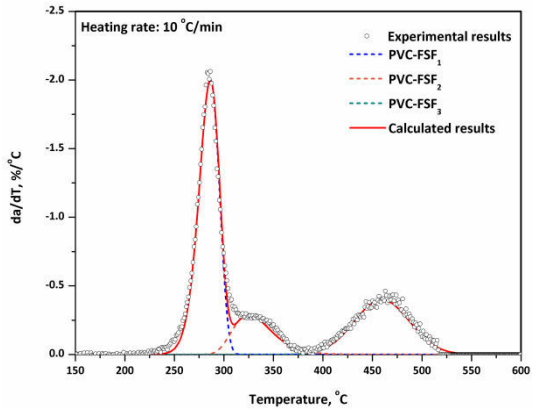

(c) PVC at 10 °C/min

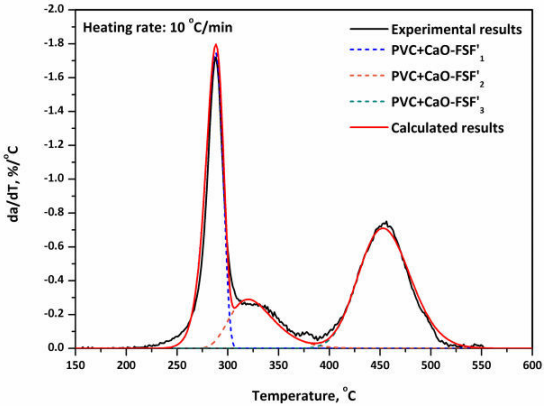

(d) PVC with CaO at 10 °C/min

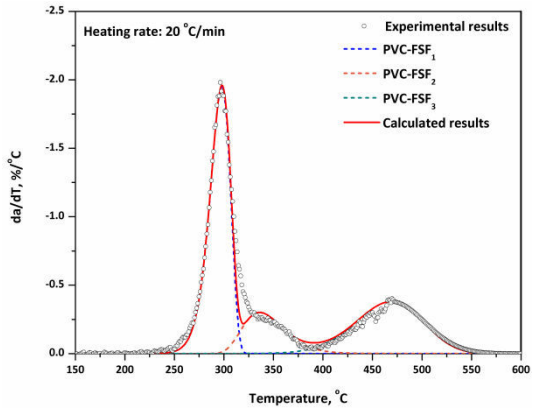

(e) PVC at 20 °C/min

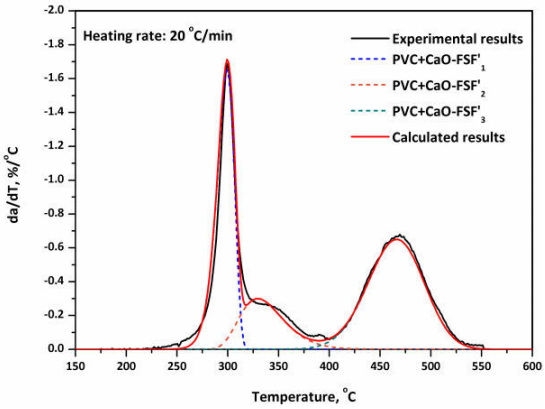

(f) PVC with CaO at 20 °C/min

Figure 4. 16 Deconvoluted DTG curves of PVC and PVC with CaO reactant pyrolysis at 5 °C/min, 10 °C /min, and 20 °C /min

Table 4. 4 Fraser-Suzuki deconvolution results for PVC pyrolysis with/without CaO reactant at 5, 10 and 20 °C/min

Single reaction		PVC 5	PVC 10	PVC 20	Single reaction		PVC with CaO 5	PVC with CaO 10	PVC with CaO 20
FSF_1: de-HCl	H_p	-2.25	-2.00	-1.95	FSF'_1: de-HCl	H_p	-2.00	-1.75	-1.65
	T_p	272.00	286.20	297.90		T_p	276.80	287.90	299.20
	W_{hf}	22.00	24.00	24.00		W_{hf}	18.00	20.00	20.00
	A_s	-0.10	-0.20	-0.30		A_s	-0.20	-0.30	-0.30
	c_i	52.88	51.83	51.46		c_i	38.88	38.48	36.27
FSF_2: de-benzene	H_p	-0.41	-0.29	-0.30	FSF'_2: de-benzene	H_p	-0.30	-0.29	-0.30
	T_p	314.90	325.30	336.00		T_p	306.90	320.00	329.50
	W_{hf}	38.00	45.00	48.00		W_{hf}	50.00	50.00	50.00
	A_s	-0.41	0.30	0.30		A_s	0.30	0.30	0.40
	c_i	16.83	14.35	11.83		c_i	16.49	15.94	16.92
FSF_3: de-polyene and cyclization	H_p	-0.48	-0.40	-0.38	FSF'_3: de-polyene and cyclization	H_p	-0.75	-0.71	-0.65
	T_p	446.60	459.50	469.00		T_p	442.10	452.80	466.40
	W_{hf}	65.00	65.00	80.00		W_{hf}	55.00	60.00	65.00
	A_s	-0.10	0.01	-0.10		A_s	-0.05	0.10	-0.05
	c_i	33.33	27.68	32.48		c_i	43.95	45.51	45.01
DEV (%)		2.99	1.84	2.65			1.90	2.37	2.36

4.4.2.2 Activation energy estimation

Following the separation of the DTG peaks by Fraser-Suzuki deconvolution, the conversion rate of each pseudo-component is determined. And then according to **Section 4.4.1.4**, the kinetic parameters can be obtained by plotting ln (β) vs 1/T curves for OFW

method and ln (β/T^2) vs 1/T curves for KAS method at the same conversion rate of 0.1, 0.2, 0.3, 0.4, 0.5, 0.6, 0.7, 0.8, and 0.9.

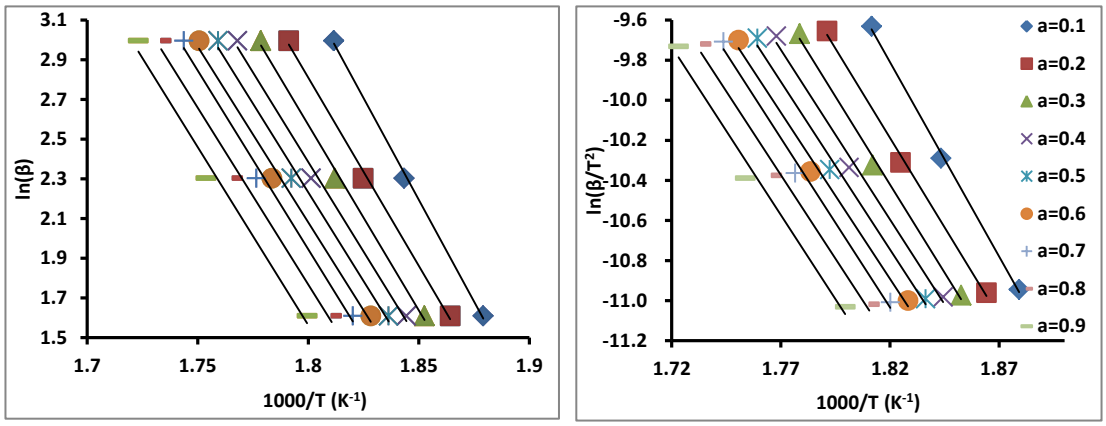

(a) FSF_1 of OFW method (b) FSF_1 of KAS method

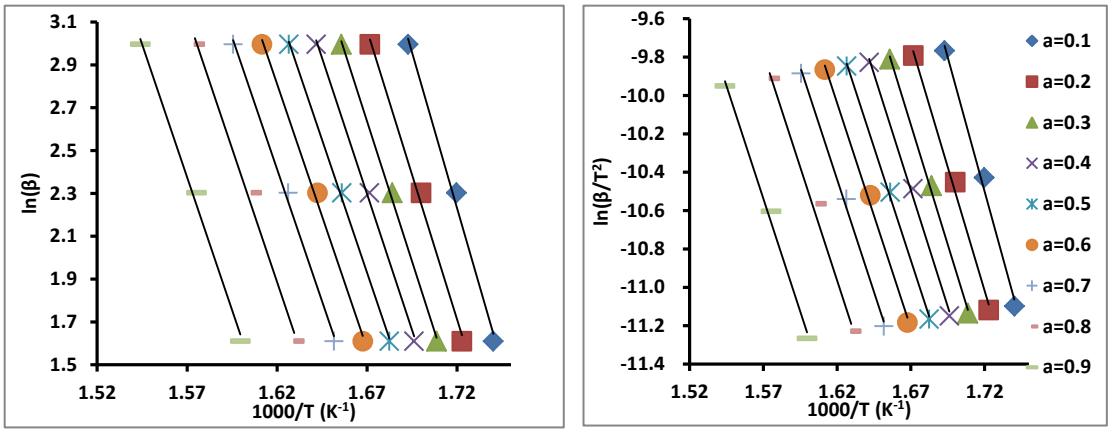

(c) FSF_2 of OFW method (d) FSF_2 of KAS method

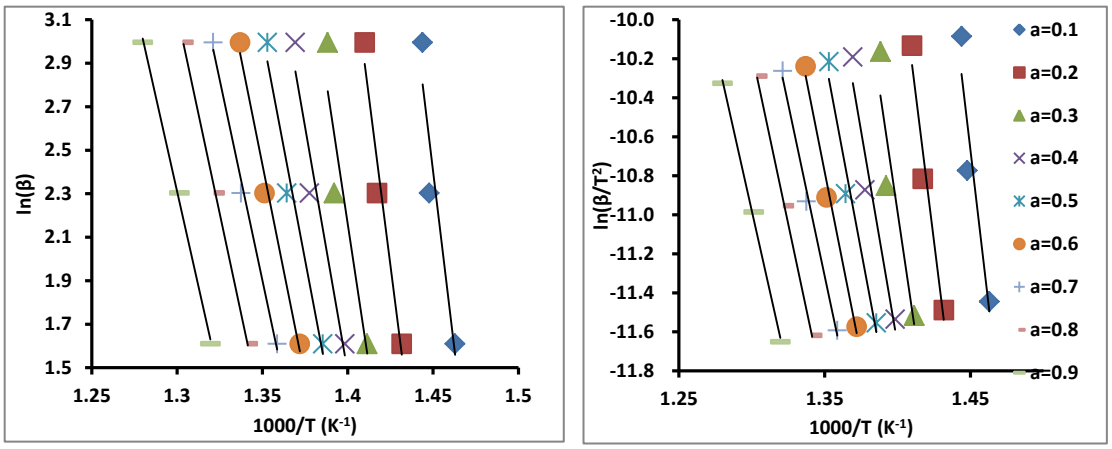

(e) FSF_3 of OFW method (f) FSF_3 of KAS method

Figure 4. 17 Kinetic plots for the pseudo-components of PVC pyrolysis between conversion rates of 0.1 and 0.9 using both OFW and KAS methods

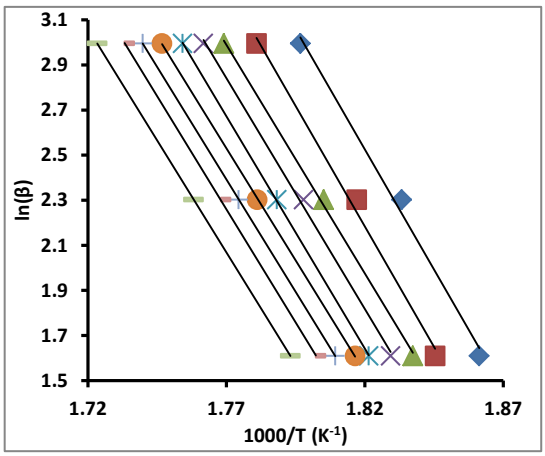

(a) FSF'1 of OFW method

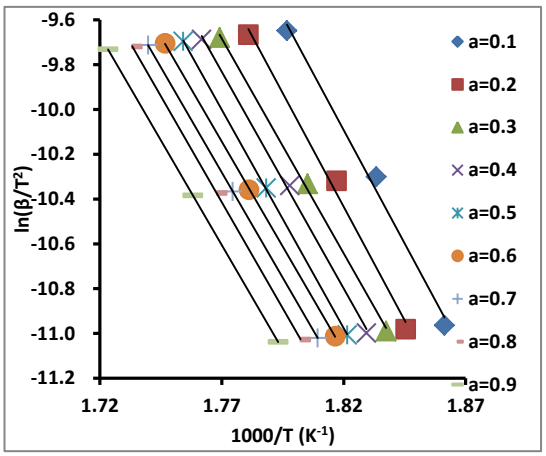

(b) FSF'1 of KAS method

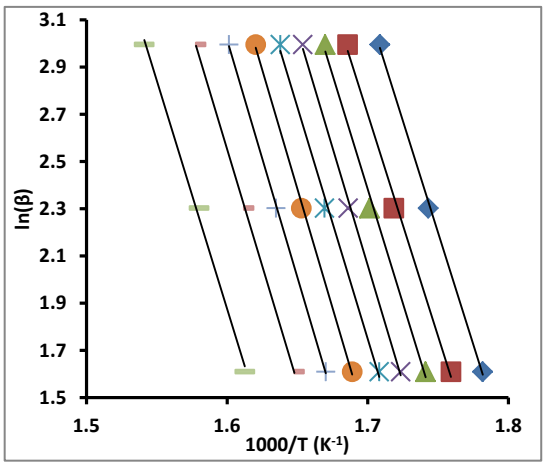

(c) FSF'2 of OFW method

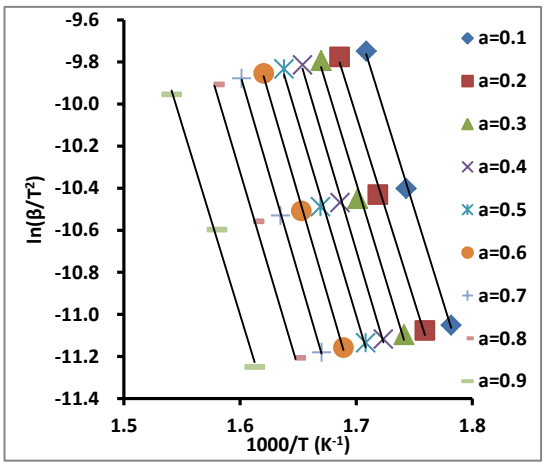

(d) FSF'2 of KAS method

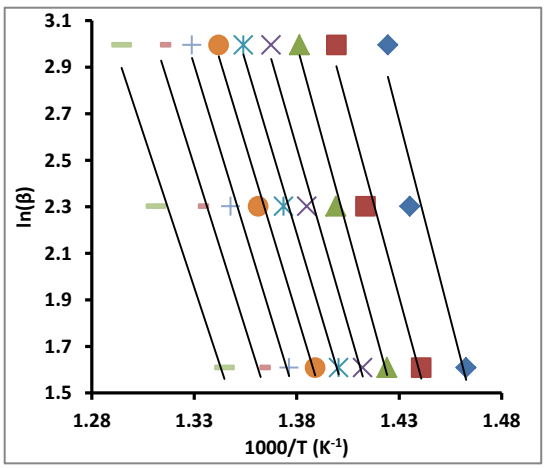

(e) FSF'$_3$ of OFW method

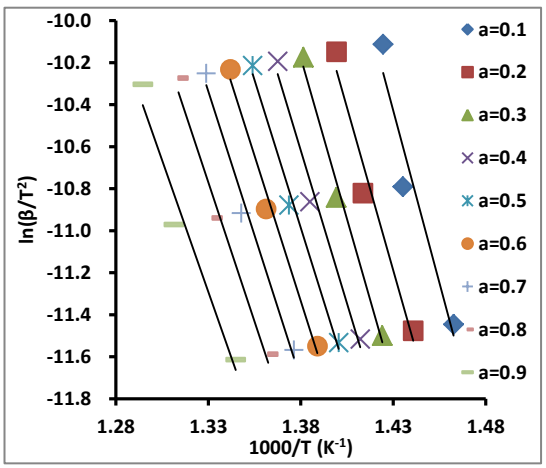

(f) FSF'$_3$ of KAS method

Figure 4. 18 Kinetic plots for the pseudo-components of PVC pyrolysis with CaO reactant between conversion rates of 0.1 and 0.9 using both OFW and KAS methods

Table 4. 5 The characteristic temperature at each conversion rate of different pseudo-component, the slope of the regression plots and the estimated activation energy of PVC pyrolysis without/with CaO reactant

PVC FSF_1	Characteristic temperature, °C			OFW method			KAS method		
Conversion rate	5	10	20	Slope	Ea	Dev%[a]	Slope	Ea	Dev%[a]
α = 0.1	259.00	269.34	278.85	-20.49	170.38	11.46	-19.41	153.39	12.36
α = 0.2	263.27	274.85	285.14	-18.94	157.47	3.01	-17.85	141.04	3.31
α = 0.3	266.63	278.72	289.09	-18.68	155.28	1.58	-17.58	138.90	1.74
α = 0.4	269.04	282.01	292.47	-18.05	150.04	-1.84	-16.94	133.88	-1.94
α = 0.5	271.41	284.76	295.28	-17.86	148.47	-2.87	-16.75	132.34	-3.06
α = 0.6	273.81	287.52	298.08	-17.71	147.24	-3.68	-16.59	131.14	-3.95
α = 0.7	276.24	289.74	300.33	-18.01	149.74	-2.04	-16.89	133.47	-2.23
α = 0.8	279.16	293.16	303.74	-17.82	148.16	-3.07	-16.69	131.93	-3.37
α = 0.9	282.56	297.07	307.20	-17.92	148.95	-2.56	-16.78	132.61	-2.86
$E_{a,mean}$					152.86			136.52	
PVC FSF_2	Characteristic temperature, °C			OFW method			KAS method		
Conversion rate	5	10	20	Slope	Ea	Dev%[a]	Slope	Ea	Dev%[a]
α = 0.1	301.50	308.36	317.58	-29.08	241.77	13.11	-27.91	220.61	13.90
α = 0.2	307.32	315.08	325.08	-26.91	223.74	4.67	-25.81	203.99	5.33
α = 0.3	312.11	320.68	330.82	-26.15	217.44	1.73	-24.97	197.30	1.87
α = 0.4	316.42	325.14	335.94	-25.43	211.42	-1.09	-24.23	191.49	-1.13
α = 0.5	321.23	330.69	341.65	-24.79	206.11	-3.57	-23.58	186.37	-3.77
α = 0.6	326.50	335.69	347.33	-24.68	205.16	-4.02	-23.46	185.38	-4.28
α = 0.7	332.31	341.76	353.58	-24.66	205.05	-4.07	-23.43	185.18	-4.39

α = 0.8	340.51	349.53	362.06	-24.89	206.93	-3.19	-23.65	186.91	-3.50
α = 0.9	352.00	361.68	374.53	-24.79	206.12	-3.57	-23.52	185.87	-4.03
$E_{a,mean}$					213.75			193.68	
PVC FSF_3	Characteristic temperature, ^oC			OFW method			KAS method		
Conversion rate	5	10	20	Slope	Ea	Dev%$_a$	Slope	Ea	Dev%$_a$
α = 0.1	410.43	417.56	419.45	-45.30	376.63	22.14	-43.93	347.21	23.31
α = 0.2	425.34	432.48	436.11	-41.48	344.89	11.85	-40.08	316.72	12.48
α = 0.3	435.38	445.22	447.21	-41.09	341.60	10.78	-40.66	321.33	14.11
α = 0.4	442.00	452.77	457.17	-40.98	340.72	10.49	-38.54	304.56	8.16
α = 0.5	448.66	459.83	466.01	-38.40	319.25	3.53	-36.94	291.93	3.67
α = 0.6	455.76	466.91	474.85	-35.16	292.34	-5.19	-34.69	274.14	-2.64
α = 0.7	462.88	474.53	483.75	-31.79	264.29	-14.29	-30.29	239.41	-14.98
α = 0.8	472.32	483.29	493.90	-30.73	255.46	-17.15	-28.22	222.98	-20.81
α = 0.9	484.69	495.29	508.18	-28.87	240.02	-22.16	-27.33	215.99	-23.30
$E_{a,mean}$					308.36			281.59	
PVC+ CaO FSF'_1	Characteristic temperature, ^oC			OFW method			KAS method		
Conversion rate	5	10	20	Slope	Ea	Dev%$_a$	Slope	Ea	Dev%$_a$
α = 0.1	264.10	272.31	283.42	-21.33	177.35	4.45	-20.24	159.94	4.80
α = 0.2	268.74	277.19	288.37	-21.38	177.75	4.68	-20.28	160.23	5.00
α = 0.3	271.11	280.81	292.11	-20.28	168.63	-0.69	-19.17	151.53	-0.71
α = 0.4	273.50	283.05	294.48	-20.47	170.21	0.24	-19.40	153.28	0.44
α = 0.5	275.87	286.07	296.92	-20.61	171.34	0.91	-19.49	154.03	0.93
α = 0.6	277.36	288.28	299.35	-19.87	165.20	-2.71	-18.75	148.17	-2.91

α = 0.7	279.54	290.41	301.64	-19.93	165.71	-2.41	-18.81	148.62	-2.62
α = 0.8	281.69	292.45	303.80	-20.07	166.86	-1.73	-18.94	149.68	-1.92
α = 0.9	284.54	295.64	307.12	-19.87	165.17	-2.73	-18.73	148.02	-3.01
$E_{a,mean}$					169.80			152.61	

PVC+ CaO FSF'$_2$	Characteristic temperature, ^oC			OFW method			KAS method		
Conversion rate	5	10	20	Slope	Ea	Dev%$_a$	Slope	Ea	Dev%$_a$
α = 0.1	288.09	300.56	312.11	-18.93	157.42	-3.07	-17.79	140.58	-3.71
α = 0.2	295.31	308.74	320.08	-18.80	156.34	-3.71	-17.64	139.43	-4.49
α = 0.3	301.19	314.63	325.73	-19.34	160.81	-1.07	-18.17	143.59	-1.64
α = 0.4	307.09	319.93	331.51	-19.88	165.28	1.56	-18.70	147.75	1.20
α = 0.5	312.27	325.92	337.40	-19.64	163.31	0.40	-18.45	145.80	-0.13
α = 0.6	318.93	331.89	344.01	-20.17	167.72	2.99	-18.97	149.88	2.67
α = 0.7	325.59	338.53	351.32	-20.14	167.41	2.81	-19.91	157.37	7.80
α = 0.8	333.69	347.16	360.60	-19.81	164.68	1.20	-18.57	146.73	0.51
α = 0.9	346.98	359.74	375.75	-19.34	160.75	-1.11	-18.07	142.78	-2.20
$E_{a,mean}$					162.63			145.99	

PVC+ CaO FSF'$_3$	Characteristic temperature, ^oC			OFW method			KAS method		
Conversion rate	5	10	20	Slope	Ea	Dev%$_a$	Slope	Ea	Dev%$_a$
α = 0.1	410.55	423.61	428.85	-34.16	284.00	13.26	-32.78	259.02	14.16
α = 0.2	420.92	434.27	441.48	-32.39	269.32	7.41	-30.99	244.89	7.94
α = 0.3	429.06	441.59	450.78	-32.15	267.32	6.61	-30.73	242.84	7.03
α = 0.4	434.97	448.89	458.10	-30.55	254.03	1.31	-29.12	230.10	1.42
α = 0.5	440.88	454.86	465.41	-29.57	245.80	-1.97	-28.11	222.18	-2.07

α = 0.6	446.79	461.50	472.06	-29.12	242.12	-3.44	-27.66	218.58	-3.66
α = 0.7	453.46	468.82	479.36	-28.87	239.98	-4.29	-27.39	216.44	-4.60
α = 0.8	460.86	477.46	488.01	-27.99	232.72	-7.19	-26.50	209.41	-7.70
α = 0.9	470.47	489.43	499.32	-26.63	221.41	-11.70	-25.12	198.50	-12.51
$E_{a,mean}$					250.74			226.88	

[a] Dev% refers to the deviation of the activation energy obtained at a certain conversion rate α to the mean activation energy and is calculated by: Dev% = $(E_{a,I} - E_{a,mean})/ E_{a,mean}$*100%.

Figure 4. 17 and **Figure 4. 18** present the kinetic plots of the pseudo-components from PVC pyrolysis without/with CaO reactant. Correlation coefficients of the linear regression, R^2, are higher than 0.90, and the plotted trend lines at different conversion rates are almost parallel, indicating that the calculation results are reliable [30]. The characteristic temperature at each conversion rate of different pseudo-component, the slope of the regression plots and the estimated activation energy are listed in **Table 4.5**. Accordingly, the Dev% values of the obtained Eα are less than 23.3% at all the conversion rates of each pseudo-components, which means, according to ICTAC Kinetics Committee recommendations, the reaction is mainly governed by a single reaction mechanism and can thus be adequately described by a single-step model [20, 33].

As listed in **Table 4.5**, the average apparent activation energies of the considered pseudo-components for PVC pyrolysis are: FSF_1 (de-HCl), 152.86 and 136.52 kJ/mol; FSF_2 (de-benzene), 213.75 and 193.68 kJ/mol, and FSF_3 (de-polyene and cyclization), 308.36 and 281.59 kJ/mol according to OFW and KAS methods, respectively. The obtained results are quite close for both calculation methods and agree well with previous findings, indicating that the activation energy for the dehyrochlorination reaction of pure PVC in the first stage are in the range of 135 – 190 kJ/mol [34, 35]. When CaO is added, the average apparent activation energies of the considered pseudo-components are: FSF'_1 (de-HCl), 169.80 and 152.61 kJ/mol; FSF'_2 (de-benzene), 162.63 and 145.99 kJ/mol, and FSF'_3 (de-polyene and cyclization), 250.74 and 226.88 kJ/mol according to OFW and KAS methods, respectively. As aforementioned in **Section 4.3**, the addition of CaO inhibited the release of HCl from PVC pyrolysis. The results are in good agreement with the apparent activation energy estimation results; because the average Eα is increased by approximately 12% when CaO is mixed with

PVC during pyrolysis. Conversely, with the addition of CaO, the average E*a* for the pseudo-component reaction related to hydrocarbons decomposition is significantly decreased by around 25% for the 2nd pseudo-component reaction (i.e. formation of aromatic compounds) and by around 19% for the 3rd pseudo-component reaction (further polyene decomposition and cyclization reaction).

4.5 Summary of the chapter

In this chapter, the generation of Cl-content contaminants from both inorganic and organic chlorine source is firstly investigated using both thermodynamic equilibrium simulation and experimental study. Then the effect of in-furnace CaO reactant on HCl mitigation is evaluated. Furthermore, the reaction kinetics of PVC pyrolysis without/with CaO reactant is estimated and the apparent activation energies of the pseudo-components are determined. The purpose of the study is three-folds: (i) to determine the influence of temperature, atmosphere, and the presence of water, inorganic materials on HCl release; (ii) to investigate the effect of temperature, Ca/Cl molar ratio, and CaO reactant particle size on HCl mitigation efficiency; and (iii) to identify the kinetic pyrolytic reaction mechanism of PVC with/without CaO reactant and to estimate the activation energy of the pseudo-component reactions.

The following conclusions have been drawn:

- Both thermodynamic equilibrium simulation and experimental study confirm that less than 1.2% of the total chlorine is converted from NaCl to Cl-content species during pyrolysis within the considered temperature range. The presence of O_2, water, and inorganic materials like SiO_2 are able to promote the conversion of NaCl to Cl-content contaminants. However, under the experimental conditions, the overall conversion rate of Cl-contaminants is less than 8%.
- HCl release from organic source PVC onsets at low temperature of around 200 ^{o}C and ends up at around 400 ^{o}C. HCl is the main products of the first degradation stage for PVC pyrolysis and nearly all the chlorine contained in PVC is discharged as HCl via dehydrochlorination reaction in this stage.
- In-furnace CaO reactant is effective for HCl mitigation during PVC pyrolysis. Higher temperature plays adverse effects on HCl mitigation efficiency. Increasing the Ca/Cl

molar ratio or reducing the particle size significantly enhances HCl mitigation efficiency. At temperature of 750 ^{o}C, HCl mitigation efficiency reaches 85.6% and 83.35% when 40-60 mesh CaO with Ca/Cl molar ratio of 2:1 and 80-120 mesh CaO with Ca/Cl molar ratio of 1:1 are used.

- SEM and EDS analysis confirm that HCl mitigation by CaO reactant is limited by both chemical reaction rate and physical surface properties. At higher temperature, the chemical reaction equilibrium shifts to the back forward direction of dechlorination reactions; meanwhile, calcination and sintering of the reactants significantly reduce the specific surface area and porosity of the reactant, resulting in the reduction of HCl mitigation efficiency at higher temperature.

- The estimated average apparent activation energy of the three pseudo-components for PVC pyrolysis is: FSF_1 (de-HCl), 152.86 and 136.52 kJ/mol; FSF_2 (de-benzene), 213.75 and 193.68 kJ/mol, and FSF_3 (de-polyene and cyclization), 308.36 and 281.59 kJ/mol, by using OFW and KAS calculation method, respectively. The use of CaO reactant increases the apparent activation energy of dehydrochlorination reaction but decreases the average E*a* of hydrocarbon decomposition reactions. The use of CaO decreased the apparent activation energy of the overall PVC decomposition reaction from 197.26 to 148.92 kJ/mol.

4.6 Bibliography

[1] Chlor E. **The Chlorine Industry Review 2016-2017**. 2017.

[2] Wu J-L, Lin T-C, Wang Y-F, Wang J-W, Wang C-T, Kuo Y-M. Polychlorinated dibenzo-p-dioxin and dibenzofuran (PCDD/F) emission behavior during incineration of laboratory waste. Part 1: Emission profiles obtained using chemical assay and bioassay. Aerosol Air Qual Res. 2014;14:1199-205.

[3] Coda B, Aho M, Berger R, Hein KR. Behavior of chlorine and enrichment of risky elements in bubbling fluidized bed combustion of biomass and waste assisted by additives. Energy & Fuels. 2001;15:680-90.

[4] Liu Z, Wang H-q, Zhang X-d, Liu J-w, Zhou Y-y. Dechlorination of organochloride waste mixture by microwave irradiation before forming solid recovered fuel. Waste Management. 2017;62:118-24.

[5] Rahim MU, Gao X, Garcia-Perez M, Li Y, Wu H. Release of chlorine during mallee bark pyrolysis. Energy & Fuels. 2012;27:310-7.

[6] Suntio LR, Shiu WY, Mackay D. A review of the nature and properties of chemicals present in pulp mill effluents. Chemosphere. 1988;17:1249-90.

[7] Jayasiri H, Purushothaman C, Vennila A. Bimonthly variability of persistent organochlorines in plastic pellets from four beaches in Mumbai coast, India. Environmental monitoring and assessment. 2015;187:469.

[8] Sánchez-Jiménez PE, Perejón A, Criado JM, Diánez MJ, Pérez-Maqueda LA. Kinetic model for thermal dehydrochlorination of poly (vinyl chloride). Polymer. 2010;51:3998-4007.

[9] Bahari SA, Grigsby W, Krause A. Thermal stability of processed PVC/bamboo blends: effect of compounding procedures. European Journal of Wood and Wood Products. 2017;75:147-59.

[10] Aljoumaa K, Ajji Z. Thermal and mechanical properties of irradiated poly (vinyl chloride)/calcium carbonate composite. Journal of Radioanalytical and Nuclear Chemistry. 2017;311:15-22.

[11] Soudais Y, Moga L, Blazek J, Lemort F. Coupled DTA–TGA–FT-IR investigation of pyrolytic decomposition of EVA, PVC and cellulose. Journal of Analytical and Applied Pyrolysis. 2007;78:46-57.

[12] Zhu HM, Jiang XG, Yan JH, Chi Y, Cen KF. TG-FTIR analysis of PVC thermal degradation and HCl removal. Journal of Analytical and Applied Pyrolysis. 2008;82:1-9.

[13] Doyle CD. Kinetic analysis of thermogravimetric data. Journal of applied polymer science. 1961;5:285-92.

[14] Sørum L, Grønli M, Hustad J. Pyrolysis characteristics and kinetics of municipal solid wastes. Fuel. 2001;80:1217-27.

[15] Saeed L, Tohka A, Haapala M, Zevenhoven R. Pyrolysis and combustion of PVC, PVC-wood and PVC-coal mixtures in a two-stage fluidized bed process. Fuel Processing Technology. 2004;85:1565-83.

[16] Fontana A, Laurent P, Jung C, Gehrmann J, Beckmann M. Municipal waste pyrolysis (2) chlorine capture by addition of calcium and sodium-based sorbents. Erdoel, Erdgas, Kohle. 2001;117:362-6.

[17] Tan J, Yang G, Mao J, Dai H. Laboratory study on high-temperature adsorption of HCl by dry-injection of Ca (OH) 2 in a dual-layer granular bed filter. Frontiers of Environmental Science & Engineering. 2014;8:863-70.

[18] Shemwell B, Levendis YA, Simons GA. Laboratory study on the high-temperature capture of HCl gas by dry-injection of calcium-based sorbents. Chemosphere. 2001;42:785-96.

[19] Sancho JA, Aznar MP, Toledo JM. Catalytic air gasification of plastic waste (polypropylene) in fluidized bed. Part I: Use of in-gasifier bed additives. Industrial & engineering chemistry research. 2008;47:1005-10.

[20] Ephraim A. Valorization of wood and plastic waste by pyro-gasification and syngas cleaning: Ecole des Mines d'Albi-Carmaux; 2016.

[21] Chen Z, Zhu Q, Wang X, Xiao B, Liu S. Pyrolysis behaviors and kinetic studies on Eucalyptus residues using thermogravimetric analysis. Energy Conversion and Management. 2015;105:251-9.

[22] Kim S. Pyrolysis kinetics of waste PVC pipe. Waste management. 2001;21:609-16.

[23] Vyazovkin S, Chrissafis K, Di Lorenzo ML, Koga N, Pijolat M, Roduit B, et al. ICTAC Kinetics Committee recommendations for collecting experimental thermal analysis data for kinetic computations. Thermochimica Acta. 2014;590:1-23.

[24] Cheng Z, Wu W, Ji P, Zhou X, Liu R, Cai J. Applicability of Fraser–Suzuki function in kinetic analysis of DAEM processes and lignocellulosic biomass pyrolysis processes. Journal of Thermal Analysis and Calorimetry. 2015;119:1429-38.

[25] Hu M, Chen Z, Wang S, Guo D, Ma C, Zhou Y, et al. Thermogravimetric kinetics of lignocellulosic biomass slow pyrolysis using distributed activation energy model, Fraser–Suzuki deconvolution, and iso-conversional method. Energy Conversion and Management. 2016;118:1-11.

[26] Millán LMR, Vargas FES, Nzihou A. Kinetic Analysis of Tropical Lignocellulosic Agrowaste Pyrolysis. BioEnergy Research. 2017;10:832-45.

[27] da Silva JCG, Alves JLF, de Araujo Galdino WV, Andersen SLF, de Sena RF. Pyrolysis kinetic evaluation by single-step for waste wood from reforestation. Waste Management. 2018;72:265-73.

[28] Wang H, Chen Z, Zhang X, Li Z, Fang N, Liu X. Thermal decomposition mechanisms of coal and coal chars under CO2 atmosphere using a distributed activation energy model. Thermochimica Acta. 2018;662:41-6.

[29] Edreis EM, Yao H. Kinetic thermal behaviour and evaluation of physical structure of sugar cane bagasse char during non-isothermal steam gasification. Journal of Materials Research and Technology. 2016;5:317-26.

[30] Lu P, Huang Q, Bourtsalas AT, Chi Y, Yan J. Experimental research of basic properties and reactivity of waste derived chars. Applied Thermal Engineering. 2017;119:639-49.

[31] Vyazovkin S. Evaluation of activation energy of thermally stimulated solid-state reactions under arbitrary variation of temperature. Journal of computational chemistry. 1997;18:393-402.

[32] Coats AW, Redfern J. Kinetic parameters from thermogravimetric data. Nature. 1964;201:68.

[33] Vyazovkin S, Burnham AK, Criado JM, Pérez-Maqueda LA, Popescu C, Sbirrazzuoli N. ICTAC Kinetics Committee recommendations for performing kinetic computations on thermal analysis data. Thermochimica Acta. 2011;520:1-19.

[34] Al-Harahsheh M, Al-Otoom A, Al-Makhadmah L, Hamilton IE, Kingman S, Al-Asheh S, et al. Pyrolysis of poly(vinyl chloride) and—electric arc furnacedust mixtures. Journal of Hazardous Materials. 2015;299:425-36.

[35] Miranda R, Yang J, Roy C, Vasile C. Vacuum pyrolysis of PVC I. Kinetic study. Polymer Degradation and Stability. 1999;64:127-44.

Chapter 5

Influence of CaO reactant on pyrolysis tar upgrading of waste single-component

5.1 Introduction

As it is well-known, tar is a typical by-product of pyro-gasification process, and its composition is very complex [1]. Generally, tar produced during pyro-gasification process causes syngas degradation and has been identified as one of the major impurities [2]. Moreover, the presence of tar also brings a series of problems like clogging and condensation followed by blocking of downstream equipment [3]. Therefore, tar reduction from pyro-gasification process has become one of the most popular topics in recent years [4-6]. Besides been treated as impurities, tar contains a large amount of high value added compounds, like benzene, toluene, and xylene; therefore, the recovery of these chemicals from pyro-gasification tar also attracts worldwide concerns.

Tar reduction can be achieved by using reactants. As presented in **Figure 5.1**, tar cracking and upgrading during pyrolysis can be divided into ex-situ and in-situ methods [7]. The addition of reactant into the furnace is an effective method to reduce the tar contained in the produced gas. Ca-based reactants are well recognized for pyrolytic tar cracking and upgrading [7-9]. Therefore, besides capturing HCl, the use of in-furnace CaO reactant is believed a promising method to accelerate the decomposition and upgrading of tar compounds during MSW pyrolysis.

Py-GC/MS is widely used as an analytical tool to determine the composition of pyrolytic tar due to its rapidity, high sensitivity, and effective separation ability of complex mixture of tar compounds [10-13]. Therefore, in this chapter, the role of CaO reactant and the effect of

temperature on pyrolytic tar cracking and composition are experimentally investigated using Py-GC/MS apparatus. Pyrolytic tar from typical MSW single components, such as food waste (occupies the largest proportions in many countries and regions), wood biomass (represents typical biomass waste), and PVC (represents plastic) are identified.

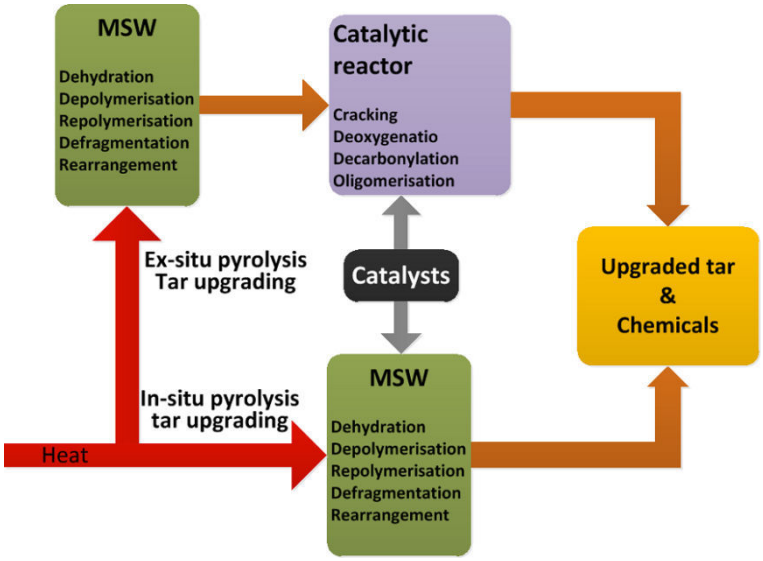

Figure 5. 1 Schematic diagram of in-situ and ex-situ of tar cracking during MSW pyrolysis, data source from Kabir et al. [7]

Accordingly, the structure of this chapter is presented as follows:

I. **Section 5.2** is focusing on the role of CaO reactant on pyrolytic tar cracking and upgrading from wood biomass, food waste and PVC pyrolysis. Pyrolysis experiments are conducted on Py-GC/MS apparatus with/without the use of CaO reactant, and pyrolytic tar composition are identified;

II. **Section 5.3** investigates the role of CaO reactant and the effect of pyrolytic temperature on PVC pyrolytic tar composition. Py-GC/MS experiments are conducted at temperature of 550, 650, 750, and 850 ^{o}C and with/without CaO addition;

III. **Section 5.4** summarizes the findings of this chapter.

5.2 Effect of CaO reactant on pyrolysis tar composition from waste single component

MSW single components pyrolysis without/with CaO reactant are conducted and investigated in this section using Py-GC/MS experimental apparatus. Pyrolytic tar compositions from experiments are identified by matching the mass spectrum with standard compounds in NIST 11 database. The relative content of each identified compound is normalized to Peak area%, which is determined by area normalizations. The relative content of a specific compound refers to the peak area of the component to the total peak area of all detected species. The calculation method of the Peak area % is described as follows:

$$Peak\ area\ \% = \frac{Peak\ area\ of\ the\ target\ compound}{Total\ peak\ area\ of\ all\ detected\ species} \times 100\% \quad (5.1)$$

5.2.1 Effect of CaO reactant on tar formation from wood biomass

Wood biomass pyrolysis at temperature of 750 ^{o}C are firstly investigated using Py-GC/MS with/without CaO reactant addition. Due to the principle of Py-GC/MS experimental set-up, only volatile organic compounds are able to be identified. Based on the gas chromatogram, **Figure 5.2** and **Figure 5.3** present the identification results of pyrolytic tar composition from wood biomass at 750 ^{o}C with/without the addition of CaO reactant. A total of 39 and 40 compounds are identified from pyrolytic tar without CaO and with CaO, respectively. However, in order to simplify the presentation of the results, the most typical compounds as suggested by the gas chromatogram (the most obvious peaks) are presented in the Figures. The selected compounds represent more than 70% of the total peak area.

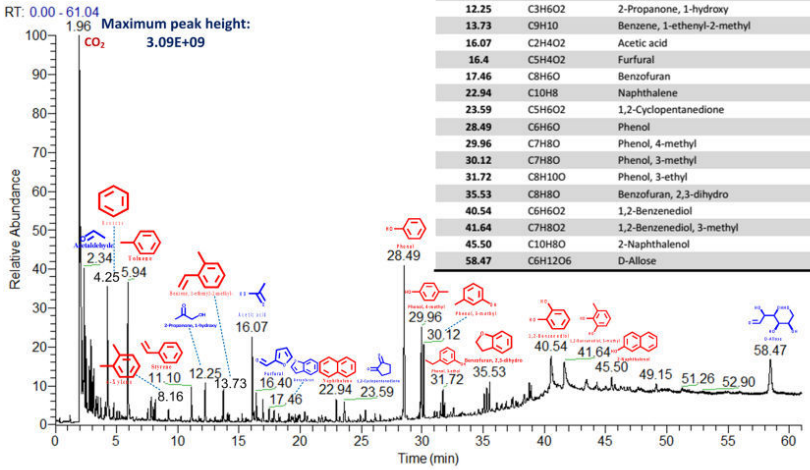

Resistance Time	Formula	Substance Name	Peak Area %
2.34	C2H4O	Acetaldehyde	6.65
4.25	C6H6	Benzene	5.61
5.94	C7H8	Toluene	6.38
8.16	C8H10	o-Xylene	0.95
11.10	C8H8	Styrene	1.84
12.25	C3H6O2	2-Propanone, 1-hydroxy	2.05
13.73	C9H10	Benzene, 1-ethenyl-2-methyl	1.86
16.07	C2H4O2	Acetic acid	5.46
16.4	C5H4O2	Furfural	1.52
17.46	C8H6O	Benzofuran	0.90
22.94	C10H8	Naphthalene	1.52
23.59	C5H6O2	1,2-Cyclopentanedione	1.60
28.49	C6H6O	Phenol	10.98
29.96	C7H8O	Phenol, 4-methyl	5.94
30.12	C7H8O	Phenol, 3-methyl	4.18
31.72	C8H10O	Phenol, 3-ethyl	1.56
35.53	C8H8O	Benzofuran, 2,3-dihydro	1.64
40.54	C6H6O2	1,2-Benzenediol	3.23
41.64	C7H8O2	1,2-Benzenediol, 3-methyl	3.20
45.50	C10H8O	2-Naphthalenol	1.28
58.47	C6H12O6	D-Allose	3.71

Figure 5. 2 Identified tar composition from wood biomass pyrolysis at 750 °C in the absence of CaO reactant

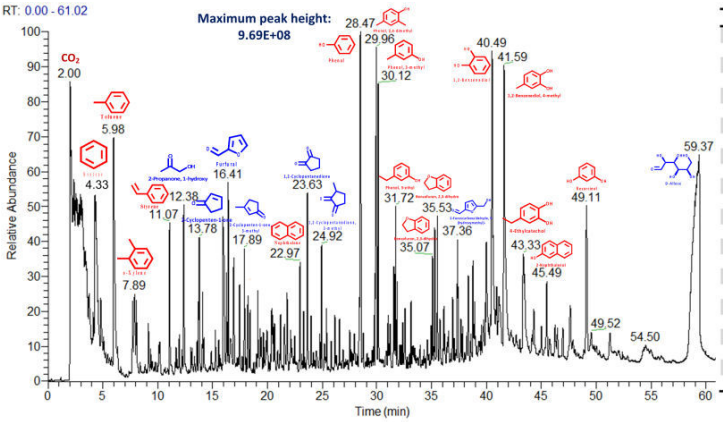

Resistance Time	Formula	Substance Name	Peak Area %
4.33	C6H6	Benzene	4.31
5.98	C7H8	Toluene	7.92
7.89	C8H10	o-Xylene	2.95
11.07	C8H8	Styrene	2.17
12.38	C3H6O2	2-Propanone, 1-hydroxy	2.17
13.78	C5H6O	2-Cyclopenten-1-one	1.97
16.41	C5H4O2	Furfural	2.59
17.89	C6H8O	2-Cyclopenten-1-one, 3-methyl	1.71
22.97	C10H8	Naphthalene	3.57
23.63	C5H6O2	1,2-Cyclopentanedione	2.31
24.92	C6H8O2	1,2-Cyclopentanedione, 3-methyl	1.80
28.47	C6H6O	Phenol	4.68
29.96	C8H10O	Phenol, 2,4-dimethyl	2.26
30.12	C7H8O	Phenol, 3-methyl	1.95
31.72	C8H10O	Phenol, 3-ethyl	1.55
35.07	C8H8O	Benzofuran, 2,3-dihydro	1.40
35.53	C8H8O	Benzofuran, 2,3-dihydro	1.90
37.36	C6H6O3	2-Furancarboxaldehyde, 5-(hydroxymethyl)-	2.35
40.48	C6H6O2	1,2-Benzenediol	3.91
41.58	C7H8O2	1,2-Benzenediol, 4-methyl	3.56
43.33	C8H10O2	4-Ethylcatechol	3.21
45.49	C10H8O	2-Naphthalenol	2.46
49.11	C6H6O2	Resorcinol	2.62
59.37	C6H12O6	D-Allose	6.74

Figure 5. 3 Identified tar composition from wood biomass pyrolysis at 750 °C with the addition of CaO reactant

Results from Py-GC/MS experiments reveal that most of the pyrolytic tar components are unaltered under experiments with/without CaO reactant. Or, in other words, the use of CaO reactant only changes the relative content of most species in pyrolytic tar. As depicted in **Figure 5.2** and **Figure 5.3**, 15 out of the 21 components contained in non-catalytic wood biomass pyrolytic tar are also identified in tar derived from catalytic pyrolysis. And only 7

new compounds are formed after CaO catalysis. However, the obtained results are to some extent in contrast to the observations concluded by Lu et al.[8], stating that the addition of CaO reactant significantly reduces or completely eliminate most of the primary tar composition and promote the formation of many new products. The properties of CaO reactant, feedstock, and operational conditions may be responsible for the difference.

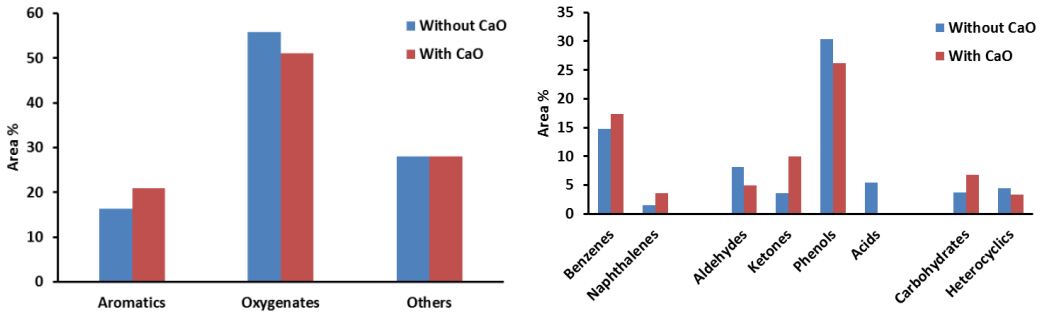

Figure 5. 4 Composition of pyrolytic tar derived from wood biomass pyrolysis at 750 °C without/with the addition of CaO reactant (others here represent the detected compounds which are not presented in Figure 5.1 and Figure 5.2)

In order to reflect the change of the pyrolytic tar composition with/without CaO reactant, the identified tar compositions are classified into 8 groups: benzenes (i.e. benzene series), naphthalenes (i.e. naphthalene-content compounds), aldehydes, ketones, phenols, acid compounds, carbohydrates, and heterocyclics compounds. The results are exhibited in **Figure 5.4**. Generally, the addition of CaO reactant promotes the formation of aromatic compounds by approximately 28.4%, and reduces the content of oxygenated compounds by 8.3%. It is believed that the presence of oxygenated compounds degrades significantly the quality of pyrolytic tar, resulting in adverse effects such as reducing the lower heating value, promoting non-volatility, high acidity, corrosiveness and aging during transportation, storage and application [14, 15]. Therefore, deoxygenation is of great importance for pyrolytic tar quality upgrading and obviously, CaO can serve as deoxygenation reactant during biomass pyrolysis.

With respect to the classified groups, pyrolytic tar compounds contain mainly benzenes (accounting for 14.8% and 17.3% for non-catalytic and catalytic pyrolysis conditions, respectively) and phenols (accounting for 30.4% and 26.2% for non-catalytic and catalytic cases). The addition of CaO increases the relative content of benzenes, naphthalenes, ketones, and carbohydrates by around 17.5%, 134.5%, 173.2%, and 81.4%, respectively.

Although the relative content of naphthalenes and ketones are dramatically enhanced (by more than 2.5 times), their relative content is quite low and in the ranges of 1.5% - 3.6% and 3.6% - 10.0%, respectively. The results are in good accordance with previous findings. Zhu et al. [16] found that the relative content of naphthalene and substituted naphthalenes are increased with the presence of CaO reactant. Lu et al. [8] stated that the use of CaO increases the relative content of ketones from 3.8% to 20.9%.

On the contrary, the relative contents of aldehydes, phenols, acid compounds, and heterocyclics compounds are decreased by 39.6%, 13.7%, 100.0%, and 24.9%, respectively. It is notable that the abovementioned four components are containing oxygen; therefore, the overall oxygenated compounds content is declined by adding CaO reactant. Among the oxygenated compounds, the addition of CaO reactant achieved elimination of acid compounds contained in wood biomass pyrolytic tar. It is quite logical, as it is obvious that CaO reactant is a typical alkaline earth metal oxide reactant and is effective to reduce acid compounds in pyrolytic tar by decarboxylation and decarbonylation reactions according to Kabir et al. [7]. Similar findings are reported by literature revealing that the pyrolytic tar is de-acidified by using CaO reactant [17].

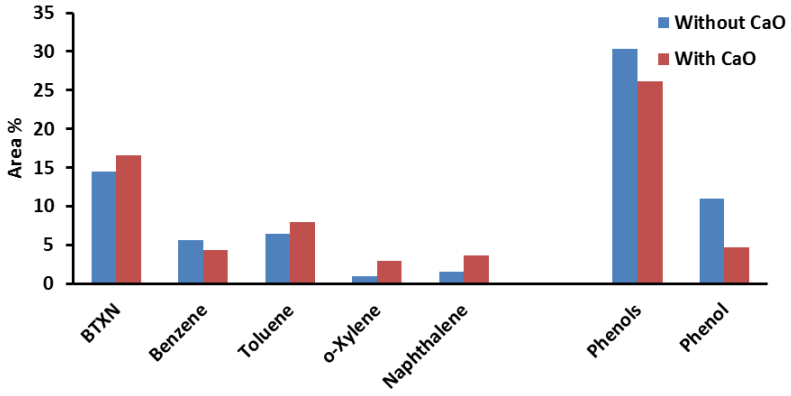

Figure 5. 5 The relative content of BTXN and Phenols in pyrolytic tar derived from wood biomass pyrolysis at 750 ^{o}C without/with CaO reactant

As aforementioned in **Section 5.1**, pyrolytic tars contain a variety of high value added chemicals, mainly light aromatic hydrocarbons such as benzene, toluene, xylene and naphthalene (BTXN) [18, 19]. It can further be extracted from pyrolytic tar and applied as fuel additives, solvents, and as raw material to produce pesticides, plastics, and fibers [20].

Figure 5.5 presents the effect of CaO reactant on the relative content of BTXN and phenols in pyrolytic tar from wood biomass pyrolysis at 750 °C. As depicted, the addition of CaO reactant promotes the total yields of BTXN by 14.9%. Among the BTXN, the relative content of toluene, xylene and naphthalene is increased by 24.3%, 211.8%, and 134.5%, respectively, when CaO reactant is used; in contrast, benzene yield is declined by 23.1% as a result of CaO addition. The results agree well with previous conclusions indicating that the use of CaO reactant promoted the formation of aromatic compounds but had a different effect on BTXN; positive effects on toluene, xylene, and naphthalene formation are reported and the influence of which was not obvious on the formation of benzene [21]. As for the catalytic influence on phenols, the relative content of total phenol and substituted phenols are slightly decreased from 30.4% to 26.2% of pyrolytic tar from wood biomass; meanwhile, the relative content of phenol is dramatically reduced by around 57.4% with the presence of CaO reactant. **Figure 5.6** shows a typical reaction pathway for decarboxylation and decarbonylation of pyrolytic tar from complex heavy compounds to light aromatic compounds over CaO reactant [7].

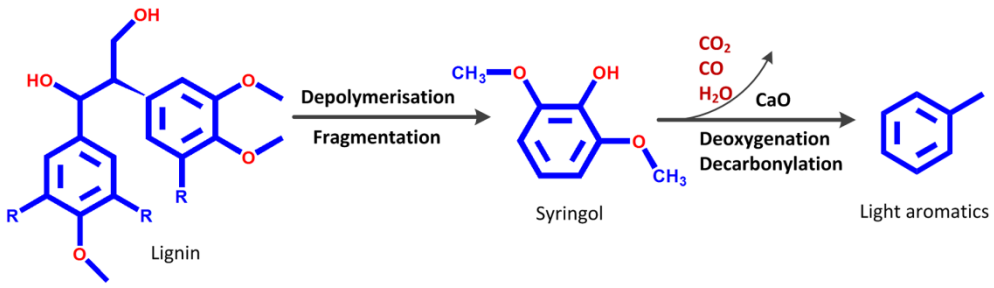

Figure 5. 6 Representative lignin pyrolysis, decarboxylation and decarbonylation of pyrolytic tar over CaO reactant

5.2.2 Effect of CaO reactant on tar formation from food waste

Typical pyrolytic tar compositions derived from food waste pyrolysis at 750 °C with/without CaO reactant are detailed in **Table 5.1**. As illustrated, a total of 27 and 35 compounds are identified without CaO and with CaO, respectively. For food waste pyrolytic tar, the addition of CaO generates more new compounds as compared with that derived from wood biomass. Although 17 out of the total 27 detected species of pyrolytic tar without reactant are also found in tar from catalytic pyrolysis, 18 new compounds are formed due to the addition of CaO reactant. As aforementioned, the results are in good accordance with the findings presented by Lu et al.[8].

Table 5. 1 Identified tar compositions and their relative contents from Py-GC/MS experiments of food waste at 750 °C with or without CaO reactant

Time (min)	Pyrolytic tar from food waste without CaO			Pyrolytic tar from food waste with CaO		
	Formula	Species	Area%	Formula	Species	Area %
2.05	*	*	*	C5H6	1,3-Cyclopentadiene	7.30
2.28	C5H11N	Pent-4-enylamine	3.81	*	*	*
2.35	C5H8	1,4-Pentadiene	2.43	*	*	*
2.42	C2H4O	Acetaldehyde	9.83	*	*	*
2.58	C5H6	1,3-Cyclopentadiene	4.91	C3H6O	Trimethylene oxide	2.03
2.81	*	*	*	C6H8O2	2-Hexynoic acid	1.41
2.85	C4H4O	Furan	5.84	C3H6O	Acetone	8.59
2.99	C3H6O	Acetone	6.29	C6H8	1,3-Cyclopentadiene, 5-methyl	1.76
3.08	*	*	*	C6H8	1,3-Cyclopentadiene, 5-methyl	2.01
3.17	*	*	*	C3H4O	2-Propenal	1.88
3.23	C3H4O	2-Propenal	3.61	C4H8O	2-Butanone	4.80
3.45	C5H6O	Furan, 3-methyl	2.99	*	*	*
3.55	C4H6O	Methacrolein	2.39	*	*	*
3.77	C4H8O	2-Butanone	1.81	C6H6	Benzene	5.41
4.30	C6H6	Benzene	3.74	C4H6O	Methyl vinyl ketone	1.89
4.37	C4H6O	Methyl vinyl ketone	3.65	C5H10O	2-Pentanone	3.26
4.47	C6H8O	Furan, 2,5-dimethyl	1.76	*	*	*
4.82	C4H6O2	2,3-Butanedione	2.41	C3H3N	2-Propenenitrile	1.56
5.06	*	*	*	C2H3N	Acetonitrile	3.87
5.27	C7H8	Toluene	2.43	C7H8	Toluene	8.41
5.98	C2H3N	Acetonitrile	7.48	C8H10	Ethylbenzene	2.98
7.86	C8H10	Ethylbenzene	2.34	C8H10	o-Xylene	1.60
8.16	*	*	*	C5H8O	Cyclopentanone	1.87
9.31	*	*	*	C8H8	Styrene	2.04
11.11	*	*	*	C3H6O2	2-Propanone, 1-hydroxy	3.60
12.27	C3H6O2	2-Propanone, 1-hydroxy	4.14	C5H6O	2-Cyclopenten-1-one	3.12
13.74	C5H6O	2-Cyclopenten-1-one	2.71	C6H8O	2-Cyclopenten-1-one, 2-methyl	2.00
14.09	*	*	*	C2H4O2	Acetic acid	2.33
16.10	C2H4O2	Acetic acid	3.78	C5H4O2	Furfural	1.80
16.42	C5H4O2	3-Furaldehyde	3.97	C9H8	Indene	1.53

16.95	*	*	*	C4H5N	Pyrrole	3.13
17.73	C4H5N	Pyrrole	2.35	C6H8O	2-Cyclopenten-1-one, 3-methyl	1.99
17.89	*	*	*	C7H10O	2-Cyclopenten-1-one, 2,3-dimethyl	1.97
18.41	*	*	*	C4H6O2	Butyrolactone	1.90
19.11	C6H6O2	2-Furancarboxaldehyde, 5-methyl	4.32	*	*	*
20.44	*	*	*	C5H6O2	2-Furanmethanol	1.48
21.19	*	*	*	C2H5NO	Acetamide	1.28
23.61	C5H6O2	1,2-Cyclopentanedione	2.41	C5H6N2	3-Aminopyridine	1.37
25.31	*	*	*	C6H6O	Phenol	4.19
28.51	C6H6O	Phenol	3.92	C7H8O	Phenol, 4-methyl-	2.36
29.99	C7H8O	Phenol, 4-methyl-	1.74	C7H8O	Phenol, 4-methyl-	1.33
37.37	C6H6O3	2-Furancarboxaldehyde, 5-(hydroxymethyl)-	2.93	*	*	*

* means not detected.

To better reflect the effect of CaO reactant on pyrolytic tar compositions, the detected components are classified into 10 groups as olefins, nitriles, amines, benzenes, furans, aldehydes, ketones, phenols, acid compounds, and others (refers to nitrogen-content heterocyclics and oxides in this section). The distributions of the detected species are exhibited in **Figure 5.7**. As presented, oxygenated compounds are the dominant species contained in pyrolytic tar, accounting to 70.5% and 55.1% under non-catalytic and catalytic conditions, followed by aromatic compounds (8.5% and 23.9%, respectively) and hydrocarbons (7.3% and 11.1%, respectively). The role of CaO reactant is obvious on oxygen-content compounds elimination and aromatic compounds promotion. By adding CaO reactant, the relative content of oxygenated compounds is decreased by 21.9%; in contrast, hydrocarbon and aromatic compounds yield are enhanced by 50.7% and 181.1%, respectively. The results are quite similar to that obtained from wood biomass pyrolysis. It is also worth noting that a certain amount of nitrogen-content compounds are produced from food waste pyrolysis, mainly C_2H_3N (acetonitrile), C_3H_3N (2-propenenitrile), C_4H_5N (pyrrole), and C_5H_6N2 (3-aminopyridine). The reason may be attributed to the relative high content of fuel-nitrogen in food waste. As presented in **Chapter 2**, **Table 2.1**, nitrogen content in food waste reaches 1.99 wt.%, approximately 7 times higher than nitrogen content in wood waste.

In regard to the classified groups, the content of aldehydes takes the highest proportion for pyrolysis in the absence of CaO, followed by ketones, furans, benzenes, nitriles, olefins, phenols and so on. However, with the addition of CaO, the relative content of ketones increased to 33.1%, ranking the first of all the groups, followed by benzenes, olefins, phenols, and so on. Accordingly, the addition of CaO reactant increases the relative content of olefins by 50.7%, benzenes by 181.1%, ketones by 41.3%, phenols by 39.1%, but reduces the content of aldehydes by 86.4%, furans by 86.0%, amines by 66.3%, nitriles by 27.4%. The relative content of acid compounds is quite stable at 3.8% and 3.7% under non-catalytic and catalytic conditions. The variation of the pyrolytic group compounds agree well with the results obtained from wood biomass pyrolysis, except for phenols. The relative content of phenols decreased during wood pyrolysis, but has been promoted during food waste pyrolysis when CaO reactant is used. However, the overall deoxygenation (i.e. reduction of the relative content of oxygenated compounds) of CaO reactant is achieved for both MSW components.

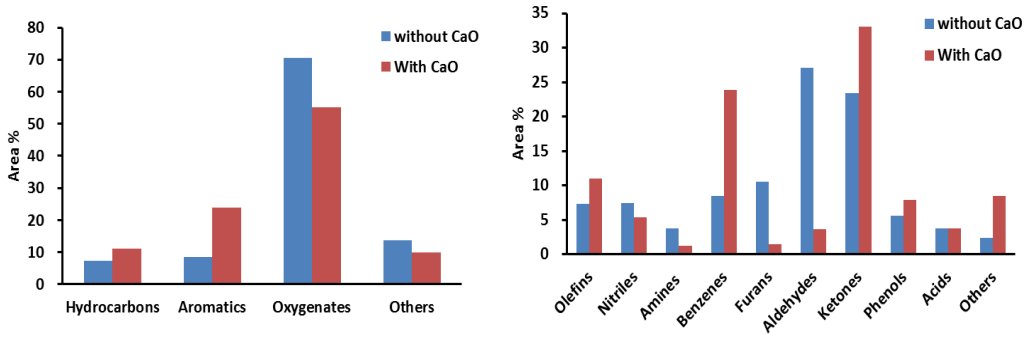

(a) (b)

Figure 5. 7 Composition of pyrolytic tar derived from food waste pyrolysis at 750 ^{o}C without/with the addition of CaO reactant (others represent mainly nitrogen-content compounds)

Figure 5.8 illustrates the effect of CaO reactant on the relative content of BTX, phenols, and ketones in pyrolytic tar from food waste at 750 ^{o}C. As presented, the content of BTX, phenols, and ketones are increased by 181.4%, 39.1%, and 41.3%, respectively, with the presence of CaO reactant. Among BTXs, toluene and o-xylene yields are dramatically enhanced from 2.4 to 8.4% and form 0% to 3.6% by adding CaO reactant. Phenol yield is slightly increased by 6.9%.

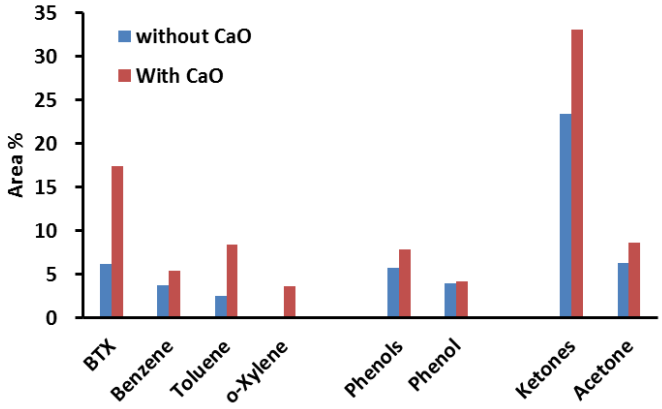

Figure 5. 8 The relative content of BTX, phenols, and ketones in pyrolytic tar derived from food waste pyrolysis at 750 °C without/with CaO reactant

5.2.3 Effect of CaO reactant on tar formation from PVC

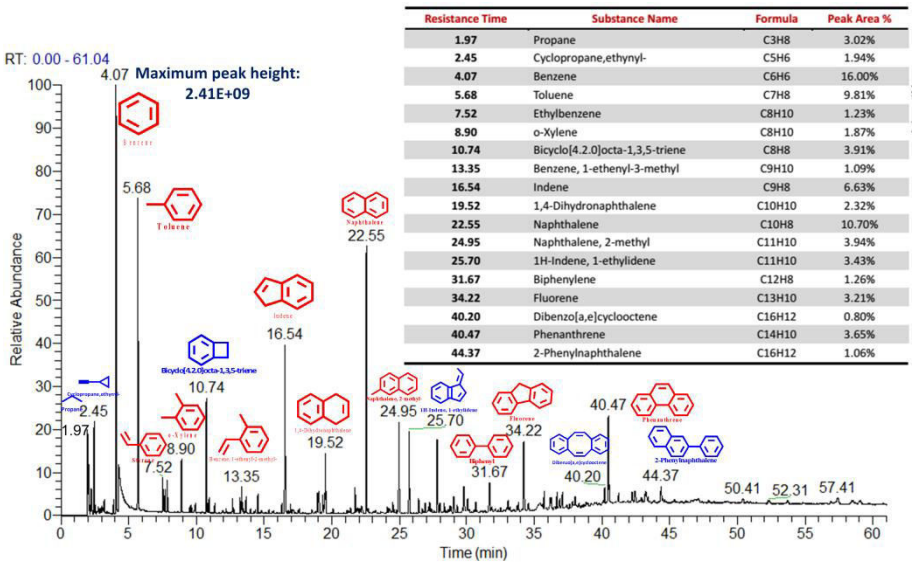

Resistance Time	Substance Name	Formula	Peak Area %
1.97	Propane	C3H8	3.02%
2.45	Cyclopropane,ethynyl-	C5H6	1.94%
4.07	Benzene	C6H6	16.00%
5.68	Toluene	C7H8	9.81%
7.52	Ethylbenzene	C8H10	1.23%
8.90	o-Xylene	C8H10	1.87%
10.74	Bicyclo[4.2.0]octa-1,3,5-triene	C8H8	3.91%
13.35	Benzene, 1-ethenyl-3-methyl	C9H10	1.09%
16.54	Indene	C9H8	6.63%
19.52	1,4-Dihydronaphthalene	C10H10	2.32%
22.55	Naphthalene	C10H8	10.70%
24.95	Naphthalene, 2-methyl	C11H10	3.94%
25.70	1H-Indene, 1-ethylidene	C11H10	3.43%
31.67	Biphenylene	C12H8	1.26%
34.22	Fluorene	C13H10	3.21%
40.20	Dibenzo[a,e]cyclooctene	C16H12	0.80%
40.47	Phenanthrene	C14H10	3.65%
44.37	2-Phenylnaphthalene	C16H12	1.06%

Figure 5. 9 Identified tar composition from PVC pyrolysis at 750 °C in the absence of CaO reactant

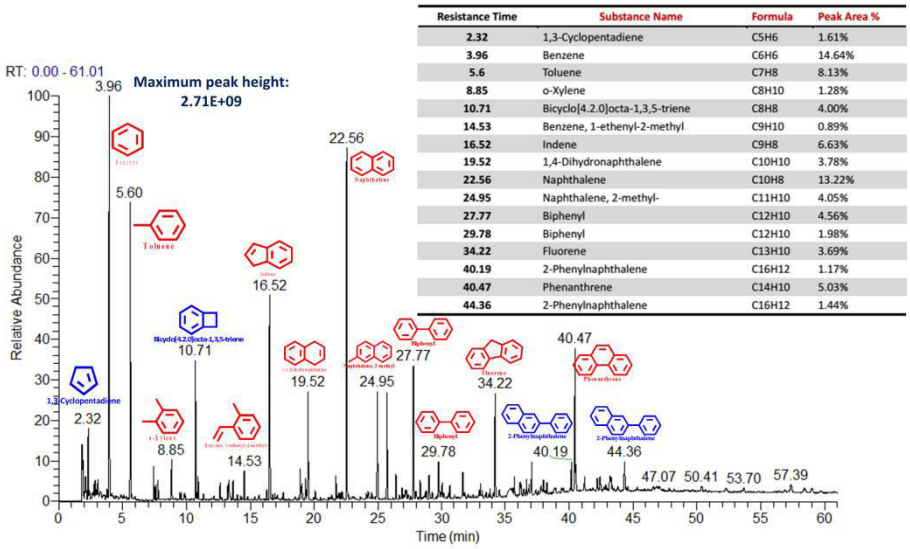

Resistance Time	Substance Name	Formula	Peak Area %
2.32	1,3-Cyclopentadiene	C5H6	1.61%
3.96	Benzene	C6H6	14.64%
5.6	Toluene	C7H8	8.13%
8.85	o-Xylene	C8H10	1.28%
10.71	Bicyclo[4.2.0]octa-1,3,5-triene	C8H8	4.00%
14.53	Benzene, 1-ethenyl-2-methyl	C9H10	0.89%
16.52	Indene	C9H8	6.63%
19.52	1,4-Dihydronaphthalene	C10H10	3.78%
22.56	Naphthalene	C10H8	13.22%
24.95	Naphthalene, 2-methyl-	C11H10	4.05%
27.77	Biphenyl	C12H10	4.56%
29.78	Biphenyl	C12H10	1.98%
34.22	Fluorene	C13H10	3.69%
40.19	2-Phenylnaphthalene	C16H12	1.17%
40.47	Phenanthrene	C14H10	5.03%
44.36	2-Phenylnaphthalene	C16H12	1.44%

Figure 5. 10 Identified tar composition from PVC pyrolysis at 750 °C with the addition of CaO reactant

PVC pyrolysis at temperature of 750 °C is also conducted without/with the addition of CaO reactant on Py-GC/MS apparatus. **Figure 5.9** and **Figure 5.10** exhibit the typical pyrolytic tar compositions. Detailed identification results are listed in **Table 5.2**. As illustrated, most of the detected compounds are aromatic compounds, and their relative content accounts for 89.5% and 93.5% of the total detected tar species from non-catalytic and catalytic pyrolysis experiments, respectively. This is mainly due to the molecular structure and the corresponding dehydrochlorination mechanism of PVC as presented in **Figure 5.11** [22]. Results from **Chapter 4.2.2** reveal that the first decomposition stage of PVC produces a large amount of HCl, leading to the formation of abundant conjugated double bond. Meanwhile, TG-FTIR experiments confirmed that dehydrochlorination of PVC is always accompanied with the formation of aromatic compounds, mainly benzenes, and the further increase of temperature will result in the acceleration of carbon chain decomposition and hydrocarbons cycloaromatization. Therefore, aromatic compounds are the dominant products during PVC pyrolysis. Different from the previous situations, no oxygenated compounds are formed from pyrolytic tar of PVC pyrolysis without CaO reactant; however, when CaO is added, a small amount of oxygen-content species are generated. It is mainly due to the fact that no oxygen is available in PVC as reported in **Table 2.1**; however, when CaO is added, oxygen is also fed into the system and a small amount of oxygenated compounds (CO_2, 2.45% and 2-Hexynoic acid, 0.99%) is produced.

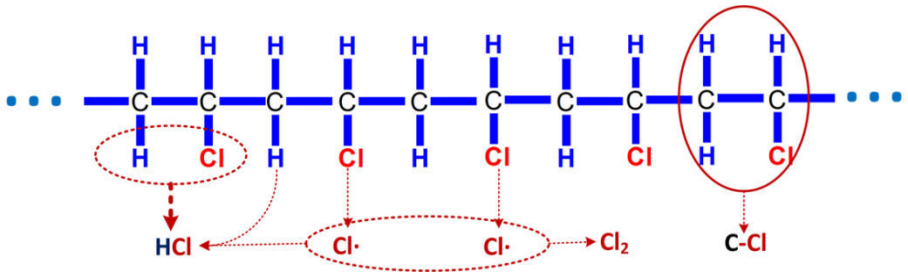

Figure 5. 11 Chlorine-content compounds formation from PVC pyrolysis, data derived from Ruizhi ZHANG [22]

Table 5. 2 Identified tar compositions and their relative contents from Py-GC/MS experiments of PVC at 750 °C with or without CaO reactant

Pyrolytic tar compounds from PVC without CaO				Pyrolytic tar compounds from PVC withCaO			
Time (min)	Formula	Species	Area %	Time (min)	Formula	Species	Area %
1.97	C3H8	Propane	3.02	1.84	CO2	Carbon dioxide	2.45
2.04	C4H6	Methylene-cyclopropane	1.52	1.97	C4H6	Methylene-cyclopropane	1.06
2.24	C5H8	1,3-Pentadiene	0.84	2.11	C6H8O2	2-Hexynoic acid	0.99
2.45	C5H6	Cyclopropane, ethynyl-	1.94	2.32	C5H6	1,3-Cyclopentadiene	1.61
4.07	C6H6	Benzene	16.00	3.08	C6H8	1,3-Cyclopentadiene, 5-methyl-	0.65
4.26	HCl	Hydrogen chloride	3.18	3.96	C6H6	Benzene	14.64
5.68	C7H8	Toluene	9.81	5.6	C7H8	Toluene	8.13
7.52	C8H10	Ethylbenzene	1.23	7.44	C8H10	Ethylbenzene	1.01
7.7	C8H10	o-Xylene	0.71	7.78	C8H10	o-Xylene	0.61
7.85	C8H10	p-Xylene	1.07	8.85	C8H10	o-Xylene	1.28
8.9	C8H10	o-Xylene	1.87	10.71	C8H8	Bicyclo[4.2.0]octa-1,3,5-triene	4.00
10.74	C8H8	Bicyclo[4.2.0] octa-1,3,5-triene	3.91	10.92	C9H10	Benzene, cyclopropyl-	0.66
13.35	C9H10	Benzene, 1-ethenyl-3-met	1.09	13.33	C9H10	Benzene, cyclopropyl-	0.89

		hyl					
14.54	C9H10	Bicyclo[4.2.0]octa-1,3,5-triene, 7-methyl	0.69	13.66	C9H10	Indane	0.62
16.54	C9H8	Indene	6.63	14.53	C9H10	Benzene, 1-ethenyl-2-methyl	0.89
18.92	C10H10	2-Methylindene	0.88	16.52	C9H8	Indene	6.63
19.04	C10H10	Naphthalene, 1,4-dihydro-	1.33	18.91	C10H10	Naphthalene, 1,4-dihydro-	1.09
19.33	C10H10	2-Methylindene	0.73	19.04	C10H10	Naphthalene, 1,2-dihydro-	0.78
19.45	C10H10	Naphthalene, 1,4-dihydro-	0.67	19.31	C10H10	Naphthalene, 1,4-dihydro-	0.68
19.52	C10H10	Naphthalene, 1,4-dihydro-	2.32	19.52	C10H10	Naphthalene, 1,4-dihydro-	3.78
21.71	C10H8	Azulene	1.04	21.7	C10H8	Naphthalene	0.81
22.55	C10H8	Naphthalene	10.70	22.56	C10H8	Naphthalene	13.22
24.95	C11H10	Naphthalene, 2-methyl	3.94	24.95	C11H10	Naphthalene, 2-methyl-	4.05
25.7	C11H10	1H-Indene, 1-ethylidene	3.43	25.7	C11H10	Naphthalene, 2-methyl-	3.51
26.4	C13H12	Naphthalene, 1-(2-propenyl)-	0.70	26.4	C13H12	1,1'-Biphenyl, 4-methyl-	0.90
27.77	C12H10	Biphenyl	3.12	27.77	C12H10	Biphenyl	4.56
29.02	C12H10	Acenaphthene	0.73	28.28	C13H12	1,1'-Biphenyl, 4-methyl-	0.63
29.79	C12H10	Biphenyl	1.75	29.01	C12H10	Acenaphthene	0.87
31.67	C12H8	Biphenylene	1.26	29.78	C12H10	Biphenyl	1.98
34.22	C13H10	Fluorene	3.21	31.67	C12H8	Biphenylene	0.90
35.73	C13H10	Fluorene	0.75	34.22	C13H10	Fluorene	3.69
36.15	C14H12	9H-Fluorene, 3-methyl	0.72	35.44	C13H10	Fluorene	0.84
36.68	C14H12	9H-Fluorene, 3-methyl	0.70	35.72	C13H10	Fluorene	0.67
37.08	C14H12	(E)-Stilbene	0.82	37.08	C14H12	Anthracene, 9,10-dihydro-	1.20

40.2	C16H12	Dibenzo[a,e] cyclooctene	0.80	40.19	C16H12	2-Phenyl naphthalene	1.17
40.47	C14H10	Phenanthrene	3.65	40.47	C14H10	Phenanthrene	5.03
40.55	C14H10	Phenanthrene	0.71	40.55	C14H10	Phenanthrene	0.76
42.21	C15H12	Phenanthrene, 2-methyl	0.67	42.42	C15H12	Anthracene, 1-methyl-	0.72
42.43	C15H12	Anthracene, 1-methyl	0.81	43.19	C15H12	Anthracene, 1-methyl-	0.61
44.37	C16H12	2-Phenyl naphthalene	1.06	44.36	C16H12	2-Phenyl naphthalene	1.44

Distributions of pyrolytic tar compositions as a function of carbon atom numbers are presented in **Figure 5. 12**. As revealed, the majority of the detected compounds belongs to C6 – C10 compounds, sharing approximately 61% of the total peak area form both non-catalytic and catalytic cases. The addition of CaO reactant slightly increases the heavy compounds and lowers the relative content of C1 – C5 by 30.2%. As aforementioned in **Chapter 4**, PVC is the most important organic chlorine source and the degradation of PVC is always accompanied with the release of HCl. Actually in this experiment, HCl release is recorded from non-catalytic experiment with a relative content of 3.18%. However, with the addition of CaO reactant, HCl is eliminated from the vapors. The results further confirm the role of CaO reactant on HCl gas removal.

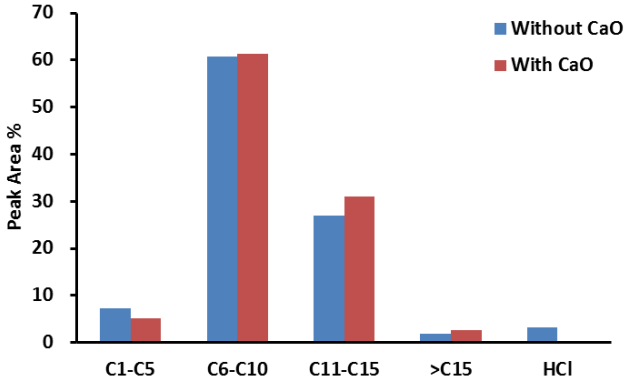

Figure 5. 12 Distributions of detected species of pyrolytic tar derived from PVC pyrolysis at 750 °C as a function of carbon atom numbers

In regard to the specific compounds, **Figure 5.13** presents the relative content of typical aromatic compounds detected from pyrolytic tar of PVC at 750 ^{o}C without/with CaO reactant. Results reveal that the content of the majority of aromatic compounds are declined due to the use of CaO reactant, except for naphthalenes, biphenyls, and phenanthrenes. The addition of CaO facilitates the decomposition of aromatic compounds. According to the literature, the active sites on CaO surface can significantly influence the π-electron cloud's stability of aromatic tar compounds due to its polarity features, thus ruptures the ring structures of aromatic compounds to light hydrocarbons. However, the results obtained from wood biomass and food waste pyrolytic tar reveal the opposite conclusions, indicating that the use of CaO promotes the formation of aromatic compounds. The reason may be attributed to two folds: on the one hand, as aforementioned in **Section 5.2.1**, only volatile organic compounds are able to be detected from Py-GC/MS experiments; therefore, the decomposition of heavy aromatic compounds (for example compounds containing 4 or more aromatic rings) is not taken into account; on the other hand, cycloaromatization reactions of aliphatic hydrocarbons occur in wood and food waste pyrolytic tar with CaO addition, which in turn accelerates the formation of aromatic compounds.

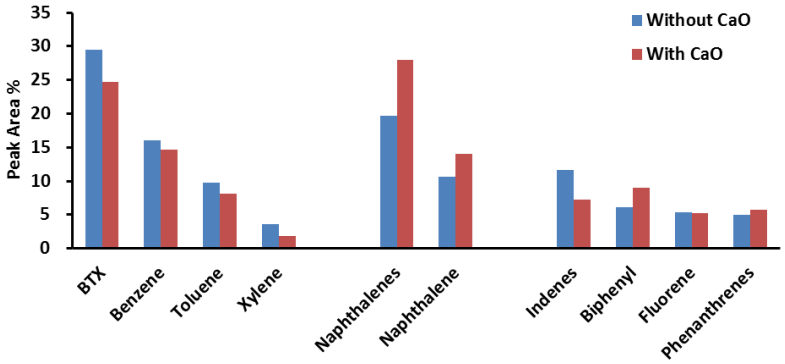

Figure 5. 13 The relative content of BTX, Naphthalene, Indene, Biphenyl, Fluorene, and Phenanthrene in pyrolytic tar derived from PVC pyrolysis at 750 ^{o}C without/with CaO reactant

5.3 Effect of temperature and CaO reactant on tar composition from PVC pyrolysis

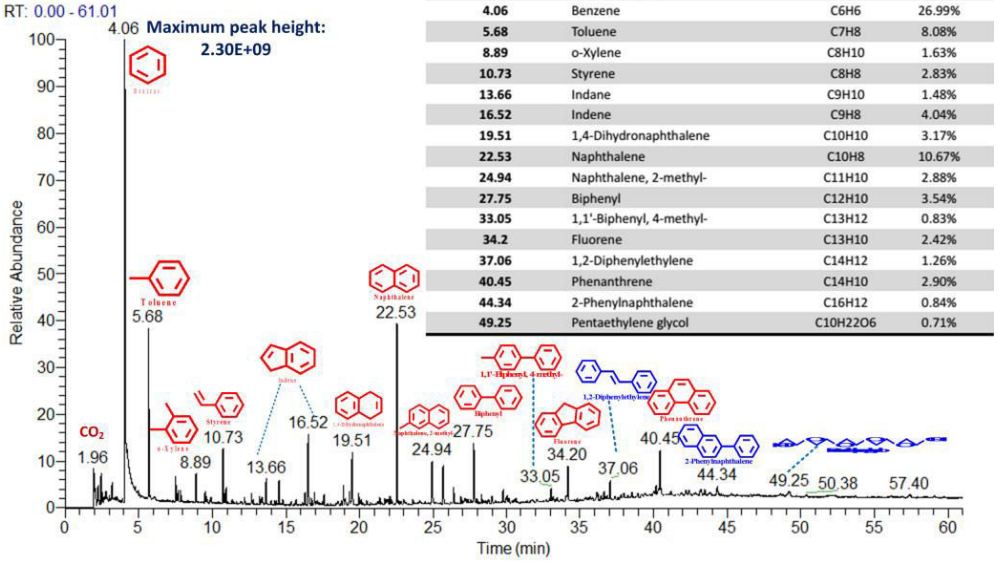

Resistance Time	Substance Name	Formula	Peak Area %
1.96	Carbon dioxide	CO2	3.50%
4.06	Benzene	C6H6	26.99%
5.68	Toluene	C7H8	8.08%
8.89	o-Xylene	C8H10	1.63%
10.73	Styrene	C8H8	2.83%
13.66	Indane	C9H10	1.48%
16.52	Indene	C9H8	4.04%
19.51	1,4-Dihydronaphthalene	C10H10	3.17%
22.53	Naphthalene	C10H8	10.67%
24.94	Naphthalene, 2-methyl-	C11H10	2.88%
27.75	Biphenyl	C12H10	3.54%
33.05	1,1'-Biphenyl, 4-methyl-	C13H12	0.83%
34.2	Fluorene	C13H10	2.42%
37.06	1,2-Diphenylethylene	C14H12	1.26%
40.45	Phenanthrene	C14H10	2.90%
44.34	2-Phenylnaphthalene	C16H12	0.84%
49.25	Pentaethylene glycol	C10H22O6	0.71%

Figure 5. 14 Identified tar composition from PVC pyrolysis at 550 °C in the absence of CaO reactant

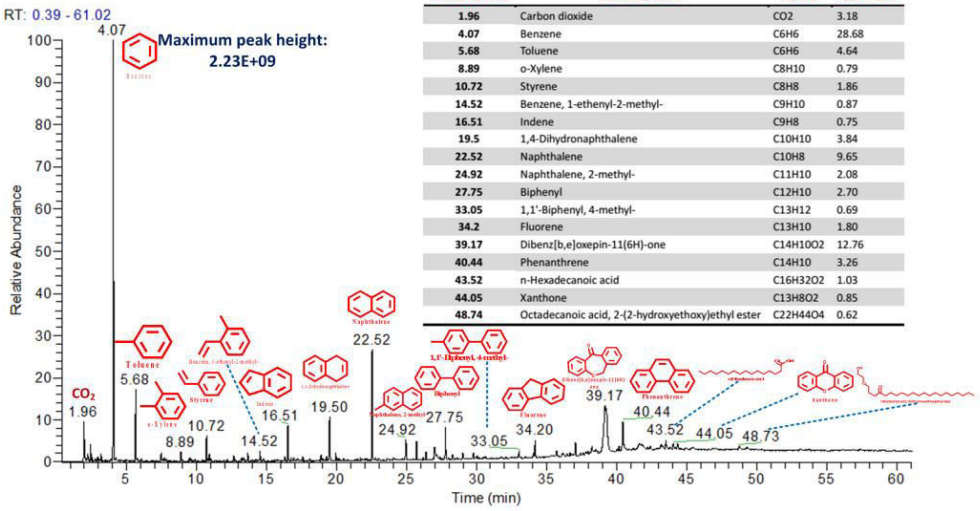

Resistance Time	Substance Name	Fumula	Peak Area %
1.96	Carbon dioxide	CO2	3.18
4.07	Benzene	C6H6	28.68
5.68	Toluene	C6H6	4.64
8.89	o-Xylene	C8H10	0.79
10.72	Styrene	C8H8	1.86
14.52	Benzene, 1-ethenyl-2-methyl-	C9H10	0.87
16.51	Indene	C9H8	0.75
19.5	1,4-Dihydronaphthalene	C10H10	3.84
22.52	Naphthalene	C10H8	9.65
24.92	Naphthalene, 2-methyl-	C11H10	2.08
27.75	Biphenyl	C12H10	2.70
33.05	1,1'-Biphenyl, 4-methyl-	C13H12	0.69
34.2	Fluorene	C13H10	1.80
39.17	Dibenz[b,e]oxepin-11(6H)-one	C14H10O2	12.76
40.44	Phenanthrene	C14H10	3.26
43.52	n-Hexadecanoic acid	C16H32O2	1.03
44.05	Xanthone	C13H8O2	0.85
48.74	Octadecanoic acid, 2-(2-hydroxyethoxy)ethyl ester	C22H44O4	0.62

Figure 5. 15 Identified tar composition from PVC pyrolysis at 550 °C with the addition of CaO reactant

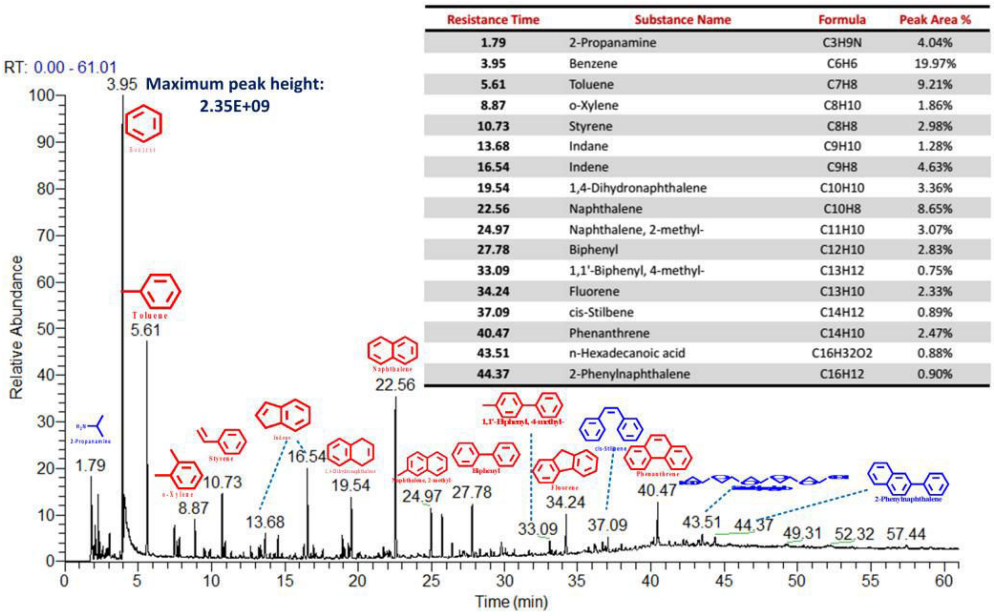

Resistance Time	Substance Name	Formula	Peak Area %
1.79	2-Propanamine	C3H9N	4.04%
3.95	Benzene	C6H6	19.97%
5.61	Toluene	C7H8	9.21%
8.87	o-Xylene	C8H10	1.86%
10.73	Styrene	C8H8	2.98%
13.68	Indane	C9H10	1.28%
16.54	Indene	C9H8	4.63%
19.54	1,4-Dihydronaphthalene	C10H10	3.36%
22.56	Naphthalene	C10H8	8.65%
24.97	Naphthalene, 2-methyl-	C11H10	3.07%
27.78	Biphenyl	C12H10	2.83%
33.09	1,1'-Biphenyl, 4-methyl-	C13H12	0.75%
34.24	Fluorene	C13H10	2.33%
37.09	cis-Stilbene	C14H12	0.89%
40.47	Phenanthrene	C14H10	2.47%
43.51	n-Hexadecanoic acid	C16H32O2	0.88%
44.37	2-Phenylnaphthalene	C16H12	0.90%

Figure 5. 16 Identified tar composition from PVC pyrolysis at 650 °C in the absence of CaO reactant

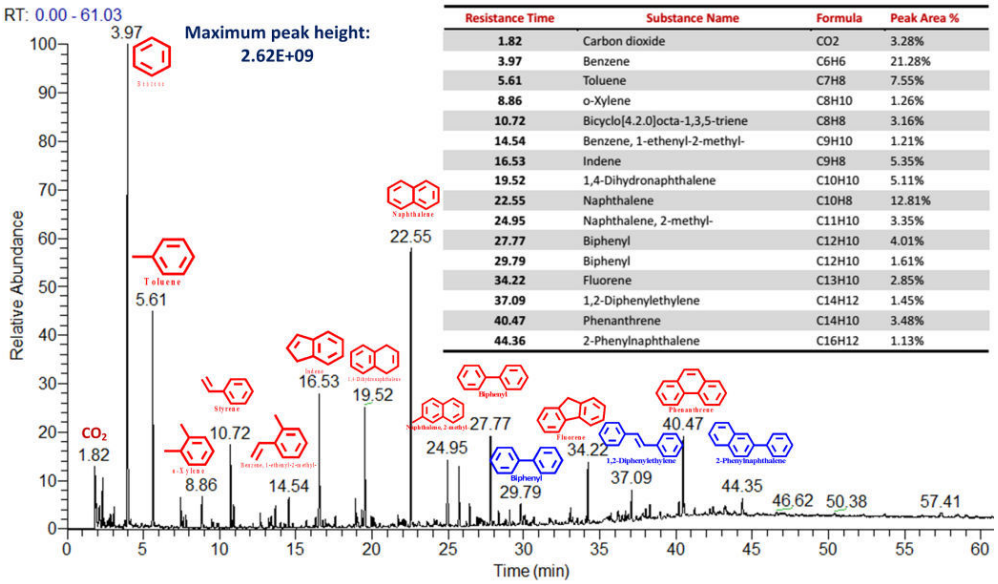

Resistance Time	Substance Name	Formula	Peak Area %
1.82	Carbon dioxide	CO2	3.28%
3.97	Benzene	C6H6	21.28%
5.61	Toluene	C7H8	7.55%
8.86	o-Xylene	C8H10	1.26%
10.72	Bicyclo[4.2.0]octa-1,3,5-triene	C8H8	3.16%
14.54	Benzene, 1-ethenyl-2-methyl-	C9H10	1.21%
16.53	Indene	C9H8	5.35%
19.52	1,4-Dihydronaphthalene	C10H10	5.11%
22.55	Naphthalene	C10H8	12.81%
24.95	Naphthalene, 2-methyl-	C11H10	3.35%
27.77	Biphenyl	C12H10	4.01%
29.79	Biphenyl	C12H10	1.61%
34.22	Fluorene	C13H10	2.85%
37.09	1,2-Diphenylethylene	C14H12	1.45%
40.47	Phenanthrene	C14H10	3.48%
44.36	2-Phenylnaphthalene	C16H12	1.13%

Figure 5. 17 Identified tar composition from PVC pyrolysis at 650 °C with the addition of CaO reactant

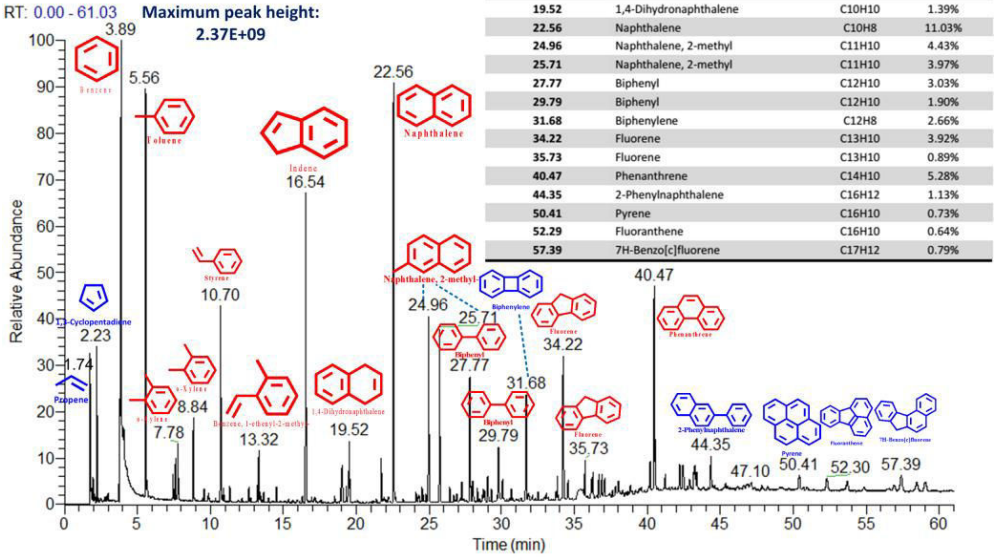

Resistance Time	Substance Name	Formula	Peak Area %
1.74	Propene	C3H6	1.97%
2.23	1,3-Cyclopentadiene	C5H6	1.61%
3.89	Benzene	C6H6	13.99%
5.56	Toluene	C7H8	8.72%
7.78	o-Xylene	C8H10	1.10%
8.84	o-Xylene	C8H10	1.66%
10.70	Styrene	C8H8	4.13%
13.32	Benzene, 1-ethenyl-3-methyl	C9H10	1.25%
16.54	Indene	C9H8	7.17%
19.52	1,4-Dihydronaphthalene	C10H10	1.39%
22.56	Naphthalene	C10H8	11.03%
24.96	Naphthalene, 2-methyl	C11H10	4.43%
25.71	Naphthalene, 2-methyl	C11H10	3.97%
27.77	Biphenyl	C12H10	3.03%
29.79	Biphenyl	C12H10	1.90%
31.68	Biphenylene	C12H8	2.66%
34.22	Fluorene	C13H10	3.92%
35.73	Fluorene	C13H10	0.89%
40.47	Phenanthrene	C14H10	5.28%
44.35	2-Phenylnaphthalene	C16H12	1.13%
50.41	Pyrene	C16H10	0.73%
52.29	Fluoranthene	C16H10	0.64%
57.39	7H-Benzo[c]fluorene	C17H12	0.79%

Figure 5. 18 Identified tar composition from PVC pyrolysis at 850 °C in the absence of CaO reactant

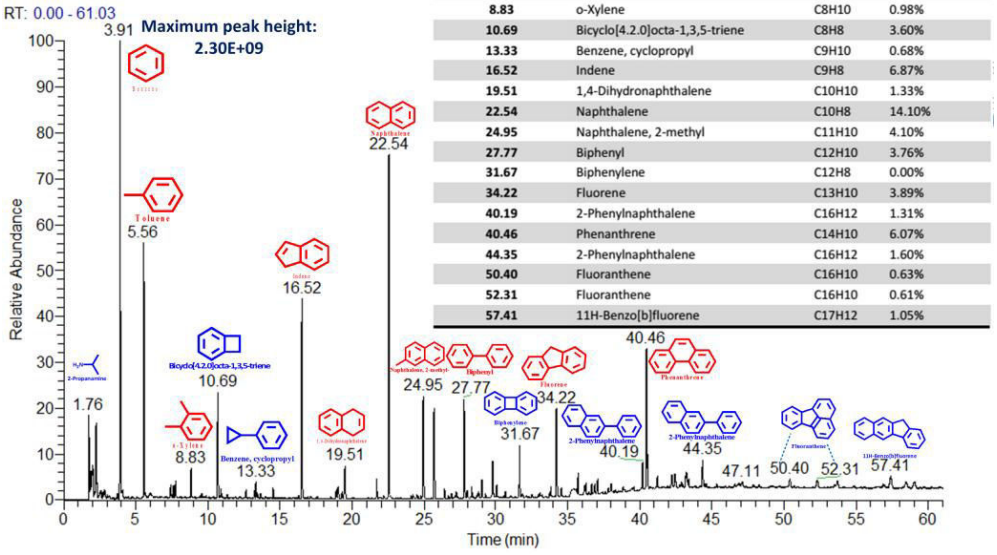

Resistance Time	Substance Name	Formula	Peak Area %
1.76	2-Propanamine	C3H9N	1.87%
3.91	Benzene	C6H6	15.86%
5.56	Toluene	C7H8	7.83%
8.83	o-Xylene	C8H10	0.98%
10.69	Bicyclo[4.2.0]octa-1,3,5-triene	C8H8	3.60%
13.33	Benzene, cyclopropyl	C9H10	0.68%
16.52	Indene	C9H8	6.87%
19.51	1,4-Dihydronaphthalene	C10H10	1.33%
22.54	Naphthalene	C10H8	14.10%
24.95	Naphthalene, 2-methyl	C11H10	4.10%
27.77	Biphenyl	C12H10	3.76%
31.67	Biphenylene	C12H8	0.00%
34.22	Fluorene	C13H10	3.89%
40.19	2-Phenylnaphthalene	C16H12	1.31%
40.46	Phenanthrene	C14H10	6.07%
44.35	2-Phenylnaphthalene	C16H12	1.60%
50.40	Fluoranthene	C16H10	0.63%
52.31	Fluoranthene	C16H10	0.61%
57.41	11H-Benzo[b]fluorene	C17H12	1.05%

Figure 5. 19 Identified tar composition from PVC pyrolysis at 850 °C with the addition of CaO reactant

Figure 5.14 – **Figure 5.19** exhibit the identification results of pyrolytic tar compositions from PVC pyrolysis at temperature of 550, 650, and 850 °C (identification results of PVC pyrolysis at temperature of 750 °C are exhibited in **Section 5.2**, as seen in **Figure 5.9** and **Figure 5.10**) and under the condition of non-catalytic and catalytic pyrolysis. As aforementioned, most of the detected tar species from PVC pyrolysis are aromatic compounds, accounting for 81.2% to 92.36% under the experimental conditions.

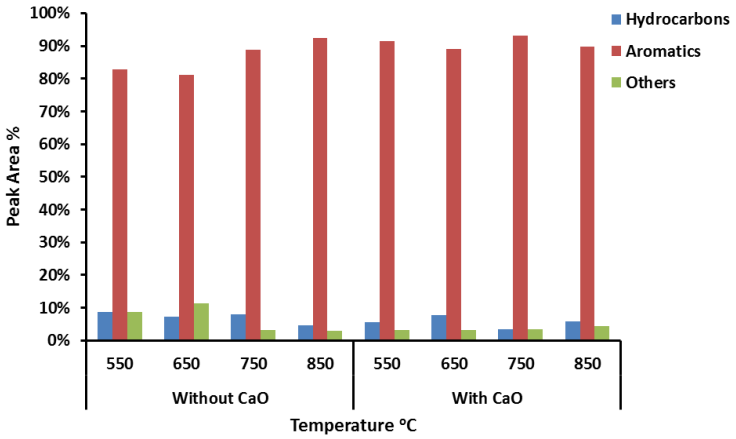

Figure 5. 20 Composition of pyrolytic tar derived from PVC pyrolysis at 550, 650, 750, and 850 °C with/without CaO addition (Others here represent CO_2, HCl, and acid compounds)

Figure 5.20 presents the relative content of pyrolytic tar from PVC pyrolysis. As illustrated, for non-catalytic pyrolysis conditions, the relative content of aromatic compounds is increased from 82.8% to 92.4% when increasing the pyrolytic temperature from 550 to 850 °C. Higher temperature accelerates the cycloaromatization reactions of the generated tar compounds and thus remarkable increase the relative content of aromatic compounds [23, 24]. However, for CaO catalytic pyrolysis conditions, the relative content of aromatic compounds is fluctuant in the range of 89.0% - 93.3%, a little bit higher than that in the absence of CaO reactant. This agrees well with the aforementioned results that the use of CaO reactant promotes the formation of aromatic compounds.

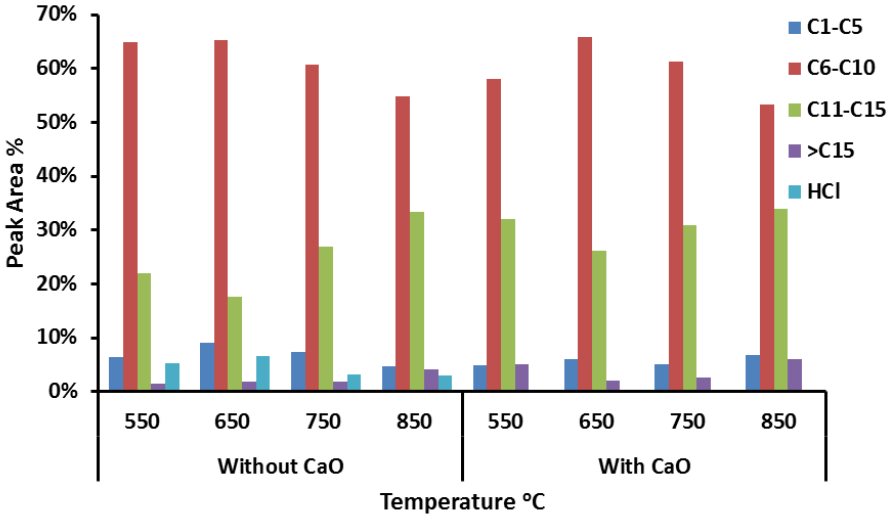

Figure 5. 21 Distributions of detected species of pyrolytic tar derived from PVC pyrolysis as a function of carbon atom numbers

Figure 5.21 exhibits the distributions of pyrolytic tar composition from PVC pyrolysis at temperature of 550, 650, 750, and 850 ^{o}C with/without CaO addition as a function of carbon atom numbers. As revealed, the majority of the detected compounds belong to C6 – C10 categories, sharing approximately 54.9% - 65.2% for non-catalytic pyrolysis and 53.3% - 65.9% for catalytic pyrolysis, followed by C11 – C15 categories, C1 – C5 categories, and >C15 categories. As indicated in the figure, with the increase of temperature, the relative content of C6 – C10 compounds is declined, while the relative content of C11 – C15 compounds are promoted. This is a counter-intuitive finding, since it is well recognized that higher temperature facilitates the thermal cracking of heavy tar compounds [25-27]. However, it is believed that the obtained results are reasonable. It is mainly due to the aforementioned fact that only volatile organic compounds are able to be detected from Py-GC/MS experiments, which means heavy compounds (for example tar components with more than 20 carbon atoms) cannot be recorded from Py-GC/MS apparatus. The possible fact is that when the pyrolytic temperature is increased from 550 to 850 ^{o}C, heavy tar compounds (which cannot be detected by Py-GC/MS) are thermally cracked and reduced, leading to the higher relative content of C11 – C15 compounds as identified in this work. The same phenomena are concluded by Lu et al. [28] and Zhang et al. [29], observing that the total peak area was increased monotonically and dramatically when increasing the pyrolysis temperature. It is worth noting that HCl is detected from non-catalytic pyrolysis, while it is eliminated from CaO catalytic pyrolysis under the considered temperature range.

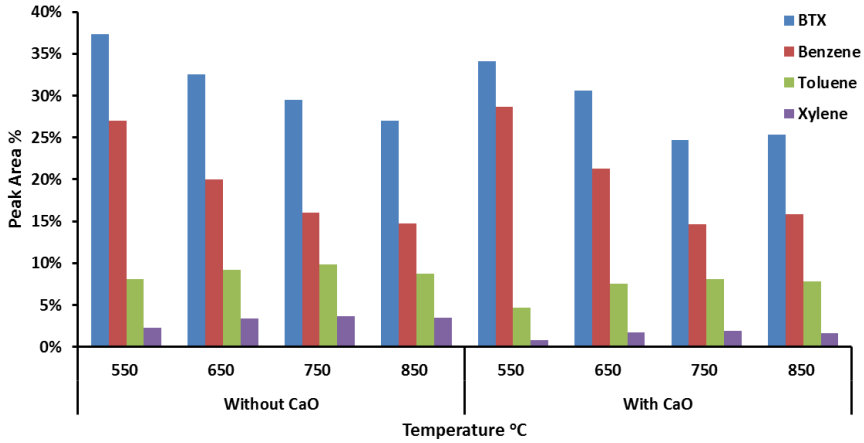

Figure 5. 22 The relative content of BTX in pyrolytic tar derived from PVC pyrolysis without/with CaO reactant

In regard to the specific tar species, **Figure 5.22** shows the relative content of BTX detected from pyrolytic tar of PVC pyrolysis at 550, 650, 750, and 850 ^{o}C without/with CaO reactant. Results reveal that the relative content of total BTX and benzene is decreased monotonically as the increase of temperature from 550 to 850 ^{o}C and with the addition of CaO reactant. However, the relative content of toluene and xylene is slightly increased from 8.1% to 9.8% and 2.3% to 3.6%, respectively for non-catalytic pyrolysis and from 4.6% to 8.1% and 0.8% to 1.9%, respectively for CaO catalytic pyrolysis under experimental temperature.

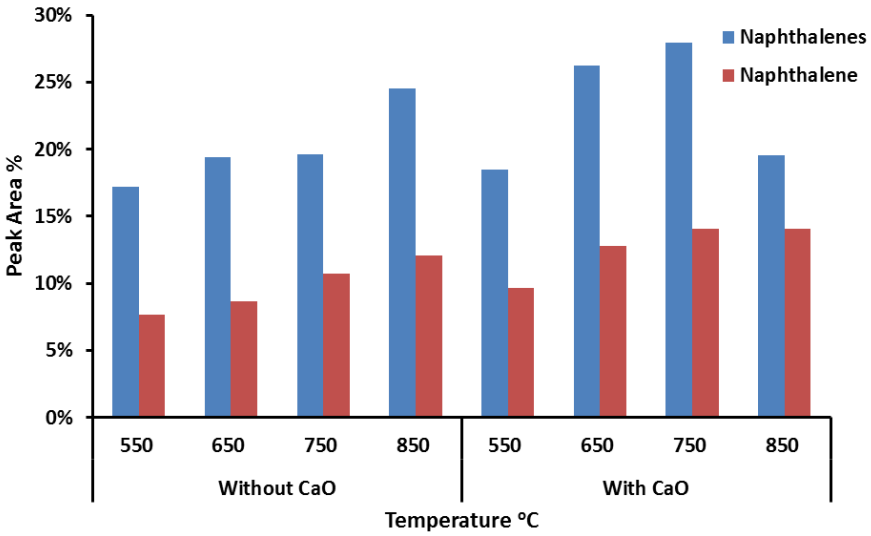

Figure 5. 23 The relative content of naphthalenes and naphthalene in pyrolytic tar derived from PVC pyrolysis without/with CaO reactant

Figure 5.23 presents the relative content of naphthalenes and naphthalene detected from pyrolytic tar of PVC pyrolysis at 550, 650, 750, and 850 ^{o}C without/with CaO reactant. As illustrated, for non-catalytic pyrolysis conditions, the relative content of both naphthalene-content compounds and naphthalene are enhanced with the increase of reaction temperature. However, for CaO catalytic pyrolysis conditions, the relative content of total naphthalene-content compounds is declined at 850 ^{o}C, whereas the content of naphthalene is still increased, indicating that the presence of CaO reactant facilitates the decomposition of branched chains on naphthalene-content species and favors the formation of naphthalene.

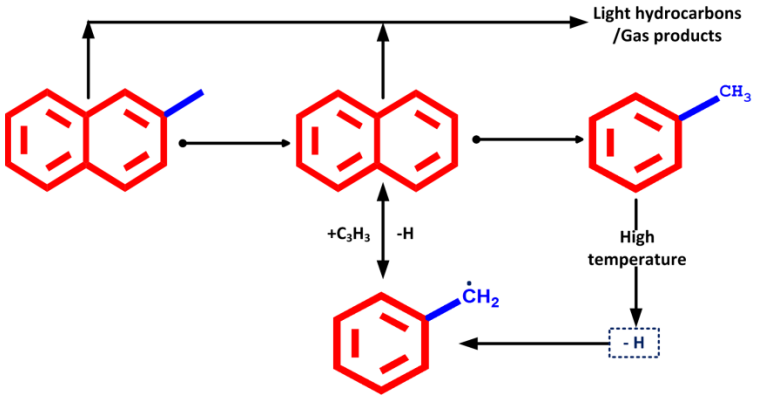

Figure 5. 24 Schematic diagram of the formation and cracking of naphthalene with CaO reactant

Figure 5.24 explains the schematic diagram of the formation and cracking of naphthalene with CaO reactant [30]. As presented, CaO acted an important role in naphthalene-content species decomposition and naphthalene formation. On the one hand, the presence of CaO will destroy the branched chains on naphthalenes, leading to the formation of naphthalene. On the other hand, at high temperature, a small amount of formed toluene loses a hydrogen atom and become free radicals; and then the free radicals react with light molecules to form naphthalene.

5.4 Summary of the chapter

In this chapter, pyrolytic tar from waste single components (wood biomass, food waste and PVC) is investigated. The role of CaO reactant and the effect of temperature on tar composition are examined.

The following conclusions can be drawn:

- The addition of CaO reactant promotes the formation of aromatic compounds and inhibits the relative content of oxygenated compounds in pyrolytic tar derived from wood biomass and food waste;
- Pyrolytic tar derived from PVC pyrolysis are mainly aromatic compounds, mainly due to the generation of abundant conjugated double bonds as a result of dehydrochlorination from PVC; and the use of CaO reactant eliminates the produced HCl from PVC pyrolytic tar species;
- High value added tar species, i.e. BTXN (benzene, toluene, xylene and naphthalene) are promoted by CaO reactant from wood biomass and food waste pyrolysis; however, the use of CaO reactant declines the relative content of BTX in pyrolytic tar from PVC;
- The relative content of BTX and benzene is decreased monotonically as the increase of temperature from 550 to 850 ^{o}C and with the addition of CaO reactant from PVC pyrolysis; whereas the relative content of naphthalene is promoted simultaneously.

5.5 Bibliography

[1] Sun Y, Liu L, Wang Q, Yang X, Tu X. Pyrolysis products from industrial waste biomass based on a neural network model. Journal of analytical and applied pyrolysis. 2016;120:94-102.

[2] Esfahani RAM, Osmieri L, Specchia S, Yusup S, Tavasoli A, Zamaniyan A. H2-rich syngas production through mixed residual biomass and HDPE waste via integrated catalytic gasification and tar cracking plus bio-char upgrading. Chemical Engineering Journal. 2017;308:578-87.

[3] Jafarian S, Tavasoli A, Karimi A. HYDROGEN RICH GAS PRODUCTION VIA STEAM GASIFICATION OF BAGASSE OVER BIMETALLIC Ni-Fe/γ-Al 2 O 3 NANO-CATALYSTS. Petroleum & Coal. 2015;57.

[4] Ramasubramanian S, Chandrasekaran M. A Statistical Analysis on Tar Reduction in Producer Gas for IC Engine Application. International Journal of Ambient Energy. 2018:1-13.

[5] Knutsson P, Cantatore V, Seemann M, Tam PL, Panas I. Role of potassium in the enhancement of the catalytic activity of calcium oxide towards tar reduction. Applied Catalysis B: Environmental. 2018;229:88-95.

[6] Din ZU, Zainal Z. Tar reduction mechanism via compression of producer gas. Journal of Cleaner Production. 2018;184:1-11.

[7] Kabir G, Hameed B. Recent progress on catalytic pyrolysis of lignocellulosic biomass to high-grade bio-oil and bio-chemicals. Renewable and Sustainable Energy Reviews. 2017;70:945-67.

[8] Lu Q, Zhang Z-F, Dong C-Q, Zhu X-F. Catalytic upgrading of biomass fast pyrolysis vapors with nano metal oxides: an analytical Py-GC/MS study. Energies. 2010;3:1805-20.

[9] Lin Y, Zhang C, Zhang M, Zhang J. Deoxygenation of Bio-oil during Pyrolysis of Biomass in the Presence of CaO in a Fluidized-Bed Reactor. Energy & fuels. 2010;24:5686-95.

[10] Li X-H, Meng Y-Z, Zhu Q, Tjong S. Thermal decomposition characteristics of poly (propylene carbonate) using TG/IR and Py-GC/MS techniques. Polymer Degradation and Stability. 2003;81:157-65.

[11] San Miguel G, Aguado J, Serrano D, Escola J. Thermal and catalytic conversion of used tyre rubber and its polymeric constituents using Py-GC/MS. Applied Catalysis B: Environmental. 2006;64:209-19.

[12] Nierop KG, van Bergen PF, Buurman P, van Lagen B. NaOH and Na4P2O7 extractable organic matter in two allophanic volcanic ash soils of the Azores Islands—a pyrolysis GC/MS study. Geoderma. 2005;127:36-51.

[13] Traoré M, Kaal J, Cortizas AM. Potential of pyrolysis-GC–MS molecular fingerprint as a proxy of Modern Age Iberian shipwreck wood preservation. Journal of Analytical and Applied Pyrolysis. 2017;126:1-13.

[14] Taarning E, Osmundsen CM, Yang X, Voss B, Andersen SI, Christensen CH. Zeolite-catalyzed biomass conversion to fuels and chemicals. Energy & Environmental Science. 2011;4:793-804.

[15] Yao G, Wu G, Dai W, Guan N, Li L. Hydrodeoxygenation of lignin-derived phenolic compounds over bi-functional Ru/H-Beta under mild conditions. Fuel. 2015;150:175-83.

[16] Tingyu Z, Shouyu Z, Jiejie H, Yang W. Effect of calcium oxide on pyrolysis of coal in a fluidized bed. Fuel Processing Technology. 2000;64:271-84.

[17] Wang D, Xiao R, Zhang H, He G. Comparison of catalytic pyrolysis of biomass with MCM-41 and CaO catalysts by using TGA–FTIR analysis. Journal of Analytical and Applied Pyrolysis. 2010;89:171-7.

[18] Granda M, Blanco C, Alvarez P, Patrick JW, Menéndez R. Chemicals from coal coking. Chemical reviews. 2013;114:1608-36.

[19] Yan L-J, Bai Y-H, Kong X-J, Li F. Effects of alkali and alkaline earth metals on the formation of light aromatic hydrocarbons during coal pyrolysis. Journal of analytical and applied pyrolysis. 2016;122:169-74.

[20] He L, Li S, Lin W. Catalytic cracking of pyrolytic vapors of low-rank coal over limonite ore. Energy & Fuels. 2016;30:6984-90.

[21] He C, Min X, Zheng H, Fan Y, Yao Q, Zhang D, et al. Study on the Volatiles and Kinetic of in-Situ Catalytic Pyrolysis of Swelling Low-Rank Coal. Energy & Fuels. 2017;31:13558-71.

[22] ZHANG R. Experimental Study on the Inhibition of C-Cl Bond by H2 during the Gasification of MSW. Shanghai, P. R. China Shanghai Jiao Tong University; 2015.

[23] Sluiter JB, Ruiz RO, Scarlata CJ, Sluiter AD, Templeton DW. Compositional analysis of lignocellulosic feedstocks. 1. Review and description of methods. Journal of agricultural and food chemistry. 2010;58:9043-53.

[24] Shen D, Zhao J, Xiao R, Gu S. Production of aromatic monomers from catalytic pyrolysis of black-liquor lignin. Journal of Analytical and Applied Pyrolysis. 2015;111:47-54.

[25] Peng W, Wang L, Mirzaee M, Ahmadi H, Esfahani M, Fremaux S. Hydrogen and syngas production by catalytic biomass gasification. Energy Conversion and Management. 2017;135:270-3.

[26] Efika CE, Onwudili JA, Williams PT. Influence of heating rates on the products of high-temperature pyrolysis of waste wood pellets and biomass model compounds. Waste Management. 2018;76:497-506.

[27] Zheng X, Ying Z, Wang B, Chen C. Effect of Calcium Oxide Addition on Tar Formation During the Pyrolysis of Key Municipal Solid Waste (MSW) Components. Waste and Biomass Valorization. 2018:1-10.

[28] Lu Q, Yang X-c, Dong C-q, Zhang Z-f, Zhang X-m, Zhu X-f. Influence of pyrolysis temperature and time on the cellulose fast pyrolysis products: Analytical Py-GC/MS study. Journal of Analytical and Applied Pyrolysis. 2011;92:430-8.

[29] Zhang B, Zhong Z, Ding K, Song Z. Production of aromatic hydrocarbons from catalytic co-pyrolysis of biomass and high density polyethylene: analytical Py–GC/MS study. Fuel. 2015;139:622-8.

[30] Wang Y, Zhao R, Zhang C, Li G, Zhang J, Li F. The Investigation of Reducing PAHs Emission from Coal Pyrolysis by Gaseous Catalytic Cracking. The Scientific World Journal. 2014;2014:6.

Chapter 6

Influence of CaO reactant on pyrolysis of simulated MSW: HCl mitigation and tar upgrading

6.1 Introduction

Apart from incineration, MSW pyrolysis is believed one of the most promising alternative WtE strategies achieving both waste treatment and energy recovery. Pyrolysis is also the most fundamental step of waste thermal conversions and determines directly the product yields and properties at the very beginning of waste thermal conversion [1]. Therefore, MSW pyrolysis is experimentally investigated in this work with the emphasis on effect of temperature and CaO reactant on both in-furnace pyrolytic product properties enhancement and contaminants (mainly tar and HCl gas) removal.

Recently, MSW pyrolysis has become one of the most popular hotspots in waste treatment fields; studies have demonstrated the effects of furnaces [2-4], pyrolysis temperature [5, 6], pyrolysis pressure [7, 8], reaction time [6, 9], and heating method [10, 11] on pyrolytic product properties. In addition to physical/chemical properties of MSW and the pyrolysis working condition, reactants are also a key factor affecting pyrolysis behavior [12, 13]. CaO reactant also plays an important role on pyrolysis products quality enhancement. Therefore, besides the aforementioned HCl mitigation and tar cracking and upgrading functions in **Chapter 3, 4, and 5**, CaO is also commonly used as the in-furnace reactant to increase the quality of the pyro-gasification products, since it can be regarded as an efficient CO_2 sorbent to increase the produced gas quality [14-17]. CaO is one of the most preferable

reactants in waste thermal conversion systems, because it is quite cheap and widely abundant on the earth [12, 18, 19].

Therefore, in this chapter, effects of temperature and CaO reactant on S-MSW pyrolysis are experimentally investigated. The content mainly consists of three parts: effect of temperature and in-furnace CaO reactant 1) on pyrolytic product properties; 2) on HCl mitigation efficiency; and 3) on tar cracking and tar composition upgrading.

Accordingly, the structure of this chapter is presented as follows:

I. **Section 6.2** is dedicated to evaluate the effect of temperature and in-furnace CaO reactant on pyrolytic products mass distribution, produced gas yield and composition, and H_2 gas yield;

II. **Section 6.3** investigates the effect of in-furnace CaO reactant on released HCl mitigation. HCl mitigation efficiency under varied temperature and reactant properties (varied Ca/Cl molar ratio and CaO particle size) are examined and morphology analysis of the spent in-furnace CaO reactant are conducted;

III. **Section 6.4** focuses on the effect of temperature and in-furnace CaO reactant on S-MSW pyrolytic tar cracking and tar composition upgrading.

IV. **Section 6.5** summarizes the findings of this chapter.

6.2 Thermochemical conversion characteristics of S-MSW pyrolysis

The influences of temperature and in-furnace CaO reactant on product mass distribution, total gas yield, produced gas composition, and H_2 yield are discussed in this section.

6.2.1 Pyrolytic product (produced gas, tar, and solid residues) mass distribution

Table 6.1 lists the experimental results of the effect of temperature and CaO reactant on product mass distribution. The results are presented as mass ratio of the specific fraction (gas, tar, or solid residues) to the total mass of the products (i.e. the sum of gas, tar, and solid residues). Results reveal that temperature significantly influences the mass distribution of gas, tar and solid residues from S-MSW pyrolysis. Higher temperature improved the mass percentage of produced gas but decreased simultaneously the proportions of tar and solid

residues. According to **Table 6.1**, when pyrolysis temperature is increased from 550 to 850 ^{o}C, yields decline significantly from 46.8 to 18.6 wt.% for tar and from 20.4 to 12.6 wt.% for solid residues; simultaneously, produced gas yield is increased continuously from 32.8 to 68.6 wt.%. The results agree well with literature data [20-22]. And it is quite reasonable, since temperature plays an important role in chemical reactions by shifting the thermodynamic equilibrium. With special regards to waste pyrolysis in the present work, increasing the temperature favors the emitting of volatiles from S-MSW at initial waste decomposition stage. And meanwhile, high temperature also significantly facilitates tar thermal cracking reactions, resulting in the reduction of tar yields and the production of more incondensable gases.

Table 6. 1 Effect of temperature and CaO reactant on pyrolysis product mass distribution

Temperature, ^{o}C	Reactant	Solid products, wt. % [a]	Tar, wt. %	Gas products, wt. %
550	Without CaO	20.4	46.8	32.8
	With CaO	25.4	37.8	36.8
650	Without CaO	15.8	35.0	49.2
	With CaO	21.6	24.0	54.4
750	Without CaO	15.0	30.6	54.4
	With CaO	18.6	15.2	66.2
850	Without CaO	12.6	18.6	68.8
	With CaO	17.6	14.0	68.4

[a] the mass of raw CaO added is subtracted from the solid residues.

When CaO reactant is co-fed with S-MSW, tar yield is significantly reduced from 4.6 to 15.4 wt. % under the experimental temperature ranges. The results are in good accordance with the findings presented in **Chapter 5**, revealing that the presence of CaO reactant promotes tar catalytic thermal cracking reactions and facilitates the conversion from bio-oil to light gas products. The yield of produced gas is also increased, except for experiments at temperature of 850 ^{o}C, mainly due to the enhancement of S-MSW decomposition and tar cracking with the addition of CaO reactant. With respect to solid fractions, the generation of solid residues is increased by 3.6 % - 5.8 % under the considered temperature ranges; reactions between CaO and pyrolysis products, such as CO_2, HCl, and etc., to form solid phase products ($CaCO_3$, $CaCl_2$, CaClOH, and etc.) may be responsible for the gradually increase of the solid residues yield.

6.2.2 Produced gas yield and combustible gas composition

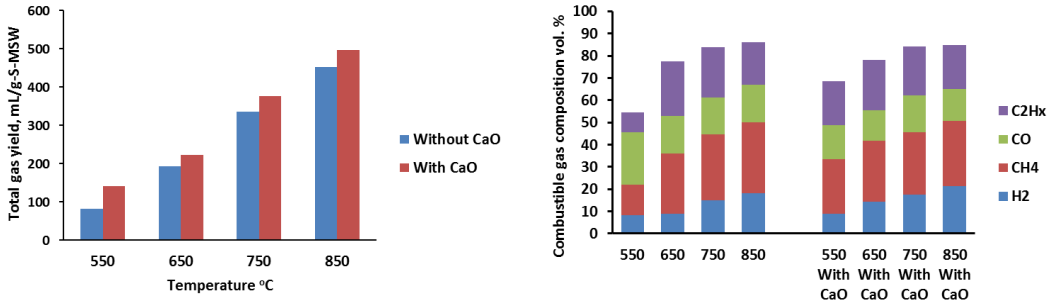

(a) (b)

Figure 6. 1 Effect of temperature and CaO reactant on produced gas characteristics: a, total gas yield; and b, combustible gas composition (the carrier gas N_2 is subtracted from the produced gas)

Figure 6.1 (a) exhibits the pyrolytic gas yield as a function of pyrolysis temperature and the effect of in-furnace CaO reactant. As aforementioned in **Section 6.2.1**, increasing the temperature significantly increases the mass percentage of produced gases. Considering the total gas yield, similar results are obtained. When the temperature is increased from 550 to 850 °C, the total gas yield is dramatically increased from 81.9 to 451.4 mL/g-S-MSW. The use of CaO reactant also favors the total generation of pyrolytic gases; gas yield is increased by 30.0 to 58.8 mL/g-S-MSW under the considered experimental conditions, accounting to approximately 10% to 72% of the gas yield at the same temperature without the addition of CaO reactant. The reasons, as previously described, are mainly attributed to the role of CaO reactant on tar compounds cracking.

Figure 6.1 (b) presents the effect of temperature and CaO reactant on the produced gas composition. Pyrolysis temperature directly determines the pyrolytic gas composition by affecting waste decomposition reaction and gas-reforming reactions. **Table 6.2** summarizes some important thermochemical reactions reflecting waste pyrolysis and the role of CaO reactant [15, 16, 23, 24].

As exhibited, with the increase of temperature from 550 to 850 °C, H_2 molecular fraction in the produced gas is continuously increased from 8.3 to 18.3 %. According to [25], at lower pyrolysis temperature, H_2 is mainly produced from decomposition of volatiles and the cracking reactions of aliphatic however, at higher temperature, the direct generation is mainly coming from dehydrogenation condensation-polymerization reactions of aromatic

hydrocarbons. Therefore, the formation of H_2 gas is significantly enhanced at higher temperature. Moreover, reforming reactions also play important roles on H_2 yield during waste pyrolysis. The enhancement of endothermic reactions at higher temperature, such as the general pyrolysis reaction (as presented in **Table 6. 2**, **Eq. (6.1)**) and the water-gas reactions (**Eq. (6.2)** and **Eq. (6.3)**) also facilitate the generation of H_2 gas. With regard to the addition of CaO reactant, H_2 yield is promoted by 0.8 – 5.5 % under the experimental temperature. It is mainly because CaO could promote both tar catalytic thermal cracking reactions (**Eq. (6.12)**) and condensation-polymerization reactions of aromatic compounds.

Similarly, CH_4 yield is also increased from 13.7 to 31.8 % when pyrolysis temperature is increased from 550 to 850 °C. The formation of CH_4 during pyrolysis is mainly due to two pathways: one is from the decomposition of volatiles and the other is the further cracking of the produced methyl, oxymethylene, polymethylene and aliphatic hydrocarbons components [25]. Increasing the temperature apparently increases the generation of CH_4. The use of CaO firstly enhance the CH_4 yield, mainly due to the enhancement of tar catalytic thermal cracking reaction (**Eq. (6.10)**); but at higher temperature, CH_4 content declined slightly because of the strengthening of hydrocarbon reforming reactions by CaO reactant.

The content of CO is varying in the range of 16.7% and 23.6% with temperature. The reason may be attributed to the competing reactions between water-gas reactions (**Eq. (6.2)** and **Eq. (6.3)**) and water-gas shift reaction (**Eq. (6.4)**). With the addition of CaO reactant, CO content is limited. That can be explained by the enhancement of water gas shift reaction (**Eq. (6.4)**) due to the absorption of CO_2 by CaO. CO_2 in the produced gas is consumed through CaO carbonation reaction (**Eq. (6.7)**), leading to the acceleration of the water-gas shift reaction towards the direction of producing more H_2 and consuming CO.

Regarding C_2Hx (the sum of C_2H_2, C_2H_4 and C_2H_6), the content increased dramatically from 8.8 to 24.7 % when increasing the temperature from 550 to 650 °C, but then declined slightly to 19.1 % when further increasing the temperature. The initial increase of C_2Hx content is mainly attributed to the enhancement of tar thermal cracking (**Eq. (6.6)**) at higher temperature; however, further increasing the temperature favors the hydrocarbon reforming reactions (**Eq. (6.5)**), thus resulting in the decline of C_2Hx content at higher temperature. Similar to CH_4, the yield of hydrocarbons (C_2H_x) is firstly enhanced with the addition of CaO, due to the enhancement of tar catalytic thermal cracking reaction; but then declined slightly because of catalytic hydrocarbon reforming reactions.

Table 6. 2 Reactions related to MSW pyrolysis and CaO reactant

Reactions related to MSW pyrolysis		
General pyrolysis	$CH_mO_n \rightarrow \alpha H_2 + \beta CO + \gamma CO_2 + \kappa C_aH_b + tar + residues$	6.1
Water-gas (i)	$CH_mO_n + (1-n)H_2O \rightarrow CO + \frac{(m-2n+2)}{2}H_2$	6.2
Water-gas (ii)	$C + H_2O \leftrightarrow CO + H_2$	6.3
Water-gas shift	$CO + H_2O \leftrightarrow CO_2 + H_2$	6.4
Hydrocarbon reforming	$C_aH_b + aH_2O \leftrightarrow aCO + \frac{2a+b}{2}H_2$	6.5
Tar thermal cracking	$Tar \xrightarrow{Heat} \alpha H_2 + \beta CO + \gamma CO_2 + hydrocarbons + \cdots$	6.6
Reactions related to CaO reactant		
Carbonation/calcination	$CaO + CO_2 \leftrightarrow CaCO_3$	6.7
Dechlorination (i)	$CaO + HCl \leftrightarrow CaClOH$	6.8
Dechlorination (ii)	$CaO + 2HCl \leftrightarrow CaCl_2 + H_2O$	6.9
Dechlorination (iii)	$CaCO_3 + HCl \leftrightarrow CaClOH + CO_2$	6.10
Dechlorination (vi)	$CaCO_3 + 2HCl \leftrightarrow CaCl_2 + H_2O + CO_2$	6.11
Tar catalytic thermal cracking	$Tar \xrightarrow{CaO} \alpha H_2 + \beta CO + \gamma CO_2 + hydrocarbons + \cdots$	6.12

6.2.3 H_2 yield from S-MSW pyrolysis without/with CaO reactant

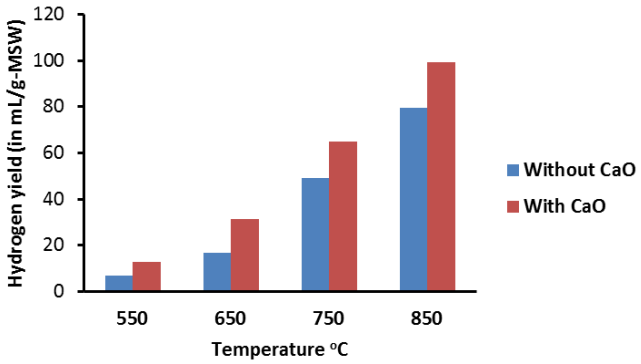

Figure 6. 2 Effect of temperature and CaO reactant on hydrogen yield (in mL/g-MSW)

H_2 gas yield is a key indicator to reflect the quality of the produced gas for further utilization. Therefore, the variation of H_2 yield as a function of temperature and CaO reactant is presented in **Figure 6.2**. As shown, the generation of H_2 is dramatically enhanced from 6.76

to 79.52 mL/g-MSW when increasing the temperature; and the presence of CaO reactant increase the H_2 yield by approximately 25% to 88% under the experimental temperature.

6.2.4 Summary of the section

This section focuses on the role of CaO reactant and the effect of temperature on MSW pyrolysis products mass distribution, gas yield and composition, and H_2 yield. Results reveal that the addition of CaO reactant and the increase of temperature enhance the generation of gas products but decline the yield of tar compounds. In regard to combustible gas composition, H_2 yield is dramatically increased from 6.76 to 79.52 mL/g-MSW when increasing the temperature from 550 to 850 ^{o}C; and the presence of CaO reactant increases the H_2 yield by approximately 25% to 88% under the experimental temperature. With respect to CO, the content is fluctuant with temperature increase and CO generation is limited when CaO reactant is used.

6.3 Effect of temperature and in-furnace CaO on HCl mitigation

6.3.1 XRD analysis of the spent CaO reactant

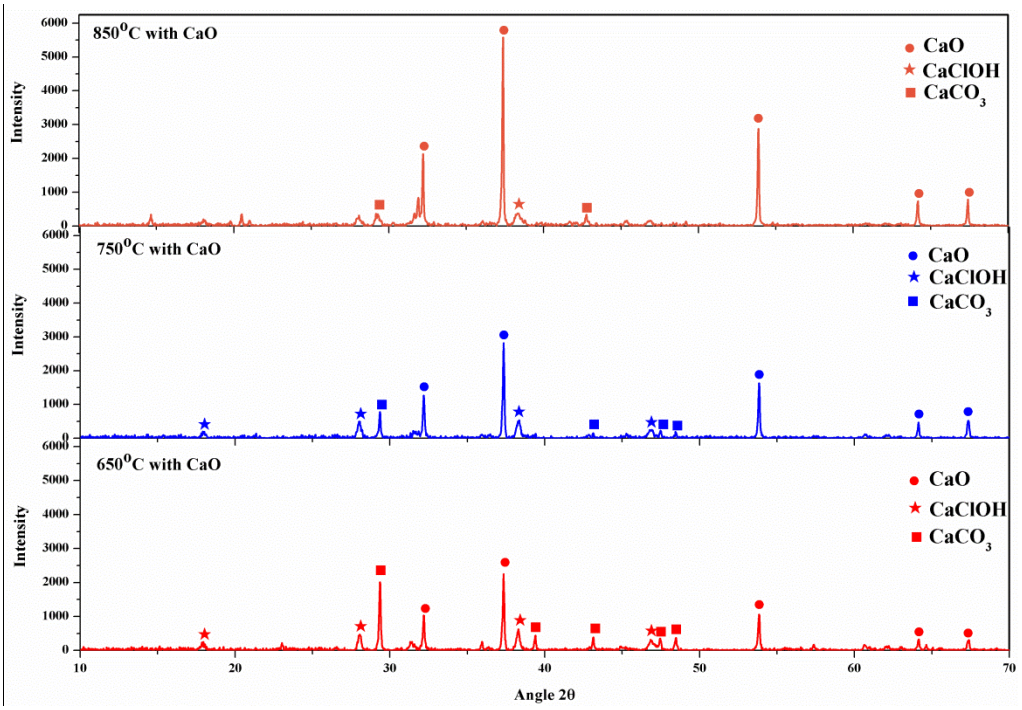

Figure 6. 3 XRD spectrums of the obtained solid residues (from bottom to top): 650 ^{o}C with CaO reactant; 750 ^{o}C with CaO reactant; and 850 ^{o}C with CaO reactant

Figure 6.3 presents the XRD spectrums of the generated solid residues from the working condition of pyrolysis with CaO reactant at 650, 750, and 850 °C, respectively. The minerals are mainly consisted of CaO, $CaCO_3$, and CaClOH, indicating that CaO related reactions of carbonation (**Eq. (6.7)**), dechlorination (i) (**Eq. (6.8)**), and/or dechlorination (iii) (**Eq. (6.10)**) occurred to form $CaCO_3$ and CaClOH under the experimental conditions. Similar results are obtained by Yingjie Li et al [26], stating that $CaCO_3$ and CaClOH are the main products of CO_2/HCl adsorption by Ca-based sorbent. According to Xin Xie et al [24], CaClOH is the main chlorination product formed with CaO reactant for short reaction time (at around tens of minutes), while $CaCl_2$ is the final chlorination product for long reaction time (at around hundreds of minutes).

As depicted in **Figure 6.3**, the intensity of CaO diffraction peaks increased significantly when increasing the temperature from 650 °C to 850 °C, while the intensity of $CaCO_3$ peaks declined simultaneously. It is mainly attributed to the fact that higher temperature shifts the thermodynamic equilibriums of carbonation/calcination reaction (**Eq. (6.7)**) towards the backward direction to decompose the crystalline $CaCO_3$ and to form more crystalline CaO. Meanwhile, the intensity of CaClOH diffraction peaks also decreased when the pyrolysis temperature reaches 850 °C, indicating a reduction of HCl mitigation capacity at higher temperature to form crystalline CaClOH.

6.3.2 Effect of temperature and CaO on HCl mitigation efficiency

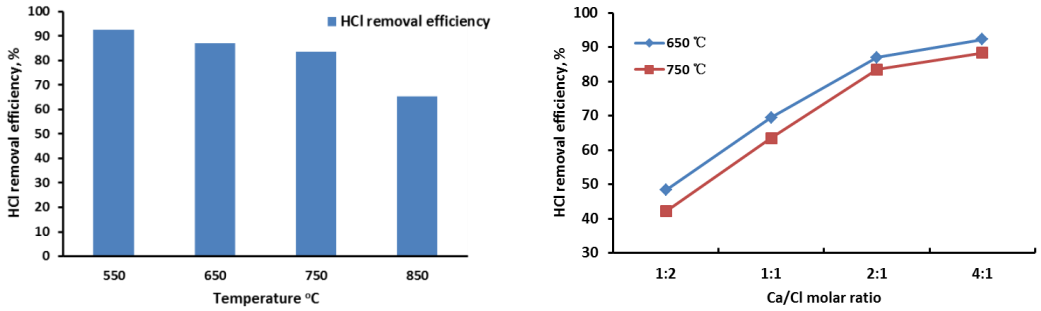

Figure 6. 4 Effect of temperature and Ca/Cl molar ratio on HCl mitigation efficiency during S-MSW pyrolysis

As aforementioned in **Section 6.3.1**, the addition of in-furnace CaO reactant captures the produced HCl gas to form CaClOH, thus immobilizing the chlorine into the solid residues, and prevents its release to the produced gas. **Figure 6.4** illustrates the effect of temperature

and Ca/Cl molar ratio on HCl mitigation efficiency. The obtained results are in good agreement with that obtained from **Section 4.3** using only PVC as the feedstock.

Increasing the temperature causes adverse effects on HCl mitigation efficiency using CaO reactant. As depicted, for the conditions of Ca/Cl molar ratio equal to 2:1, the removal efficiency declines continuously from 92.4 to 65.2% when the temperature is increased from 550 to 850 ^{o}C. It is noted that higher temperature accelerates the decrease of HCl mitigation efficiency; the efficiency decreased by 8.8% from temperature of 550 to 750 ^{o}C, but reduced sharply by 18.3% when further increasing the temperature to 850 ^{o}C. According to the thermodynamic calculation conducted in **Section 3.2**, the binding capacity of CaO and HCl is limited at higher temperature due to the shift of the thermodynamic equilibrium of CaO dechlorination reactions (i.e. **Eq. (6.8)**). Results from XRD spectrums and SEM photographs also reveals that the CaClOH content in the solids reduced apparently at 850 ^{o}C due to its decomposition and evaporation. Therefore, the feasible temperature window for HCl mitigation under the experimental conditions is below 750 ^{o}C.

With respect to the effect of Ca/Cl molar ratio, the stoichiometric Ca/Cl molar ratio of the HCl mitigation reactions is 1:2 and 1:1 respectively according to (**Eq. (6.8)** and **Eq. (6.10)**) and (**Eq. (6.9)** and **Eq. (6.11)**). However, HCl mitigation efficiencies under such molar ratios are quite low and only in the ranges of 42.2 - 69.6% under 650 and 750 ^{o}C. This indicates that the excessive use of CaO reactant than theoretical stoichiometric amount is essential to achieve acceptable removal efficiency levels. The removal efficiency raise rapidly by approximately 40% when increasing Ca/Cl ratio from 1:2 to 2:1; however, further increasing the ratio to 4:1 lead to a limited enhancement by around 5%. Therefore, the Ca/Cl molar ratio of 2:1 is believed the most effective amount of CaO for HCl gas removal under the experimental conditions.

6.3.3 Morphology analysis of the spent in-furnace CaO reactants

Figure 6.5 shows the SEM photographs of raw CaO and obtained solid residues. As presented, the fresh CaO reactant is a low-porosity material. The SEM image of the solid residues obtained at temperature of 650 ^{o}C shows clearly the formation of porous solid products on the surface of CaO reactant, indicating that the chemical reaction of CaO reactant and pyrolysis products occurs. When increasing the reaction temperature to 750 ^{o}C, the microstructures of the reactant and surface products become quite smooth and dense, mainly attributed to the melting of the formed products (the melting temperature of $CaCl_2$ is

772 °C). Conversely, the surface morphology of the solids obtained at 850 °C becomes much more fluffy and porous even compared with that at 650 °C. The decomposition of the produced $CaCO_3$ and CaClOH and the evaporation of the dechlorination products are responsible for the formation of the porous particle surfaces.

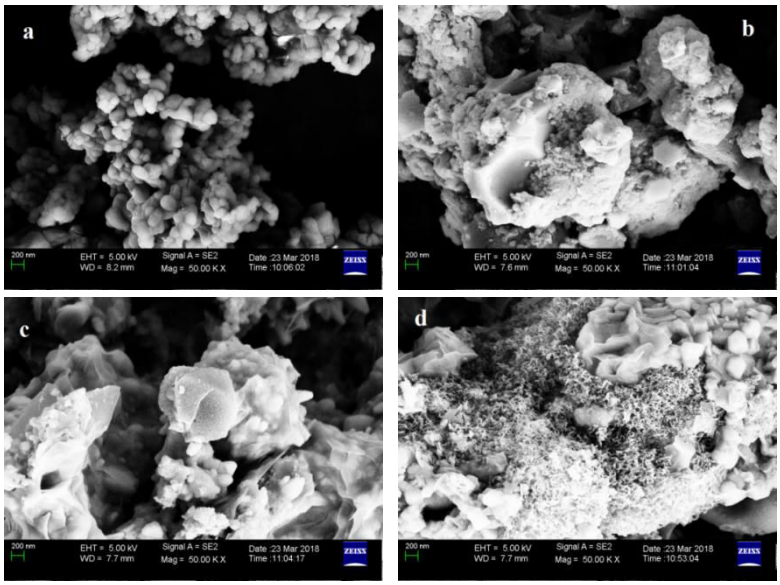

Figure 6. 5 SEM images of fresh (a) and spent CaO reactants (b, pyrolysis residues at 650 °C; c, pyrolysis residues at 750 °C; and d, pyrolysis residues at 850 °C)

6.4 Effect of temperature and in-furnace CaO reactant on S-MSW pyrolysis tar yield and tar composition

6.4.1 Tar yield and tar reduction efficiency

Figure 6.6 reports the effect of temperature and CaO reactant on tar yield and tar reduction efficiency. Tar reduction efficiency is divided into tar thermal reduction efficiency and tar catalytic thermal reduction efficiency as presented in **Figure 6.6 (b)** by solid and dotted lines, respectively. Tar reduction efficiency is defined as follows:

$$\text{Tar thermal reduction efficiency} = \frac{\text{Tar yields at 550 °C - Tar yields}}{\text{Tar yields at 550 °C}} \times 100\% \quad (6.13)$$

$$\text{Tar catalytic thermal reduction efficiency} = \frac{\text{Tar yields at 550 °C - Tar yields with CaO addition}}{\text{Tar yields at 550 °C}} \times 100\% \quad (6.14)$$

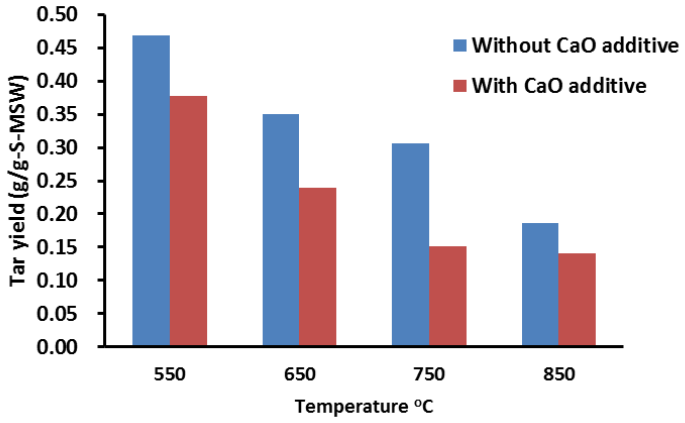

(a)

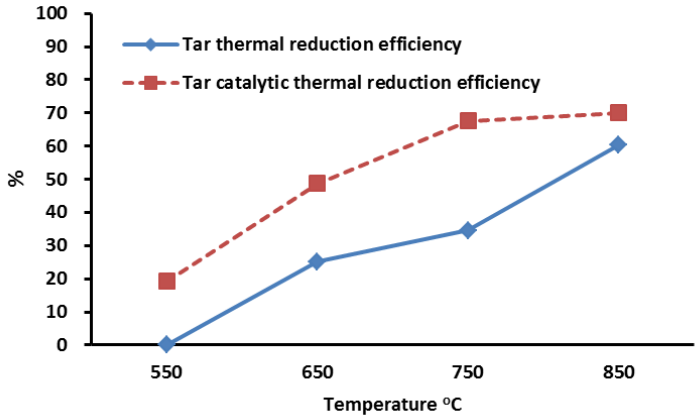

(b)

Figure 6. 6 Effect of temperature and CaO reactant on pyrolysis tar yield and tar reduction efficiency under the experimental conditions

Results reveal that both increasing the temperature and the addition of CaO significantly reduce the yield of pyrolytic tar content. As aforementioned in **Chapter 5**, tar decomposition is accelerated through both tar thermal cracking reactions (**Eq. (6.6)**) at higher temperature and tar catalytic thermal cracking reactions (**Eq. (6.12)**) with the addition of CaO reactant.

As depicted in **Figure 6.6 (a)**, tar content declines largely from 0.47 to 0.19 g/g-S-MSW as the pyrolysis temperature increased from 550 to 850 ^{o}C. Increasing the temperature significantly favors the decomposition of large organic compounds to produce light hydrocarbons as well as incondensable gases. When in-furnace CaO reactant is used, tar catalytic thermal cracking reactions are accelerated and tar yield is thus reduced and ranges from 0.38 to 0.14 g/g-S-MSW.

With respect to tar reduction efficiencies as presented in **Figure 6.6 (b)**, tar thermal reduction efficiency is significantly increased from 0 to 60.3% when increasing the temperature from 550 to 850 ^{o}C. When CaO is introduced into the furnace, tar catalytic thermal reduction efficiency is dramatically promoted from 19.2 to 70.1% under the experimental temperature. It is worth mentioning that the increment of tar catalytic thermal reduction efficiency declines with the increase of temperature. With the addition of CaO, tar catalytic thermal efficiency raises dramatically by 48.3% when pyrolytic temperature is increased from 550 to 750 ^{o}C; however, further increase of the temperature to 850 ^{o}C results in a limited enhancement of tar removal efficiency by approximately 2.5%. It is mainly attributed to the fact that at higher temperature as 850 ^{o}C, a great deal of tar is thermal cracked and the role of CaO reactant on tar cracking is not as important as that at lower temperature.

At temperature of 750 ^{o}C, pyrolytic tar yield reaches 0.31 and 0.15 g/g-S-MSW without and with the addition of CaO reactant; tar thermal reduction efficiency is 34.6% and tar catalytic thermal reduction efficiency achieves 67.5%.

To summarize, the most preferable working condition concerning both tar catalytic thermal cracking and HCl mitigation efficiency as discussed in **Section 6.3** is at temperature of 750 ^{o}C and Ca/Cl molar ratio of 2:1. Under such circumstance, HCl mitigation efficiency is 83.6%, pyrolytic tar yield is 0.15 g/g-S-MSW, and tar catalytic reduction efficiency reaches 67.5%.

6.4.2 Effect of temperature and CaO reactant on pyrolysis tar composition

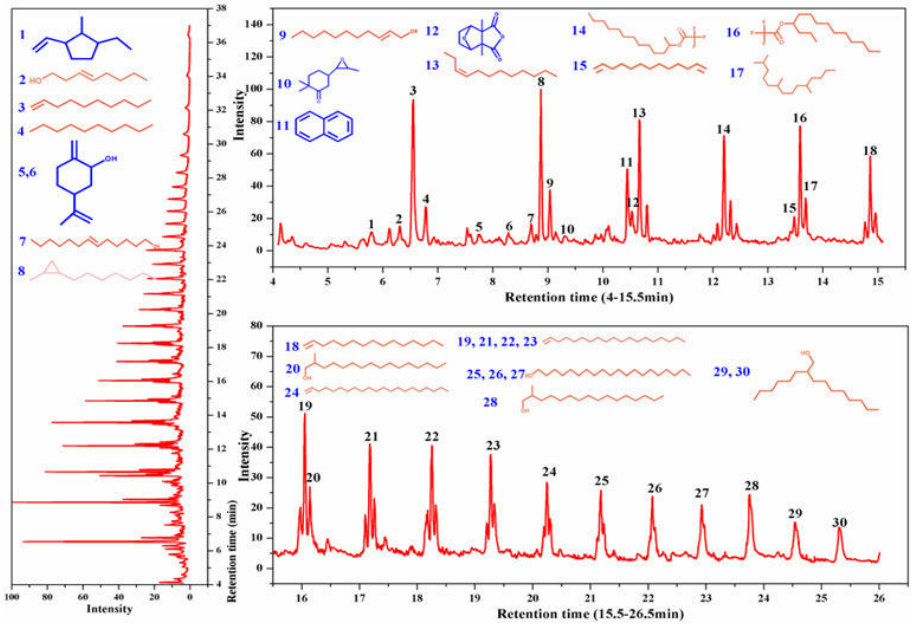

Figure 6. 7 Tar produced form S-MSW pyrolysis without CaO reactant at 550 °C

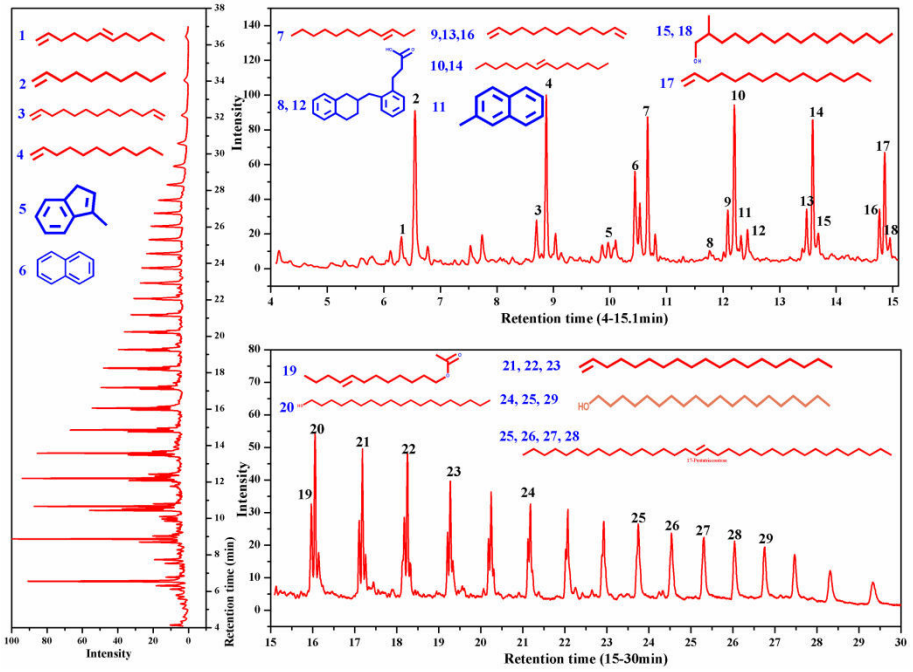

Figure 6. 8 Tar produced form S-MSW pyrolysis with CaO reactant at 550 °C

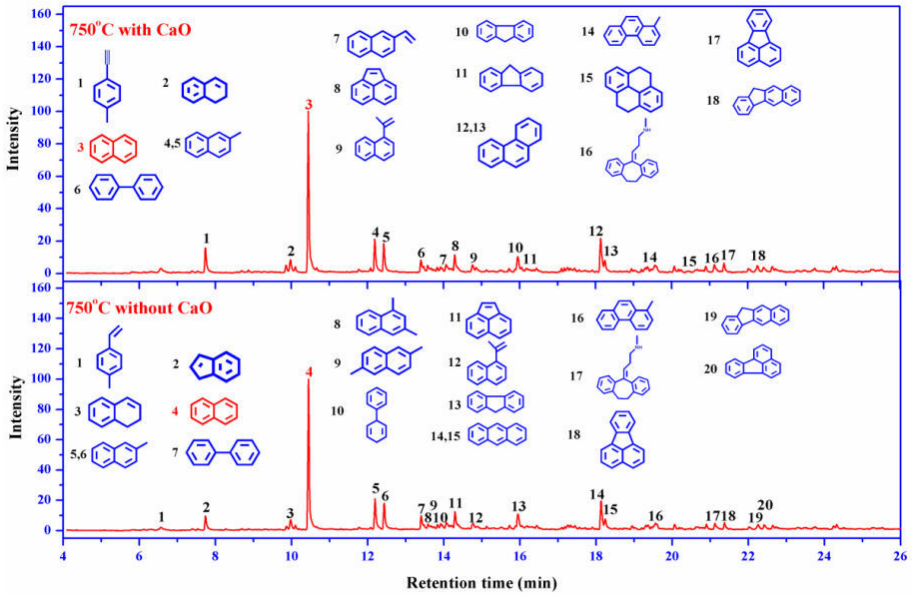

Figure 6. 9 Tar produced form S-MSW pyrolysis without/with CaO reactant at 750 °C

Figure 6.7, **Figure 6.8** and **Figure 6.9** present the typical pyrolytic tar compounds derived from S-MSW pyrolysis at 550 and 750 °C with and without the addition of CaO reactant. The detailed information about the detected compounds is summarized in **Table 6.3** and **Table 6.4**. As aforementioned in Section 5.2.1, the relative content of pyrolytic tar compounds are normalized and presented as Peak area% (the calculation method can be found as **Eq. (5.1)**).

As depicted in **Figure 6.7**, **Figure 6.8** and **Figure 6.9**, at lower temperature of 550 °C, aliphatic hydrocarbons are the major compounds in tar and only few aromatic species are detected. It is mainly due to the relative high content of plastics (PE 15% and PVC 10%) in S-MSW. Plastics easily decompose at low temperature and produce a great amount of olefins. However, at higher temperature of 750 °C, no aliphatic hydrocarbons are observed in the detected tar compounds and only aromatic compounds are identified. The reasons may be two folds: on the one hand, higher temperature facilitates the decomposition and reforming reactions of aliphatic hydrocarbons to form light gases such as CH_4, H_2, CO, and CO_2; on the other hand, dehydrocyclization reactions are accelerated at higher temperature to form aromatic compounds. Therefore, under the experimental conditions, aliphatic hydrocarbons are consumed and only aromatic compounds are found in pyrolytic tar at temperature of 750°C.

Table 6. 3 Typical tar compounds detected by GC/MS derived from S-MSW pyrolysis at 550 °C with or without CaO reactant

Time	550 °C pyrolysis without CaO			550 °C pyrolysis witht CaO		
(min)	Formula	Species	Area %	Formula	Species	Area %
5.80	C10H18	Cyclopentane, 1-ethenyl-3-ethyl-2-methyl	1.18	*	*	*
6.31	C8H16O	3-Octen-1-ol	1.32	C11H20	1,6-Undecadiene	2.32
6.55	C10H20	1-Decene	7.08	C10H20	1-Decene	8.07
6.78	C10H22	Decane	0.93	*	*	*
7.75	C10H16O	cis-p-mentha-1(7), S-dien-2-ol	0.98	*	*	*
8.28	C10H16O	cis-p-mentha-1(7), S-dien-2-ol	1.25	*	*	*
8.69	C14H28O	E-7-Tetradecenol	2.30	*	*	*
8.70	*	*	*	C13H24	1,12-Tridecadiene	2.46
8.87	C11H22	1-Undecene	6.15	C11H22	1-Undecene	6.32
9.04	C11H22O	trans-2-Undecen-1-ol	4.71	*	*	*
9.31	C11H18O2	Cyclohexanone, 2,2-dimethyl-5-(3-methyloxiran y)-	3.00	*	*	*
10.10	*	*	*	C10H10	1H-Indene, 3-methyl-	2.95
10.44	C10H8	Naphthalene	2.94	C10H8	Naphthalene	4.23
10.52	C10H12O4	Cantharidin	1.18	*	*	*
10.66	C12H24	3-Dodecene	5.05	C12H24	3-Dodecene	5.60
11.76	*	*	*	C20H22O2	Hydrocinnamic acid, o-[1,2,3,4-tetrahydro-2-naphthy)methyl)methyl]-	4.39
12.08	*	*	*	C13H24	1,12-Tridecadiene	2.19
12.20	C13H26	2-Trifluoroacetoxy tridecane	4.31	C14H28	7-Tetradecene	6.20
12.43	*	*	*	C11H10	2-methyl-Naphthalene	2.91
12.76	*	*	*	C20H22O	Hydrocinnamic	2.28

				2	acid, o-[1,2,3,4-tetrahydro-2-naphthy)methyl)methyl]-	
13.48	C13H24	1,12-Tridecadiene	2.20	C13H24	1,12-Tridecadiene	2.59
13.59	C14H28	7-Tetradecene	4.54	C14H28	7-Tetradecene	5.26
13.68	C17H35	Tetradecane, 2,6,10-trimethyl-	3.60	C17H35	Tetradecane, 2,6,10-trimethyl-	2.66
14.76	*	*	*	C13H24	1,12-Tridecadiene	2.49
14.86	C15H30	1-Pentadecene	3.77	C15H30	1-Pentadecene	4.13
14.95	*	*	*	C17H36O	2-methyl-1-Hexadecanol	2.27
15.97	*	*	*	C14H26O2	8-dodecen-1-ol, acetate	4.70
16.05	C19H38	1-Nonadecene	3.42	C19H40O	1-Nonadecene	6.34
16.14	C17H36O	1-Hexadecanol, 2-methyl-	3.00	*	*	*
17.18	C19H38	1-Nonadecene	3.71	C19H38	1-Nonadecene	2.67
18.25	C19H38	1-Nonadecene	3.83	C19H38	1-Nonadecene	2.66
19.27	C19H38	1-Nonadecene	3.53	C19H38	1-Nonadecene	2.16
20.24	C22H44	1-Docosene	3.90	*	*	*
21.18	C20H42O	1-Eicosanol	4.12	C20H42O	1-Eicosanol	2.18
22.07	C20H42O	1-Eicosanol	3.51	*	*	*
22.92	C20H42O	1-Eicosanol	3.59	C20H42O	1-Eicosanol	2.55
23.75	C17H36O	1-Hexadecanol, 2-methyl-	4.73	C17H36O	1-Hexadecanol, 2-methyl-	2.55
24.54	C16H34O	1-Decanol, 2-hexyl-	3.22	C16H34O	1-Decanol, 2-hexyl-	2.38
25.30	C16H34O	1-Decanol, 2-hexyl-	2.95	C16H34O	1-Decanol, 2-hexyl-	2.50

Table 6. 4 Typical tar compounds detected by GC/MS derived from S-MSW pyrolysis at 750 °C with or without CaO reactant

Time	750 °C pyrolysis without CaO			750 °C pyrolysis with CaO		
(min)	Formula	Species	Area %	Formula	Species	Area %
6.57	C9H10	Benzene, 1-ethenyl-4 -methyl-	1.89	*	*	*
7.74	C9H8	Indene	3.08	C9H8	Benzene, 1-ethenyl-4 -methyl-	5.85
9.98	C10H10	Naphthalene, 1,2-dihydro-	3.01	C10H10	Naphthalene, 1,2-dihydro-	3.48
10.44	C10H8	Naphthalene	27.19	C10H8	Naphthalene	31.13
12.19	C11H10	Naphthalene, 2-methyl-	8.15	C11H10	Naphthalene, 2-methyl-	8.36
12.43	C11H10	Naphthalene, 2-methyl-	6.84	C11H10	Naphthalene, 2-methyl-	6.65
13.40	C12H10	Biphenyl	4.36	C12H10	Biphenyl	2.75
13.58	C12H12	Naphthalene, 1,3-dimethyl-	1.60	*	*	*
13.92	C12H12	Naphthalene, 2,6-dimethyl-	2.30	*	*	*
14.07	C12H12	Benzene, 2,5-cyclohexadien-1-yl-	4.12	C12H10	Naphthalene, 2-ethenyl-	3.89
14.30	C12H8	Acenaphthylene	6.21	C12H8	Acenaphthylene	5.66
14.77	C13H12	1-Isopropeny1 naphthalene	2.15	C13H12	1-Isopropeny1 naphthalene	2.16
15.94	C13H10	Fluorene	5.39	C13H10	Fluorene	5.18
16.18	*	*	*	C13H12	Fluorene,2,4a -dihydro-	2.10
18.14	C14H10	Anthracene	7.18	C14H10	Phenanthrene	8.51
18.23	C14H10	Anthracene	2.98	C14H10	Phenanthrene	3.66
19.55	C15H12	Phenanthrene, 1-methyl-	2.84	C15H12	Phenanthrene, 1-methyl-	3.27
20.68	*	*	*	C16H14	Pyrene, 4,5,9,10- -tetrahydro-	1.88
21.12	C19H21N	Norrtriptyline	2.90	C19H21N	Norrtriptyline	1.34
21.37	C16H10	Fluoranthene	2.69	C16H10	Fluoranthene	2.08
22.26	C17H12	11H-Benzo [b]fluorene	2.55	C17H12	11H-Benzo [b]fluorene	2.04
22.42	C17H12	Fluoranthene, 2-methyl-	2.56	*	*	*

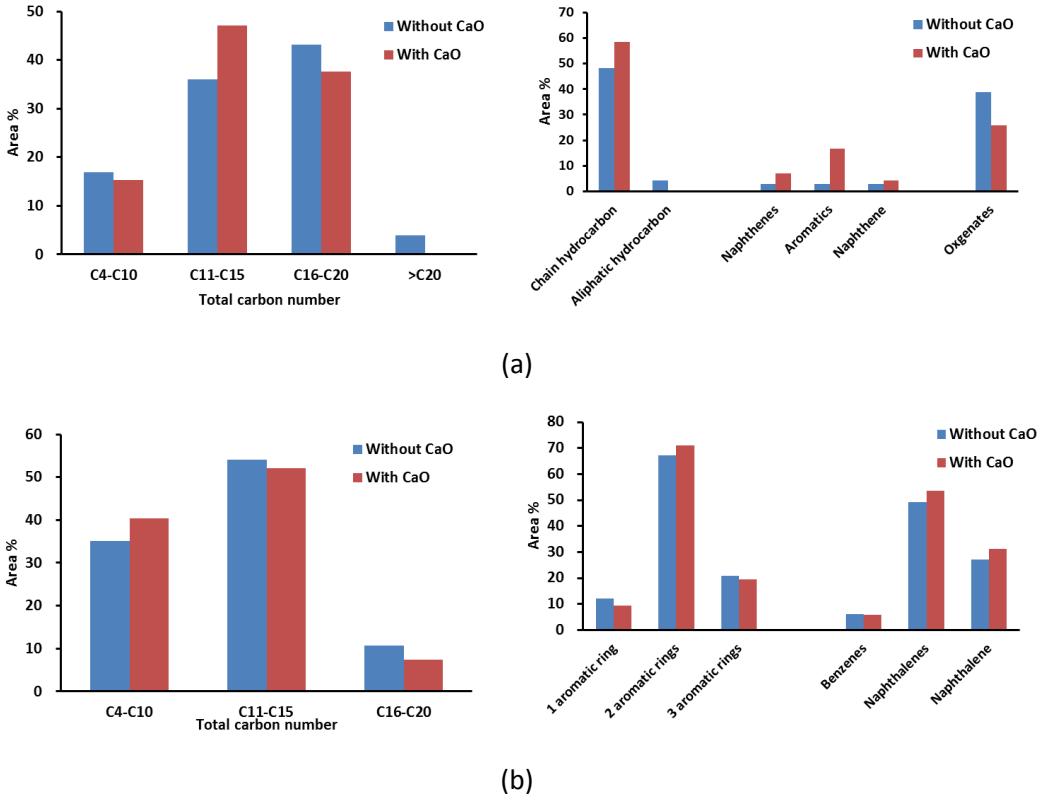

Figure 6. 10 Distributions of products in pyrolytic tar with and without the addition of CaO reactant: (a) pyrolysis at 550 °C and (b) pyrolysis at 750 °C

Figure 6.10 summarizes the relative content distribution of the products derived from S-MSW pyrolytic tar with and without the addition of CaO reactant at temperature of 550 and 750 °C.

As illustrated, at 550 °C, the main compounds are C11-C20 both in the absence of CaO reactant and with the addition of CaO, accounting for more than 79 % and 84% of the total relative content, respectively. The addition of CaO reactant slightly decreases the relative content of heavy compounds: no >C20 is identified with the addition of CaO, while without CaO, the content is approximately 4%; C16-C20 is reduced from 43% to 37% with CaO reactant. With regard to the relative distribution of organic categories, the addition of CaO reactant increases the content of both hydrocarbons (from 52% to 58%) and aromatic compounds (from 3% to 17%), but significantly decreases the relative content of oxygenated compounds from 39% to 25%, indicating that CaO reactant is effective to upgrade the quality of pyrolytic tar by deoxygenation reactions and thus reduce the oxygen content in tar compounds. Similar observations are reported by Zhu et al. [27], stating that tar produced are deoxygenated and desulfurized with the presence of CaO during coal pyrolysis.

In regard to the experiment conducted at temperature of 750 ^{o}C, only aromatic compounds are detected by GC/MS. It is observed that the carbon atom numbers of the major components are C11 - C15 under both non-catalytic and catalytic conditions. The compounds are a little bit lighter than that identified at 550 ^{o}C, where the major compounds are C11 - C20. With the increase of temperature from 550 to 750 ^{o}C, C16 - C20 species reduced dramatically from 43 - 11% without CaO addition and 37 – 7% in the presence of CaO reactant. This phenomenon directly demonstrates that thermal cracking and dehydrocyclization reactions of tar compounds occur with the increase of pyrolytic temperature. Similarly, the addition of CaO reactant slightly reduces the relative content of heavy compounds. C16 – C20 is reduced from 11% to 7% and C11 – C15 is declined from 54% to 52%. With respect to specific species, naphthalene and substituted naphthalene compounds are increased due to the addition of CaO reactant while the relative content of benzene is slightly decreased.

6.5 Summary of the chapter

Pyrolysis of S-MSW is experimentally investigated in this chapter. The effect of temperature and CaO reactant on pyrolytic product mass distribution, gas product characteristics, solid products characteristics, HCl gas removal and tar cracking and upgrading are determined. The main findings are as follows:

- Temperature is the determining factor affecting product yields by shifting the thermodynamic equilibriums of related chemical reactions. Higher temperature favors the generation of produced gas but declines the generation of tar and solid residues. When increasing the temperature from 550 to 850 ^{o}C, gas yield increased sharply from 81.9 to 451.4 mL/g-S-MSW. The presence of CaO increased the total gas yield by 30.0 to 58.8 mL/g-S-MSW and enhanced the H_2 yield by approximately 25% to 88% under experimental temperature.

- HCl is captured by CaO reactant and retained in solid phase products. Immobilization of chlorine can thus be achieved by using CaO reactant to avoid the presence of HCl in the produced gas. CaClOH is identified as the main dechlorination product by XRD observations. Increasing the temperature causes adverse effects on HCl mitigation efficiency and the increasing of Ca/Cl molar ratio promotes the efficiency.

- Both increasing the temperature and the use of in-furnace CaO reactant are effective ways to reduce pyrolytic tar content. At lower temperature, aliphatic hydrocarbons are the major compounds of pyrolytic tar, while at higher temperature, only aromatic species are detected. Increasing the temperature decomposes the heavy compounds and facilitates the formation of aromatic by thermal cracking and dehydrocyclization reactions. The use of in-furnace CaO reactant reduces the oxygen content in tar compounds and improves the content of naphthalene and substituted naphthalene compounds.

- The recommended working condition concerning both tar cracking and HCl mitigation efficiency from the present work is: temperature of 750 ^{o}C and Ca/Cl molar ratio of 2:1. Under such circumstance, HCl mitigation efficiency is 83.6%, pyrolytic tar yield is 0.15 g/g-S-MSW, and tar catalytic reduction efficiency reaches 67.5%.

6.6 Bibliography

[1] Naik DV, Kumar R, Tripathi D, Singh R, Kanaujia PK. Co-pyrolysis of Jatropha curcas seed cake and bituminous coal: Product pattern analysis. Journal of Analytical and Applied Pyrolysis. 2016;121:360-8.

[2] Al-Farraji A, Marsh R, Steer J. A comparison of the pyrolysis of olive kernel biomass in fluidised and fixed bed conditions. Waste and Biomass Valorization. 2017;8:1273-84.

[3] Iisa K, French RJ, Orton KA, Yung MM, Johnson DK, ten Dam J, et al. In situ and ex situ catalytic pyrolysis of pine in a bench-scale fluidized bed reactor system. Energy & Fuels. 2016;30:2144-57.

[4] Amutio M, Lopez G, Alvarez J, Olazar M, Bilbao J. Fast pyrolysis of eucalyptus waste in a conical spouted bed reactor. Bioresource technology. 2015;194:225-32.

[5] Liu G, Xu Q, Dong X, Yang J, Pile LS, Wang GG, et al. Effect of Protective Gas and Pyrolysis Temperature on the Biochar Produced from Three Plants of Gramineae: Physical and Chemical Characterization. Waste and Biomass Valorization. 2016;7:1469-80.

[6] Zhang J, Liu J, Liu R. Effects of pyrolysis temperature and heating time on biochar obtained from the pyrolysis of straw and lignosulfonate. Bioresource technology. 2015;176:288-91.

[7] Gumeci C, Leonard N, Liu Y, McKinney S, Halevi B, Barton SC. Effect of pyrolysis pressure on activity of Fe–N–C catalysts for oxygen reduction. Journal of Materials Chemistry A. 2015;3:21494-500.

[8] Manyà JJ, Ortigosa MA, Laguarta S, Manso JA. Experimental study on the effect of pyrolysis pressure, peak temperature, and particle size on the potential stability of vine shoots-derived biochar. Fuel. 2014;133:163-72.

[9] Touray N, Tsai W-T, Li M-H. Effect of holding time during pyrolysis on thermochemical and physical properties of biochars derived from goat manure. Waste and Biomass Valorization. 2014;5:1029-33.

[10] Zhang X, Rajagopalan K, Lei H, Ruan R, Sharma BK. An overview of a novel concept in biomass pyrolysis: microwave irradiation. Sustainable Energy & Fuels. 2017;1:1664-99.

[11] Prathiba R, Shruthi M, Miranda LR. Pyrolysis of polystyrene waste in the presence of activated carbon in conventional and microwave heating using modified thermocouple. Waste Management. 2018.

[12] Zheng X, Ying Z, Wang B, Chen C. Effect of Calcium Oxide Addition on Tar Formation During the Pyrolysis of Key Municipal Solid Waste (MSW) Components. Waste and Biomass Valorization. 2018:1-10.

[13] Kabir G, Hameed B. Recent progress on catalytic pyrolysis of lignocellulosic biomass to high-grade bio-oil and bio-chemicals. Renewable and Sustainable Energy Reviews. 2017;70:945-67.

[14] Wei L, Xu S, Liu J, Liu C, Liu S. Hydrogen production in steam gasification of biomass with CaO as a CO2 absorbent. Energy & Fuels. 2008;22:1997-2004.

[15] Han L, Wang Q, Yang Y, Yu C, Fang M, Luo Z. Hydrogen production via CaO sorption enhanced anaerobic gasification of sawdust in a bubbling fluidized bed. International journal of hydrogen energy. 2011;36:4820-9.

[16] Dong J, Nzihou A, Chi Y, Weiss-Hortala E, Ni M, Lyczko N, et al. Hydrogen-Rich Gas Production from Steam Gasification of Bio-char in the Presence of CaO. Waste and Biomass Valorization. 2017;8:2735-46.

[17] Dong J. MSWs gasification with emphasis on energy, environment and life cycle assessment: Ecole des Mines d'Albi-Carmaux; 2016.

[18] Nie F, He D, Guan J, Zhang K, Meng T, Zhang Q. The influence of abundant calcium oxide addition on oil sand pyrolysis. Fuel Processing Technology. 2017;155:216-24.

[19] Chen H, Dou B, Song Y, Xu Y, Zhang Y, Wang C, et al. Pyrolysis characteristics of sucrose biomass in a tubular reactor and a thermogravimetric analysis. Fuel. 2012;95:425-30.

[20] Efika EC, Onwudili JA, Williams PT. Products from the high temperature pyrolysis of RDF at slow and rapid heating rates. Journal of Analytical and Applied Pyrolysis. 2015;112:14-22.

[21] Li AM, Li XD, Li SQ, Ren Y, Chi Y, Yan JH, et al. Pyrolysis of solid waste in a rotary kiln: influence of final pyrolysis temperature on the pyrolysis products. Journal of Analytical and Applied Pyrolysis. 1999;50:149-62.

[22] Özbay N, Pütün A. Pyrolysis of peach pulp: effect of chemical additives. Energy Sources, Part A: Recovery, Utilization, and Environmental Effects. 2014;36:2546-54.

[23] Florin NH, Harris AT. Enhanced hydrogen production from biomass with in situ carbon dioxide capture using calcium oxide sorbents. Chemical Engineering Science. 2008;63:287-316.

[24] Xie X, Li Y, Wang W, Shi L. HCl removal using cycled carbide slag from calcium looping cycles. Applied Energy. 2014;135:391-401.

[25] Yongbin J, Jiejie H, Yang W. Effects of calcium oxide on the cracking of coal tar in the freeboard of a fluidized bed. Energy & fuels. 2004;18:1625-32.

[26] Li Y, Wang W, Cheng X, Su M, Ma X, Xie X. Simultaneous CO2/HCl removal using carbide slag in repetitive adsorption/desorption cycles. Fuel. 2015;142:21-7.

[27] Tingyu Z, Shouyu Z, Jiejie H, Yang W. Effect of calcium oxide on pyrolysis of coal in a fluidized bed. Fuel Processing Technology. 2000;64:271-84.

Chapter 7

Life cycle assessment of MSW thermal technologies with different dehydrochlorination options

7.1 Introduction

Municipal solid waste (MSW) thermal technologies have become one of the most promising options to achieve both waste treatment and energy recovery [1]. MSW incineration, for example, is playing an increasingly important role and is developing rapidly worldwide in the past few decades [2-5]. By incineration, mass and volume of MSW can be dramatically reduced and its heating value can be recovered to generate electricity and/or heat [6-8]. However, the release of harmful pollutants, especially NO_x, SO_x, dioxins and heavy metals from stack causes severe environmental burdens and seriously threatens human health [9]. In addition, as previously mentioned, chlorine in MSW causes serious problems during MSW incineration, related to corrosion, toxic organics formation, and acidification, etc.

Instead of converting all the energy contained in MSW to thermal energy in flue gas by incineration, pyro-gasification technology allows the generation of fuel gases (syngas) and bio-oil (tar) from MSW that can be further utilized to create heat and/or electricity or alternatively as feedstocks to produce fuels or chemicals [10-12].

As stated by **Chapter 1**, thorough and systematic evaluation of current MSW thermal technologies is of great importance to determine a more energy efficient and environmental friendly waste to energy (WtE) route. As a result, this chapter is focused on the assessment

and optimization of current MSW thermal conversion technologies using LCA methodology. In addition, special attention has been paid to pyro-gasification-based WtE systems with different dehydrochlorination strategies (for example ex-situ low temperature dehydrochlorination; ex-situ high temperature dehydrochlorination, and in-situ dehydrochlorination). The aim is to provide scientific basis for decision makers regarding the improvement of local waste management plan. With this overall objective, two LCA studies are performed:

- **Section 7.2** is mainly dedicated to give a systematic and holistic comparison between current commercial MSW thermal conversion technologies including conventional incineration, pyrolysis, gasification-melting, and gasification with ex-situ high temperature dehydrochlorination as performed by Lahti Energia; environmental burdens caused by different systems as well as the main contributor process are identified in this section;

- **Section 7.3** is mainly focused on the environmental performance of pyro-gasification-based WtE systems with different dehydrochlorination strategies, including ex-situ low temperature dehydrochlorination (gasification-melting); ex-situ high temperature dehydrochlorination (gasification, Lahti), and hypothetical in-situ dehydrochlorination systems; the aim is to determine the role of dehydrochlorination strategy in WtE systems;

- **Section 7.4** conducts the sensitivity analysis; key parameters adopted in this study are varied to examine the effect of data use on the final results;

- **Section 7.5** summarizes the chapter.

7.2 LCA of four current commercial technologies

Guided by ISO standards 14040 series [13], the general framework of LCA studies consists of four phases: (1) goal and scope definition; (2) life cycle inventory (LCI); (3) life cycle impact assessment (LCIA); and (4) interpretation. These four steps are described separately below.

7.2.1 Goal and scope definition

According to literature [10, 14], there are more than 100 gasification-based WtE plants around the world so far; and most of them are located in Japan, generally based on gasification-melting technology; or on a small scale, based on pyrolysis. In Europe, the implementation of pyro-gasification-based WtE technologies have become more and more

popular in recent years, such as Lahti in Finland [15], Averoy in Norway [16], and waste pyrolysis plant Burgau in Germany [17]. **Table 7.1** generally summarizes some of the waste gasification plants running in Europe [18].

Table 7. 1 Waste gasification plants running in Europe, data source from Molino et al. [18]

Site	Input	Technology
Averoy, Norway	MSW	Gasification and combustion
Hurum, Norway	MSW and industrial waste	Gasification and combustion
Sarpsborg, Norway	MSW and industrial waste	Gasification and combustion
Forus, Norway	MSW	Gasification and combustion
Karlsruhe, Germany	MSW and commercial waste	Pyrolysis and gasification
Minden, Germany	MSW and commercial waste	Gasification and combustion
SchwarzePumpe, Germany	plastics, RDF, wood, sewage, sludge, lubricants, coal RDF	Gasification
Rudersdorf, Germany	plastics, RDF, wood, sewage, sludge, lubricants, coal RDF	Gasification
Freiberg, Germany	sewage sludge + MSW	Pyrolysis and entrained flow gasification
Lathi, Finland	biomass fuels (up to 40% RDF)	Circulating fluidized-bed boiler with gasification
Greve-in-Chianti, Italy	pelletized RDF	Gasification
Norrsundet, Sweden	MSW and industrial waste	Gasification

Among those applications, it is observed that most of the pyro-gasification processes are linked to a downstream energy recovery device, or known as “two-step oxidation” WtE scheme [10, 19-21]. One of the advantages of pyro-gasification technologies is the possibility to achieved energy efficient and environmental friendly utilization of the produced gas rather than directly incinerate the heterogeneous waste.

Therefore, the primary aim of this section is to comprehensively evaluate the environmental performance of pyro-gasification-based WtE systems and to compare them with typical conventional MSW incineration scenario. As a result, a total of four systems are

considered in this section, with the LCA system boundaries illustrated in **Figure 7.1**. S1 represent conventional waste incineration plants and it is set as the baseline scenario for the comparison; S2 is a pyrolysis-based WtE system; S3 represent gasification with ex-situ high temperature dehydrochlorination as performed by Lahti Energia; and S4 refers to gasification-melting technology.

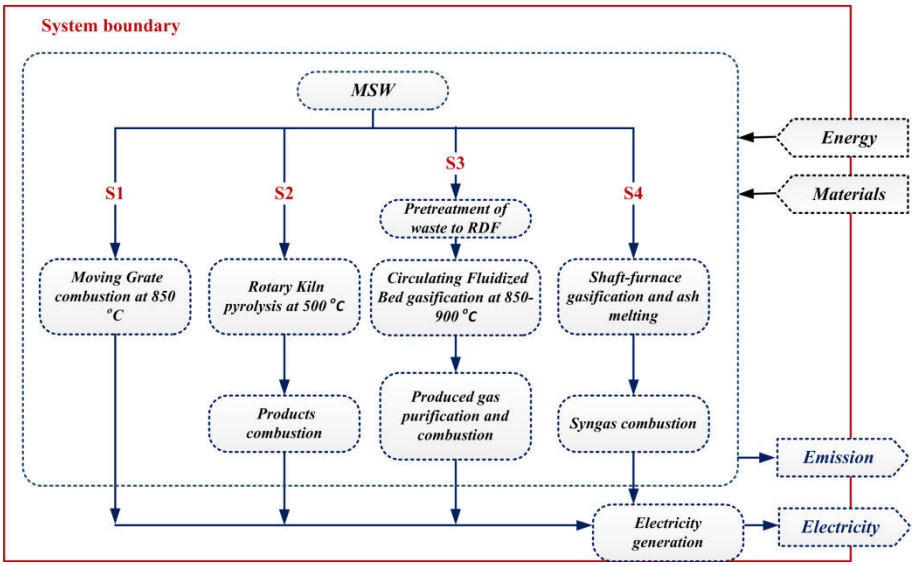

Figure 7. 1 System boundary of the considered scenarios

Accordingly, the life cycle assessment of the present work starts from the entry of MSW into waste treatment plant, and includes MSW pretreatment, MSW thermal conversion (incineration, pyrolysis, or gasification), downstream electricity generation, air pollution control and final residues disposal stages as illustrated in **Figure 7.1**. Input and output energy/material flows are shown with arrows in the figure. MSW collection and transportation before entering the system boundary are excluded from this, as they are identical in all systems [22]. Wastewater effluent during treatment is not considered due to the lack of data; however this assumption will not cause significant deviations since modern incinerators are designed with wastewater treatment, recycling and reused equipment in the plant to meet the 'zero discharge' target [23, 24]. Besides, energy/emission due to plant construction and demolition is also omitted, as it is negligible compared to the total burdens aroused by plant operation [25].

Not only the direct energy/material consumption and emission are considered, the upstream and downstream input and output from background system are also taken into account in this study. Acquisition of auxiliary materials and energy, such as diesel, lime, etc.,

is also considered; thus, the calculation type of 'cradle to grave' is achieved. The output electricity from the systems are used to substitute the same amount of electricity from the E.U. average electricity grid, and thus the corresponding environmental emissions to produce the same amount of electricity is considered to be avoided.

One tonne of MSW (as received basis) is defined as the functional unit. Therefore, inventory data of all input and output materials, energy and emissions are converted to this basis. MSW characteristics are determined in accordance with typical values of the E.U. average MSW fractions, and are shown in **Table 7.2** [26, 27]. Background data related to raw material production are mainly obtained from Gabi software.

Table 7. 2 Physical compositions of MSW

	MSW composition (wt. %)						
	Bridgeable waste	Paper	Plastic	Textile	Glass	Metal	Other [a]
European average	35.0	22.0	10.0	3.0	6.0	4.0	20.0

[a] "other" waste include mixed textiles, leather, rubber, laminates, e-waste, inert materials (e.g. gravel, ceramics, ash), etc.

7.2.2 Process description and data source

7.2.2.1 S1: MSW Direct Incineration

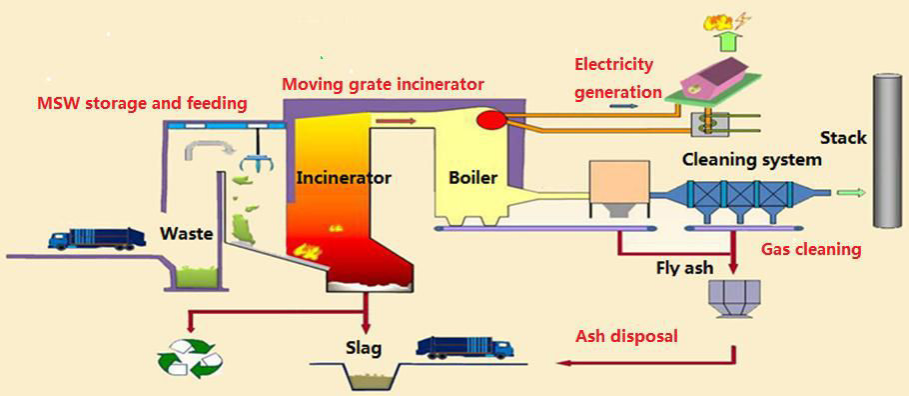

Figure 7. 2 Schematic diagram of the considered incineration system

As aforementioned, S1 reflects the conventional incineration process under the local condition of France and is set as the baseline scenario for the comparison. Data used for the calculation are mainly from the research of Beylot et al. [8] and Nzihou et al. [28]. According to the literature, incinerators in France are predominately moving grate (MG) type. A main

advantage of MG incinerator is its capacity to treat unsorted waste. Therefore, a typical MSW incineration plants using MG type technologies is adopted in this work and the schematic diagram of the considered incineration system is illustrated in **Figure 7. 2**. The electricity generation efficiency is considered at average level according to the literature surveys and set as 18%. The APC systems consists of selective non-catalytic reduction (SNCR) for denitrification with use of reagents for dioxins abatement, dry process for acid gas removal, and bag filter for particles removal [2, 8]. Metal content in the bottom ash is recovered and the rest of the residues (APC residues are firstly solidified/stabilized) are disposed in landfill site.

7.2.2.2 S2: MSW pyrolysis system

S2 refers to the MSW pyrolysis system. The selected plant "Burgau MW Pyrolysis Plant", located in Günzburg, Germany, has a capacity of 20,000 t/a [29]. After shredded to 30 cm, the MSW is decomposed in the absence of air in an indirect heated rotary kiln at temperature of 500-600 °C with a residence time of 1 h. The rotary kiln is heated indirectly with flue gas from the pyrolysis gas incineration. The pre-dedusted pyrolysis gas is extracted and charged to a combustion chamber to be incinerated with an excess air of approx. 5 to 8 %, at temperature of approximately 1,200 °C. The residues are considered to be landfilled and the metals are recycled. The plant electricity efficiency (gross) is around 25.9%. The same APC systems as incineration systems are considered.

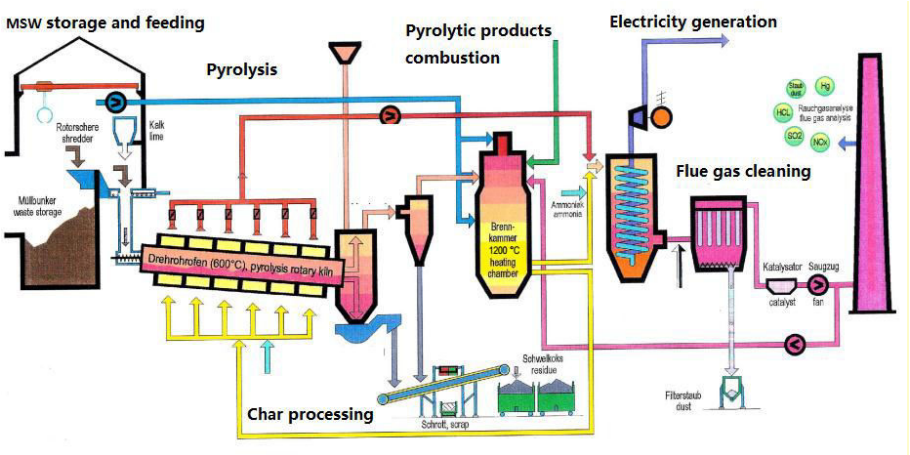

Figure 7. 3 Schematic diagram of the considered pyrolysis system, data obtained from the report of DGEngineering [29]

7.2.2.3 S3: MSW gasification system

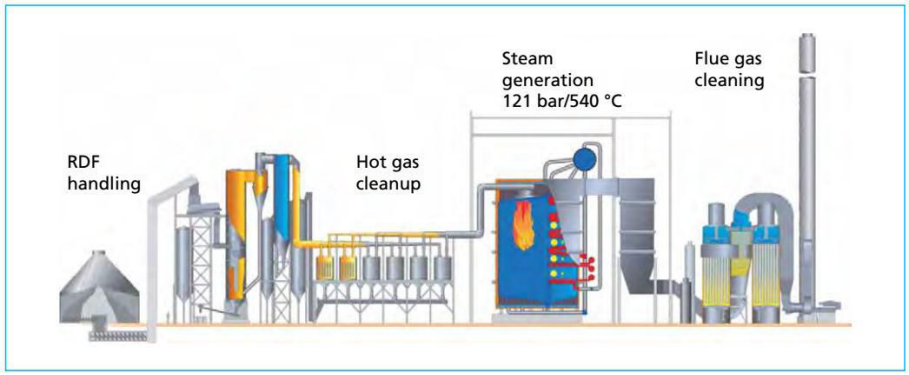

Figure 7. 4 Schematic diagram of the considered gasification system, data obtained from the work of Bolhàr-Nordenkampf et al. [30]

As aforementioned in **Chapter 1**, S3 represents gasification system with ex-situ high temperature purification of the produced syngas as performed by Lahti Energia [30, 31]. The plant is based on circulating fluidized bed (CFB) for the production of electricity (50 MW) and district heat (90 MW). Its commercial operation was started in 2012, and approximately 250,000 tons of SRF can be handled annually [32]. The gasifier runs at 850-900 ^{o}C under atmospheric pressure. As a result of gasification, the feedstock (SRF) turns into produced syngas. The produced syngas then undergoes a cooling and purification step at 400 ^{o}C. This temperature is chosen because on one hand, corrosion caused impurities (e.g. alkali chlorides) can condense as solid particles; on the other hand, avoid tar condensation. Heat from the gas cooling step is recovered to preheat the feed water. The cleaned syngas passes through a filter to remove particles, before combustion in a secondary chamber at 850 ^{o}C. The flue gas is relatively clean to bear a higher quality of steam superheated in the boiler (540 ^{o}C, 121 bar). The electricity generation efficiency is calculated as 27.4% based on the technical report. And the same APC systems are assumed as for the incineration case. For solid residues disposal, the produced bottom ash is landfilled; while the fly ash and air pollution control (APC) residues require safety stabilization before final disposal

7.2.2.3 S4: MSW gasification-melting system

As previously mentioned, MSW gasification-melting plants is the most popular gasification-based WtE technologies. The main reason to choose this kind of technology is its possibility to effectively recover materials [33]. The selected plant, having a total throughput of 80 MW, is located in Japan and is one of the largest gasification-melting facilities in the

world. The MSW is charged into a shaft-furnace type gasifier from the top with coke and limestone, and the ash is melt at the bottom by O_2-rich air at 1000–1800 °C. No pre-treatment of the incoming waste is required. The syngas is combusted to generate steam at 400 °C and 3.92 MPa. The net electricity efficiency reaches 17% [33]. The APC system is considered the same as that adopted in incineration system. The molten materials from the gasifier are magnetically separated into slag and metals, which can be completely recycled.

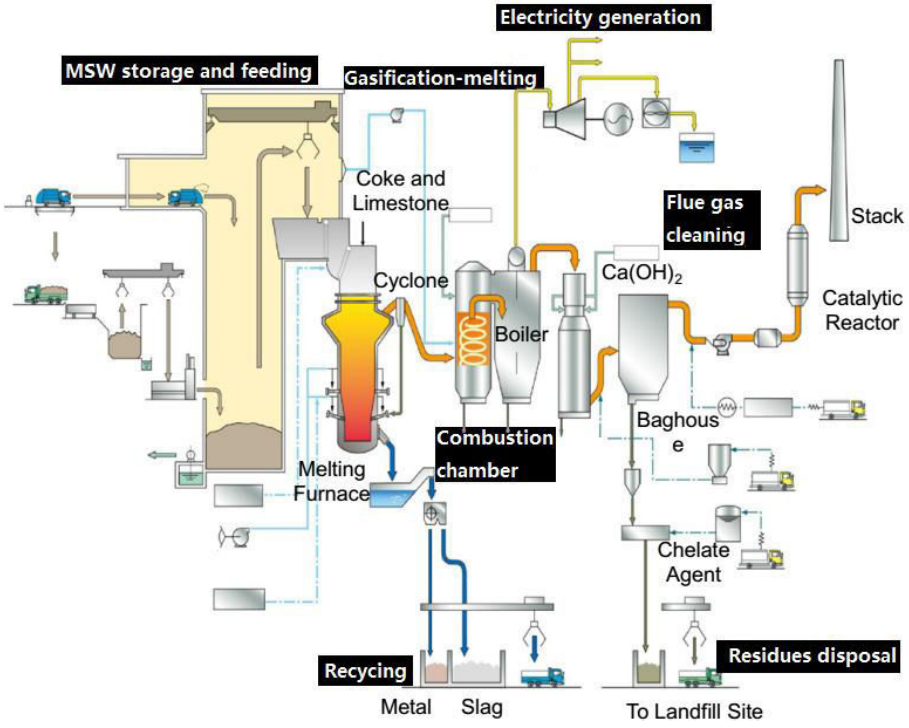

Figure 7. 5 Schematic diagram of the considered gasification-melting system, data obtained from the work of Tanigaki et al. [33]

7.2.2.4 Pretreatment of MSW

Since SRF is used in gasification scenario (i.e. S3), energy and materials consumption during SRF production is also considered as input streams. According to previous works [34, 35], energy consumption in the SRF production process mainly includes electricity and fuels and is estimated at 804 MJ of electricity and 32.3 MJ of diesel per ton of MSW.

Storage for dehydration and shredding for size reduction of MSW is also important for other systems; however, electricity consumption in this stage is considered as internal electricity consumption of the power plant and has been considered in this study.

7.2.2.5 Energy and materials recovery

In the present work, only electricity generation is considered as energy recovery, which means heat recovery or combined electricity and heat (CHP) system is not taken into account. For materials recovery, ferrous metals and aluminum recovery from bottom ash is included in this work.

7.2.3 Life cycle inventory

The compiled life cycle inventory (LCI) of the present LCA study is displayed in **Table 7.3**. Besides, some key assumptions are made to fulfill the calculation and are listed as follows:

- Only fossil-derived CO_2 emission is considered as a contributor to GW, biogenic CO_2 emission is regarded to be carbon neutral.
- The raw MSW compositions are considered identical for all the systems.
- Emissions during the ash disposal process are obtained from literature, in which statistical data that are currently used for dealing with MSW in the UK and in Europe are applied as the calculation basis [36].

Table 7. 3 Material and energy flows for the considered systems (data are presented based on 1 t/MSW)

	Unit	S1	S2	S3	S4
Input streams					
Electricity for MSW pretreatment	kWh			70.00	
Coke as reducing agent and auxiliary fuel	kg				49.00
Electricity for ash treatment	kWh	2.48	2.74	4.79	2.32
Diesel for ash treatment	L	0.41	0.31	0.46	0.18
Limestone as viscosity regulator	kg				70.20
Lime for flue gas purification	kg	16.63	18.58	18.71	18.70
Ammonia	kg	0.52	0.52	0.52	0.52
Active carbon	kg	0.56	0.56	0.56	0.56
$FeSO_4 \cdot 7H_2O$	kg	3.85	5.18	10.07	5.19
Output streams					
Electricity output a	kWh	506.76	593.17	783.49	558.90
Bottom ash	kg	277.43	266.56	102.73	165.76
Air pollution control residues	kg	48.09	64.72	125.93	64.90
Ferrous metals recovery	kg	15.46	10.76	7.98	12.60
Aluminum recovery	kg	11.83	6.82	4.64	0.05
Process-specific emissions					
PM	g	5.68	6.90	9.86	12.57
SO_2	g	40.46	39.43	34.50	18.86
HCl	g	31.07	25.13	4.93	21.15
NO_x	g	763.17	822.52	793.44	120.01
NH_3	g	24.64	24.64	24.64	28.57
Dioxins	g	4.51E-08	4.93E-09	9.86E-09	4.97E-09
CO	g	35.11	49.28	9.86	35.43
VOC	g	2.78	0.00	0.00	0.00
HF	g	0.87	0.00	0.00	0.00
Waste-specific emissions					
CO_2-total	kg	802.48	808.15	808.21	808.17
CO_2-fossil	kg	416.97	419.92	419.95	602.29
Hg	g	3.14E-02	5.42E-02	4.93E-04	9.86E-02

As aforementioned, electricity generation is served to substitute the same amount of electricity from conventional electricity matrix (in this study, the E.U. average electricity matrix is adopted as the reference and it is presented in **Table 7.4** [37]).

Table 7. 4 The E.U. average electricity matrix (Unit: %)

	EU average electricity matrix, %
Fossil fuels	47.2
Nuclear	24.09
Hydroelectric	16.64
Geothermal	0.33
Solar	1.99
Tide and wave	0.01
Wind	5.92
Biomass and waste	4.14

7.2.4 Life cycle impact assessment

As pointed out in **Chapter 2**, the CML (baseline) methodology is used to aggregate the LCI results [38]. Six impact categories are considered, including three non-toxic and three toxic impacts: non-toxic, Climate change - GWP100, Acidification Potential - AP, and Eutrophication Potential - EP; and toxic, Terrestrial eco-toxicity - TETP, Freshwater aquatic eco-toxicity - FAETP and Human toxicity - HTP. Results based on characterized values are used. Besides, normalized LCIA values are also used to quantify the relative magnitude of different impacts.

7.2.5 Interpretation and discussion

7.2.5.1 Characterized environmental impact assessment results

Figure 7. 6 reports the characterized environmental impacts of the considered four MSW thermal conversion systems. As aforementioned, the environmental impact categories of three non-toxic (i.e. GWP, AP, and EP), and three toxic (i.e. TETP, FAETP, and HTP) parameters are taken into consideration in this work. Results reveal that negative impacts (i.e. environmental savings) can always be obtained for the environmental impact categories of AP, FAETP, and HTP from the four considered systems; however, positive impacts (i.e.

environmental burdens) of GWP is observed for all the systems, which is principally due to the fossil-origin CO_2 emission derived from MSW.

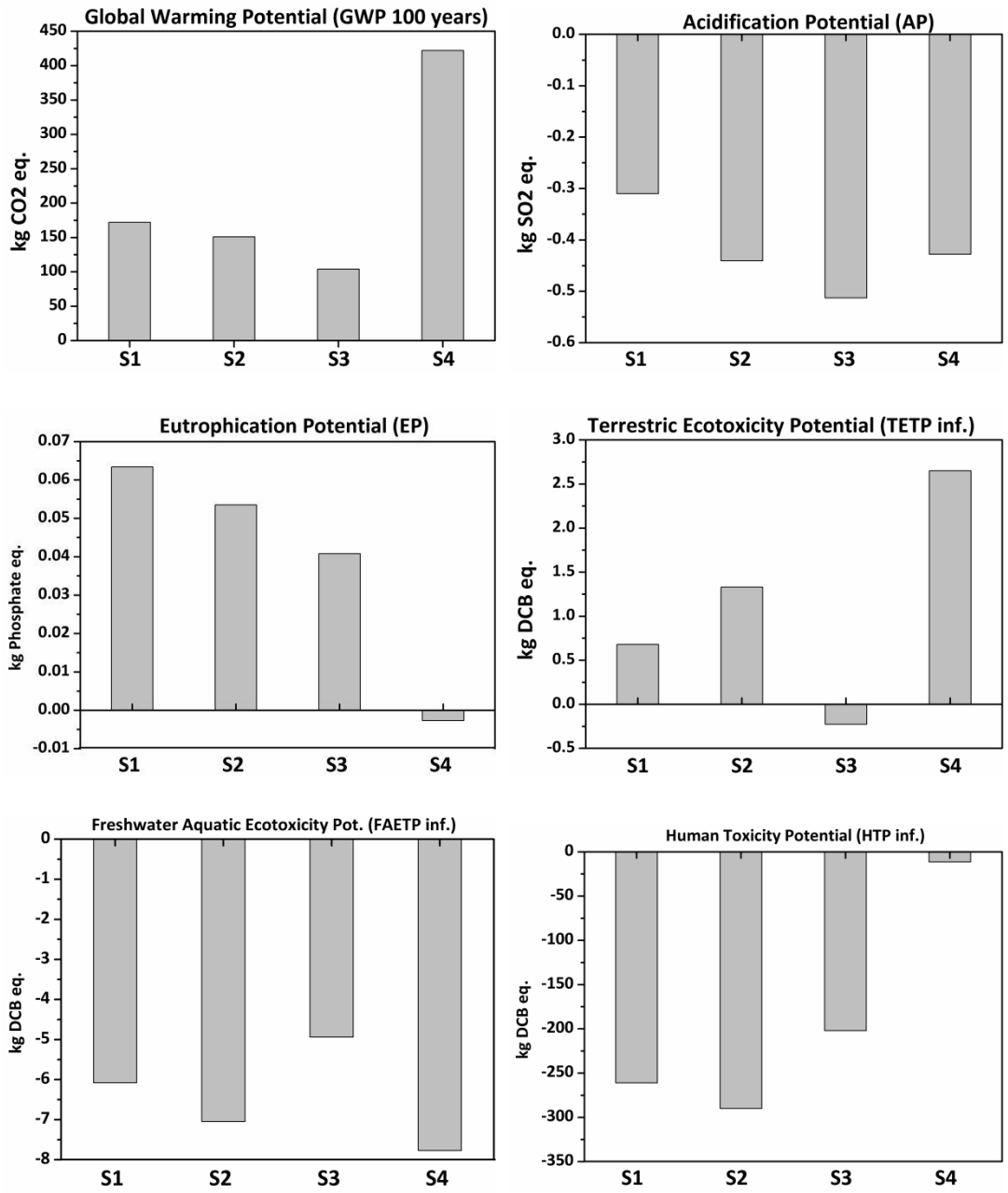

Figure 7. 6 Characterized environmental impacts of different systems: S1, Incineration system; S2, Pyrolysis system; S3, Gasification system; and S4, Gasification-melting system

Gasification system (S3) leads the least environmental impacts for most of the considered categories such as GWP, AP, and TETP; but it also causes the highest environmental burdens of FAETP. Besides, the environmental impact category of HTP from S3 is also relatively high and ranked 3rd among the evaluated systems. Gasification-melting

system (S4) performs worst in the environmental categories of GWP, TETP, and HTP; and it also has a relatively poor behavior on environmental impact of AP, ranking 3rd among the four systems. However, S4 system is effective to reduce the environmental impact of EP and FAETP; least environmental burdens of EP and FAETP are generated from S4 compared to the other three systems. For MSW direct incineration system (S1), the environmental impacts of AP and EP from S1 are the highest of all the systems; unfortunately, no impact category from S1 is ranked the best among the systems. Most of the environmental impacts derived from pyrolysis system (S2) are ranked in the middle level of the four systems, except for HTP; HTP from S2 is the lowest among the systems. **Table 7.5** summarizes the ranking results of the impact categories. Accordingly, the environmental sustainability of each system in descending order is: S3, Gasification > S2, Pyrolysis > S4, Gasification-melting > S1, Incineration (">" means the former system performs better than the latter one).

Table 7. 5 Summary of the ranking results of environmental impact categories

System	Non-toxic impact categories			Toxic impact categories			SUM [b]
	GWP	AP	EP	TETP	FAETP	HTP	
S1	3 [a]	**4**	**4**	2	3	2	18
S2	2	2	3	3	2	**1**	13
S3	**1** [c]	**1**	2	**1**	**4**	3	12
S4	**4**	3	**1**	**4**	**1**	**4**	17

[a] the number represent the ranking result of the impact categories: 1 refers to the best performance and 4 represent the worst performance;

[b] the sum of the ranking results is a reference to compare the overall performance of the systems;

[c] the best and worst performances of the considered system on the specific impact categories are represented by bold type and marked as red and dark blue, respectively.

7.2.5.2 Contribution analysis of the environmental impacts

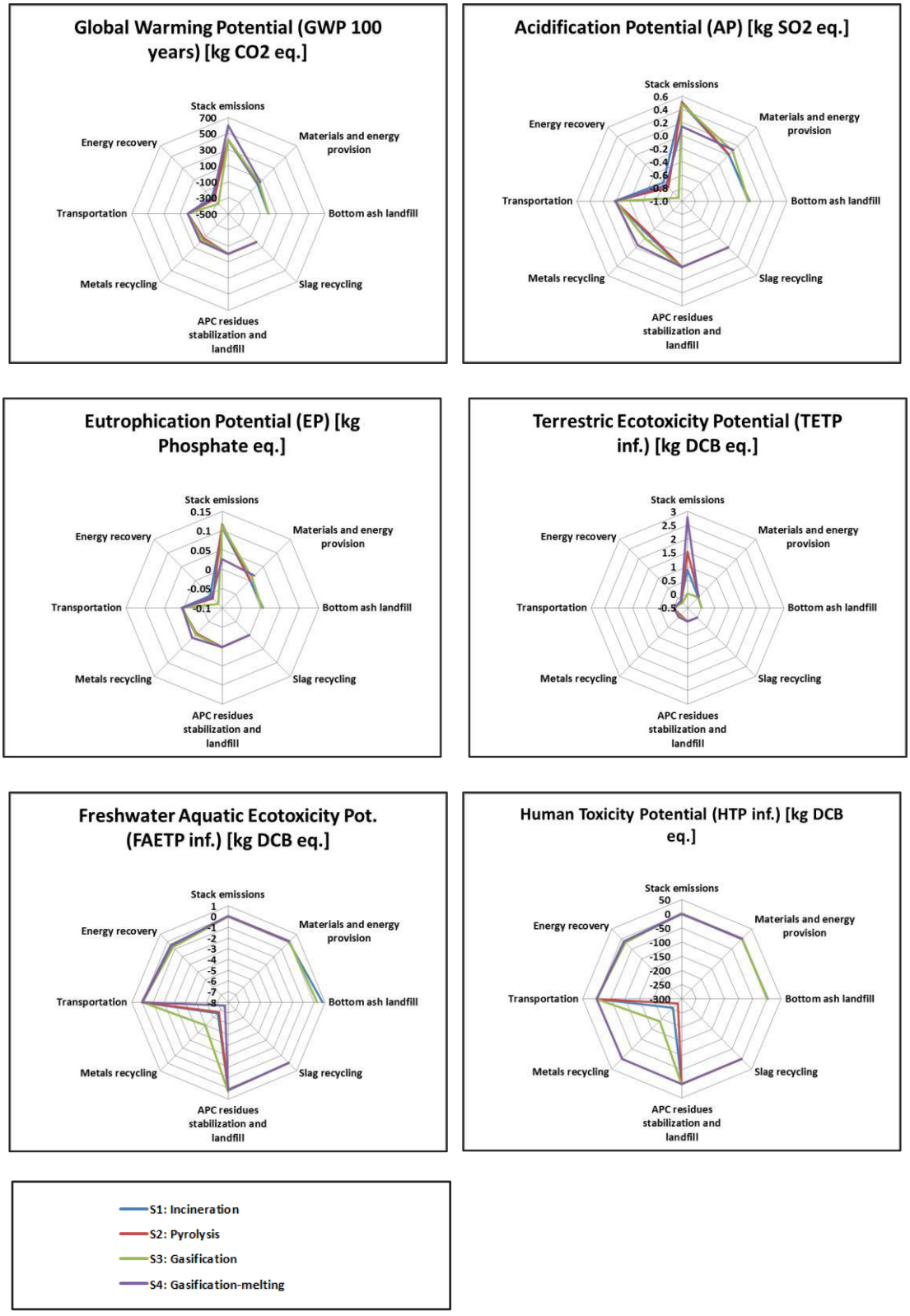

Figure 7. 7 Contribution analysis of the selected environmental impact categories

In order to identify the main sources of environmental burdens and benefits, the overall environmental impacts are distributed into eight life cycle stages, including: stack emissions, materials and energy provision, bottom ash landfill, slag recycling, APC residues stabilization and landfill, metals recycling, residues transportation, and energy recovery. **Figure 7.7** reports the contribution analysis results of different contributors. Generally, the impacts from "stack emissions", "energy recovery" and "metals recycling" are the most noteworthy contributors, with the former one being the most important environmental burdens and the latter two being environmental savings (negative values as shown in **Figure 7. 7**). "Energy recovery", due to the substitution of fossil fuels combustion related to electricity production, makes a significant contribution to reduce the GWP, AP, and EP impacts. "Metals recycling" shows also a further avoided contribution, in particular for toxicity impacts regarding FAETP and HTP.

With respect to specific impact categories, the environmental burdens of GWP is mainly caused by "stack emission", accounting for approximately 417, 420, 420, and 602 kg CO_2 eq. of S1, S2, S3, and S4 system, respectively. It is worth noting that GWP from "stack emission" of S1, S2 and S3 systems is quite similar (ranges from 417 - 420 kg CO_2 eq.), but the value is much higher from S4 system. The reason is mainly attributed to the use of coke as auxiliary fuel in S4 system, leading to much higher fossil CO_2 generation and more contribution to GWP [33]. As compared to S1 (conventional incineration), GWP emission from "materials and energy provision" of pyro-gasification systems (S1, S2, and S3) is 2-3 times higher. It is mainly due to the additional energy and materials consumption in these systems, for example, MSW pre-treatment of S3, and limestone and coke addition of S4. As aforementioned, "energy recovery" and "metal recycling" are the environmental benefits from WtE systems. S3 leads to the highest environmental savings of GWP from "energy recovery" among the considered systems, mainly attributed to the highest net electricity generation efficiency of 27.4% as aforementioned. Emissions from "bottom ash landfill" of S1 and S3, "slag recycling" of S2 and S4, "APC residues stabilization and landfill", and "transportation" cause negligible GWP impacts of all the considered systems, ranging from -0.6 to 5.0 kg CO_2 eq.

In regard to the impact category of AP, "stack emission" is also found the major contributor of AP emission. However, AP emission from "stack emission" of S4 is much lower than that of S1, S2, and S3, mainly attributed to the reduction of NO_x emission from gasification-melting-based WtE system as presented in **Table 7.3**. Comparable environmental savings of AP from "metals recycling" is observed as that from "energy recovery" of the considered systems, except for S4; savings of AP from "metals recycling" of S4 is one order of

magnitude lower than that of other systems. The reason is mainly attributed to the fact that aluminum coming from gasification-melting process is present as amorphous phase and is thus not recyclable in S4 [39].

For the toxic impacts of FAETP and HTP, “stack emission” is no longer the key contributor of the environmental burdens; instead “metals recycling” shows significantly avoided contribution on FAETP and HTP. For the impact of FAETP, the recycling of ferrous metals accounts for more than 96% of the total credits. The benefit comes from the saving of virgin metals production, which indicates, the environmental impacts for scrap metals separation, upgrading, and reprocessing are considerably lower than their production from virgin materials. S4 leads to the best FAETP savings, mainly attributed to the highest ferrous metals recovery of 12.60 kg as presented **Table 7.3**. For the impact of HTP, the credits are nearly completely ascribed to Al recycling. Therefore, as aforementioned, HTP savings from S4 system is the worst among the four systems and S2 performs the best due to the highest Al recovery of 6.82 kg, followed by S1 (Al recovery of 6.26 kg) and S3 (Al recovery of 4.64 kg).

7.2.6 Summary of the section

In this section, environmental impact from four considered MSW thermal conversion systems are evaluated by LCA methodology. The considered systems include the conventional MSW incineration (S1, the baseline case) and pyro-gasification based WtE systems (S2, pyrolysis-based system; S3, gasification-melting based system; and S4, gasification based system). Results reveal that the environmental performance of the considered systems in descending order is: S3, Gasification > S2, Pyrolysis > S4, Gasification-melting > S1, Incineration. In regard to the contributor of the environmental impacts, “stack emissions” are the most important environmental burdens for the impact of GWP, AP, EP, and TETP. “Energy recovery” makes a significant contribution to reduce the GWP, AP, and EP impacts. And “metals recycling” shows also a further avoided contribution, in particular for toxicity impacts regarding FAETP and HTP.

7.3 Gasification-based WtE system with different dehydro-chlorination strategies

In this section, a simplified, idealized, and hypothetical gasification-based WtE system using in-furnace dehydrochlorination strategy is proposed on basis of S3 system. Assumption has been made that:

- By adding in-furnace CaO reactant, all the released chlorinated contaminants are absorbed and stored into the solid residues, which means, no chlorine-content product (HCl, Cl_2, chlorides, chlorinated organics, etc.) contained in the produced gas. Therefore, the produced gas cooling down and purification stage (as applied in S3) of the hypothetical system is not essential. And the steam parameters can achieve as high as that used in S3;
- The use of in-furnace CaO acts as CO_2 absorption sorbent to decrease the fossil CO_2 emission; however, the catalytic effect on produced syngas quality enhancement is not taken into account due to the lack of available data;
- Due to the assumption of completely Cl abatement, no HCl and dioxins are discharged at the stack.

The aim of this section is to estimate the potential environmental benefits from complete in-situ dehydrochlorination during MSW gasification. The systems considered and the corresponding system boundaries in this section are presented in **Figure 7. 8**. The same function unit and LCIA method are used as for the previous section. The material and energy flows for the considered systems in this section are listed in **Table 7. 6** (data are presented based on 1 t/MSW).

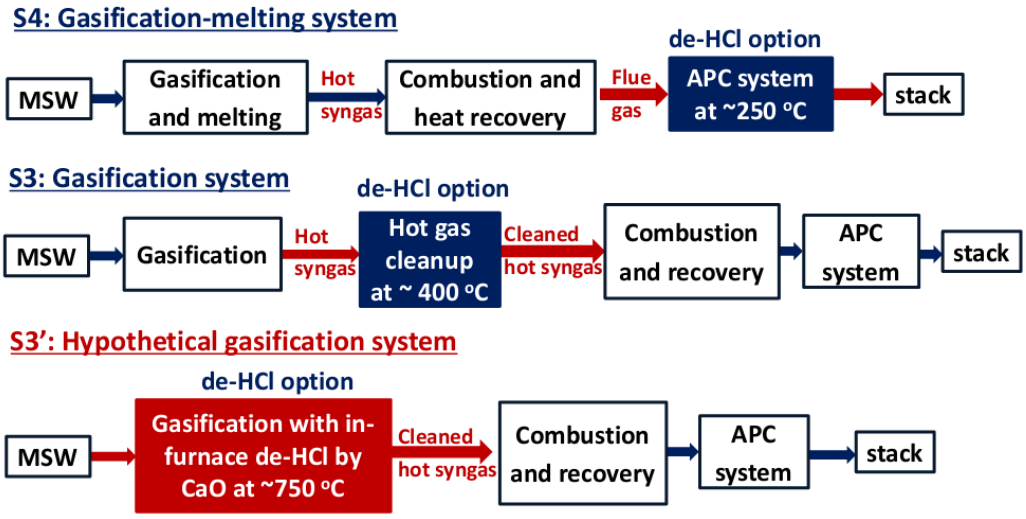

(a)

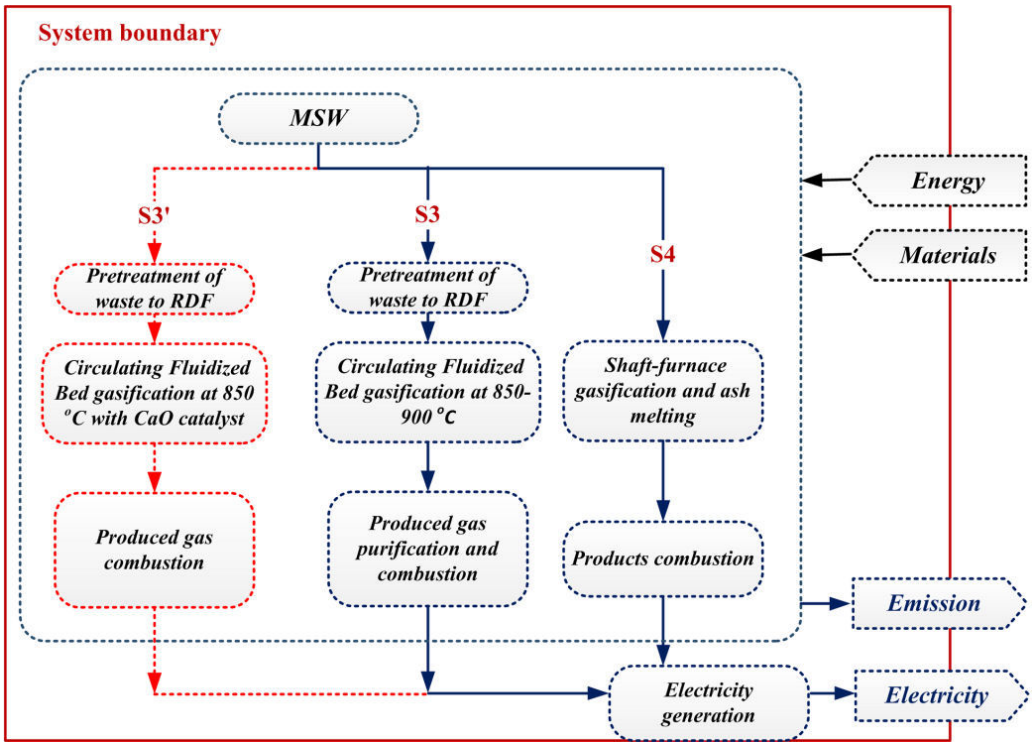

(b)

Figure 7. 8 The considered systems focusing on different de-HCl options (a) and system boundaries (b)

Table 7. 6 Material and energy flows for the considered systems (data are presented based on 1 t/MSW)

	Unit	S3’	S3	S4
Input streams				
Electricity for MSW pretreatment	kWh	70.00	70.00	
Coke as reducing agent and auxiliary fuel	kg			49.00
Electricity for ash treatment [a]	kWh	5.35	4.79	2.32
Diesel for ash treatment [a]	L	0.51	0.46	0.18
Limestone as viscosity regulator	kg			70.20
Lime for flue gas purification	kg	18.71	18.71	18.70
CaO as in-furnace reactant [b]	kg	7.89	0.52	0.52
Ammonia	kg	0.52	0.56	0.56
Active carbon	kg	0.56	10.07	5.19
$FeSO_4 \cdot 7H_2O$	kg	10.07	70.00	

Output streams				
Electricity output [c]	kWh	897.87	783.49	558.90
Bottom ash [d]	kg	129.98	102.73	165.76
Air pollution control residues	kg	125.93	125.93	64.90
Ferrous metals recovery	kg	7.98	7.98	12.60
Aluminum recovery	kg	4.64	4.64	0.05
Process-specific emissions				
PM	g	9.86	9.86	12.57
SO_2	g	34.50	34.50	18.86
HCl [e]	g	0	4.93	21.15
NO_x	g	793.44	793.44	120.01
NH_3	g	24.64	24.64	28.57
Dioxins [e]	g	0.00	9.86E-09	4.97E-09
CO	g	9.86	9.86	35.43
VOC	g	0.00	0.00	0.00
HF	g	0.00	0.00	0.00
Waste-specific emissions				
CO_2-total [f]	kg	803.51	808.21	808.17
CO_2-fossil [f]	kg	415.25	419.95	602.29
Hg	g	4.93E-04	4.93E-04	9.86E-02

[a] the consumption of electricity and diesel is increased because more bottom ash is produced due to the addition of in-furnace CaO;

[b] according to Jhong-Lin Wu et al [40], chlorine content in MSW ranges from 800 – 2500 mg/kg. The value of high chlorine content as 2500 mg/kg is adopted in this study. The in-furnace CaO amount is calculated based on Ca/Cl molar ratio of 2:1 according to the conclusions obtained from **Chapter 4** and **Chapter 6**;

[c] due to the in-furnace removal of chlorinated contaminants, produced gas cooling down and purification stage is not essential in the proposed system. Therefore, the apparent energy of the produced gas can be utilized to generate electricity. The calculation is based on our previous work [21], revealing that hot gas efficiency is approximately 15% higher than cold gas efficiency during MSW gasification at 850 ^{o}C; Taking into account the electricity efficiency of S3 (27%), the increase of the electricity generation as compared to S3 is approximately 4%;

[d] due to the addition of CaO, the amount of bottom ash is increased. The calculation method includes the complete absorption of Cl by CaO reactant and CO_2 absorption by CaO;

[e] due to the assumption of complete Cl removal, no HCl and dioxins is considered;

[f] CO_2 emission is slightly decreased due to CO_2 absorption by CaO;

[g] the rest of the parameters are adopted from S3.

Accordingly, the characterized environmental impacts of the considered system are listed in **Table 7. 7** and the contribution analysis results are illustrated in **Figure 7.9**.

Table 7. 7 Characterized environmental impacts of the considered system

	Categories and Unit	S3': Hypothetical gasification	S3: Gasification	S4: Gasification-melting
Non-toxic impacts	GWP [kg CO2 eq.]	**56.12**	104.00	422.00
	AP [kg SO2 eq.]	**-0.64**	-0.51	-0.43
	EP [kg Phosphate eq.]	0.03	0.04	**-2.69E-03**
Toxic impacts	TETP [kg DCB eq.]	**-0.24**	-0.23	2.65
	FAETP [kg DCB eq.]	-5.00	-4.94	**-7.77**
	HTP [kg DCB eq.]	**-203.89**	-202.00	-11.50

[a] the best performance of the impact categories are represented by bold type and marked as red.

Results reveal that as compared to S3 (Gasification system) and S4 (Gasification-melting system), the proposed hypothetical gasification-based system (S3') leads to the best environmental performance on the impact categories of GWP, AP, TETP, and HTP; while the S4 system still causes excellence behavior over the impact of EP and FAETP (as aforementioned in **Section 7.2**). It is worth mentioning that GWP from S3' is significantly reduced compared with S3; the reason may be attributed to the increase of electricity generation from the hypothetical system. Actually, it is observed that when compared with S3, all the environmental burdens from S3' are declined, which means, from the present study, the proposed hypothetical gasification-based system using in-situ dehydrochlorination strategy has a better environmental performance than gasification system with ex-situ dehydrochlorination. However, the obtained results are mainly based on the assumptions that most of the operation conditions and parameters of S3' are similar to that of S3; but

approximately 4% of the electricity is additionally generated owning to energy savings from produced gas apparent energy. Further consideration and examination of the parameters adopted and the process system should be investigated on these two complex systems.

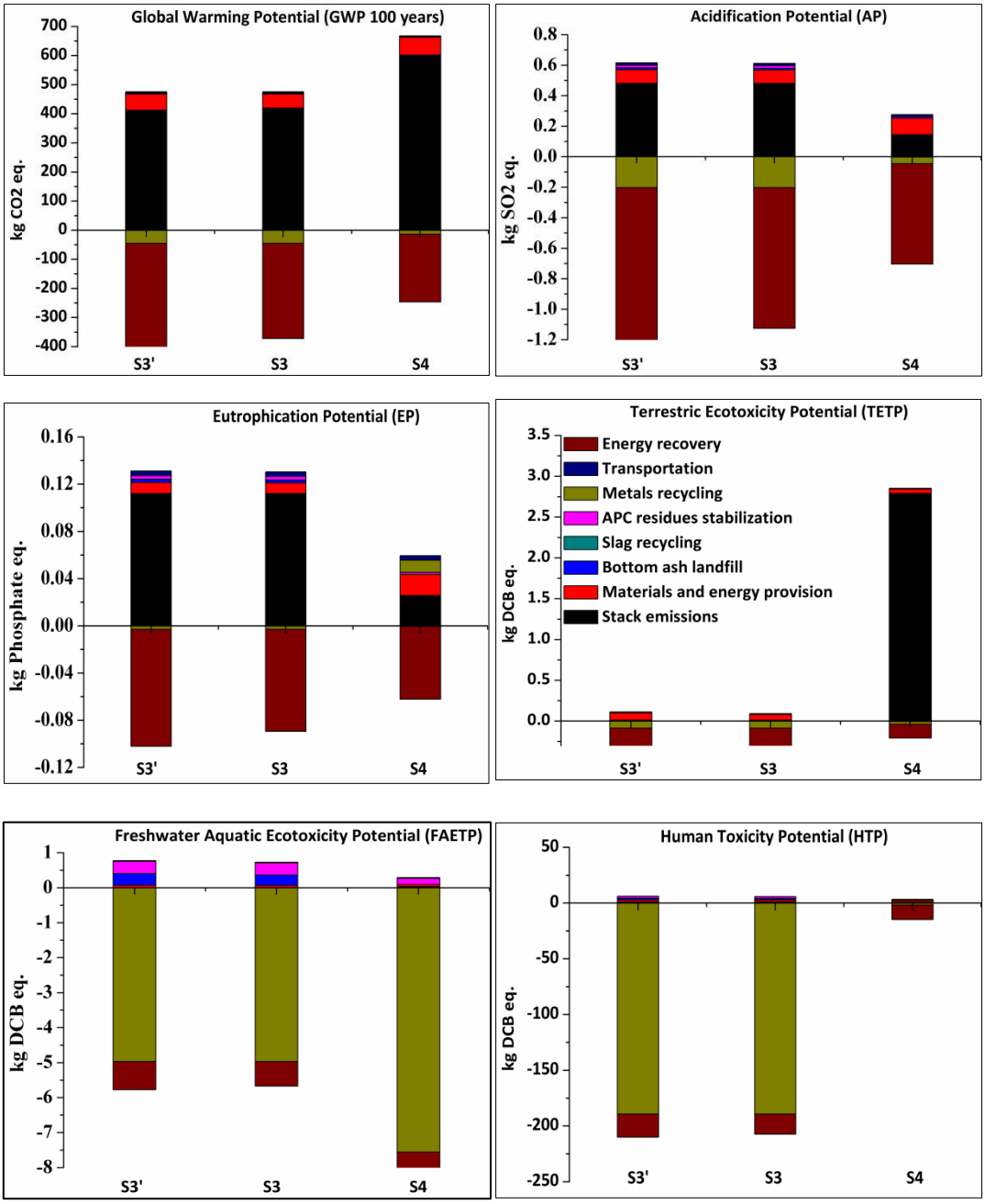

Figure 7. 9 Contribution analysis of the selected environmental impact categories from the considered systems: S3', the proposed hypothetical gasification-based system; S3 gasification system; and S4, gasification-melting system

Figure 7.9 illustrates the contribution analysis results of the considered systems (S3', the proposed hypothetical gasification-based system; S3 gasification system; and S4, gasification-melting system) in this section. Similar to the results obtained from **Section 7.2**, "stack emissions" are the most important environmental burdens for the impact of GWP, AP, EP, and TETP. "Energy recovery" makes a significant contribution to reduce the GWP, AP, and EP impacts. And "metals recycling" shows a further avoided contribution, in particular for toxicity impacts regarding FAETP and HTP. When compared to S3, the credits from "energy recovery" are slightly increased due to the increase of electricity generation; while the environmental burdens from "materials and energy provision", "bottom ash landfill", and "transportation" is slightly increased owning to the in-furnace addition of CaO and the increase of the produced bottom ash.

7.4 Summary of the chapter

In this chapter, LCA investigations of four WtE thermal conversion systems (including S1, conventional waste incineration system; S2, pyrolysis-based WtE system; S3, gasification system with ex-situ dehydrochlorination as performed by Lahti Energia; and S4, gasification-melting technology) are firstly conducted to determine the environmental performance of pyro-gasification-based WtE systems when compared with conventional MSW incineration. Then a simplified LCA comparison between gasification-based systems with different dehydrochlorination strategies is carried out. The main findings are as follows:

- Gasification system (S3) leads the least environmental impacts for most of the considered categories such as GWP, AP, and TETP; but it also causes the highest environmental burdens of FAETP. Gasification-melting system (S4) performs worst in the environmental categories of GWP, TETP, and HTP; but S4 system is efficient to reduce the environmental impact of EP and FAETP;
- The environmental performance of the considered systems in descending order is: S3, Gasification > S2, Pyrolysis > S4, Gasification-melting > S1, Incineration (">" means the former system performs better than the latter one).
- In regard to the contributors of the overall systems, "stack emissions" are the most important environmental burdens for most of the impact categories; "energy recovery" and "metal recycling" account for most of the environmental savings. "Materials and energy provision" makes only a minor contribution to S1 and S2 scenarios, however it is more noteworthy in S3 and S4, for pretreatment of MSW

and the addition of auxiliary fuel, respectively.

- The proposed hypothetical gasification-based system (S3') leads to the best environmental performance on the impact categories of GWP, AP, TETP, and HTP; while gasification-melting based system (S4) still causes excellence behavior over the impact of EP and FAETP. It is concluded that the environmental performance of S3' is superior to that of S3. However, it should be mentioned that the evaluation is mainly based on assumptions and it is an idealized and simplified estimation. Therefore, the parameters adopted and the whole system flow sheet of the hypothetical gasification-based system with in-situ dehydrochlorination should be further identified and examined.

7.5 Bibliography

[1] Rylander H, Haukohl J. Status of WTE in Europe. Waste Management World, International Solid Wastes Association. 2002.

[2] Beylot A, Muller S, Descat M, Ménard Y, Villeneuve J. Life cycle assessment of the French municipal solid waste incineration sector. Waste Management. 2018;80:144-53.

[3] Jeswani H, Azapagic A. Assessing the environmental sustainability of energy recovery from municipal solid waste in the UK. Waste Management. 2016;50:346-63.

[4] Nie Y. Development and prospects of municipal solid waste (MSW) incineration in China. Frontiers of Environmental Science & Engineering in China. 2008;2:1-7.

[5] Zheng L, Song J, Li C, Gao Y, Geng P, Qu B, et al. Preferential policies promote municipal solid waste (MSW) to energy in China: Current status and prospects. Renewable and Sustainable Energy Reviews. 2014;36:135-48.

[6] Lopes EJ, Queiroz N, Yamamoto CI, da Costa Neto PR. Evaluating the emissions from the gasification processing of municipal solid waste followed by combustion. Waste Management. 2018;73:504-10.

[7] Thanopoulos S, Karellas S, Kavrakos M, Konstantellos G, Tzempelikos D, Kourkoumpas D. Analysis of Alternative MSW Treatment Technologies with the Aim of Energy Recovery in the Municipality of Vari-Voula-Vouliagmeni. Waste and Biomass Valorization. 2018:1-17.

[8] Beylot A, Hochar A, Michel P, Descat M, Ménard Y, Villeneuve J. Municipal Solid Waste Incineration in France: An Overview of Air Pollution Control Techniques, Emissions, and Energy Efficiency. Journal of Industrial Ecology. 2017.

[9] Li H, Nitivattananon V, Li P. Municipal solid waste management health risk assessment from air emissions for China by applying life cycle analysis. Waste Management & Research. 2015;33:401-9.

[10] Arena U. Process and technological aspects of municipal solid waste gasification. A review. Waste management. 2012;32:625-39.

[11] Guan Y, Luo S, Liu S, Xiao B, Cai L. Steam catalytic gasification of municipal solid waste for producing tar-free fuel gas. International journal of hydrogen energy. 2009;34:9341-6.

[12] Hu M, Guo D, Ma C, Hu Z, Zhang B, Xiao B, et al. Hydrogen-rich gas production by the gasification of wet MSW (municipal solid waste) coupled with carbon dioxide capture. Energy. 2015;90:857-63.

[13] Finkbeiner M, Inaba A, Tan R, Christiansen K, Klüppel H-J. The New International Standards for Life Cycle Assessment: ISO 14040 and ISO 14044. The International Journal of Life Cycle Assessment. 2006;11:80-5.

[14] Pennington D, Potting J, Finnveden G, Lindeijer E, Jolliet O, Rydberg T, et al. Life cycle assessment Part 2: Current impact assessment practice. Environment International. 2004;30:721-39.

[15] Kumar Y. Biomass Gasification—A Review. International Journal of Engineering Studies and Technical Approach. 2015;1:12-28.

[16] Seo Y-C, Alam MT, Yang W-S. Gasification of Municipal Solid Waste. Gasification for Low-grade Feedstock: IntechOpen; 2018.

[17] Bolhar-Nordenkampf M, Isaksson J. Operating experiences of large scale CFB-gasification plants for the substitution of fossil fuels. 24th European Biomass Conference, Amsterdam–The Netherlands2016.

[18] Molino A, Chianese S, Musmarra D. Biomass gasification technology: The state of the art overview. Journal of Energy Chemistry. 2016;25:10-25.

[19] Castaldi M, Van Deventer J, Lavoie J-M, Legrand J, Nzihou A, Pontikes Y, et al. Progress and prospects in the field of biomass and waste to energy and added-value materials. Waste and Biomass Valorization. 2017;8:1875-84.

[20] Dong J, Chi Y, Tang Y, Ni M, Nzihou A, Weiss-Hortala E, et al. Effect of operating parameters and moisture content on municipal solid waste pyrolysis and gasification. Energy & Fuels. 2016;30:3994-4001.

[21] Tang Y, Dong J, Chi Y, Zhou Z, Ni M. Energy and exergy analyses of fluidized-bed municipal solid waste air gasification. Energy & Fuels. 2016;30:7629-37.

[22] Dong J, Chi Y, Zou D, Fu C, Huang Q, Ni M. Energy–environment–economy assessment of waste management systems from a life cycle perspective: Model development and case study. Applied Energy. 2014;114:400-8.

[23] Ning S-K, Chang N-B, Hung M-C. Comparative streamlined life cycle assessment for two types of municipal solid waste incinerator. Journal of Cleaner Production. 2013;53:56-66.

[24] Chen D, Christensen TH. Life-cycle assessment (EASEWASTE) of two municipal solid waste incineration technologies in China. Waste Management & Research. 2010;28(6):508-19.

[25] McDougall FR, White PR, Franke M, Hindle P. Integrated solid waste management: a life cycle inventory. 2nd ed. ed. UK: Blackwell Science Ltd.; 2008.

[26] Dong J, Tang Y, Nzihou A, Chi Y, Weiss-Hortala E, Ni M, et al. Comparison of Waste-to-Energy technologies of gasification and incineration using life cycle assessment: case studies in Finland, France and China. Journal of Cleaner Production. 2018.

[27] Christensen TH, Simion F, Tonini D, Møller J. Global warming factors modelled for 40 generic municipal waste management scenarios. Waste Management & Research. 2009;27:871-84.

[28] Nzihou A, Themelis NJ, Kemiha M, Benhamou Y. Dioxin emissions from municipal solid waste incinerators (MSWIs) in France. Waste management. 2012;32:2273-7.

[29] Burgau MW Pyrolysis Plant D. Waste Pyrolysis Plant "Burgan". 2009.

[30] Bolhàr-Nordenkampf M, Isaksson J. Refuse derived fuel gasification technologies for high efficient energy production. Waste Management: Waste to Energy. 2014;4:379-88.

[31] Lahti Energia. http://www.lahtigasification.com/.

[32] Savelainen J, Isaksson, J. Kymijärvi II Plant: High-Efficiency Use of SRF in Power Production through Gasification. 2015.

[33] Tanigaki N, Manako K, Osada M. Co-gasification of municipal solid waste and material recovery in a large-scale gasification and melting system. Waste Management. 2012;32:667-75.

[34] Pressley PN, Aziz TN, DeCarolis JF, Barlaz MA, He F, Li F, et al. Municipal solid waste conversion to transportation fuels: a life-cycle estimation of global warming potential and energy consumption. Journal of Cleaner Production. 2014;70:145-53.

[35] Roberts KG, Gloy BA, Joseph S, Scott NR, Lehmann J. Life cycle assessment of biochar systems: estimating the energetic, economic, and climate change potential. Environmental Science & Technology. 2009;44:827-33.

[36] DEFRA UK. Review of Environmental and Health Effects of Waste Management: municipal solid waste and similar wastes. London: Defra Publications; 2004.

[37] U.S. Energy Information Administration (EIA). International Energy Statistics 2012 (http://www.eia.gov/). 2012.

[38] Wu Y, Su D, Peng W, Zhang Q. Application of lifecycle assessment and finite element analysis in the design of raised access floor products. 2017.

[39] Arena U, Di Gregorio F. Element partitioning in combustion-and gasification-based waste-to-energy units. Waste Management. 2013;33:1142-50.

[40] Wu J-L, Lin T-C, Wang Y-F, Wang J-W, Wang C-T, Kuo Y-M. Polychlorinated dibenzo-p-dioxin and dibenzofuran (PCDD/F) emission behavior during incineration of laboratory waste. Part 1: Emission profiles obtained using chemical assay and bioassay. Aerosol Air Qual Res. 2014;14:1199-205.

Chapter 8

General conclusions and prospects

8.1 Conclusions

The presence of chlorine in MSW causes a variety of troubles such as corrosion, toxic organics formation, acidification, etc., during MSW pyro-gasification. Besides, it also degrades the quality of produced bio-oil by forming chlorinated components. In order to develop an energy-efficient and environmental-sound pyro-gasification-based MSW thermal system, this research work focused on "Chlorinated contaminants mitigation during pyro-gasification of wastes using CaO reactant: experimental and life cycle assessment". The effect of CaO reactant is experimentally examined on both in-furnace HCl mitigation and pyrolytic tar upgrading; and life cycle assessment is conducted to identify the environmental performance of pyro-gasification based WtE systems. Based on the research work, some conclusions are obtained:

- **High temperature HCl mitigation by CaO reactant: breakthrough experiments and kinetics modeling**

Gas-solid reaction mechanism between CaO reactant and HCl gas is studied by both theoretical calculation and experimental investigation. Thermodynamic analysis is firstly conducted to determine the Gibbs free energy and standard equilibrium constant of the reaction. Breakthrough experiments and kinetic modeling of the reaction are then performed to identify the effect of key parameters on HCl mitigation efficiency. The microscopy images of the spent CaO reactant reveal the formation mechanism of the product-layer.

Results reveal that increasing the temperature, reducing raw concentration of HCl gas, and the presence of CO, and H_2 in carrier gas causes the reduction of HCl mitigation capacities and CaO bed conversion efficiency. Higher temperature shifts the chemical equilibrium of the absorption reaction and reduces surface area and pore volumes of CaO reactant, thus resulting in a decreasing of HCl mitigation capacity from 778.9 to 173.9 mg/g-CaO with the increase of temperature from 550 to 850 ^{o}C. Higher raw HCl concentration increase the breakthrough and saturation time of CaO bed, but decrease HCl mitigation capacities due to the reduction of both physical adsorption and chemical reaction rates. The presence of CO and H_2 will occupy the number of free active sites on CaO surface and cause adverse effects on HCl mitigation.

A kinetics analysis has been developed by comparing experimental data with models describing the reaction at the particle surface. It has been concluded that the HCl mitigation at the CaO particle surface is firstly limited by the heterogeneous gas-solid reaction, and then by the HCl diffusion through this porous growing layer. Furthermore, morphology analysis of the spent CaO reactants are examined to reveal the formation process of the product-layer; and the spent CaO physical properties further indicates that both the shifts of chemical equilibrium and the reduction of surface area and closure of pore structures at higher temperature are responsible for the decline of HCl mitigation efficiency by CaO.

- **HCl release from organic and inorganic sources and effect of in-furnace CaO reactant on HCl mitigation and pyrolytic tar upgrading**

To simulate the in-situ generation of HCl from organic source, pyro-gasification of PVC has been performed with or without CaO addition. The experimental data have been then used for the modeling of the different PVC decomposition steps. Although the average apparent activation energy of pseudo dehydrochlorination reaction is increased from 136.52 to 152.61 kJ/mol with the addition of CaO, the apparent activation energy of the overall PVC decomposition has been decreased from 197.26 to 148.92 kJ/mol using CaO reactant.

HCl emission from organic and inorganic sources has also been conducted using simulated MSW. Results reveal that in-situ addition of CaO reactant is effective for HCl mitigation. CaClOH is identified as the main dehydrochlorination product by XRD observations. Increasing the temperature causes adverse effects on HCl mitigation efficiency and the increase of Ca/Cl molar ratio promotes the efficiency. The optimized working

conditions observed in this work are at temperature of 750 ^{o}C and Ca/Cl molar ratio of 2:1.

The role of CaO reactant on pyrolytic tar is also determined by identifying the chemical speciation of the produced tars under catalytic and non-catalytic conditions. Using CaO, the amount of oxygenated organic compounds has been reduced, improving the quality of the tars for a further bio-oil upgrading.

- **Life cycle assessment of pyro-gasification-based WtE systems and WtE systems with different dehydrochlorination options**

Firstly, LCA investigation of four WtE thermal conversion systems (including S1, conventional waste incineration system; S2, pyrolysis-based WtE system; S3, gasification system with ex-situ dehydrochlorination as performed by Lahti Energia; and S4, gasification-melting technology) is conducted to determine the environmental performance of pyro-gasification-based WtE systems when compared with conventional MSW incineration. Results reveal that the gasification system (S3) leads to the least environmental impacts for most of the considered categories such as GWP, AP, and TETP; but it also causes the highest environmental burdens of FAETP. Gasification-melting system (S4) performs worst in the environmental categories of GWP, TETP, and HTP; but S4 system is effective to reduce the environmental impact of EP and FAETP. The environmental performance of the considered systems in descending order is: S3, Gasification > S2, Pyrolysis > S4, Gasification-melting > S1, Incineration (“>” means the former system performs better than the latter one).

Then a simplified LCA comparison between gasification-based systems with different dehydrochlorination strategies (S3, gasification system using ex-situ produced gas purification; S4, gasification-melting system using APC systems for acid gas removal; and S3’, the hypothetical gasification-based system using in-situ dehydrochlorination) is carried out. Results reveal that the proposed hypothetical gasification-based system (S3’) leads to the best environmental performance on the impact categories of GWP, AP, TETP, and HTP; while gasification-melting based system (S4) still causes excellence behavior over the impact of EP and FAETP. It is concluded that the environmental performance of S3’ is superior to that of S3. However, it should be mentioned that the present work is mainly based on assumption and is an idealized and simplified estimation. Therefore, the parameters adopted and the whole system flow sheet of the proposed hypothetical gasification-based system should be further identified and examined.

8.2 Prospects

Pyro-gasification-based MSW thermal conversion system is attracting more and more concerns due to the potential to achieve energy efficient and environmental sound waste to energy routes. However, there are several bottlenecks needs to be overcome for its popularization and worldwide applications. Chlorine content is one of the biggest challenges during MSW thermal conversion. Besides, new challenges will also come up from both technological and theoretical evaluation perspectives. This section is dedicated to the prospects for future research investigations.

- **Improvement of reactant properties for high temperature HCl mitigation**

Results from this study indicated that the use of in-furnace CaO reactant is effective to absorb the released HCl during MSW pyro-gasification; however, the removal capacity declined with the increase of temperature. Therefore, in-depth investigation in this field is essential to fulfill the research, which could include:

(i) Enhancement of reactant properties. In this study, only the base reactant CaO is investigated for both HCl mitigation and pyrolytic tar upgrading. It is concluded that the excessive use of CaO than the stoichiometric amount is essential to achieve acceptable HCl mitigation efficiency. Therefore, further investigations could be focused on the enhancement of reactant properties, such as pretreatment of CaO [1], reactive metals loading on CaO surface [2, 3], and mixing with other reactants [4];

(ii) Re-generation or use of Ca-content waste as in-situ reactant. Re-generation of spent reactant is of great importance to achieve environmental sustainability [5]; but it is not investigated in the present work. Therefore, further study work could be focused on this aspect. Another option can be focused on the reuse of Ca-content waste, for example carbide slag, as indicated by previous studies [6, 7];

(iii) Development of high temperature HCl mitigation reactant. As aforementioned, the capacities of CaO reactant on HCl mitigation declines rapidly with the increase of temperature. Therefore, the development of new and effective reactant, which works at higher temperature windows, is also a fascinating research field [8].

- **Thorough and detailed life cycle assessment of pyro-gasification-based WtE systems**

In this work, the comparisons between MSW pyro-gasification and incineration, as well as the potential products downstream applications, have been evaluated using LCA methodology. However, the evaluation is only based on four selected plants. Therefore, thorough and detailed comparison of all kinds of MSW thermal conversion systems should be conducted to further optimize the MSW thermal conversion systems and to guide the future application of pyro-gasification based WtE systems.

Bibliography

[1] Manovic V, Anthony EJ. Thermal activation of CaO-based sorbent and self-reactivation during CO2 capture looping cycles. Environmental science & technology. 2008;42:4170-4.

[2] Mansir N, Teo SH, Rabiu I, Taufiq-Yap YH. Effective biodiesel synthesis from waste cooking oil and biomass residue solid green catalyst. Chemical Engineering Journal. 2018;347:137-44.

[3] Huang B-S, Chen H-Y, Chuang K-H, Yang R-X, Wey M-Y. Hydrogen production by biomass gasification in a fluidized-bed reactor promoted by an Fe/CaO catalyst. International Journal of Hydrogen Energy. 2012;37:6511-8.

[4] Zhang H, Zheng J, Xiao R, Jia Y, Shen D, Jin B, et al. Study on Pyrolysis of Pine Sawdust with Solid Base and Acid Mixed Catalysts by Thermogravimetry–Fourier Transform Infrared Spectroscopy and Pyrolysis–Gas Chromatography/Mass Spectrometry. Energy & Fuels. 2014;28:4294-9.

[5] Dong J. MSWs gasification with emphasis on energy, environment and life cycle assessment: Ecole des Mines d'Albi-Carmaux; 2016.

[6] Xie X, Li Y, Wang W, Shi L. HCl removal using cycled carbide slag from calcium looping cycles. Applied Energy. 2014;135:391-401.

[7] Li Y, Wang W, Cheng X, Su M, Ma X, Xie X. Simultaneous CO2/HCl removal using carbide slag in repetitive adsorption/desorption cycles. Fuel. 2015;142:21-7.

[8] Cao J, Zhong W, Jin B, Wang Z, Wang K. Treatment of Hydrochloric Acid in Flue Gas from Municipal Solid Waste Incineration with Ca–Mg–Al Mixed Oxides at Medium–High Temperatures. Energy & Fuels. 2014;28:4112-7.

Chapter 9

French summary of the thesis

Résumé du Chapitre 1

Etat de l'art

L'objectif de ce chapitre est de présenter l'état de l'art de la recherche bibliographique et les motivations de ce travail de recherche. Ainsi, sont présentés et discutés les progrès des recherches en cours concernant : l'émission de HCl lors de la conversion thermochimique des déchets municipaux et les méthodes de contrôle associées ; le rôle joué par le réactif CaO sur le craquage et la valorisation des goudrons lors de son utilisation in-situ dans le réacteur ; et la méthodologie d'analyse de cycle de vie (ACV) et son application aux systèmes de conversion thermochimique des déchets municipaux.

Ainsi, la section 1.1 détaille la motivation du présent travail qui est l'amélioration simultanée de l'efficacité énergétique et de la performance environnementale des procédés de traitement thermique de ces résidus solides. Les déchets municipaux sont constitués, en fractions variables, de déchets organiques, papier, plastiques, verre, métaux et textiles. Ainsi, ces résidus solides contiennent des proportions non négligeables de sources chlorées, de nature organique (plastique) ou inorganique (sel). Lors d'un traitement thermochimique de composés chlorés, de l'acide chlorhydrique (HCl) est formé, conduisant à des désagréments tels que la corrosion, la formation de contaminants toxiques, l'acidification… La Figure 1.0.1 présente la philosophie générale du travail, à savoir l'utilisation in-situ du réactif CaO lors de la pyro-gazéification des résidus solides. La présence de ce réactif in-situ a pour objectifs de :

- Modérer l'émission de HCl lors du procédé de pyro-gazéification des résidus solides qui se déroule à hautes températures. Le but est d'immobiliser le chlore dans la fraction solide restant à l'intérieur du réacteur.

- Eviter/limiter les phénomènes de corrosion des installations initiés par la présence du gaz HCl émis.

- Limiter la formation de dioxines, qui résultent de réactions hétérogènes entre le résidu solide et la présence de chlore à l'état gazeux (200-400°C). Les dioxines sont des polluants toxiques qu'il convient d'éliminer pour une utilisation ultérieure du syngas.

- Générer un syngas de qualité supérieure, en considérant qu'une partie importante de polluants a été éliminée, et que le ratio H_2/CO peut aussi être amélioré. En effet, le but de la pyro-gazéification est de fournir un gaz énergétique appelé syngas, composé majoritairement de H_2 et de CO. Les proportions de chacun de ces 2 gaz, mais le taux et la nature des polluants, orientent à la fois son utilisation subséquente et les méthodes de purification nécessaires.

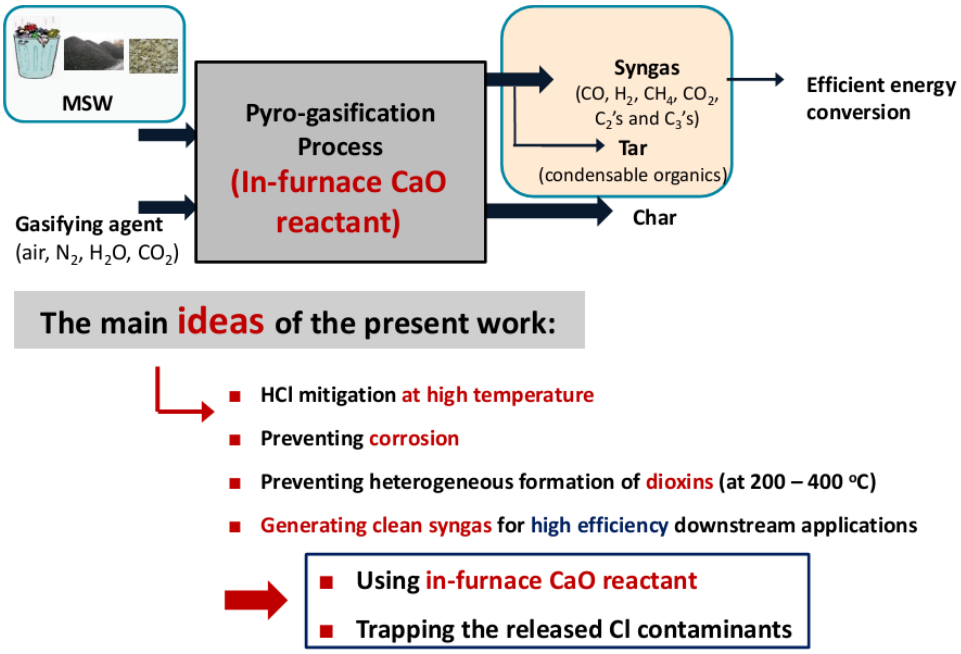

Figure 1. 0.1 Philosophie du travail de recherche : étudier le captage et l'immobilisation in-situ du chlore émis lors de la pyro-gazéification de résidus organiques solides en utilisant un réactif CaO

La section 1.2 présente les caractéristiques de l'émission de HCl et les méthodes de contrôle appliquées aux technologies de traitement thermique des déchets municipaux. La quantité de chlore présente dans ces résidus est relativement élevée (de 800 à 2500 mg/kg). Ainsi le traitement thermochimique conduit à la formation d'acide chlorhydrique (HCl),

conduisant à des désagréments tels que des pluies acides formées localement, la corrosion à haute température des chaudières (ce qui réduit de manière significative l'efficacité à la conversion énergétique des installations d'incinération), la formation de contaminants toxiques tels que les dibenzo-p-dioxines et les dibenzofuranes polychlorés. De ce fait, il convient contrôler l'émission de HCl dans ces procédés afin de limiter les risques de contamination par des éléments chlorés, et bien sûr respecter les limites d'émission imposées par les réglementations en vigueur. Actuellement, les outils de contrôle des émissions de HCl existants sont : (1) le contrôle de la quantité de chlore dans les résidus solide avant traitement thermochimique, en utilisant par exemple le lavage, le tri, des prétraitements à basse température… ; (2) le contrôle de la quantité de chlore sous forme d'HCl dans le gaz émis après le traitement thermochimique (traitement par voie sèche ou voie humide, ou un procédé intermédiaire) ; (3) le contrôle peut être réalisé au cours du traitement thermochimique. C'est précisément cette dernière option de contrôle in-situ qui a été sélectionnée pour la présente étude.

La section 1.3 introduit l'effet de l'utilisation de CaO comme réactif in-situ sur l'amélioration de la qualité du syngas produit lors de la pyro-gazéification, et sur le craquage des goudrons. En résumé, CaO permet de capter partiellement le CO_2, un gaz non énergétique, et ainsi d'améliorer la qualité énergétique du syngas. De plus CaO participe au craquage des goudrons, permettant d'augmenter le taux de conversion de la ressource en syngas.

La section 1.4 décrit l'approche et la méthodologie globale d'une analyse de cycle de vie et sa mise en œuvre dans le cadre du traitement thermique des déchets municipaux. Le travail est découpé en 4 phases : la définition des objectifs et du champ d'investigation, l'inventaire des données et des flux associés aux frontières définies lors de la phase précédente, l'évaluation de l'impact environnemental (en général des paramètres tels que l'acidification, l'écotoxicité, l'impact sur le changement climatique … sont évalués) et enfin la dernière étape constitue l'interprétation des résultats.

Ainsi, le présent travail de thèse est focalisé sur « l'abattement des contaminants chlorés lors de la pyro-gazéification de déchets en utilisant un réactif de CaO : étude expérimentale et analyse du cycle de vie ». La structure du manuscrit est présentée à la figure 1.0.2.

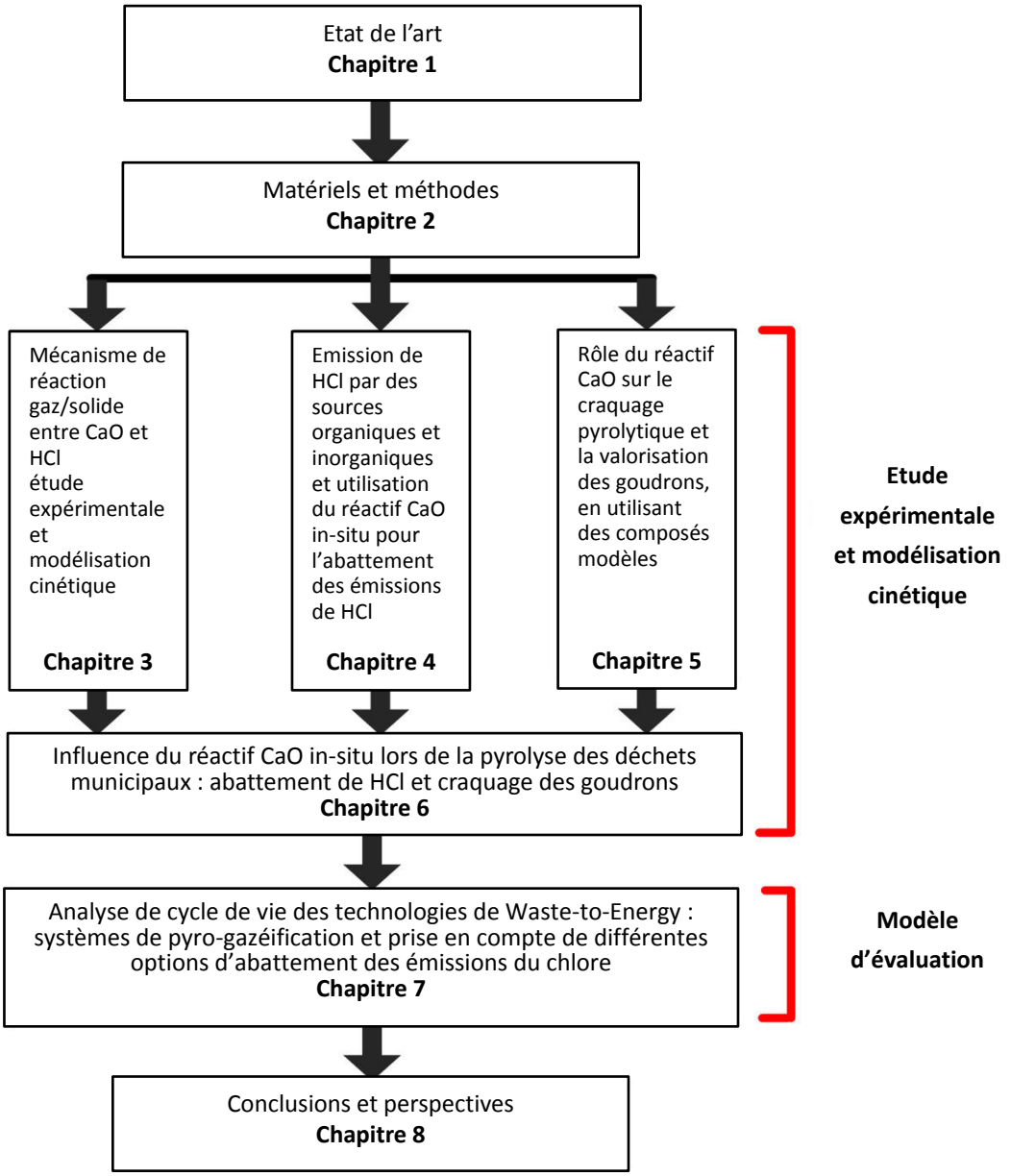

Figure 1.0.2 Structure et principaux aspects traités dans la thèse

Résumé du Chapitre 2

Matériels et méthodes

Ce chapitre présente la caractérisation des ressources et des réactifs utilisés dans cette étude ; les différents montages expérimentaux, les conditions opératoires, les méthodes d'échantillonnage et d'analyses ; et pour finir la méthodologie appliquée pour l'étude d'analyse de cycle de vie.

Dans la section 1.2, les caractéristiques des déchets municipaux considérés et du réactif CaO sont introduites. Ce sont 5 composés modèles, représentatifs des 5 grandes classes de déchets municipaux, qui sont sélectionnés et caractérisés pour la mise en œuvre de l'étude : du PVC et du PE (pour représenter les plastiques et en particulier la fraction chlorée organique), du bois, des déchets alimentaires et du papier. Les analyses immédiates et ultimes ont été réalisées sur ces matériaux avant leur utilisation. De même, le réactif CaO a été caractérisé du point de vue de ses propriétés physico-chimiques telles que la surface spécifique, la porosité et la composition.

La section 2.2 décrit les montages expérimentaux utilisés, ainsi que les conditions opératoires appliquées à chaque partie de l'étude. Un réacteur tubulaire vertical, chauffé électriquement, est utilisé pour la mise en œuvre des expériences de mitigation de HCl. Dans ce cas, du gaz HCl est introduit directement dans le réacteur, et la capacité de rétention de HCl par le lit de réactif CaO est évaluée, selon différentes conditions opératoires. Dans un second temps, l'abattement de HCl est étudié en présence de CaO et d'une source générant le HCl in-situ. Dans ce cas, un réacteur tubulaire horizontal est utilisé, contenant du PVC ou du NaCl (sources organiques et inorganiques de chlore), et le lit fixe de CaO. En fonction des conditions opératoires de pyro-gazéification, la quantité de HCl mesurée en sortie de réacteur est comparée, en présence et en l'absence de CaO. Un montage expérimental couplé Py-GC/MS (Pyrolyse – chromatographie gazeuse / spectroscopie de masse) a été utilisé pour l'étude spécifique d'identification et de quantification des goudrons issus de la pyrolyse de composés modèles (PVC, déchets alimentaires, bois) en présence ou en l'absence de réactif CaO. Enfin, l'équipement d'analyse thermogravimétrique est décrit, celui-ci servant l'étude de compréhension de la cinétique de formation de HCl à partir de PVC.

La section 2.3 décrit les méthodes d'échantillonnage et d'analyses. En particulier, la méthode de captage du gaz HCl par absorption dans une solution basique, et l'analyse par chromatographie ionique sont décrites. La caractérisation des goudrons par chromatographie gazeuse couplée à la spectrométrie de masse est détaillée. Enfin, les techniques permettant de caractériser le résidu solide de pyrolyse sont expliquées : l'analyse thermogravimétrique, la fluorescence X, la microscopie électronique à balayage et la microanalyse EDS, la diffraction de rayons X et l'adsorption de gaz. Ces techniques permettent d'accéder à la morphologie, la texture, mais aussi à la composition globale et locale.

Pour compléter ce travail, une étude thermodynamique théorique a été menée à l'aide du logiciel FactSage 6.3. Le fonctionnement du logiciel (données d'entrée et de sortie) et les bases de données associées sont détaillés à la section 2.4.

Enfin la dernière section (2.5) s'attache à décrire la méthodologie et les paramètres évalués lors de l'analyse de cycle de vie. Il est en particulier détaillé les catégories d'impacts sélectionnées et les références de normalisation.

Résumé du Chapitre 3

Etude expérimentale et modélisation cinétique de la mitigation de HCl en présence du réactif CaO

Le but de ce chapitre est d'étudier la capacité du réactif CaO à immobiliser le gaz HCl à l'intérieur du réacteur et d'étudier le mécanisme de réaction afférent à la réaction gaz/solide. Pour se faire, les courbes de percée ont été obtenues sous différentes conditions opératoires, puis les modélisations thermodynamique et cinétique ont permis de mieux évaluer les conditions opératoires favorables à l'immobilisation de HCl, et le mécanisme associé. Les principales conclusions de ce chapitre sont résumées comme suit.

Dans la section 3.2, les calculs thermodynamiques, à l'aide du logiciel FactSage, ont été menés. Il apparaît que dans une gamme de température de 500 à 1200 K (227 à 927°C), l'enthalpie libre de la réaction entre CaO et HCl est négative, la réaction est donc favorisée dans le sens de la formation de $CaCl_2$ et H_2O. Cependant, l'augmentation de température a un effet néfaste sur l'équilibre de la réaction, provoquant une augmentation significative de l'enthalpie libre. La valeur de la constante d'équilibre de la réaction passe ainsi de presque $7x10^{16}$ à 500 K à environ $2x10^{4}$ à 1200 K. Ainsi la réaction reste spontanée, mais l'équilibre est affecté.

La section 3.3 décrit les résultats expérimentaux (courbes de percée) obtenus à différentes températures (550, 650, 750 et 850°C) en présence de CaO. En augmentant la température, les temps caractéristiques de percée et de saturation diminuent significativement : de 197,8 à 21,8 min (temps de percée à 550 et 850°C), et de 268,9 to 69,6 min (saturation à 550 et 850°C). De plus, la capacité de rétention de HCl par CaO diminue de 778,9 à 173,9 mg/g-CaO lorsque la température augmente de 550 à 850°C.

Les résultats expérimentaux ont été comparés à 3 modèles décrivant l'étape cinétiquement limitante de la réaction gaz/solide dans le modèle du noyau rétrécissant : diffusion externe de HCl, diffusion interne de HCl à travers la couche de produit en cours de formation, la réaction de surface entre HCl et CaO. Les résultats montrent que l'étape cinétique déterminante est la réaction chimique, puis la diffusion à travers la couche de produit formée. Entre ces 2 régimes, une zone de régime mixte apparaît dont l'étendue dépend de la température. En effet, à basse température (550°C), le régime mixte apparaît pour un taux de conversion de CaO d'environ 40%, tandis qu'à 750°C, le régime mixte apparaît dès 2% de taux de conversion. Une proposition de mécanisme est suggérée à la figure 3.0.1.

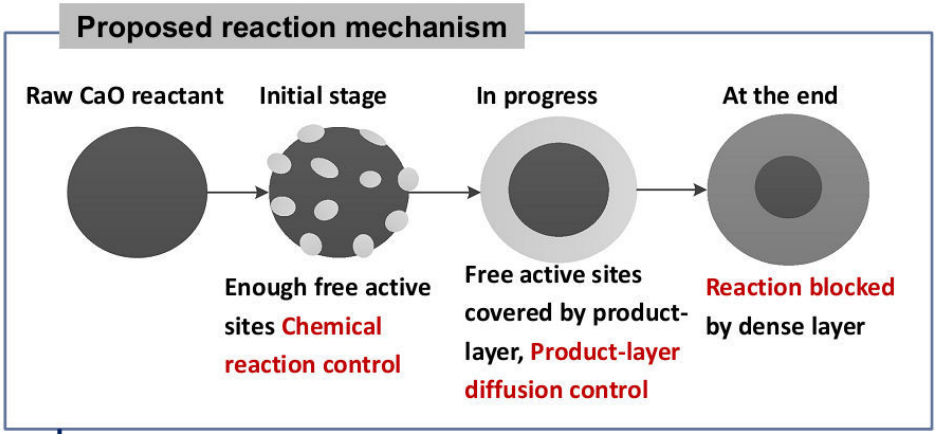

Figure 3.0.1 Mécanisme de réaction entre CaO et HCl proposé : le premier régime correspond à une limitation de la cinétique par la réaction hétérogène de surface, laquelle conduit à la formation de $CaCl_2$ (en gris clair). Plus la réaction avance, plus le réactif CaO est converti en $CaCl_2$ qui représente une couche s'épaississant à la surface du CaO qui n'a pas encore réagi. Ceci traduit que la diffusion de HCl à l'intérieur de cette couche ainsi formée devient l'étape limitante du processus. L'augmentation de densité de la couche, observée notamment par microscopie électronique à balayage, bloque la réaction en inhibant la diffusion.

Résumé du Chapitre 4

Influence du réactif CaO sur l'émission de HCl provenant de la conversion thermochimique de sources organiques et inorganiques

Contrairement au chapitre 3, dans lequel le gaz HCl était directement introduit dans la chambre du réacteur, ce chapitre se concentre sur la génération in-situ de HCl à partir de sources organiques (PVC) et inorganiques (NaCl). Cette étude vise à quantifier l'effet du lit fixe de CaO sur l'immobilisation du HCl produit localement lors de la conversion thermochimique des 2 ressources sélectionnées.

La section 4.2 présente les calculs thermodynamiques et les résultats expérimentaux menés en l'absence de CaO. Concernant NaCl, seulement 1,2% du contenu chloré est converti en phase gazeuse lors de la pyrolyse de la ressource (jusqu'à 850°C). Il a aussi été montré que le taux de conversion du chlore vers la phase gazeuse est légèrement augmenté en présence de dioxygène, d'eau ou de minéraux tels que SiO_2. Expérimentalement, le taux de conversion maximal atteint était de 8% en combinant les 3 promoteurs à 950°C. Par contre, la pyrolyse du PVC conduit à la libération de HCl dès 200°C. L'analyse thermogravimétrique, couplée à une analyse des gaz émis par FTIR, a montré que la gamme de température d'émission de HCl à partir du PVC se situe entre 200 et 400°C. Ainsi, toute la fraction chlorée du PVC conduit à la formation de HCl, dans cette gamme de température, par des réactions de déchloration. Les pertes de masses observées au-delà de 400°C concernent la pyrolyse de la matière organique restante.

La section 4.3 est dédiée à l'étude de l'efficacité de la rétention d'HCl par le réactif CaO lors de la pyrolyse du PVC. De manière générale, il est démontré que l'efficacité à la mitigation du HCl généré in-situ est meilleure à 550°C comparativement aux autres températures (650, 750 et 850°C). L'efficacité à l'abattement de HCl augmente de manière significative lorsque le rapport molaire Ca/Cl est augmenté, et la taille des particules de CaO diminué. Pour une pyrolyse de PVC réalisée à 750°C, le taux de chlore piégé par CaO est de 85,6% lorsque le ratio molaire Ca/Cl est fixé à 2:1.

Enfin, la section 4.4 présente les calculs de modélisation cinétique de la conversion du PVC. La modélisation a été réalisée à partir d'essais d'analyse thermogravimétrique à différentes vitesses de montée en température, et en considérant une séparation du phénomène global en 3 composantes : (1) la déchloration, (2) la formation de composés

aromatiques benzéniques et (3) la décomposition des polyènes et la cyclisation. Les paramètres cinétiques caractéristiques ont été extraits en présence et en l'absence du réactif CaO. En l'absence de CaO, les calculs ont montré que l'énergie d'activation apparente vaut 136,5 kJ/mol, 193,7 kJ/mol, et 281,6 kJ/mol pour, respectivement, les composantes 1, 2 et 3. L'ajout de CaO modifie de manière significative l'énergie d'activation apparente globale, en la diminuant de 197,3 à 148,9 kJ/mol, et l'énergie d'activation de la composante 1, en l'augmentant de 136,5 kJ/mol à 152,6 kJ/mol. D'un point de vue cinétique, la présence de CaO est ainsi favorable à l'immobilisation du chlore dans le réacteur, et à la pyrolyse de la matière organique

Résumé du Chapitre 5

Influence du réactif CaO sur l'émission de goudrons lors de la pyrolyse des composés modèles représentatifs des déchets municipaux

Ce travail vise à étudier la capacité de CaO à limiter les goudrons émis par les composés modèles des déchets municipaux. Ainsi, les expériences sont menées avec chaque composé modèle (bois, déchet alimentaire, PVC) pris individuellement en présence et en l'absence de CaO. Les goudrons émis sont identifiés et quantifiés. Ce travail a été réalisé avec le montage Py-GC/MS à différentes températures. Les conclusions principales sont résumées ci-dessous :

- La présence de CaO, lors de la pyrolyse du bois et des déchets alimentaires, favorise la formation de composés aromatiques et limite la quantité relative de composés oxygénés dans les goudrons
- Le PVC produit principalement des dérivés aromatiques en raison de l'élimination du chlore (voir figure 5.0.1). Le rôle du réactif CaO est surtout mesuré en termes d'immobilisation de HCl, conduisant à une réduction des dérivés organiques chlorés

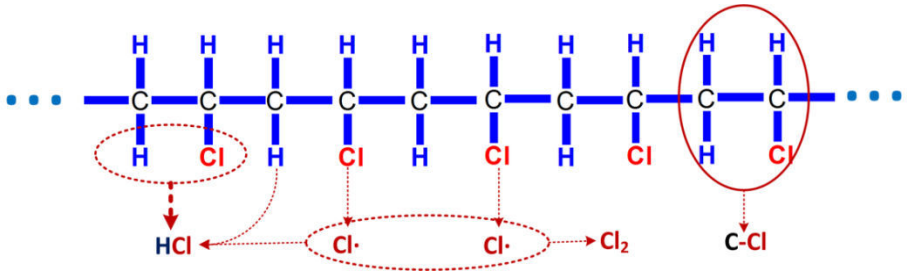

Figure 5.0.1 Mécanisme de formation des composés chlorés lors de la pyrolyse du PVC

- La présence du réactif CaO augmente la production de goudrons à haute valeur ajoutée, tels que les BTXN (benzène, toluène, xylène et naphtalène), issus de la pyrolyse du bois et des déchets alimentaires.
- A l'inverse, le taux de BTXN est significativement réduit lors de la pyrolyse du PVC en présence de CaO
- En présence de CaO, l'augmentation de la température conduit à une décroissance monotone du taux de BTX entre 550 et 850°C, et à une augmentation simultanée du taux de naphtalène.

Résumé du Chapitre 6

Influence du réactif CaO sur l'émission de HCl et de goudrons lors de la pyrolyse d'un mélange simulé de déchets municipaux

Dans ce chapitre, les déchets municipaux sont simulés par un mélange modèle contenant des fractions définies de chaque composé modèle. Le but est d'évaluer l'effet du réactif CaO placé in-situ dans le réacteur et de la température sur la rétention du chlore, et sur la qualité/quantité des goudrons émis. Les résultats expérimentaux sont présentés en développant successivement : (1) le bilan matière et la composition du gaz ; (2) l'efficacité à l'abattement de HCl et (3) le craquage des goudrons.

Les expériences menées à partir de la composition simulée sont présentées à la section 6.2. Les résultats montrent que l'augmentation de température augmente le taux de gaz produit et donc diminue les fractions du résidu solide et des goudrons. Ainsi, en l'absence de CaO, la quantité de gaz produite représente 81,9 mL/g-mélange à 550°C et 451,4 mL/g-mélange à 850°C. En présence de CaO, et aux mêmes températures, ces valeurs sont portées à 110,9 et à 510,2 mL/g-mélange. Du point de vue de la qualité énergétique du gaz produit, les quantités de H_2 produites représentent 6,76 à 79,52 mL/g-mélange à respectivement 550 et 850°C, puis sont augmentées de 25 et 88% en présence de CaO aux mêmes températures.

Les expériences menées en utilisant le réactif CaO à la section 6.2 montrent que le taux de résidu solide a tendance à augmenter tandis que la production de goudrons diminue. L'augmentation de masse du solide provient de la rétention efficace des gaz acides tels que HCl et CO_2 par CaO. En effet, à la section 6.3, la rétention du chlore est évaluée à 92,4% à 550°C et 65,2% à 850°C, pour un ratio molaire Ca/Cl de 2:1. L'augmentation du ratio molaire de Ca/Cl améliore significativement le taux de rétention du chlore (par exemple, à 750°C, la rétention du chlore augmente de 42% à 86% pour des ratios molaires de 1:2 et 4:1). Les analyses physico-chimiques du solide après les tests montrent que le chlore est immobilisé dans la fraction solide, principalement sous forme de CaClOH. Ces travaux menés avec le mélange simulé montrent que les conditions optimales pour immobiliser le chlore et fournir un gaz de bonne qualité énergétique en quantités élevées sont 750°C et un ratio molaire Ca/Cl de 2:1.

Enfin, la section 6.4 montre que l'utilisation de CaO, ainsi que l'augmentation de la température, permettent de réduire efficacement la quantité de goudrons produits au cours de la pyrolyse du mélange simulé. La composition des goudrons est aussi affectée par les conditions opératoires. En effet, à basse température les composés majoritaires sont de nature aliphatique, tandis que les hautes températures conduisent à la formation de composés aromatiques, par des réactions de craquage et de cyclisation. En présence de CaO, l'impact majoritairement observé est la réduction des goudrons de nature oxygénée, et l'augmentation de naphtalène et de ses dérivés.

Résumé du Chapitre 7

Analyse de cycle de vie appliquée aux technologies de conversion thermochimique des déchets municipaux et évaluation des technologies de contrôle du HCl émis

L'objectif de ce chapitre est l'évaluation et l'optimisation des technologies actuelles de traitement thermique des déchets municipaux par analyse du cycle de vie (ACV). De plus, une attention particulière a été portée aux systèmes de pyro-gazéification couplés à diverses stratégies de d'abattement des émissions de HCl (par exemple ex-situ à basse température, ex-situ à haute température, et in-situ à la température de pyro-gazéification). L'objectif de cette étude est d'apporter des éléments et outils décisionnels pour l'amélioration locale des stratégies de management des déchets municipaux. Dans ce but, deux études d'ACV ont été menées.

La première étude (section 7.2) est principalement dédiée à l'évaluation de différents systèmes de traitement thermique des déchets municipaux existants : incinération conventionnelle (S1), pyrolyse (S2), gazéification (S3), et le système de gazéification / fusion des cendres (S4). L'étude se concentre sur l'impact environnemental de chaque système et les principaux processus en cause. Le périmètre d'étude est exposé à la figure 7.0.1.

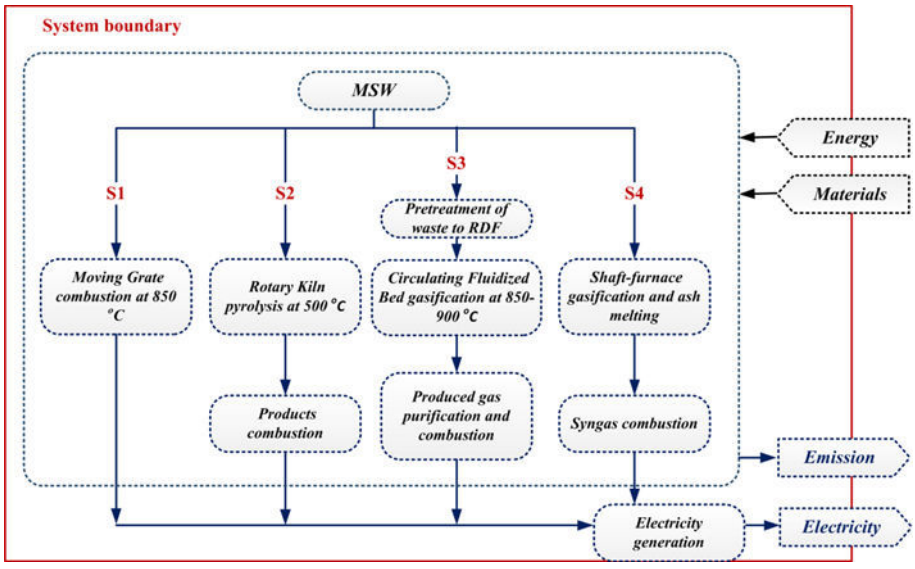

Figure 7.0. 1 Périmètre d'étude des 4 scénarios évalués: S1 = incinération, S2 = pyrolyse, S3 = gazéification et S4 = gazéification et fusion de cendres

Les calculs montrent que le scénario 3 (gazéification) conduit aux meilleures performances environnementales pour les principales catégories suivantes : le réchauffement climatique (GWP), l'acidification (AP) et l'écotoxicité terrestre (TETP) ; mais conduit à un impact négatif sur l'écotoxicité aquatique (FAETP). Le scénario 4 apparaît comme le pire scénario lors de l'évaluation de GWP, TETP, et la toxicité humaine (HTP) ; mais en contrepartie apparaît efficace pour réduire l'impact environnemental associé à l'eutrophisation (EP) et à l'écotoxicité aquatique. Basé sur les performances environnementales, les scénarios peuvent être classés comme suit (du meilleur au moins performant) : S3, Gazéification > S2, Pyrolyse > S4, Gazéification-fusion de cendres > S1, Incinération.

Parmi les principaux facteurs susceptibles d'impacter l'environnement, les fumées de cheminées ont un impact négatif pour la plupart des catégories, tandis que les paramètres « économie d'énergie » et « recyclage des métaux » ont les impacts les plus positifs. L'approvisionnement en matière et en énergie a un impact mineur dans les scénarios S1 et S2, tandis qu'il est beaucoup plus significatif pour les scénarios S3 et S4, en raison des étapes de prétraitement et d'addition d'une énergie auxiliaire.

Dans la section 7.3, la performance environnementale est évaluée en prenant en compte différentes technologies et options de réduction des émissions de chlore. Trois scénarios sont ainsi évalués et représentés à la figure 7.0.2 : S4, gazéification avec fusion des cendres puis une étape de traitement du chlore ex-situ à basse température (APC) ; S3, gazéification suivie d'une étape d'épuration du chlore ex-situ à haute température (système existant sur le site de Lahti) ; et un scénario S3' hypothétique, proposant la gazéification et l'abattement du chlore in-situ en présence du réactif CaO. Le but est ainsi de comparer ces 3 scénarios du point de vue du potentiel bénéfice que pourrait apporter l'abattement du chlore in-situ.

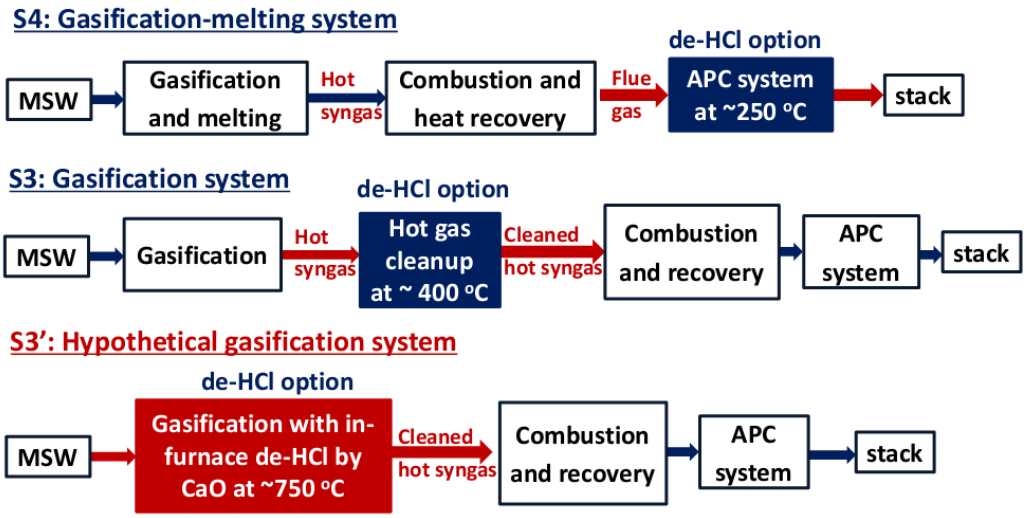

Figure 7.0.2 Présentation des 3 scénarios couplant le traitement thermique des résidus solides avec l'abattement du chlore, par méthode ex-situ ou in-situ : S4, gazéification avec fusion des cendres puis traitement du chlore ex-situ à basse température (APC) ; S3, gazéification puis épuration du chlore ex-situ à haute température ; et S3', gazéification et abattement du chlore in-situ en présence du réactif CaO

Les résultats montrent que le scénario hypothétique (S3'), basé sur l'abattement in-situ du chlore, atteint les meilleures performances environnementales évaluées sur les catégories GWP, AP, TETP, et HTP. Le scénario S4 présente lui aussi d'excellentes performances, relatives à l'eutrophisation (EP) et à l'écotoxicité aquatique (FAETP), comme déjà identifié à la section précédente. Finalement, le scénario hypothétique S3' offre des performances environnementales supérieures au scénario S3, en raison de l'utilisation d'une seule étape combinée. Tout ce travail doit cependant être utilisé et commenté avec précautions, car l'évaluation de S3 et S4 a été menée avec des données existantes tandis que le scénario S3' a été construit de manière théorique et simplifiée.

Résumé du Chapitre 8

Conclusion générale et perspectives

Ce chapitre résume les conclusions principales du travail réalisé ainsi que les perspectives. La présence de chlore dans les résidus solides de type déchets municipaux entraine différents désagréments, qui nuisent au bon fonctionnement d'une unité de thermoconversion, tels que la corrosion, la formation de polluants toxiques, l'acidification.... De plus, la présence de chlore dégrade la qualité de l'huile de pyrolyse, de par la présence de composés chlorés. En vue de développer des technologies de pyro-gazéification à la fois efficaces énergétiquement et respectueuses de l'environnement, ce travail de thèse s'est focalisé sur l'utilisation d'un réactif CaO in-situ pour évaluer son impact sur les émissions de chlore et de goudrons. En complément, une analyse de cycle de vie a été menée afin d'évaluer les performances environnementales des systèmes de pyro-gazéification de déchets. Les principales conclusions sont présentées au travers des 3 points suivants.

- **Mitigation de HCl à haute température par le réactif CaO : courbes de percée et modélisation cinétique**

Le but était d'étudier la capacité du réactif CaO à immobiliser le gaz HCl à l'intérieur du réacteur et d'étudier le mécanisme de réaction afférent à la réaction gaz/solide. Pour se faire, les courbes de percée ont été obtenues sous différentes conditions opératoires, puis une modélisation cinétique a permis de mettre en évidence les régimes cinétiques.

D'abord, les calculs thermodynamiques ont permis de déterminer l'enthalpie libre et la constante d'équilibre de la réaction entre CaO et HCl. La formation de $CaCl_2$ et H_2O à partir de CaO est HCl est une réaction spontanée dont la constante d'équilibre de la réaction vaut environ $7x10^{16}$ à 500 K et $2x10^4$ à 1200 K. Expérimentalement, la tendance dégagée par les calculs thermodynamiques est confirmée. En effet, la capacité de rétention d'HCl diminue de 778,9 à 173,9 mg/g-CaO lorsque la température augmente de 550 à 850°C. Cependant la température n'est pas seule responsable de cette diminution. En effet, le produit de la réaction, $CaCl_2$, forme une couche plus ou moins poreuse en surface du CaO.

La confrontation des résultats expérimentaux avec les modèles cinétiques montre que l'étape cinétique déterminante est la réaction chimique hétérogène (à la surface du CaO non réagi), puis la diffusion de HCl à travers la couche de produit formée ($CaCl_2$). Entre ces 2 régimes, une zone de régime mixte apparaît dont l'étendue dépend de la température.

Les analyses physico-chimiques menées sur les résidus solides après abattement de HCl montrent que la surface spécifique et le volume poreux du solide diminuent significativement avec l'augmentation de la température. Les images de microscopie électronique à balayage confirment que la texture poreuse se densifie d'autant plus rapidement (sous-entendu à plus faible taux de conversion de CaO) que la température est élevée.

- **Utilisation d'un réactif CaO in-situ dans le réacteur de pyro-gazéification : impact sur l'abattement des émissions de HCl et sur la valorisation des goudrons**

L'étude porte sur la capacité de CaO à retenir le HCl généré in-situ dans le réacteur par pyro-gazéification de ressources contenant du chlore organique ou inorganique. Typiquement pour les températures de pyrolyse envisagées (550-850°C), l'émission de HCl provient quasi exclusivement de ressources organiques. L'efficacité de la rétention d'HCl par le réactif CaO lors de la pyrolyse du PVC atteint 85,6% à 750°C et pour un ratio molaire Ca/Cl de 2:1. La cinétique de la pyrolyse du PVC a été étudiée au travers de 3 composantes : (1) l'émission de chlore, (2) la formation de composés aromatiques benzéniques et (3) la décomposition des polyènes et la cyclisation. L'ajout de CaO modifie de manière significative l'énergie d'activation apparente globale, en la diminuant de 197,3 à 148,9 kJ/mol, et l'énergie d'activation de la composante 1, en l'augmentant de 136,5 kJ/mol à 152,6 kJ/mol.

L'émission de HCl et son immobilisation par CaO ont été étudiées en utilisant un mélange simulé de résidus solides. La quantité de gaz produite augmente de 336.2 mL/g-mélange à 375.7 mL/g-mélange en présence de CaO à 750°C. La qualité énergétique du gaz produit, est aussi augmentée par l'ajout de CaO. A 750°C, les quantités de H_2 produites augmentent de 49.3 mL/g-mélange à 64.7 mL/g-mélange.

L'amélioration de la qualité du gaz produit est à la fois le résultat de l'abattement de polluants tels que HCl mais aussi CO_2, et le craquage des goudrons ; augmentant ainsi le taux de conversion vers la phase gazeuse. De plus, la présence de CaO améliore la qualité de l'huile de pyrolyse en réduisant la part de composés oxygénés.

Le meilleur compromis quantité de gaz / qualité énergétique du gaz / immobilisation de HCl / craquage des goudrons est obtenu à 750°C et pour un ratio molaire Ca/Cl de 2:1.

- **Analyse de cycle de vie appliquée aux technologies de conversion thermochimique des déchets municipaux couplées à différentes options d'abattement des émissions chlorées**

L'évaluation de différents systèmes existants de traitement thermique des déchets municipaux : incinération conventionnelle (S1), pyrolyse (S2), gazéification (S3), et le système de gazéification / fusion des cendres (S4) a été réalisée. Les calculs montrent que le scénario 3 (gazéification) conduit aux meilleures performances environnementales pour les catégories suivantes : le réchauffement climatique (GWP), l'acidification (AP) et l'écotoxicité terrestre (TETP) ; mais conduit à un impact négatif sur l'écotoxicité aquatique (FAETP). Le scénario 4 a l'impact le plus négatif sur les facteurs GWP, TETP, et la toxicité humaine (HTP) ; mais en contrepartie apparaît efficace pour réduire l'impact environnemental associé à l'eutrophisation (EP) et à l'écotoxicité aquatique. Basé sur les performances environnementales, les scénarios peuvent être classés comme suit (du meilleur au moins performant) : S3, Gazéification > S2, Pyrolyse > S4, Gazéification-fusion de cendres > S1, Incinération.

Dans un second temps, la performance environnementale a été évaluée en prenant en compte différentes technologies et options de contrôle des émissions chlorées. Trois scénarios sont ainsi évalués : S4, gazéification avec fusion des cendres puis une étape de traitement du chlore ex-situ à basse température (APC) ; S3, gazéification suivie d'une étape d'épuration du chlore ex-situ à haute température (système existant sur le site de Lahti) ; et un scénario S3' hypothétique, proposant la gazéification et l'abattement du chlore in-situ en présence du réactif CaO. Les résultats montrent que le scénario hypothétique (S3'), basé sur l'abattement in-situ du chlore, atteint les meilleures performances environnementales évaluées sur les catégories GWP, AP, TETP, et HTP. Le scénario S4 présente lui aussi d'excellentes performances, relatives à l'eutrophisation (EP) et à l'écotoxicité aquatique (FAETP), comme montré à la section précédente. Finalement, le scénario hypothétique S3' offre des performances environnementales supérieures au scénario S3, en raison de l'utilisation d'une seule étape combinée. Tout ce travail doit cependant être utilisé et commenté avec précautions, car l'évaluation de S3 et S4 a été menée avec des données existantes tandis que le scénario S3' a été construit de manière théorique et simplifiée.

À partir des conclusions établies par ce travail, de futures recherches pourraient permettre d'approfondir les points suivants :

- **Amélioration des propriétés du réactif CaO pour la mitigation de HCl à haute température :**

(i) Modifier les propriétés physico-chimiques pour augmenter la capacité de rétention.

(ii) Etudier la régénération ou la réutilisation du CaO usagé.

(iii) Développer un réactif efficace à haute température.

- **Compléter et détailler l'analyse de cycle de vie incluant les options de d'abattement du chlore**

Appendix

Appendix I

List of Figures

Appendix II

List of Tables

Appendix III

Publications related to this work

Publications in International Journals

- Tang Yuanjun, Dong Jun, Chi Yong, et al. Energy and Exergy Analyses of Fluidized-Bed Municipal Solid Waste Air Gasification[J]. **Energy & Fuels**, 2016, 30(9): 7629-7637.
- Tang Yuanjun, Dong Jun, Chi Yong, et al. Energy and exergy optimization of food waste pretreatment and incineration[J]. **Environmental Science and Pollution Research**, 2017, 24(22): 18434-18443.
- Dong Jun, Tang Yuanjun, Nzihou Ange, et al. Life cycle assessment of pyrolysis, gasification and incineration waste-to-energy technologies: Theoretical analysis and case study of commercial plants[J]. **Science of the Total Environment**, 2018, 626: 744-753.
- Zhou Zhaozhi, Tang Yuanjun, Chi Yong, et al. Waste-to-energy: A review of life cycle assessment and its extension methods[J]. **Waste Management & Research**, 2018, 36(1): 3-16.
- Dong Jun, Tang Yuanjun, Nzihou Ange, et al. Comparison of Waste-to-Energy technologies of gasification and incineration using life cycle assessment: case studies in Finland, France and China[J]. **Journal of Cleaner Production**, 2018, 203:287-300..

Publications in international conferences

- Yuanjun TANG, Yong CHI. Exergy analysis and exergetic life cycle assessment of MSW pyrolysis and gasification. **5th International Conference on Engineering for Waste and Biomass Valorization.** August 25-28, 2014, Rio de Janeiro, Brazil (Oral presentation)
- Yuanjun TANG, Jun DONG, Yong CHI, and Mingjiang Ni. Effects of calcium oxide as in-gasifier additive on the behavior of MSW air gasification. **6th International Conference on Engineering for Waste and Biomass Valorization**. May 23-26, Albi, France (Oral presentation)
- Yuanjun TANG, Yong CHI, Jun DONG, Ange. NZIHOU, Elsa WEISS-HORTALA, Mingjiang NI. Effects of CaO Additive on Simulated Municipal Solid Waste Pyrolysis. **7th International Conference on Engineering for Waste and Biomass Valorization**. July2-5, Prague, Czech (Oral presentation)

Abattement des contaminants chlorés lors de la pyro-gazéification de déchets en utilisant un réactif à base de CaO : étude expérimentale et analyse du cycle de vie

Le traitement thermique des déchets municipaux suscite de plus en plus l'attention du fait des gains énergétiques et environnementaux associés. Cependant, du fait de la présence de composés chlorés (sels, plastiques) de l'acide chlorhydrique (HCl) est généralement produit lors de ce traitement et provoque des désagréments tels que la corrosion, la formation de contaminants organiques toxiques, une acidification, etc. De ce fait, le but du présent travail de thèse vise à étudier le rôle d'un réactif à base de CaO (oxyde de calcium) pour l'abattement in-situ des émissions de HCl issues du traitement thermique des déchets.

Dans ce travail, l'absorption/réaction du gaz HCl par le lit catalytique de CaO a été étudiée expérimentalement et théoriquement. Tout d'abord, il a été montré que le lit de CaO conduit à un abattement significatif du HCl généré, formant une couche de $CaCl_2$ en surface des particules de CaO. Cependant, la température opératoire est un facteur important du procédé, la capacité d'absorption de HCl diminuant de 778,9 à 173,9 mg/g-CaO en augmentant la température de 550 à 850°C. L'analyse cinétique de la réaction, en confrontant les données expérimentales à différents modèles de réaction de surface sur une particule, montre que la diffusion du gaz HCl au travers de la couche de $CaCl_2$ (produit de la réaction de surface) est d'abord limitée par la réaction à l'interface puis par la diffusion de HCl dans cette couche poreuse en croissance.

Pour simuler la génération de HCl in-situ par une source organique, la pyro-gazéification du PVC a été effectuée en présence ou en absence de CaO. Une modélisation des différentes étapes de la décomposition du PVC en présence de CaO a montré que l'énergie d'activation apparente de la réaction de déchlorination était légèrement augmentée (de 136,5 à152,6 kJ/mol) tandis que l'énergie apparente globale de la pyro-gazéification du PVC est diminuée de 197,3 à 148,9 kJ/mol en utilisant CaO.

La génération in-situ de HCl a aussi été réalisée en utilisant un mélange modèle de déchets municipaux, contenant du chlore organique et inorganique. L'abattement en HCl a été évalué, et la nature chimique des goudrons a été analysée. En présence de CaO, la part de composés organiques oxygénés est réduite, améliorant ainsi la qualité des goudrons en vue d'un raffinage en bio-huile.

Une approche par analyse de cycle de vie a aussi été réalisée pour la pyro-gazéification et l'incinération des déchets municipaux. La modélisation a été réalisée en envisageant 3 scénarios de déchlorination : (1) gazéification avec fusion des cendres puis une étape de traitement du chlore ex-situ à basse température, (2) gazéification suivie d'une étape d'épuration du chlore ex-situ à haute température, (3) gazéification couplée à une déchlorination in-situ en présence du réactif CaO. Ce dernier scénario hypothétique offre les meilleures performances environnementales (par exemple: acidification, réchauffement, émissions polluantes toxiques….) mais reste un modèle théorique et simplifié.

Mots-clés: Déchets municipaux; Pyro-gazéification; Mitigation de HCl; Réactif CaO; Déchlorination in situ; Analyse du cycle de vie

Chlorinated contaminants mitigation during pyro-gasification of wastes using CaO reactant: experimental and life cycle assessment

Thermal treatment of municipal solid waste (MSW) attracts increasing attention due to the associated environmental and energy benefits. However, due to the chlorinated components of the MSW (salts, plastics) hydrogen chloride (HCl) is usually generated and may cause corrosion, toxic organic contaminants formation, acidification, etc. The present study focuses on the reactivity of a calcium oxide (CaO) reactant for in-situ mitigation of released HCl from thermal treatment of MSW.

In this work, sorption of HCl gas in CaO reactive bed has been experimentally and theoretically studied. First, it is shown that the use of CaO is effective to remove released HCl gas, by forming a $CaCl_2$ layer at the surface of CaO particles. However, temperature of the reactor is a key process parameter, since the removal capacity of HCl decreases significantly from 778.9 to 173.9 mg/g-CaO with the increase of temperature from 550 ^{o}C to 850 ^{o}C. A kinetics analysis has been developed by comparing experimental data with models describing the reaction at the particle surface. It has been concluded that the sorption of HCl at the CaO particle surface is firstly limited by the heterogeneous gas-solid reaction, followed by the HCl diffusion through this porous growing layer.

To simulate the in-situ generation of HCl from organic source, pyro-gasification of PVC has been performed with or without CaO addition. The experimental data have been then used for the modeling of the different PVC decomposition steps. Although the average apparent activation energy of pseudo dehydrochlorination reaction is increased from 136.5 kJ/mol to 152.6 kJ/mol with the addition of CaO, the apparent activation energy of the overall PVC decomposition has been decreased from 197.3 to 148.9 kJ/mol by using CaO reactant.

In-situ generation of HCl from organic and inorganic sources has also been conducted using simulated MSW. HCl mitigation has been evaluated together with the chemical speciation of the produced tars. Using CaO, the amount of oxygenated organic compounds has been reduced, improving the quality of the tars for a further bio-oil upgrading.

To complete the aforementioned works, life cycle assessment (LCA) of three typical pyro-gasification and incineration processes is conducted to compare their overall environmental sustainability. Moreover, pyro-gasification-based WtE systems with different dehydrochlorination strategies are further modeled: 1) conventional gasification system; 2) novel gasification coupled with ex-situ high temperature dehydrochlorination system; and 3) hypothetical gasification coupled with in-situ dehydrochlorination system. The obtained results could be applied to optimize the current waste pyro-gasification systems, with special focus on developing strategies for in-situ dehydrochlorination purpose.

Keywords: Municipal solid waste; Pyro-gasification; HCl mitigation efficiency; CaO reactant; In-situ dehydrochlorination; Life cycle assessment